Développement de nouvelles chambres à projection temporelle pour applications sociétales et académiques : tomographie muonique en environnement restreint et upgrade du détecteur proche de T2K

Marion Lehuraux

université PARIS-SACLAY

Development of new Time Projection Chambers for societal and academic applications : muon tomography in confined environment and T2K upgrade of the near detector

Développement de nouvelles chambres à projection temporelle pour applications sociétales et académiques : tomographie muonique en environnement restreint et upgrade du détecteur proche de T2K

Thèse de doctorat de l'université Paris-Saclay

École doctorale n°576 : Particules, hadrons, énergie et noyau : instrumentation, imagerie, cosmos et simulation (PHENIICS)
Spécialité de doctorat : Physique des Particules
Graduate School : Physique, Référent : Faculté des Sciences d'Orsay

Thèse préparée dans le Département d'Electronique des Détecteurs et d'Informatique pour la Physique (Université Paris-Saclay, CEA) sous la direction de David ATTIÉ, Directeur de Recherche

Thèse soutenue à Paris-Saclay, le 01 Décembre 2022, par

Marion LEHURAUX

Composition du jury
Membres du jury avec voix délibérative

Boris TUCHMING Directeur de Recherche, CEA/IRFU, Université Paris-Saclay	Président
Olivier DRAPIER Directeur de Recherche, LLR, Institut Polytechnique de Paris	Rapporteur & Examinateur
Alessandra TONAZZO Professeure, CNRS/APC, Université Paris Cité	Rapporteure & Examinatrice
Gianmaria COLLAZUOL Professeur, Universita de Padova	Examinateur
Boris POPOV Directeur de Recherche, CNRS/LPNHE, Sorbonne Université	Examinateur

THESE DE DOCTORAT
NNT : 2022UPASP157

Acknowledgements

I am not sure I had ever fully appreciated the meaning of an *Acknowledgements* section before today, as I am about to write my own, but it all makes sense now. Unlike every other section of this manuscript that has been carefully thought, corrected, revised, and required years of work, these few lines just came naturally and sincerely.

Before going any further, I would like to thank the members of the jury: Gianmaria Collazuol, Boris Popov, Boris Tuchming, and more particularly Olivier Drapier and Alessandra Tonazzo who kindly accepted to review my manuscript.

A work as personal, demanding and rewarding as the writing of a PhD necessarly comes with a little self-introspection: there are a few people in my life without whom I could not have achieved this, for various reasons, and these few words cannot begin to express the gratitude I feel towards them. I will try nonetheless.

My first thoughts are for my PhD supervisor David Attié. I am both sorry for putting you through the writing of a thesis again and immensely proud to be your first student. I would not have wanted anyone else to guide me and share this journey with. But no, I will not go for a run with you anymore, you are way too fast I think I almost died last time.

I would probably never have followed an education in Physics in the first place if it was not for the exceptional teachers I had in high school: Sébastien Lamothe, Cédric Pereira, Michel Jacquet and Alain Garnier. Thank you for always preserving and feeding my relentless (dare I say, sometimes probably annoying...) interest for sciences.

I know that I have not always been an easy child to raise, and today I would like to thank both my parents, Sophie and Vincent Lehuraux, the first doctors of the family. I know the sacrifices you made for me and how much you carried me over the years. Looking at where we are now, I hope you can feel proud.

To some of you I am a daughter, a colleague, a friend. To you Gilles, I am your canary deep down the coal mine! Yet for once, I am the one who wrote the book ! I apologize in advance, it is certainly not as entertaining as yours... Thank you for being my best friend, for making me part of your life and family. Speaking about family, thank you Chloe for being my crazy yet surprisingly wise for your young age other sister, as well as Tim's "Tata-ke". I cannot wait to see what you will teach him behind my back...

The little sanity I have left is without a doubt thanks to the constant support of my friends, colleagues (sometimes both) and family. I'd like to thank the CEA/DRF/Irfu/DEDIP for welcoming me these past few years, in particular Eric Delagnes, Alain Delbart, Esther Ferrer-Ribas, Nathalie Le Devedec, Christine Porcheray and Maxence Vandenbroucke without whom the daily life would definitely not have been the same. Special mention to Hector Gómez, even though you do not like chocolate, you have been my best Kapton and coffee break team mate !
I also had the chance to be partially adopted by the DPhP which is why I would like to thank Sara Bolognesi and Paul Colas. I am particularly grateful towards Samira Hassani, who could always understand (if not share) my pain and whose support has been invaluable, and Jean-François Laporte who was always as enthusiast as I was about any new idea my weird brain would come up with instead of writing... I would also like to thank Denis Calvet and Irakli Mandjavidze for their incredible help about the electronics: I may not be fluent in hexadecimal quite yet but it is definitely thanks to you that I can decode binaries with only minor headaches !
Before I joined CEA for my PhD, I spent a year as a master student working on LHCb in Edinburgh: this is where I realized that I wanted to do research in particle physics for the rest of my life. For this, I will forever be grateful to Greig Cowan and Marco Pappagallo. I only started believing in myself because you did (and I tend to trust you more than myself...). I would not be here today if it was not for you.

Finally, to you Eric, my almost-husband, my rock, thank you for carrying our little family alone while I was not much help and following me towards new dreams. I am so lucky to have you by my side and I cannot

wait to see what our life will look like. And to you my son, Timothée. For so long in my life I was convinced that my PhD would be my greatest accomplishment, I could not have been more wrong.

Résumé

Les chambres à projection temporelles (TPC) sont des trackers gazeux particulièrement utilisés sur les expériences de physique des particules pour leurs performances en terme de résolution spatiale et en énergie. Une particule chargée, en traversant la TPC, ionise les atomes de gaz sur son passage tandis que l'application d'un champ électrique permet de guider les électrons ainsi produits jusqu'au plan de lecture. Il s'agit du premier détecteur permettant une reconstruction tridimensionnelle directe, utilisant la projection de la trace pour reconstruire les coordonnées (x, y) et le temps d'arrivée des électrons pour déduire la coordonnée z. Par ailleurs, en présence d'un champ magnétique, la mesure simultanée de l'impulsion de la particule ainsi que de son énergie permet son identification. Les performances de tels detecteurs dependent du champ électrique appliqué, du choix du gaz, mais aussi du système d'amplification et de lecture utilisé. Dans le cadre de cette thèse, les TPC développées sont lues par des détecteurs Micromégas. Le concept du détecteur Micromégas repose sur l'utilisation d'un tissu métallique qui permet l'application d'un champ électrique beaucoup plus intense au voisinage du plan de lecture. Les électrons sont guidés au travers du maillage fin de ce tissu et vont alors créer des avalanches, amplifiant ainsi le signal collecté. Depuis leur invention en 1996, ces détecteurs ont été considérablement perfectionnés et optimisés pour un vaste champ d'applications possibles[1].

Dans le cadre de ce travail, deux instruments sont développés en parallèle, chacun reposant sur une technologie spécifique et pour une application précise. D'une part, le détecteur D3DT (Détecteur 3D pour Tomographie muonique) est une TPC lue par un détecteur Micromégas 2D-multiplexé pour répondre à des contraintes de compacité, et qui vise à être utilisé pour l'étude des sous-sol par tomographie muonique. D'autre part, les modules ERAM (Encapsulated Resistive Anode Micromegas) constituent les plans de lecture résistifs des nouvelles TPCs qui seront installées au niveau du détecteur proche de l'expérience T2K au Japon. Les chapitres 2 à 5 se concentrent sur D3DT tandis que les suivants présentent les contributions faites à l'expérience T2K.

Pour mieux comprendre les motivations et le design du détecteur D3DT, il faut s'attarder plus en détail sur le concept de tomographie muonique détaillé dans le chapitre 2. Cela consiste en le fait d'utiliser les muons issus d'intéractions entre le rayonnement cosmimque et des noyaux de la haute atmosphère comme des sondes pour étudier la densité d'objets divers. En fonction des dimensions de l'objet en question, plusieurs configurations sont possibles. S'il est envisageable de placer des détecteurs en amont et en aval, on va reconstruire la direction de chaque muon avant et après avoir traversé l'objet. L'angle de déviation entre ces deux directions donne une indication sur la densité de l'objet traversé, on parle alors de muographie par déviation. Le cas échéant, on peut placer des détecteurs en aval uniquement et mesurer le flux de muons détectés en fonction de leurs directions. On parle alors de muographie par absorption.

Le développement du premier détecteur Micromégas multiplexé en 2013 ouvrit la porte à des applications de tomographie muonique. En effet, les bancs de mesure précédents étaient trop volumineux pour

1: Plus de détails sur le fonctionnement des TPCs, détecteurs Micromégas et leurs applications sont donnés dans Chapitre 1.

envisager être déployés. Grâce au multiplexage, qui permet de lire plusieurs pistes du détecteur avec une seule voie d'électronique sans pour autant perdre en résolution, le volume ainsi que la consommation électrique des télescopes à muons ont pu être suffisemment réduits pour en faire un instrument transportable. Après quelques années de perfectionnement, ces détecteurs ont pu être installés dans la pyramide de Khéops afin de participer à la mission ScanPyramids et ont permis de découvrir des cavités inconnues jusqu'alors. Fort de ce succès, le CEA entreprit d'élargir encore le spectre d'applications de la tomographie muonique en développant un détecteur encore plus compact et avec une acceptance angulaire proche de 2π, D3DT. En effet, une limite importante des télescopes à muons réside dans leur directionnalité. Si la position de l'objet à étudier est connue, on peut déterminer l'emplacement optimal où placer le télescope de façon à ce que l'objet en question se retrouve dans son acceptance angulaire. À l'inverse, si l'on chercher à étudier une zone sans connaissances préalables, l'acceptance angulaire du télescope limite la zone scannée et donc la durée de la mesure. L'acceptance angulaire accrue de D3DT permettrait de sonder toutes les directions à la fois.

Lorsque j'ai rejoint l'équipe, le design du détecteur était tout juste terminé et l'objectif était donc d'assembler et tester divers prototypes ainsi que de mettre au point un algorithme de reconstruction de traces adapté au multiplexage du plan de lecture. Il s'agirait d'une TPC cylindrique de 40 cm de long pour 14 cm de diamètre (dimensions choisies afin de pouvoir être inséré dans des trous de forage) lue par un détecteur Micromégas. Afin d'optimiser au maximum la compacité et la consommation électrique de cet instrument, plan de lecture est 2D-multiplexé, c'est-à-dire que chaque voie d'électronique lit 6 à 9 pixels différents. Entre la cage de champ et l'enceinte mécanique, un cylindre creux de plastique scintillateur lu par des fibres optiques servira de trigger externe. Le chapitre 3 décrit en détail le design du détecteur ainsi que les divers prototypes qui ont été développés au cours de ce travail. Ils peuvent être classés en 3 catégories : des prototypes dits préliminaires lorsque l'on ne disposait pas encore de toutes les pièces mécaniques nécessaires à l'assemblage du détecteur, des prototypes de courte dérive permettant une caractérisation précise et systématique du plan de lecture, et enfin des prototypes taille réelle qui correspondent au design final. Les difficultés rencontrées, principalement dues aux tensions d'alimentations importantes pour les dimensions du détecteur, sont également reportées.

Une partie importante de mon travail fut la caractérisation du plan de lecture Micromégas. Une première campagne de mesure permit de valider les performances globales du détecteur en terme de gain et résolution en énergie. Cependant, étant donné qu'il s'agit du premier Micromégas 2D-multiplexé, certains comportements étaient encore inconnus. En particulier, je voulais étudier les variations de performances en fonction de la position du signal détecté pour vérifier la présence d'éventuelles corrélations avec le facteur de multiplexage. Pour cela, j'ai développé spécifiquement un banc de test automatisé à partir d'une imprimante 3D permettant de déplacer une source de Fer 55 précisément au dessus de chacun des 1344 pixels du plan de lecture. Pour chaque position, le spectre en énergie de la source est reconstruit et ajusté par une Gaussienne pour extraire le gain et la résolution en énergie. On a pu observer que les performances sont uniformes à plus ou moins 10% et l'origine de cette

dispersion a pu être identifiée comme un défaut de construction des PCBs (Printed Circuit Board) qui pourra être corrigé pour les futures versions. Par ailleurs, aucune corrélation n'est observée entre les performances locales du détecteur et le facteur de multiplexage ce qui permet de valider les performances du plan de lecture. Ces résultats ont été présentés et publiés en tant que proceedings pour les conférences VCI 2022[2] et ICHEP 2022[3].

2: https://vci2022.hephy.at

3: https://www.ichep2022.it

En paralèlle du développement des prototypes et de leur caractérisation, il eu fallut préparer l'analyse des données en en particulier la reconstruction des traces. Du fait que le détecteur soit multiplexé, le rapport signal à bruit de chaque évènement est nécessairement inférieur à 14% ce qui rend inutilisable la plupart des algorithmes de reconstructions habituels. J'ai donc conçu un algorithme de reconstruction basé principalement sur la méthode RANSAC (RANdom SAmple Consensus) qui permet d'estimer les paramètres d'un modèle pour un set de données bruité. Une première phase vise à identifier grossièrement la direction de la trace pour supprimer une partie du bruit, puis des ajustements plus fins sont faits sur les données pré-sélectionnées. J'ai pu réaliser des simulations qui ont permis de tester cet algorithme et estimer à 90% ses performances de reconstruction en comparant la direction reconstruite à la direction générée. Finalement, ces simulations peuvent également être utilisées pour prédire la meilleure résolution angulaire atteignable par D3DT avec cette reconstruction : on obtient 6.5 mrad, ce qui est comparable à la résolution angulaire des télescopes qui varie entre 4 et 10 mrad.

Comme précédemment mentionné, au cours de ma thèse j'ai également pu contribuer à l'expérience T2K, installée au Japon, qui vise à étudier le phénomène d'oscillation des neutrinos. Un détecteur proche ND280 caractérise précisément le faisceau de neutrino tandis que le détecteur lointain reconstruit le spectre en énergie des neutrinos détectés 290 km plus loin. Depuis sa mise en service en 2010, T2K a déjà publié d'importants résultats concernant les paramètres de la matrice PMNS et l'observation d'oscillation de neutrinos muoniques en neutrinos électroniques. Néanmoins, il a été montré par simulation que l'on pourrait encore réduire les incertitudes sur les valeurs des paramètres mesurés voire investiguer la violation de symmétrie CP si le détecteur proche subissait une mise à niveau. Plus particulièrement, des TPCs horizontales (que l'on nommera par la suite HA-TPCs) doivent être ajoutées afin d'améliorer l'acceptance du détecteur ainsi que l'efficacité de reconstruction des traces à grand angle[4]. Le CEA est en charge du développement des modules ERAM qui sont les plans de lecture des HA-TPCs. Étant donné que les performances des TPCs déjà installées sur ND280 étaient très satisfaisantes, l'idée était que le design des HA-TPCs soit identique. Cependant, pour des raisons d'occupation et d'électronique, la même segmentation du plan de lecture ne pouvait pas être conservée. Pour ne pas perdre en résolution spatiale, la technologie du Micromégas résistif est utilisée : une couche résistive de Diamond-Like-Carbon (DLC) est déposée sur les pads et permet d'induire le signal sur plusieurs pads adjacents. Il faut ensuite utiliser une méthode de reconstruction connue sous le nom de Pad Response Function (PRF) pour reconstruire la position de l'avalanche électronique avec une précision meilleure que ce que permet en théorie la segmentation spatiale.

4: Le chapitre 6 présente en détails le design de l'expérience ainsi que des motivations pour l'upgrade.

J'ai eu la chance d'intégrer l'équipe alors que le premier prototype résistif

venait d'être assemblé et allait être testé en faisceau à DESY. J'ai donc eu la chance d'assister et de contribuer à l'évolution du design des modules ERAM, du premier prototype jusqu'au début de la production de série en 2020 et des tests de validation de performances[5].

5: Présenté en détails dans le chapitre 7

Dans un premier temps, j'ai travaillé sur un logiciel de monitoring dont l'objectif était de visualiser les traces détectées à partir des fichiers de données brutes et pendant la prise de données. C'est un outil crucial, particulièrement en test faisceau, car il facilite et accélère énormément l'installation, l'alignement et les différents réglages du détecteur. Plusieurs fonctions supplémentaires ont été implémentées, en particulier la génération d'histogrammes d'analyse préliminaire qui se remplissent au fur et à mesure de l'acquisition et fournissent diverses informations sur le run. Ce programme est toujours utilisé aujourd'hui lors des tests en laboratoire.

Après le test faisceau, j'ai participé à l'analyse des données en implémentant la méthode de la PRF pour reconstruire la position des différents hits et en déduire la résolution spatiale du détecteur. La méthode de la PRF est une méthode itérative calibrée sur des données réelles : un modèle phénoménologique décrivant l'étalement spatial de la charge est ajusté sur les données en en supposant que l'on connait la position des avalanches électroniques. On utilise en première approximation un fit global de la trace ou le barycentre des charges dans chaque cluster. Cette paramétrisation du modèle est ensuite utilisé pour extraire une meilleure estimation de la position du signal induit, ce qui permet de répéter le processus à l'itération suivante jusqu'à ce que les valeurs des paramètres du modèle convergent. La résolution spatiale du premier prototype, noté MM1, a pu être estimée à 200 µm pour les traces horizontales ce qui satisfait pleinement les exigences de T2K qui sont de 800 µm. Pour les traces à angle, la méthode utilisée précédemment, et plus particulièrement la définition des clusters selon une colonne, n'est plus valable ce qui conduit à une dégradation de la résolution spatiale allant jusqu'au millimètre pour les traces à 45°. En adoptant une définition des clusters dépendante de la trace, on peut corriger cet effet et obtenir une résolution spatiale répondant aux critères de l'expérience pour tous les angles possibles. Les résultats de cette analyse ont été publiés dans la revue *N*uclear Instruments and Methods in Physics Research.

Malgré les résultats satisfaisants obtenus avec le détecteur MM1, d'autres prototypes ont été développés avec différentes valeurs de résistivité et capacitance de la couche résistive avec l'objectif d'étaler le signal sur un plus grand nombre de pads afin d'améliorer encore les performances du détecteur. Suite à la pandémie du Covid, ces détecteurs n'ont pas tous pu êtres testés en faisceau mais ont été caractérisés en laboratoire en utilisant les muons cosmiques. Une étude détaillée du gain et de la résolution spatiale de chaque détecteur en fonction des paramètres de la couche résistive a permis de fixer en 2020 le design de production présenté à la collaboration dans une Production Readiness Review.

En plus des paramètres de la couche résistive, des ajustements ont pu être faits au niveau du PCB comme par exemple l'utilisation d'un filtre haute tension intégré pour minimiser le nombre de boîtiers externes et l'occupation lors de l'installation au Japon. Aussi, des inhomogénéités de gain ont été observées lors de mesures systématiques des performances

utilisant un banc de test X-ray et ont pu être corrélées au masque de soudure du PCB qui a par conséquent été retiré dans les versions ultérieures.

Finalement, une nouvelle électronique de lecture a été développpée, utilisant les mêmes ASICs mais conçus pour être plaqués contre le détecteur pour répondre à des contraintes d'espace. A cette occasion, j'ai recherché une nouvelle paramétrisation de la réponse électronique. En effet, celle qui était utilisée jusqu'alors était phénoménologique et comportait trop de paramètres ce qui devenait limitant pour l'analyse des signaux. J'ai utilisé un logiciel de simulation pour modéliser l'ASIC AFTER directement pour obtenir une paramétrisation dont les paramètres peuvent être déduits des valeurs des composants électroniques. En utilisant le pulser interne des cartes électroniques j'ai pu obtenir des données de calibration, avec et sans détecteur connecté, sur lesquelles j'ai pu ajuster ce nouveau modèle et tester l'uniformité des réponses électroniques d'un ASIC à l'autre. Cette nouvelle description est maintenant utilisée dans l'analyse des données.

Au cours de ma thèse j'ai également travaillé sur la simulation de détecteurs Micromégas résistifs, et plus particulièrement sur l'étalement du signal induit. Jusqu'à maintenant, ce phénomène est décrit par une dérivation de l'équation du Télégraphe mais des formalismes mathématiques plus poussés existent et seraient à priori plus à même de tenir compte des phénomènes physiques en jeu. J'ai commencé à travailler en collaboration avec Werner Riegler suite à un meeting RD51 au cours duquel il avait présenté un formalisme dérivé du théorème de Ramo et formulé le souhait de le tester sur une géométrie d'un détecteur en particulier. J'ai donc implémenté ces calculs pour la situation partiuclière des modules ERAM comme détaillé dans le chapitre 8. Finalement, il s'avère que cette description est tout à fait compatible avec le modèle du Télégraphe et bien plus coûteuse en terme de ressources ce qui a permis de valider l'utilisation du modèle télégraphique pour notre analyse.

Contents

List of Figures

List of Tables

Part I

Introduction

Introduction

Time Projection Chambers (TPCs), as further explained in Chapter 1, are gaseous tracking detectors usually used in particle physics experiments. However, they can also make good candidates for societal applications such as muon tomography, which consist of using cosmic muons naturally produced in the high atmosphere to probe the density of objects. This is further explained in Chapter 2. My work, which is oriented towards instrumentation, presents the development of two TPCs with very different applications.

First the so-called D3DT (Detector 3D for muonic Tomography) detector, described in Chapter 3, which aims to detect cosmic muons to probe the underground. In order to fulfill the compacity requirements imposed by such application, the readout plane is a 2D-multiplexed Micromegas detector, which is a technology never used before. When I joined the team, the design was done but no prototype had been built yet. My work consisted in developing several prototypes to adjust the design accordingly to the difficulties encountered during the assembly or operation of the detector. In addition, I performed a precise characterization of the Micromegas readout plane, presented in Chapter 4, which lead to the development of an automatized test bench that can be used to characterize any small area detector in the lab. Finally, I developed a track reconstruction algorithm, presented in Chapter 5, adapted to the multiplexing of the readout plane.

The second is part of a larger experiment, called T2K, which study the oscillation of neutrinos thus probing the limits of the Standard Model. As a long baseline experiment, it is made of a near and far detector: the near detector is currently being upgraded in order to improve the efficiency of high angle tracks reconstruction thus reducing the systematic errors. This is explained in further details in Chapter 6. In the context of this upgrade, TPCs will be added to the existing near detector and read by resistive Micromegas readout plane called ERAM (Encapsulated Resistive Anode Micromegas). I contributed to the development of these modules, through the development of a monitoring software or the analysis of the data collected during a test beam in 2019. I was given the opportunity to present these results to external reviewers at the occasion of a Production Readiness Review. I also participated to the many tests conducted in the lab to optimize the performances of the detector before production. All these developments are reported in Chapter 7. Finally, I initiated a simulation effort to better understand and describe the charge spreading on the resistive layer. This work is presented in Chapter 8.

TIME PROJECTION CHAMBERS AND MICROMEGAS DETECTORS

1

During my PhD I had the chance to contribute to scientific development for both societal and academic applications, the common denominator being Time Projection Chambers (TPCs) and Micromegas detectors. In this Chapter, the general concepts required to understand the functioning of these two types of gaseous detectors are detailed with a specific attention given to experimental considerations. Finally, some examples of particularly successful applications of such technologies are also presented.

1.1 Brief history of Time Projection Chambers

If the atomistic view of matter was suggested as early as 500 BC in Ancient Greece philosophers like Leucippus, it is only in the 1900s that the first elementary particles were discovered. At this stage, particle detectors were mostly cloud chambers consisting of a sealed volume filled with a supersaturated vapour of alcohol or water. When an ionizing particle passes through the active volume, the produced ions act as condensation centers for the gas mixture thus creating droplets that are actually visible by the naked eye. Cloud chambers were invented by the physicist Charles Thomson Rees Wilson in 1911 [1] and allowed Carl Anderson to discover the positron in 1932 as well as the muon in 1936. Fig 1.1 shows a photograph of a positron track in a cloud chamber obtained by Carl Anderson at the time.

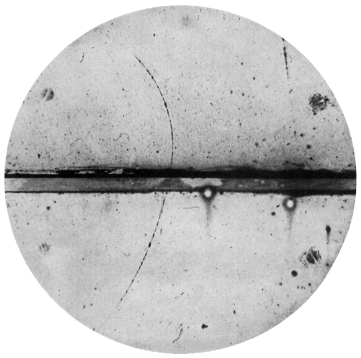

Figure 1.1: Cloud chamber photograph used to prove the existence of the positron. Observed by C. Anderson.

These discoveries fueled technological progress to develop new particle detectors that would not only allow for the visualization of particle tracks but also measuring the particle charge, energy, or even its mass. Years later, in 1968, Georges Charpak developed the first wire chamber at CERN [2]. Consider a volume delimited by grounded plates defining the cathode of the detector. Inside, taut anode wires at high voltage produce an electric field as shown in Fig 1.2. When an ionizing particle passes through the detector, the ionized electrons are drifted towards the closest wires where the signal is amplified and readout by an electronics. Another set of wires can be placed perpendicularly to the first one to obtain 2D information. This new detector comes with tremendous advantages compared to the cloud chambers:

- **it can be read by an electronics:** cloud chambers, as well as bubble chambers in the mean time, used photographic readout. Each event had to be photographed and analyzed by hand afterwards which is, at least inconvenient, and more importantly a strong limitation for large statistics analysis.
- **it does not require a metastable phase:** whether it was supersaturated vapour for cloud chambers or liquid heated just below boiling point for bubble chambers, both detectors required a lot of preparation for the active volume filling material.

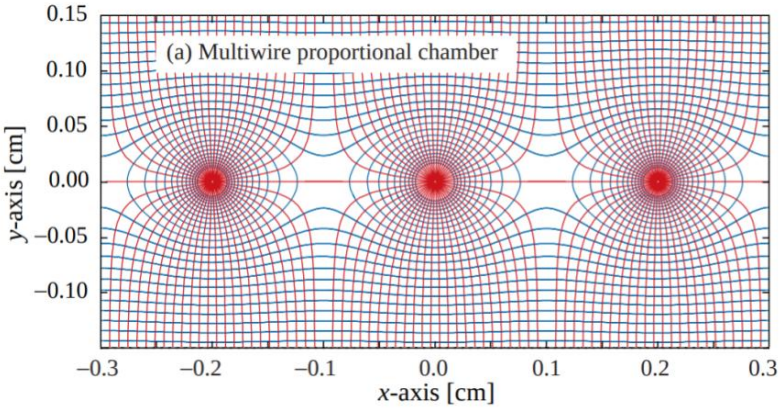

Figure 1.2: Electric field lines and equipotentials in a multiwire proportional chamber. Taken from [3].

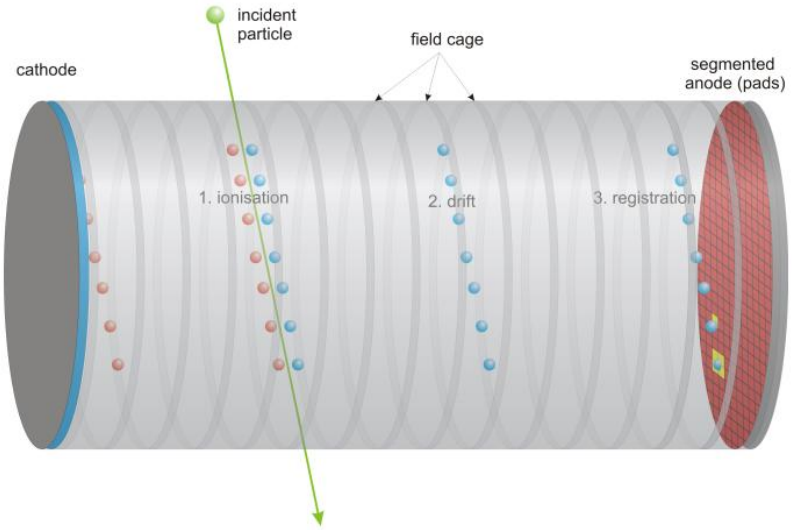

Figure 1.3: Working principle of a TPC (by O. Schäfer)

- **particle identification is made possible:** by carefully setting the anode voltage, the gas amplification near the wire is proportional and the detector works as a proportional counter (more details in Section 1.2). It means that the measured signal is proportional to the deposited energy which allows to measure the ionization energy loss of the particle. Combining this information with the particle momentum, that can be measured in the presence of a magnetic field to bend the particle track, particles can be discriminated.

However, the spatial resolution was limited by the spacing between the wires, and more importantly the wires were not ageing very well. The electron avalanche formation in the neighbouring of the wires act like micro plasma discharges creating radicals and polymers on the wires thus degrading the gas amplification, the wires and detector performances in general.

It is only a few years later, in 1974, that David R. Nygren offered a solution and designed the first Time Projection Chamber (TPC). This detector is the only electronically read gaseous detector delivering direct three-dimensional track information as well as particle identification capabilities based on ionization energy loss measurements. The working principle of a TPC is illustrated by Fig 1.3. The cathode is now at an extremity of the active volume while the anode, instead of being multiple

wires, is at the other end and usually segmented for the readout. A field cage uniformly degrades the drift electric field oriented so that electrons are guided towards the anode while cations are drifted towards the cathode. Two coordinates (r, ϕ) are extracted from the projection on the readout plane while the third z is obtained using the timing of drift of the electrons. Amplifying the signal using only the readout electronics can add a lot of electrical noise so usually an amplification stage is added upstream of the readout taking advantage of the gas gain: a higher electric field is applied near the anode so that primary electrons from the ionization create Townsend avalanches. This leads to a gain of the order of 10^4-10^5 for an amplification electric field of few tens of kV cm^{-1}. Micro-Pattern Gaseous Detectors (MPGDs) such as Gas Electron Multiplier (GEM) or Micromegas are good candidates to achieve both amplification and readout of a TPC. This thesis will particularly focus on Micromegas detectors that are described in Section 1.3.

More details about the general concepts at play in TPCs are given in the next section. Fig 1.4 summarizes the progress made in gaseous detectors development over the past century as well as some of the most important discoveries in the field of particle physics.

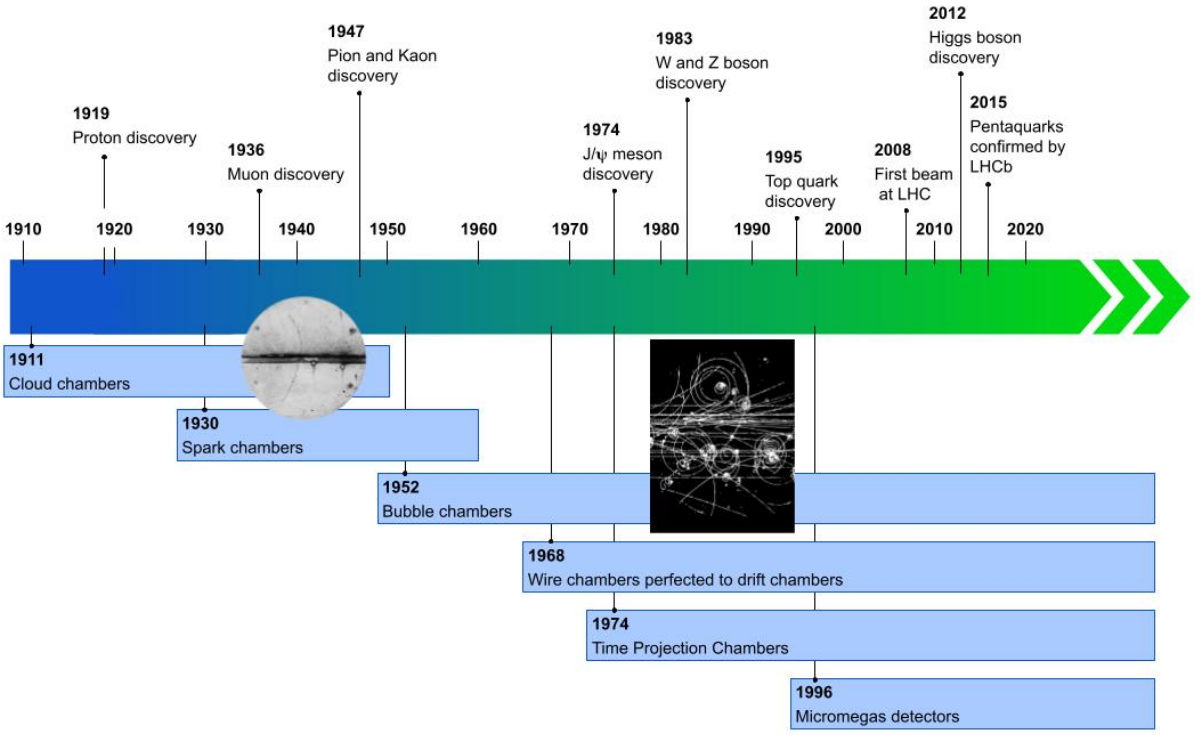

Figure 1.4: Timeline of the evolution of gaseous detectors viewed in parallel of some of the most important discoveries in the field of particle physics.

1.2 General concepts of Time Projection Chambers

1.2.1 Passage of an ionizing particle through the gas

Gas ionisation

When a charged particle passes through the detector active volume, it can either ionize or excite the gas atoms along the way. The number of ionizing collisions along a segment s of the track follows Poisson statistics so that the probability of having k ionizing collisions is given by:

$$P(k) = \frac{s^k}{\lambda^k k!} \exp(-s/\lambda) \qquad \lambda = \frac{1}{N_e \sigma_I} \tag{1.1}$$

where λ is the average distance between ionization clusters, N_e is the electron density of the gas and σ_I the cross-section of the ionization process. Fig 1.5 shows the distribution of this probability computed for a segment of track of $s = 1$ cm and for Argon gas properties in normal conditions of temperature and pressure (NTP). Sometimes, the electrons produced during an ionizing collision are energetic enough to further ionize the medium. The probability that a released electron has an energy E or larger follows Rutherford law which can be approximated by a $1/E^2$ dependence as illustrated by Fig 1.6 in the case of Ar-CH_4 (90:10) at NTP. This figure also shows in a dot-dashed line the practical range of the electrons in that same gas: it increases with the electron energy and reaches for example 70 µm for a 1 keV electron which represents about 0.6% of the primarily ionized electrons. This shows that the ionized electrons are actually organized in primary clusters which sizes depend on the statistics of the ionization processes as well as the gas properties, the charged particle energy loss, and the primary electrons energies. These fluctuations in ionization represent a limitation for the determination of the coordinates as well as particle identification.

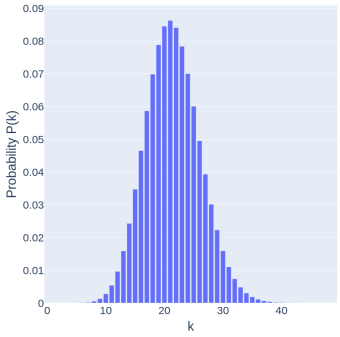

Figure 1.5: Distribution of the probability $P(k)$ of having k ionizing collisions computed for a segment of track $s = 1$ cm and assuming $\sigma_I = 10^{-19}$ cm^2 and $N_e = 2.14 \times 10^{20}$ cm^{-3} for Argon.

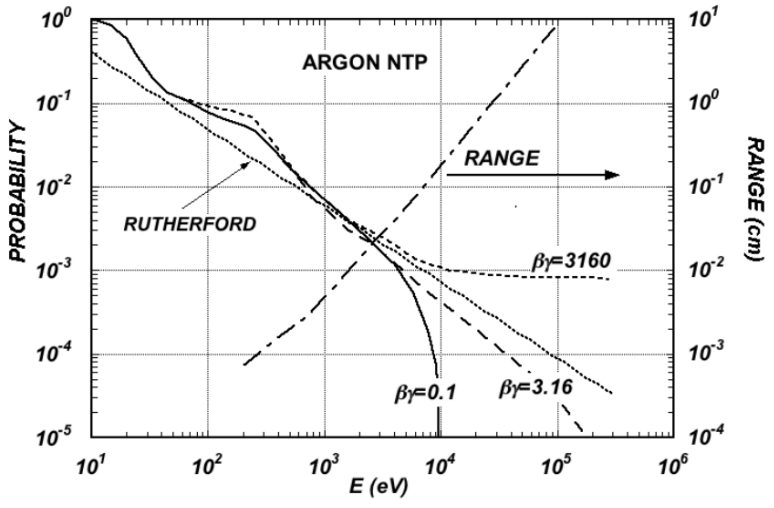

Figure 1.6: Probability of single collisions in which released electrons have an energy E or larger (left scale) and practical range of electrons in Ar/CH_4 (90:10) at NTP (dot-dashed curve, right scale). Taken from [3].

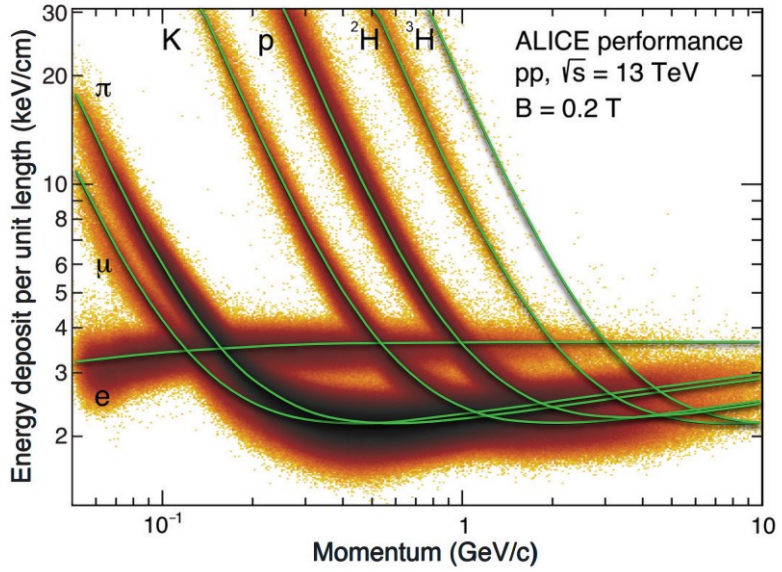

Figure 1.7: Energy deposit as a function of momentum measured in the ALICE TPC. Taken from [4].

Energy loss per unit of length and particle identification

The energy loss per unit of length, also denoted dE/dx, of the particle is a very important quantity to measure as, combined with the momentum, it can allow to identify the particle as illustrated by Fig 1.7 using the example of ALICE TPC [4]. The fluctuations of energy loss by ionization of a charged particle in a thin layer of matter can be described by a Landau distribution: the variations around the Most Probable value (MPV) are due to the previously discussed fluctuations in the number of electrons per primary clusters while the long tail can be explained by energetic knock-on electrons also called δ rays. Although rare events, the δ rays are energetic enough to shift the mean of the dE/dx distribution into the tail so that the mean energy loss computed using the Bethe equation discussed in section 2.1.3 is not representative of experimentally obtained distributions. This is why it is common to use the so-called *truncated mean* method where an optimized percentage of the most energetic hits is discarded so that the mean of the distribution can be used. The Bethe-Bloch formula can then be applied giving the mean deposited energy per unit of length as function of $\beta\gamma = p/m$ which is independent of the particle type. As illustrated by Fig 1.7, if plotted as a function of the particle momentum, the mean energy loss distributions are now shifted according to the mass which allows to perform particle identification. The separating power to discriminate two particles A and B is given by:

$$S_{AB} = \frac{2|\langle dE/dx\rangle_A - \langle dE/dx\rangle_B|}{\sqrt{\sigma^2_{\langle dE/dx\rangle_A} + \sigma^2_{\langle dE/dx\rangle_B}}} \tag{1.2}$$

where the energy resolution $\sigma_{\langle dE/dx\rangle_i}$ is empirically given by:

$$\sigma_{\langle dE/dx\rangle} = 0.41 N^{-0.43} (tP)^{-0.32} \tag{1.3}$$

where N is the number of measurements, t the thickness of sampling layer and P the gas pressure. The achieved energy resolution performances are usually below 10%.

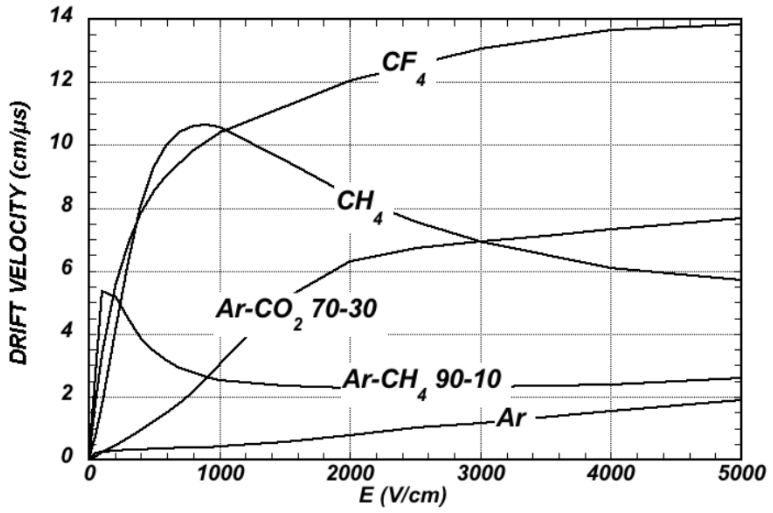

Figure 1.8: Computed electron drift velocity as a function of electric field in several gases at NTP and with no magnetic field computed with MAGBOLTZ [5]. Taken from [3].

1.2.2 Transport of electrons and ions

Drift velocities

The electric field E_{drift} applied between the two electrodes will cause the electrons and ions from the multiple ionization processes to be drifted in opposite directions. In a TPC, the electrons drift velocity is an important parameter because it limits the event rate accessible to the detector. While drifting, the electrons scatter isotropically on the gas atoms but are accelerated in the direction of the electric field in between collisions which results in a drift velocity v that can be approximated using gas kinetic theory and expressed as:

$$v = \frac{eE_{\text{drift}}\tau}{m_e} \tag{1.4}$$

where τ is the mean collision time, e the elementary charge and m_e the electron mass. Electrons can also loose energy by exciting the atoms of the gas which is why the electrons drift velocity highly depends on the inelastic cross-section involving the rotational and vibrational levels of the molecules. This motivates the use of noble gases in TPC as the inelastic cross-section is zero below excitation and ionization thresholds so that once the electrons have been cooled down into the appropriate energy range, they can drift through the gas with minimum interaction. The addition of polyatomic gas such as CH_4, CO_2 or CF_4, in the gas mixture allows to strongly increase the electrons drift velocities: their large inelastic cross-section at moderate energy range will allow to facilitate the electrons cool down minimizing the excitation of noble gas atoms. This is illustrated in Fig 1.8 where it can be observed, for example, that the maximum drift velocity in Ar-CO_2 (70:30) is about 6 times larger than in pure Argon for $E_{\text{drift}} = 3\,\text{kV/cm}$. In TPCs, a magnetic field B is often applied in order to bend the tracks of charged particles and measure their momentum to allow for particle identification. Under such conditions, the drift velocity expression changes to:

$$v = \frac{e\tau}{m_e(1+\omega^2\tau^2)}\left(\vec{E_{\text{drift}}} + \frac{\omega\tau}{B}(\vec{E_{\text{drift}}} \times \vec{B}) + \frac{\omega^2\tau^2}{B^2}(\vec{E_{\text{drift}}} \cdot \vec{B})\vec{B}\right) \tag{1.5}$$

where $\omega = eB/m_e$ is the Larmor frequency. For TPCs, the configuration is usually such that the electric and magnetic fields are parallel in which case there is no effect on the drift velocity.

Diffusion

Because of the random collisions with atoms and molecules of the gas mixture, a pointlike cloud of electrons diffuses as Gaussians such that the transverse and longitudinal diffusions after drifting over a distance z, namely $\sigma_i(z)$ with $i = L, T$, are given by:

$$\sigma_i^2 = \sigma_{i0}^2 + D_i^2 z \tag{1.6}$$

where σ_{i0} is the standard deviation at zero drift and the D_i are diffusion coefficient that depend on the gas properties. Transverse diffusion is a limitation to the achievable spatial resolution of the detector and thus of its particle identification capabilities in general. The optimal spatial resolution in the transverse plane that can be obtained for a single energy deposit is given by:

$$\sigma_{\text{opt}} = \frac{\sigma_T \sqrt{z}}{\sqrt{n}} \tag{1.7}$$

where n is the number of electrons collected. In the presence of a magnetic field B parallel to the drift field, the transverse diffusion can be strongly reduced:

$$\sigma_T(B) = \frac{\sigma_T(B = 0\ \text{T})}{\sqrt{1 + \omega^2 \tau^2}} \tag{1.8}$$

For a drift field $E_{\text{drift}} \sim 200$ V/cm in a Ar-iC_4H_{10}-CF_4 (95:2:3) gas mixture at NTP, MAGBOLTZ [5] simulations give $\sigma_T(B = 0\ \text{T}, z = 0\ \text{cm}) = 314\ \mu\text{m}$ while $\sigma_T(B = 4\ \text{T}, z = 0\ \text{cm}) = 22\ \mu\text{m}$.

1.2.3 Amplification

When the electrons reach the amplification region, they are usually subject to a much higher electric field E_{amp} of a few tens of kV/cm. At this point, the accelerated electrons are energetic enough to further ionize the medium and create a Townsend avalanche as illustrated by Fig 1.9. The number of electrons N is given by:

$$N = N_T e^{\int_s \alpha(E_{\text{amp}}(s))ds} \tag{1.9}$$

where N_T is the total number of electrons arriving into the amplification gap, α is the first Townsend coefficient that depends on the value of the electric field E_{amp}, and s is the electrons path along a field line. The gas gain G is then defined as:

$$G = \frac{N}{N_T} \tag{1.10}$$

The two amplification systems commonly used to replace wire chambers are GEMs and Micromegas as shown in Fig 1.10.

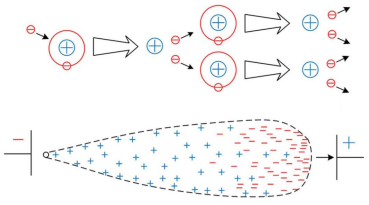

Figure 1.9: Schematic view of the formation of a Townsend avalanche. Taken from [6].

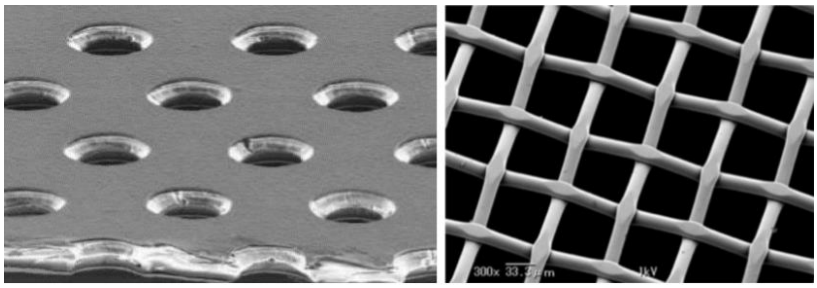

Figure 1.10: Left: Electron microscope picture of a standard GEM foil; **Right:** Microscope photograph from a woven calendered mesh; Copyright 2019© NBC Meshtec Americas Inc.

1.3 Micromegas detectors

Micromegas (for Micromesh gaseous) detectors [7], in a sense, can be understood as TPCs with a drift space limited to few centimeters. It can be used to read out a TPC or standalone as a tracker in which case only the hit positions in the readout plane will be reconstructed. The specificity of the Micromegas detector lies in the micromesh which is used to apply a much higher electric field in the amplification region: the field lines are bent around the mesh fibers guiding the primary electrons through to create Townsend avalanches. Fig 1.12 summarizes the functioning of a Micromegas detector and presents some examples of possible anode segmentation for the readout.

Since its invention in 1996, Micromegas detectors have strongly evolved, improving both its performances and fabrication technique, to accommodate for a wide range of applications. The following sections will present a non-exhaustive list of the Micromegas possible variations and performances, a more detailed review can be found here [8].

1.3.1 Variations

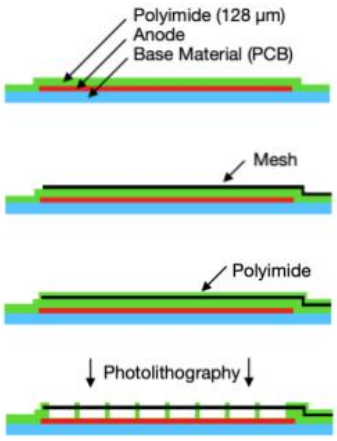

Figure 1.11: Main production steps of a bulk Micromegas: the mesh is laminated between polyimide layers, the material between the mesh and the anode is removed with a lithographic process using a mask so that only the supporting pillars and frame structures remain. Taken from [8].

Bulk and microbulk Micromegas

One of the difficulties of the initial fabrication technique was to keep the micromesh stretched for the amplification gap to be uniform. Usually, insulating spacers called pillars are placed regularly over the active area to maintain an equal spacing between the micromesh and the anode but the risk is that the micromesh locally peel off from the pillars. The bulk technology [9] offers a solution to this problem with a fabrication technique that encapsulates the micromesh inside the pillars using lithographic processes as illustrated by Fig 1.11. This new structure makes the detector more robust and allows to produce detectors with large active areas. In addition, since the micromesh is fixed to each pillar, non-planar detector can be designed like the vertex tracker of the CLAS12 experiment for example [10].

The idea behind the microbulk technology is similar except that in order to fix the micromesh to the pillars and readout plane, everything is produced as a single structure from a Kapton foil with both sides covered by a copper layer [11].

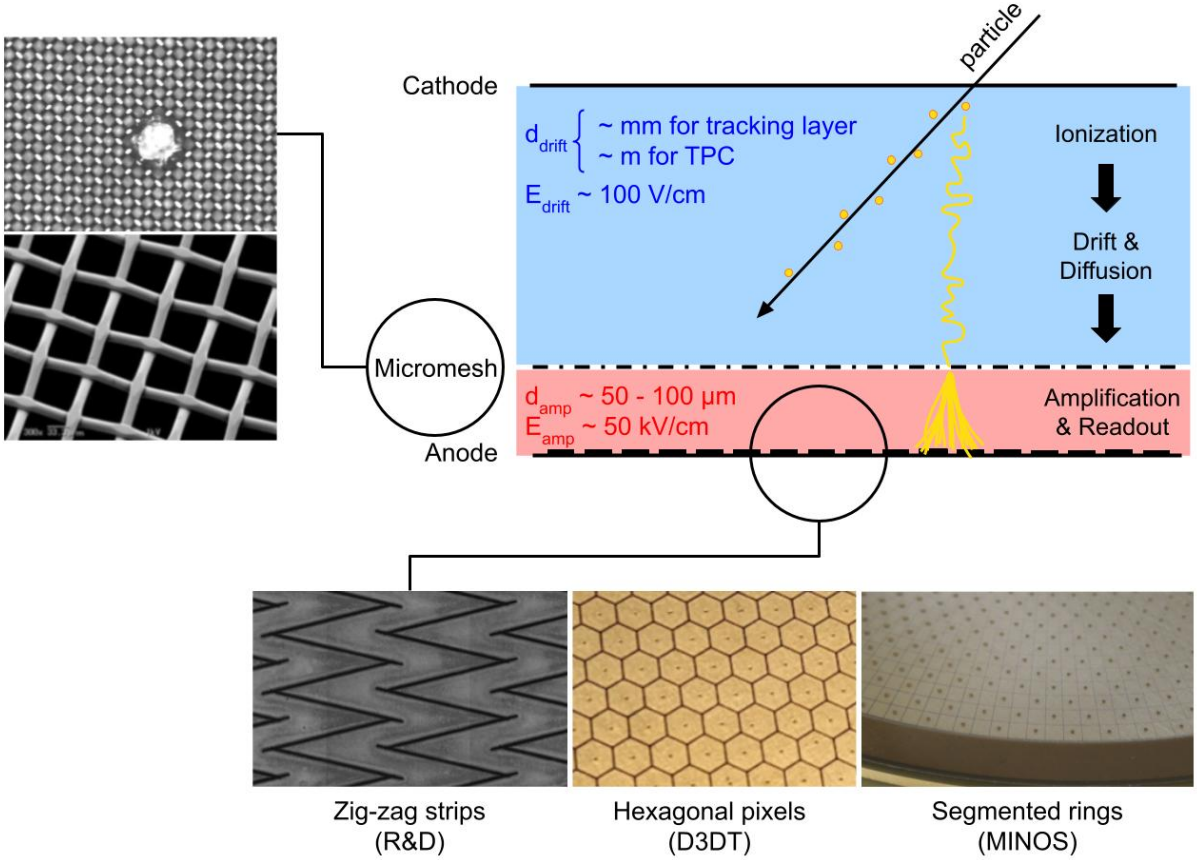

Figure 1.12: Schematic view of a Micromegas detector. Photographs are added to show examples of micromesh (the white spot on the top picture is a support pillar) and readout segmentation.

Micromegas integrated on silicon wafers

The InGrid Micromegas [12] was developed in 2006 and allows to instrument a silicon wafer with an aluminum grid. Using again lithographic processes, readout pixels can be precisely aligned underneath each hole of the grid and even scaled to resolve primary electrons. An example of such technology is the integration of a Micromegas detector on a Timepix chip, shown in Fig 1.13 (Left), with 55×55 µm^2 readout pixels arranged in an array of 256×256. Such detectors were combined into a matrix of 4×2 Ingrids, called *Octopuce*, as illustrated by Fig 1.13 (Right), and used for the R&D of the International Linear Collider (ILC) TPC during test beam campaigns. Some of these data are analyzed to experimentally extract gas ionization properties, as described in Chapter 8.

Resistive Anode Micromegas

In the case of resistive anode Micromegas, a resistive layer is deposited onto the segmented anode in order to spread the charge onto several strips or pads to improve charge sharing and by doing so the spatial resolution for the given segmentation. It can also improve the Micromegas stability and protect the electronics against sparking events. Different material can be used for the resistive layer: as an example Diamond-Like Carbon (DLC) is used for the T2K High Angle TPCs (further developed

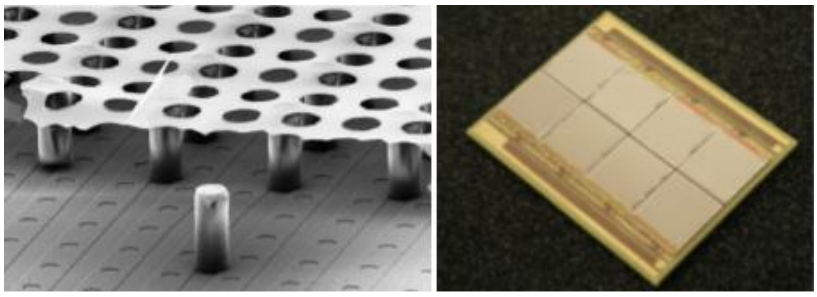

Figure 1.13: Left: Scanning Electron Microscope (SEM) image of an Ingrid Micromegas on a Timepix chip ; **Right:** Octopus module.

in Chapter 6) providing low resistivity $R \sim$ 200-400 kΩ/□ while Carbon Loaded Kapton (CLK) is used for R&D on the ILC TPC with a resistivity of $R \sim$ 3-5 MΩ/□. Resistive ink can also be used to coat copper strips giving access to a range of resistivities depending on the mixture used.

1.3.2 Performances and use in particle physics experiments

With the numerous developments of fabrication techniques for specific applications came better performances. While Micromegas spatial resolution is usually of the order of 100 µm, a spatial resolution of only 12 µm at normal incidence was obtained during a test beam at CERN PS using CF_4-iC_4H_{10} (80:20) gas mixture with anode strips of 100 µm pitch [13]. The use of solid photocathodes to convert Cherenkov light allows to reach timing resolution of the order of 25 ps as demonstrated by the PICOSEC Micromegas [14].

The excellent energy resolution of the Micromegas, for a gaseous detector, combined with its low material budget makes it a perfect candidate for tracking. Indeed, Micromegas are used as trackers on ATLAS muon spectrometer as developed in Section 1.5, on the CLAS12 Vertex Tracker [10], in the COMPASS experiment [15], or in muon tomography [16]. It can also be used to read out TPCs as it is the case for the T2K near detector [17] or the ILC TPCs [18].

1.4 Detector development considerations

Choosing a gas mixture for TPC operation

As it has been discussed in the previous section, many physical effects at play in the TPCs depend very strongly on the nature of the gas. In order to optimize the performances of the detector, the goals are to:

1. optimize ionization with regard to excitation
2. minimize the energy fluctuations
3. maximize the electrons drift velocity
4. minimize the transverse diffusion
5. maximize the number of collected electrons

Depending on the application, the flammable nature of the gas can also be a parameter to take into account. Environmental factors such as the material of the detector and gas system should also be considered. The

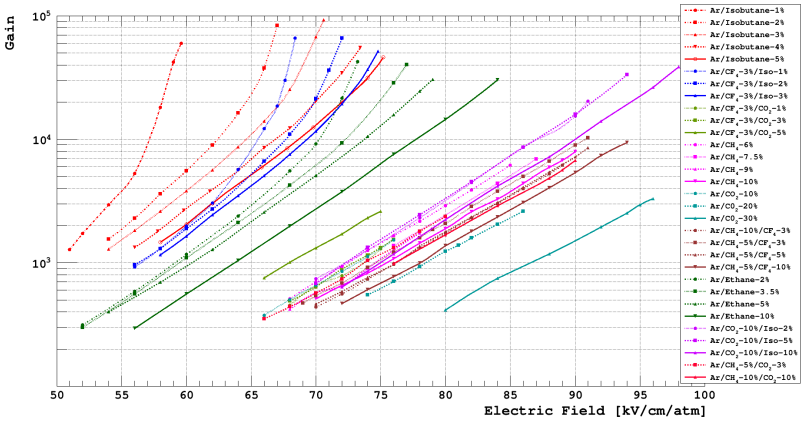

Figure 1.14: Gain measurements as a function of the amplification electric field provided by a 50 µm gap Micromegas detector using gas mixtures containing argon and a few percent of other constituents (CO_2 , CH_4 , C_2H_6, i-C_4H_{10}, CF_4 etc.). Taken from [19].

choice of the optimal gas mixture is usually based on the combination of simulations as well as experimental studies as illustrated by Fig 1.14 that shows the measurement of the gain of a microbulk-Micromegas detector as a function of the amplification electric field for a wide range of gas mixtures. Nonetheless, some known gas properties allow to draw some guidelines:

- **The main gas in the mixture is a noble gas:** this ensures an inelastic cross-section of zero below excitation and ionization threshold.
- **Adding i-C_4H_{10} increases the gain via Penning effect:** some additional electrons are obtained when molecules of i-C_4H_{10} are ionized by excited atoms of Argon.
- **Polyatomic gases are used as quenchers:** during the avalanche process, excited Argon atoms emit ultra-violet photons that could induce uncontrolled avalanches causing discharges and affect the TPC operation stability. Polyatomic gases such as i-C_4H_{10}, CH_4 or CO_2 are added in order to absorb such photons.
- **Gases with large τ are used to increase the electrons drift velocity as well as reduce the transverse diffusion:** when $\vec{E}_{\text{drift}}$ and $\vec{B}$ are parallel, the electron drift velocity v increases with the mean collision time τ as $v \propto \tau$ while the transverse diffusion σ_T decreases as $\sigma_T \propto 1/\tau$. The addition of a gas presenting a large τ like CF_4 in the mixture usually increases the performances.

In this thesis, the gas mixtures used are Ar-iC_4H_{10} (95:5) and the so-called *T2K gas* which is a mixture of Ar-iC_4H_{10}-CF_4 (95:2:3) which ensure both a good electron drift velocity and a limited transverse diffusion.

Penning effect

Considering a gas mixture composed of A and B, the Penning effect is the ionisation of B induced by the cooling of A.

Taking the example of Argon and i-C_4H_{10}, the ionisation potential of isobutane is given by $I_{\text{i-C}_4\text{H}_{10}} = 10.67\,\text{eV}$ while the Argon excitation levels are $E^*_{\text{Ar, S}} = 11.55\,\text{eV}$, $E^*_{\text{Ar, P}} = 13.0\,\text{eV}$ and $E^*_{\text{Ar, D}} = 14.0\,\text{eV}$ which allows the following reaction to happen:

$$\text{Ar}^* + \text{i-C}_4\text{H}_{10} \rightarrow \text{Ar} + \text{i-C}_4\text{H}_{10}{}^+ + e^- \tag{1.11}$$

Experimental complications

The concepts previously developed describe an ideal operation of TPCs. However, especially when building prototypes, one may be confronted to some experimental complications worth mentioning.

One of these is electron attachment: if the gas mixture is contaminated by electronegative components, for example oxygen in case of leaks, drifting electrons can be absorbed before reaching the readout plane thus affecting the performances of the detector. As it is a side-effect of the drift process, it is all the more important that the drift length is large which is why it is relevant in TPCs and should be controlled. There are several mechanisms through which the attachment can occur but the Bloch-Bradbury process is an important one as it describes the attachment of low energy electrons to O_2 molecules. It is a three body mechanism as the dioxygen molecule must be stabilized by collision with another molecule in order to retain the attached electron:

$$e^- + O_2 + X \rightarrow O_2^{-*} + X \rightarrow O_2^- + X$$

The attachment reaction rate A can be written as a function of the gases partial pressure p_i and the attachment coefficient $C_{O_2,X}$:

$$A = C_{O_2,X} \times p_O \times p_X$$

Precise measurements of attachment coefficient for various gas mixtures are presented in [20].

Gaseous detectors also suffer from sparking events. Those can appear naturally if the detector is operated at high gain or when a high energy particle (an α for example) is absorbed, but can also indicate a manufacturing issue or impurities in the gas.

In the amplification region, the ions produced via Townsend avalanche are drifted in the opposite direction towards the cathode. This is known as ion backflow and create a space-charge field that modifies the electric field in the amplification gap. In the case of an amplification using a Micromegas, the gap is only about 100 µm so that the space charge buildup can usually be neglected at reasonable rates. However, if the gain is high enough for the space charge field to compare with the amplification field, the avalanche can grow in all directions and form a thin plasma filament or streamer. This will usually happen when there are about 10^8 electrons in the avalanche, known as the Raether limit. With typical gas gain of the order of 10^4 it translates into ionization processes creating more than 1000 electrons over the spatial extension of an avalanche which is a few 100 µm. Due to the high voltages applied to operate a TPC, sparking can also appear between the high voltage connection and a close grounded surface if the connection is not protected.

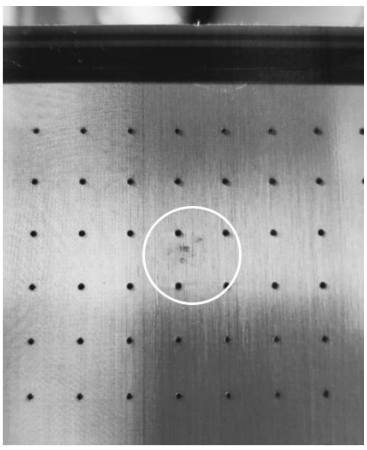

Figure 1.15: Photograph of a bulk Micromegas damaged by repetitive sparking events. The black dots are the pillars supporting the micromesh, the damaged area is highlighted by the circle.

Sparking events can lead to large dead times if followed by a breakdown of the high voltage supply, but also damage the detector itself, as illustrated by Fig 1.15, or the readout electronics. As a result, many efforts are made towards building spark-resistant detectors [21] using for example resistive anodes.

1.5 Examples of successful TPC and Micromegas applications

1.5.1 ATLAS New Small Wheels

ATLAS is one of the 4 main detectors installed on the Large Hadron Collider (LHC) interaction points. It is primarily known for contributing to the discovery of the Higgs boson in 2012 but has been designed for a more general purpose: probing the limits of the Standard Model.

Figure 1.16: Photograph of the first completed NSW stored at CERN.

As many collider experiments in particle physics, it is composed of many subdetectors, each one bringing valuable information to properly reconstruct the events that were produced by the billions interactions per second taking place in the center of the detector. The muon spectrometer is responsible for the identification of the muons as well as measuring their momenta. Muons also play an important role in the trigger as they leave a clear signal and can be precisely reconstructed to separate primary vertices. In order to meet the requirements set by the extremely high rate of the High Luminosity LHC (HL-LHC), the internal wheels of the muon spectrometer are being replaced by a new device: New Small Wheels (NSW). Fig 1.17 shows a scheme of the location of NSW inside the ATLAS detector as well as its structure: it consists of a 10 m diameter wheel made out of fanned out sectors. Each sector itself is an assembly of Micromegas modules sandwiched with small-strip thin gap Chambers (sTGCs). In the end, a total area of about 1200 m^2 of Micromegas detectors has been produced, a third of which was done at Irfu (Institute of Research into the Fundamental Laws of the Universe). This pioneering achievement represents, to this day, the largest surface covered by Micromegas detectors. The first of the NSWs was installed in July 2021 and is now successfully taking data.

1.5.2 ALICE TPC

At another interaction point of the LHC stands A Large Ion Collider Experiment (ALICE), a detector designed to study the physics of heavy ions and probe matter at such energy densities that Quark Gluon Plasma (QGP) can be produced. The ALICE TPC is the main device of the central barrel region and performs tracking as well as particle identification.

As illustrated by Fig 1.18 (Left), it consists of a 90 m^3 cylinder divided in two drift regions by a central cathode. The TPC is read at both ends by readout wire chambers, each end plate being divided into 18 sectors made of an inner and outer readout chamber module. The amplification is provided by an optimized multi-layer configuration of GEM foils.

The incredible challenge of the ALICE TPC is the event rate that it must sustain combined with the charged particles multiplicity to reconstruct during Pb-Pb collisions: the expected collision rate is about 50 kHz for Run 3 which corresponds to 5 Pb-Pb events in the TPC drift time and yields a charged particle density of up to $dN/d\eta \sim 10000$, where η is the pseudo-rapidity. As an example, a typical Pb-Pb collision event at 2.76 TeV is shown in Fig 1.18 (Right) to illustrate the difficulty of the reconstruction. Under such conditions, the ion induced space-charge

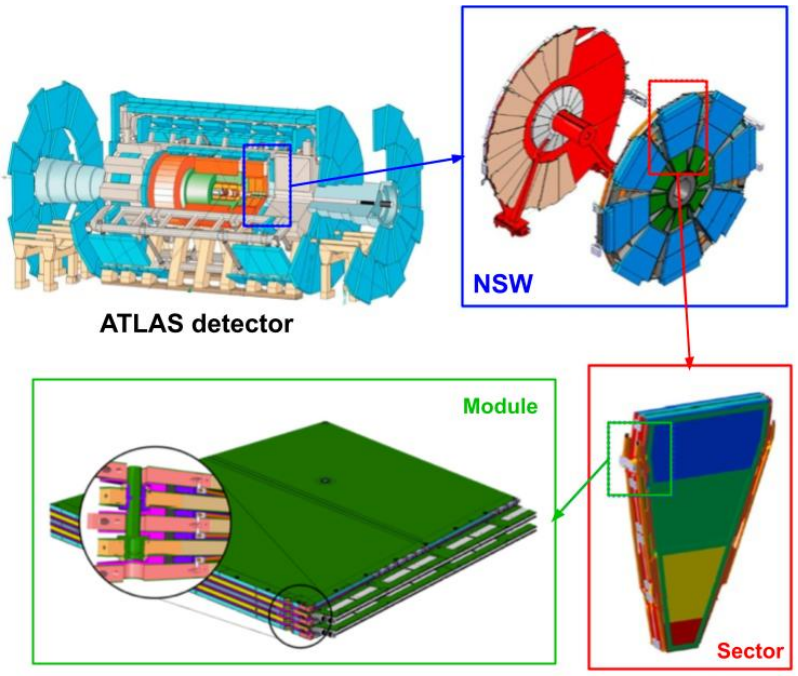

Figure 1.17: Scheme of the location of NSW in the ATLAS detector and its structure.

distortions cannot be neglected making the track reconstruction all the more difficult. Nonetheless, the ALICE TPC showed incredible tracking and reconstruction performances already for Run 1: a resolution on the particles transverse momenta of $\sigma(p_T)/p_T = 3.5\%$ could ultimately be reached and an energy resolution $\sigma_{dE/dx} = 5\%$ was obtained for the tracks with the maximum number of samples as presented in [22].

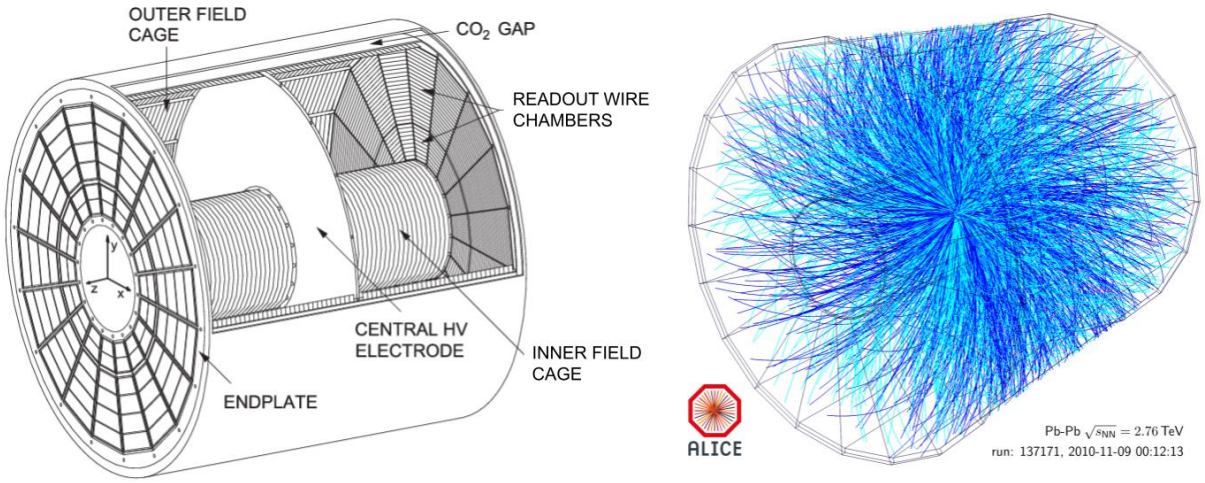

Figure 1.18: Left: Scheme of the ALICE TPC. Taken from [23]; **Right:** ALICE event display of a Pb-Pb collision at 2.76 TeV.

Part II

Development of a new instrument for muon tomography

MUON TOMOGRAPHY: TOWARDS NEW APPLICATIONS

2

In this chapter, the principle of muon tomography is developed, from the production of the cosmic muons to their interaction with matter at the origin of their imaging power. A brief description of the muon tomography activities at CEA is presented in Section 2.2 leading to a dedicated section on the ScanPyramids mission. Finally, the limitations of muon telescopes are highlighted, justifying the development of a new detector such as D3DT to expand the spectrum of applications of muon tomograhy.

2.1 Cosmic muons

2.1.1 Production

Cosmic rays are a population of ionizing particles of energy ranging from a few MeV to millions of GeV and with multiple sources across the Universe such as supernovae, gamma-ray bursts or active galactic nuclei to only cite a few. This particle flux is composed of about 90% of protons, 9% of alphas and a small fraction of heavier ions up to iron, as illustrated by Fig 2.2. When cosmic rays interact with the nuclei of the high atmosphere, it generates air showers, as illustrated by Fig 2.1, which produce many energetic hadrons such as pions and kaons. Those subsequently decay following:

$$\pi^{\pm} \longrightarrow \mu^{\pm}\nu_{\mu} \text{ with a branching ratio of } 99.988\% \tag{2.1a}$$

$$K^{\pm} \longrightarrow \mu^{\pm}\nu_{\mu} \text{ with a branching ratio of } 63.56\% \tag{2.1b}$$

thus producing muons. Muons mean lifetime is given by $\tau \sim 2.2{\times}10^{-6}$sec which, although quite high compared to other unstable particles (*e.g.* $\tau_{\pi^{\pm}} \sim 2.6 \times 10^{-8}$ sec, $\tau_{\pi^0} \sim 8.5 \times 10^{-17}$ sec, $\tau_{K^{\pm}} \sim 1.2 \times 10^{-8}$ sec), should only allow them to travel for about 660 m through the atmosphere before decaying to electrons. Yet, muons were discovered on the ground by American physicists Carl D. Anderson and Seth Neddermeyer in 1936 while studying the nature of cosmic ray particles using cloud chambers [24]. Indeed, the probability for muons to cross the atmosphere is enhanced by two major effects:

muons are relativistic particles ie. the muon lifetime actually undergoes Lorentz time dilatation so that $\tau^{\text{rel}} = \gamma\tau$ with a Lorentz factor $\gamma \sim 28$ for a 3 GeV muon.

muons are massive particles ($m_{\mu} \sim 207 m_e$) so muons lose less energy to Bremsstrahlung and can penetrate far deeper into matter.

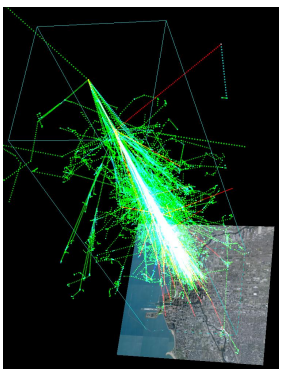

Figure 2.1: Cosmic ray air shower created by a 1 TeV proton hitting the atmosphere 20 km above the Earth. The shower was simulated using the AIRES package.

2.1.2 Flux at sea level

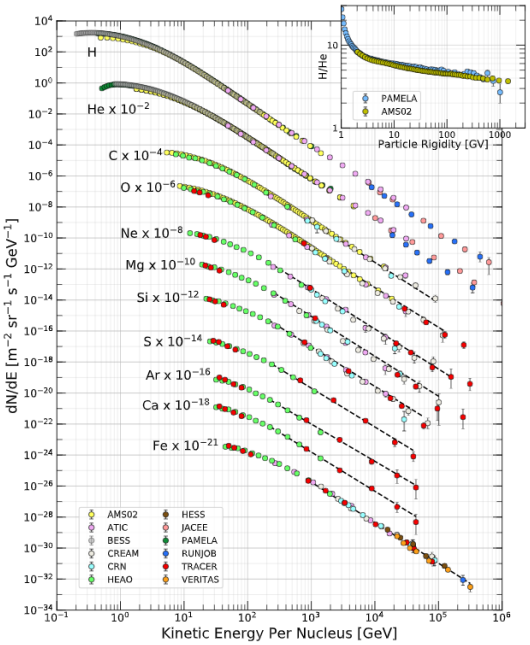

Figure 2.2: Fluxes of nuclei of the primary cosmic radiation in particles per energy-per-nucleus are plotted vs energy-per-nucleus. Taken from [3].

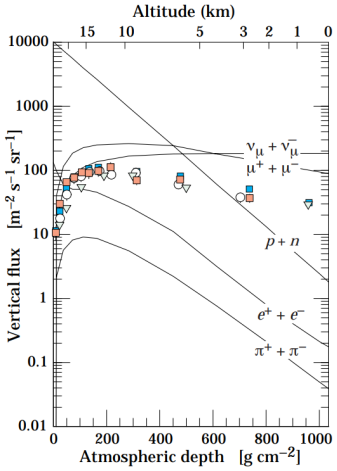

Figure 2.3: Vertical fluxes of cosmic rays in the atmosphere as a function of the atmospheric depth. The points show measurements of negative muons with $E_\mu > 1$ GeV. Taken from [3].

Thanks to the enhancing effects discussed in the previous section, the muon vertical flux is clearly dominant at sea level as shown by Fig 2.3. Considering the zenith angle θ, an approximate extrapolation formula gives the mean muon flux at sea level in the hypothesis if high energy muons ($E_\mu > 100/\cos\theta$ GeV) and neglecting the Earth curvature ($\theta < 70°$) [3]:

$$\frac{dN_\mu}{dE_\mu d\Omega} \approx \frac{0.14 E_\mu^{-2.7}}{\text{cm}^2 \text{ s sr GeV}} \times \left\{ \frac{1}{1 + \frac{1.1 E_\mu \cos\theta}{115\text{GeV}}} + \frac{0.054}{1 + \frac{1.1 E_\mu \cos\theta}{850\text{GeV}}} \right\} \quad (2.2)$$

where the first and second term give the pions and kaons contributions respectively. This is the so-called Tang model or modified Gaisser model. However, the limited validity of Gaisser's formula lead to the development of many other parametrizations, either empirical or analytical, to overcome Tang model shortcomings. Fig 2.4 shows a comparison of 4 different parametrizations and the good agreement between those. If not specified otherwise, the Guan model [25] is used for CEA muography analysis.

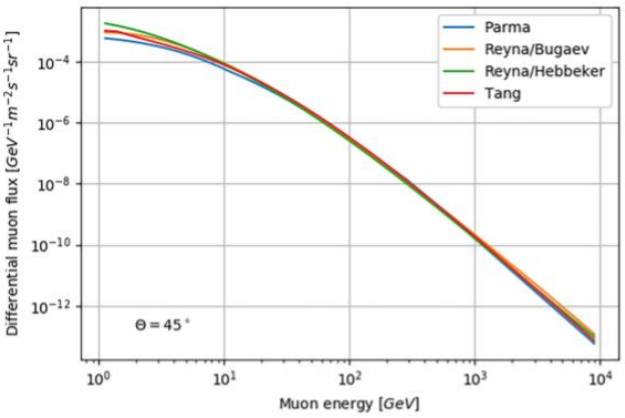

Figure 2.4: Comparison of 4 muon flux models including an uncertainty estimate for a zenith angle of $\theta = 45°$; differential muon flux as a function of energy. Taken from [26].

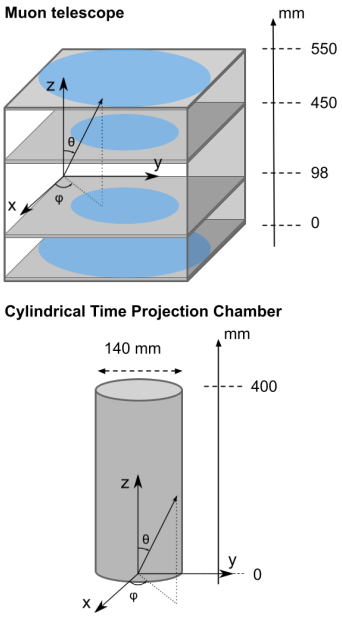

Figure 2.5: Geometry definition for numerical application. The blue disks illustrate the angular acceptance of the detector.

Muon rate at sea level for CEA muon telescope and TPC

The geometries used for this numerical application are presented in Fig 2.5 as well as the usual spherical coordinates system. In each case, the total muon flux is computed by numerical integration of Guan [25] and Shukla's parametrization [27] for muons momentum ranging from 0 to 1000 GeV/c.

Muon telescope

Computing the detector angular acceptance in this case yields:

$$\theta_{\text{range}} = [0°, 48°] \text{ and } \phi_{\text{range}} = [0°, 360°]$$

Numerical integration gives in this case, for an active area of 50×50 cm^2:

	Guan	Shukla
Muon flux [m^{-2} s^{-1}]	68.36	59.47
Muon rate [s^{-1}]	17.09	14.87

The 13% difference is due to the fact that Shukla's parametrization assumes vertical muons and is thus less accurate for large angular acceptance like in this case. These values are to be compared to the experimental rate measured at 25 s^{-1}. Muon rate are underestimated due to the approximation made while computing the angular acceptance computation, equating the active area to its inner disk. Correcting the expected rate given by the Guan parametrization by a $4/\pi$ factor yields a value of 21.76 s^{-1}. The remaining difference can be attributed to the trigger that will count muon as long as it is detected in three out of the four Micromegas planes, effectively increasing the angular acceptance of the telescope.

Cylindrical TPC

The estimation of the muon rate is more complicated in the case of the cylindrical TPC: the angular acceptance is in this case almost 2π ($\theta_{\text{range}} = [0°, 90°]$ and $\phi_{\text{range}} = [0°, 360°]$ but the detector saturates for vertical muons) and instead of an active area, muons can be detected through the entire volume.

First of all the total muon flux is computed for the angular range of interest which gives:

	Guan	Shukla
Muon flux [m^{-2} s^{-1}]	177.71	176.42

Two approaches can then be considered:

1. Naive approach

Noting r the radius of the TPC, h its drift length and $\langle\theta_{\text{in}}\rangle = 37.7°$ the averaged angle of incidence of the muons, an effective cross section σ_{eff} can be defined for the TPC as:

$$\sigma_{\text{eff}} = \pi r^2 + 2rh \sin\langle\theta_{\text{in}}\rangle = 0.05 \text{ m}^2$$

In this case the muon rate is:

	Guan	Shukla
Muon rate on detector [s^{-1}]	8.01	7.95

2. Simulation based approach
Using the G4TomoMu framework based on the GEANT4 toolkit [28] and the Livermore[1] models, 5 millions of muons are simulated as well as a cylinder to represent the TPC. Every physical processes involving muons are taken into account, mainly multiple scattering, ionization, pair production and Bremsstrahlung radiation. The expected muon rate can be estimated by computing the simulation real time and the number of muons actually detected. Muons are generated from a surface S_{gen} large enough to eventually pass through the detector independently from their incidence angle. It is a disk centered on the cylinder center of mass with a radius $r_{gen} = \sqrt{(h/2)^2 + r^2}$ so that

$$S_{gen} = \pi[(h/2)^2 + r^2] = 0.14 \text{ m}^2$$

The total muon flux combined with this surface allows to estimate:

	Guan	Shukla
Muon rate on S_{gen} [s^{-1}]	24.69	24.51
Simulation real time [s]	202511	203998

In the simulation file, 1310536 muons out of the 5 millions simulated actually deposited energy inside the cylinder, leading to the final muon rates:

	Guan	Shukla
Muon rate on detector [s^{-1}]	6.47	6.42

The naive approach overestimates the muon rate because the top and exterior surfaces of the cylinder and accounted for separately while muons crossing both should only be counted once.

1: https://geant4.web.cern.ch/node/1619

2.1.3 Interaction with matter

The incredible imaging power of muons lies in the fact that they are naturally abundantly produced as seen in the previous section, but also that they can be detected. This is made possible by the fact that, as they travel through matter, muons interact via two main mechanisms:

- energy loss
- multiple scattering

Energy loss

Muons loose energy through electronic interactions leading to ionization, atomic or collective excitation of the medium. The dominating effect varies as a function of the muon energy as shown in Fig 2.6. In the specific case of cosmic muons, the energy is typically of a few tens of GeV/c and the radiative effects can thus be neglected. The mean rate of energy loss

by relativistic charged particles such as cosmic muons is well described by the so-called "Bethe equation":

$$\left\langle -\frac{dE}{dx} \right\rangle = Kz^2 ZA \frac{1}{\beta^2} \left[\frac{1}{2} \ln \left(\frac{2m_e c^2 \beta^2 \gamma^2 W_{\max}}{I^2} \right) - \beta^2 - \frac{\delta(\beta\gamma)}{2} \right] \tag{2.3}$$

where $K = 4\pi N_A r_e^2 m_e c^2$ is a constant coefficient, z is the charge number of the particle, Z and A are respectively the atomic number and mass number of the medium nuclei, $W_{\max}$ is the maximum possible energy transfer, I the mean excitation energy and $\delta(\beta\gamma)$ the density effect correction to ionization energy loss. However, in the energy range of interest, muons behave as Minimum Ionizing Particles (MIPs) and the energy loss in any material is approximately constant and equals to $\langle -dE/dx \rangle_{\text{MIP}} \sim 2\ \text{MeV cm}^2/\text{g}$.

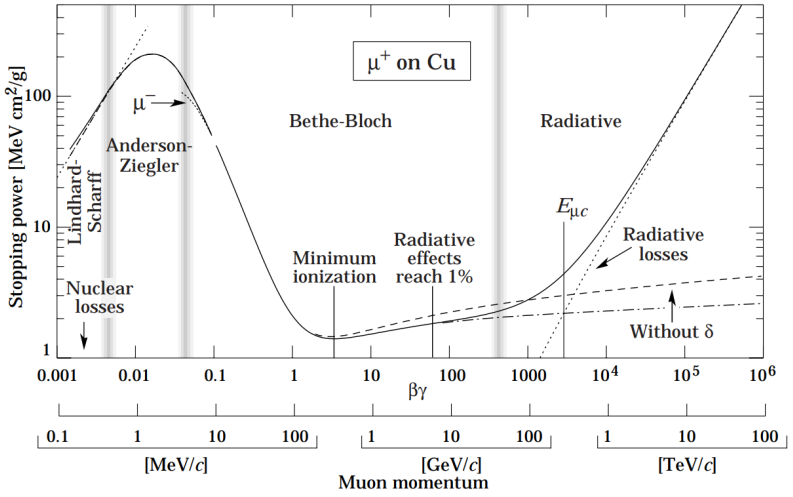

Figure 2.6: Muon energy loss in Copper as a function of its energy. Taken from [3]

Multiple scattering

As a charged particle travels through matter, it is deflected multiple times by small angles as it is subject to Coulomb scattering from the nuclei constituting the traversed material. This effect is well described by the theory of Molière [29] according to which the Coulomb scattering distribution can be approximated by a Gaussian of zero mean value for small deflection angles and tends to Rutherford scattering for larger angles. According to this theory, the standard deviation of the projected scattering angle distribution σ_θ can be written as:

$$\sigma_\theta = \frac{13.6\ \text{MeV}}{\beta c p} \times z\sqrt{x/X_0} \times \left[1 + 0.038 \ln\left(x/X_0\right) \right] \tag{2.4}$$

where p and βc are respectively the momentum and velocity of the incident particle while x is its path length and X_0 the radiation length of the traversed material.

The radiation length X_0 of a material is a quantity expressed in g cm^{-2} that reflects the length scale on which a particle would loose energy through radiative processes while traversing it. A complex expression

has been established by Y. S. Tsai [30] but a good approximation is given by the simpler form:

$$X_0 = \frac{716.4\ \mathrm{g.cm^{-2}} A}{Z(Z+1)\ln(287/\sqrt{Z})} \tag{2.5}$$

σ_θ for a muon traversing a 10 cm thick lead brick

Considering a vertical muon with $p_\mu = 10$ GeV/c crossing a 10 cm thick lead brick as shown in Fig 2.7, Eq 2.5 gives:

$$X_0^{\mathrm{Pb}} = 6.33\ \mathrm{g\,cm^{-2}} \text{ or } 0.56\ \mathrm{cm} \text{ after dividing by } \rho$$

Making the simplifying hypothesis that $\beta = 1$, and using x =10 cm, Eq 2.4 yields:

$$\sigma_\theta^{\mathrm{Pb}} = 60\ \mathrm{mrad} \text{ or } 0.37°$$

It is important to note that Eq 2.4 is accurate for particle traversing a single material defined by the atomic number Z and mass number A of its nuclei. However in most applications the considered material requires a more complex description and an effective path length x_{eff} and radiation length $X_{0,\mathrm{eff}}$ should be computed before applying the formula.

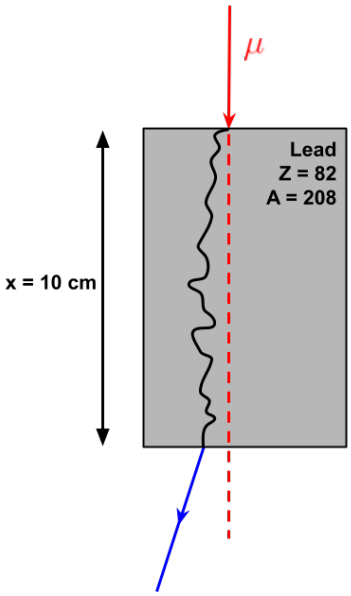

Figure 2.7: Multiple scattering in a 10 cm lead brick.

2.2 Muon tomography principle

Depending on the object that one wants to probe, several method can actually be used: Fig 2.8 resumes in a schematic view muon tomography principle in both deviation and absorption mode with associated examples of results.

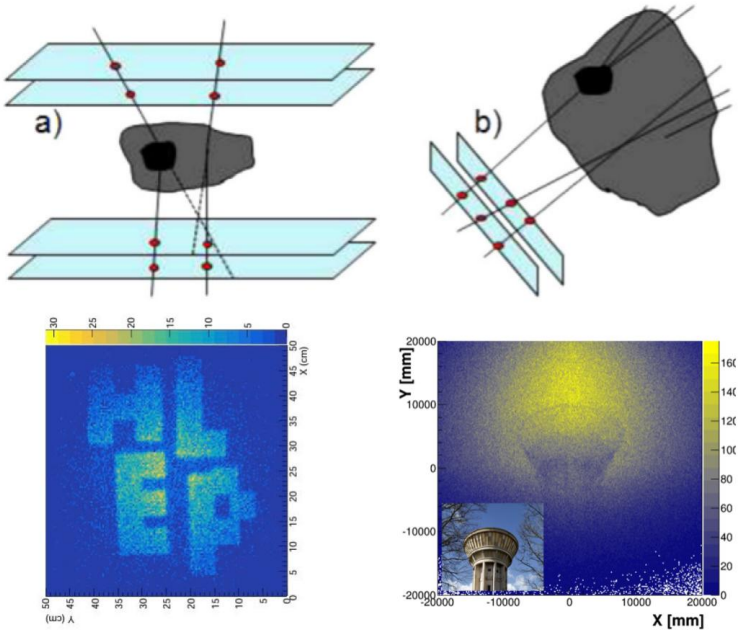

Figure 2.8: Schematic view of muon tomography principles with example of typical results **a)** in deviation mode: muography made using the PoCA method as a result of master labwork; **b)** in absorption mode: muography of Saclay water tower, based on [16].

2.2.1 Deviation

Muography in deviation mode relies on the multiple scattering of muons in matter, and more specifically on the fact that the standard deviation of the scattering angle σ_θ depends on the radiation length of the crossed material and thus its density. That is to say that in measuring the deviation angle of muons traversing an object, one actually probes the density ρ of said object.

As shown in Fig 2.8, the idea is thus to reconstruct the direction of the incident muon before passing through the object and after being scattered. Selecting then the muons for which the deviation angle was different from zero and assuming that the multiple Coulomb scattering can be assimilated to a single larger diffusion, the Point of Closest Approach (PoCA) method is often used to map the density of the object.

The Point of Closest Approach (PoCA) method

Due to both multiple scattering process and detector resolution effects, the reconstructed direction of the incident and outgoing muon usually do not intersect. In order to estimate the scattering position, the minimum sized segment between these two lines is computed, its center defining the PoCA while its length is called Distance of Closest Approach (DoCA) as shown in Fig 2.9. By accumulating muons and mapping the diffusion centers weighted by the value of the associated scattering angle, a 3D density map of the object can be extracted. As an example, Fig 2.8(a) shows a 2D muography of the word "HELP" drawn using lead bricks and imaged over a 48 hours time period. A radial effect due to the detector angular acceptance can also be observed.

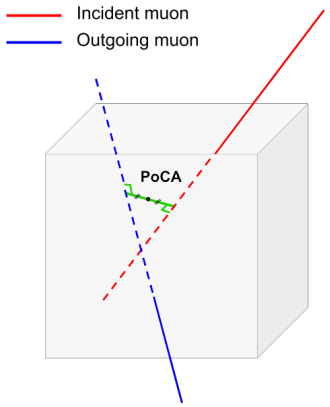

Figure 2.9: Point of Closest Approach

Deviation mode is preferably used for small objects given that it requires for the region to probe to fall into the angular acceptance of the quadruplet of trackers. In addition, the assumption that a single main diffusion took place can only be made for an object with relatively low opacity. Recent applications include for example transport control [31] or material identification [32].

2.2.2 Absorption

In the case of very large structures, surrounding the object to probe with detectors is not a possible solution and muography by absorption becomes more relevant. The probability of a muon being absorbed by a given material depends on the linear stopping power of said material as well as the muon path length. Keeping in mind that the linear stopping power is defined as $\rho\langle dE/dx\rangle$, the fraction of muons crossing the material can thus naturally be expressed as a function of the integrated density over the path length also called opacity $\zeta = \int \rho(x)dx$. By measuring the differential muon flux along multiple directions, the map of integrated opacity along these directions can be obtained. Thanks to the wide variety of precise parametrizations of muon flux at sea level, such measurements can be compared to the expected flux in case of a uniform density for the object to probe and discrepancies can be further investigated. Combining

multiple measurements from various points of view allows to triangulate the position and even characterize the detected anomalies. This method has been used for the discovery of the Big void in Khufu's pyramid [33] but also for nuclear safety [34], monitoring of buildings stability [35] or vulcanology [36] to only cite a few.

2.2.3 Muon tomography activities at CEA

CEA Saclay has always been specialized in Micromegas detectors as they were designed and developed by IRFU researchers in 1996 [7]. Since then, this technology has been increasingly used and the strong potential of such detectors in fields extending from particle physics to biomedical and industrial applications motivated many R&D efforts to always improve these instruments [8]. It is only in 2014, following the development of the first multiplexed bulk Micromegas detector, that muon tomography applications were considered. A timeline of the main events leading to or contributing to muography activities at CEA Saclay is presented in Fig 2.10.

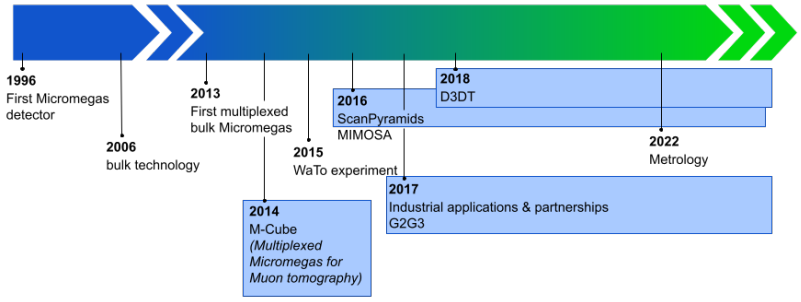

Figure 2.10: Timeline of the main events and projects leading to or contributing to muon tomography activities at CEA Saclay.

It started with the M-Cube *(Multiplexed Micromegas for Muon tomography)* project, funded by the NRBC-E CEA-DGA funding, thanks to which the first multiplexed prototype called MultiGen [16] was perfected and its performances validated for muon tomography purposes. The objective was to build and characterize a muon scanner to probe containers and detect nuclear waste smuggling within a few minutes. A demonstrator made out of 16 MultiGen detectors for an active volume of 1 m^3 was able to successfully detect 4 kg of depleted Uranium in less than two minutes. The next year, the first muon telescope was built and successfully operated combining these newly validated detectors with the new self-triggering DREAM electronics [37]. The water tower of Saclay was successfully imaged (see Fig 2.8(b)), even allowing to detect a draining of the tank during the data taking period [16].

At the end of 2015, CEA joined the ScanPyramids[2] mission and contributed to the discovery of Khufu's big void [33] in 2016. This mission motivated significant improvements of the muon telescope to make it more compact, more robust to temperature variations, accessible remotely and less power consuming. During the time of my PhD I had the chance to take part in this project which is briefly developed in the following section.

2: http://www.scanpyramids.org/

With the new visibility came a lot of interest from industrial leading to various projects, from simulation based proof of concept to the develop-

ment of new instruments, and partnerships such as the joint laboratory between CEA and IRIS Instruments[3].

3: https://www.iris-instruments.com/fr/

2.3 The ScanPyramids mission

Following the success of the WaTo experiment [16] that illustrated the potential of Micromegas detectors for muon tomography, CEA was able to join the ScanPyramids mission which started in 2015 and aims to investigate the structure of the great pyramids of Egypt using non-invasive nor destructive methods. Various technologies are used simultaneously in order for any eventual discovery to be cross-checked and validated by a different approach. To this end, the ScanPyramid mission regroups among others three muon tomography teams:

- Nagoya University (Japan) using nuclear emulsion films,
- KEK (Japan) using scintillator hodoscopes,
- and CEA (Saclay) using Micromegas detectors

each time to probe the pyramids structure using cosmic muons. Table 2.1 compares the performances of each technology showing the complementarity of these techniques.

Table 2.1: Comparison of the technical solutions used in the ScanPyramids mission.

Technology	Spatial resolution	Angular resolution	Covering area	Power consumption	Analysis time
Nuclear emulsions	1 μm	1.8 mrad	$7 \times [75 \times 30]$ cm^2	0 W	Development - Long
Scintillator hodoscope	3 mm	10 mrad	120×120 cm^2	300 W	Online processing
Micromegas telescopes	200 μm	1 mrad	$5 \times [50 \times 50]$ cm^2	3×35 W	Online processing

In addition, two campaigns of infrared thermography are conducted by the LedLiquid firm as well as Laval University from Canada. Finally, the Iconem firm uses drones to realise a photogrammetry measurement to provide a 3D model of the full Giza plateau with a precision of the order of the centimeter never achieved before.

I joined the team at CEA, first as a master student, in April 2019. At that time, Khufu's big void had already been discovered [33] as well as the so-called North-Face Corridor (NFC) behind the chevrons structure. Both cavities are illustrated on the artist view Fig 2.11.

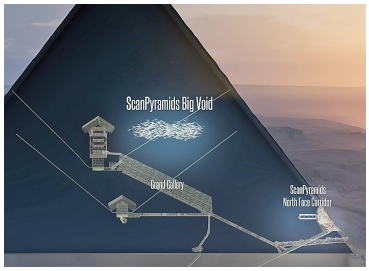

Figure 2.11: Artist view of the known structures of Khufu's pyramid thanks to the ScanPyramids mission in 2019.

2.3.1 October 2019 mission

The objective of this mission was to move the muon telescopes already inside the pyramid to more optimal positions in order to allow for a precise triangulation and characterization of the NFC [38]. Its shape and location can be fully parametrized by: its width W, height H and length L, as well as its position along the North-South axis X, East-West axis Y and altitude Z, and finally its slope α. For this analysis, 3 telescopes were used:

- *Joliot*, with an active area of 50×50 cm^2 and located in the descending corridor,
- *Charpak*, made of two smaller telescopes for a total active area of 100×50 cm^2 and located in the descending corridor,
- *Degennes*, identical to *Charpak* and placed on a dedicated wooden platform at the intersection between the ascending and descending corridors.

Compared to the previous measurement campaigns [33], a more compact version of the telescopes was used as shown in Fig 2.12.

Muon telescopes for the October 2019 ScanPyramids mission

A muon telescope is made of 4 bulk-Micromegas tracker planes of 50×50 cm^2 each and arranged in a total volume of $50 \times 50 \times 55$ cm^3. Each detector reads both X and Y coordinates separately via 2 sets of 1037 multiplexed strips placed perpendicularly to one another and separated by an insulator. A resistive film is printed on top of the readout strips allowing for a more stable operation and higher gain [39].

A non-flammable gas mixture made out of Ar-iC_4H_{10}-CF_4 (95-2-3) is circulated through all 4 detectors before being filtered and recirculated [40] allowing the total gas consumption to be as low as 0.5 L/h when acquiring data.

Each telescope is operated using a Intel NUC mini-PC running GNU/Linux which controls all the electronics (the power supply, the readout electronics and a patended amplitude feedback allowing for real-time adjustment of the detector gain to follow the extreme environmental conditions of the Giza plateau) as well as the pre-processing of the data.

The telescopes are connected together via an Ethernet cable installed inside the descending corridor and can be controlled remotely thanks to a 4G router which antenna is placed below the Chevron structure. This connection also ensure the post-processed data transfer from Egypt to CEA in France to be analyzed.

Figure 2.12: Comparison of CEA muon telescopes design between the first and last ScanPyramids mission.

2.3.2 Results

At the end of this measurement campaign, the equivalent of 140 days of data taking was acquired resulting in more than 116 millions of muons reconstructed. Raw muographies are obtained by plotting the 2D angular distributions ($\tan\theta_x$, $\tan\theta_y$) of the reconstructed muons and compared to GEANT4 [28] simulations. Six cosmic muon flux parametrizations are implemented to normalize the data, all of which revealing an excess with a significance above 10 σ corresponding to the NFC as shown in Fig 2.14. Slicing the normalized muographies from all instruments allows to extract the extremities of the NFC in each angular plane and draw the cones shown in Fig 2.13 which intersections are used to precisely determine the L, α and Z parameters. A dedicated χ^2 analysis is required to extract Y, W and H. The final measurements are presented in Table 2.2.

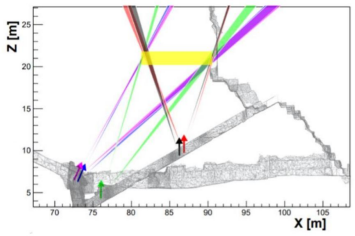

Figure 2.13: Triangulation of the NFC using the 5 instruments, where each cone represents the extremity of the NFC found in one data set. The width of each cone represents the uncertainty of its direction, i.e. from 0.5° to 1.5°. The arrows show the orientation of each instrument. The yellow rectangle represents the position and size of the NFC as determined from the CEA analysis. Taken from [38].

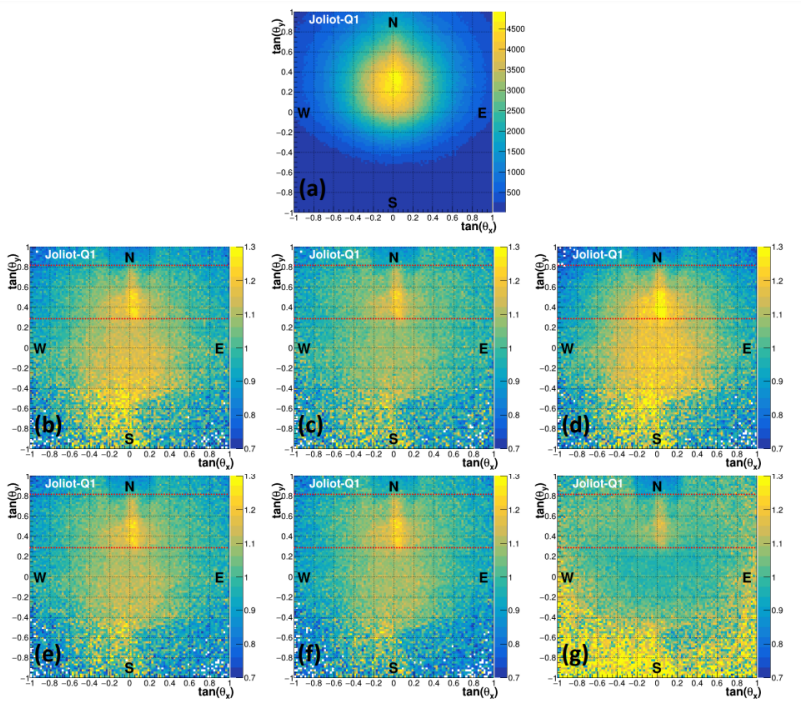

Figure 2.14: (a) Muography of the Joliot instrument; **(b-g)** Ratio between Joliot muography and GEANT4 simulations of the known structures, using parametrizations from Tang **(b)**, Reyna **(c)**, Matsuno **(d)**, Bogdanova **(e)**, Guan **(f)** and Shukla **(g)**. Taken from [38].

Table 2.2: Summary of the NFC dimensions, positions and orientation as obtained independently by Nagoya and CEA analyses. The East-West shift is taken from the Descending Corridor. X is positive for South. Y is positive for West. Taken from [38]

Parameter	Nagoya estimate	CEA estimate
W [m]	2.02 ± 0.06	1.87 ± 0.11
H [m]	2.18 ± 0.17	1.86 ± 0.12
L [m]	9.06 ± 0.07	9.23 ± 0.48
X [m]	0.84 ± 0.05	0.45 ± 0.22
Y [m]	0.03 ± 0.04	-0.07 ± 0.11
Z [m]	0.72 ± 0.13	1.34 ± 0.53
α [°]	-0.3 ± 1.5	$-1.9\ ^{+7.3}_{-4.7}$

2.4 Toward new applications

2.4.1 Probing the underground with muon tomography

Muons can penetrate so deep into matter that the flux is still non-zero a few hundreds meters underground as highlighted in Fig 2.15. This realisation made muon tomography a potential technical solution for underground probing. There could be many applications extending from civil engineering and archeology to mining exploration or geothermal fields sounding. One could imagine installing a few muon detectors around an area of archeological interest to image the main structures before excavating.

A more tangible example would be the monitoring of Tunnel Boring Machines (TBMs). The fact that TBMs progress only by a few meters per day made them perfect candidates to host muon detectors that would probe the surroundings of the machine and raise an alarm if any unknown structures is detected on the path or cavities in the overburden that would risk collapsing. This specific application have been further studied in the context of a proof of concept for an industrial in 2018. Simulations were conducted using GEANT4 [28] to estimate the muon flux that could be

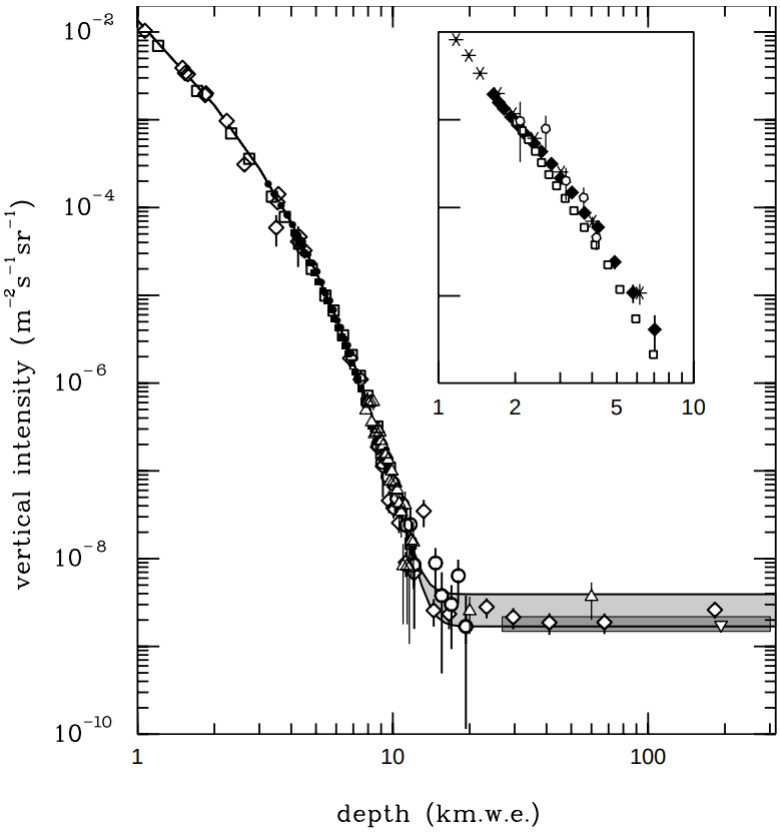

Figure 2.15: Vertical muon intensity as a function of depth (1 kmwe = 105 g cm^{-2} of standard rock). Taken from [3].

detected according to the topology of the terrain and the sensibility to which defects could be detected in the allowed amount of time.

2.4.2 Muon telescopes limitations

First of all, muon telescopes are not very easy to operate underground: as they function as trackers, it is actually several detectors that need to be operated which multiply the power consumption and complicates the gas circulation system as well as the risk of leaks. In addition, its compacity is limited. As mentioned in Section 2.3, the most recent and compact version of the telescopes occupies a volume of $50 \times 50 \times 55$ cm^3. Efforts can be made to design much smaller telescopes [41] but at the expense of the active area and thus the muon rate. Although using muon telescopes underground is not impossible, their limitations become quite obvious when the location of the objects to probe is unknown. As illustrated in Fig 2.16, the directionality of the telescopes makes it so that in order to probe the entire overburden, it is necessary to acquire data for various inclinations and positions of the telescope. In such conditions, the minimum amount of time required to detect a potential cavity is arbitrarily increased. To exploit the full potential of muon tomography in view of probing the underground, there must be a more suitable instrument.

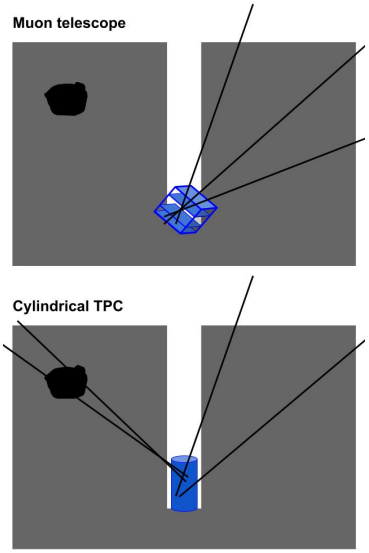

Figure 2.16: Schematic view of muon tomography for underground probing application using a muon telescope **(top)** or a cylindrical TPC **(bottom)**.

2.4.3 The ideal instrument

Following the previous considerations, one of the most critical constraint is the possibility to probe all directions which translates, in terms of detector requirements, into a 2π angular acceptance. In order to facilitate underground operation, the electric consumption should be as low as possible which point towards a single detector, yet allowing 3D reconstruction of muon tracks. In addition, assuming that a Micromegas detector will be used as readout plane due to CEA expertise in the field, the detector should ideally be sealed. Finally, in terms of compacity, it would prove very convenient to be able to use existing boreholes to install the detector underground, thus minimizing any additional costs for installation. This imposes a limit on the detector geometry that should present an active area with a diameter smaller than 20 cm. An overview of the constraints and technical solution considered is shown in Table 2.3.

Next Chapter presents D3DT, a new instrument developed at CEA aiming to meet these requirements to be used for underground exploration.

Table 2.3: Comparison of the technical solutions used in the ScanPyramids mission.

Constraint	**Requirement on the instrument**	**Technical solution**
Probe all directions	2π angular acceptance	Cylindrical multiplexed TPC
Minimum electric consumption	1 detector with 3D reconstruction	
Maximum compacity	Minimum electronic channels	
Fit into existing boreholes	$\varnothing < 20$ cm	$\varnothing < 20$ cm
Use CEA expertise	Use Micromegas detector	Micromegas readout plane

D3DT: FROM DESIGN TO PROTOTYPE 3

Following the motivations for developing a new muon tomography instrument expressed in Chapter 2, this chapter focuses on the design and experimental developments of D3DT (Detector 3D for muonic Tomography). After briefly studying the feasibility of underground muon tomography in the first section, each part of the detector design is carefully detailed in Section 3.2. Finally, the first experimental developments and prototypes will be presented in a last section.

3.1 Proof of concept

GEANT4 simulations were conducted to study the sensitivity of an ideal instrument as described in the previous chapter. The objective is to determine the type of underground objects (cavities, dense material...) that could be detected using a cylindrical active volume with the same dimensions as planned for the D3DT detector. This study was carried by Benjamin Gallois as part of his work-linked training.

3.1.1 Geometry definition and simulation parameters

Muons direction and energy are sampled from Shukla's parametrization before being propagated using the G4Tomomu framework [34]. More details about muons generation and propagation can be found in Chapter 5. The detector is simulated as a cylindrical active volume with the same dimensions as D3DT design ie. 40 cm height and 6 cm radius. At this stage, detector effects are not taken into account: any muon reaching the active volume is counted as detected. The cylinder is placed 30 m underground into standard soil of uniform density $\rho_{\text{soil}} = 2.2\,\text{g}\,\text{cm}^{-3}$. Underground objects are simulated as infinite cylinders along the z axis so that the sensitivity of the detector can be studied as a function of the elevation angle $\alpha = \pi/2 - \theta$, where θ is the zenithal angle, without having to run multiple simulations. This is illustrated by Fig 3.2. In addition, taking advantage of the rotational symmetry of the problem, multiple situations (different cavity parameters) are simulated in a single simulation by surrounding the detector with a network of 8 cavities equally placed every 45° of azimuthal angle, again reducing the computation time. As shown by Fig 3.1, three parameters are studied:

1. the radius r of the cavity
2. the distance d of the cavity
3. the density ρ of the cavity filling material

Each simulation generates about 20 millions events which is about 43 days of data taking. The simulated configurations are summarized in Table 3.1.

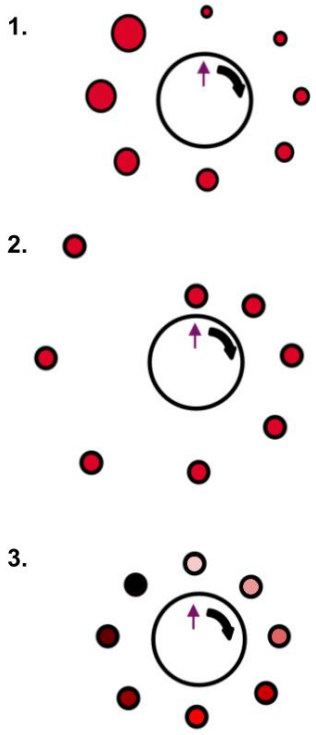

Figure 3.1: Studied parameters of the simulated cavities: 1. radius; 2. distance; 3. density of filling material.

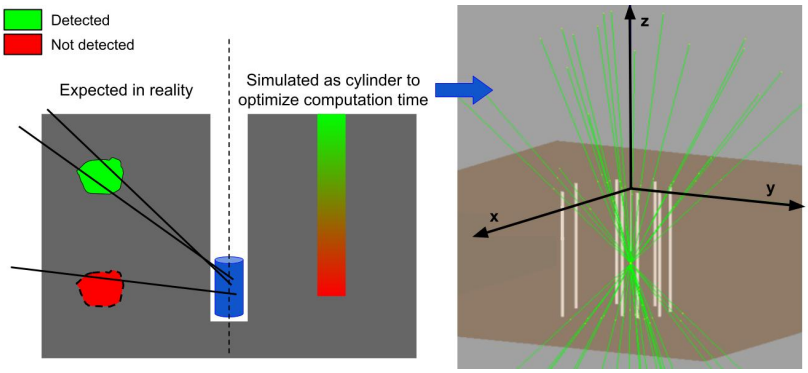

Figure 3.2: Left: Scheme explaining why cavities are simulated as cylinders; **Right:** Visualization of one of the simulated situations: the detector is placed 30 m underground and surrounded by a network of cylindrical cavities placed every 45° of azimuthal angle. The green lines show some example of muon trajectories.

Table 3.1: Summary of the run simulations for D3DT sensitivity study.

Simulation n°	Parameter studied	Cavities
0	Reference	No cavity
1	Radius	$\rho = 1\,\mathrm{g\,cm^{-3}}$ $d = 10\,\mathrm{m}$ $r = [0.25, 2]\,\mathrm{m}$
2	Distance	$\rho = 1\,\mathrm{g\,cm^{-3}}$ $d = [7, 28]\,\mathrm{m}$ $r = 0.75\,\mathrm{m}$
3	Density of filling material (soil)	$\rho = [0.001, 2]\,\mathrm{g\,cm^{-3}}$ $d = 10\,\mathrm{m}$ $r = 0.75\,\mathrm{m}$
4	Density of filling material (soil)	$\rho = [2.5, 9.5]\,\mathrm{g\,cm^{-3}}$ $d = 10\,\mathrm{m}$ $r = 0.75\,\mathrm{m}$
5	Density of filling material (water)	$\rho = [0.001, 2]\,\mathrm{g\,cm^{-3}}$ $d = 10\,\mathrm{m}$ $r = 0.75\,\mathrm{m}$
6	Density of filling material (water)	$\rho = [2.5, 9.5]\,\mathrm{g\,cm^{-3}}$ $d = 10\,\mathrm{m}$ $r = 0.75\,\mathrm{m}$

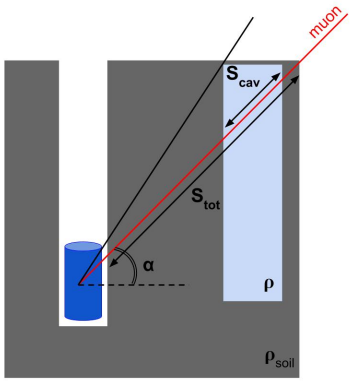

Figure 3.3: Scheme of a muon traversing a cavity as simulated and definition of the S_{tot} and S_{cav} parameters as well as the elevation angle α.

3.1.2 Analysis method

In order to be able to compare the results from the various simulations, the opacity difference $\Delta\zeta$ is introduced and defined as:

$$\Delta\zeta = \frac{|\zeta_{\mathrm{tot}} - \zeta_{\mathrm{ref}}|}{\zeta_{\mathrm{ref}}} \tag{3.1}$$

where ζ_{ref} is the opacity of the ground without any cavity while ζ_{tot} is the opacity seen by the muon traversing the cavity. Noting S_{tot} the muon path and S_{cav} the muon path inside the cavity only, the opacities are computed as follows:

$$\begin{aligned} \zeta_{\mathrm{ref}} &= \int_{S_{\mathrm{tot}}} \rho_{\mathrm{soil}} dx \\ \zeta_{\mathrm{tot}} &= \int_{S_{\mathrm{cav}}} \rho dx + \int_{S_{\mathrm{tot}} - S_{\mathrm{cav}}} \rho_{\mathrm{soil}} dx \end{aligned} \tag{3.2}$$

This is illustrated by Fig 3.3. In addition, the residual R is used to compare the number of detected muons to the reference simulation and is defined

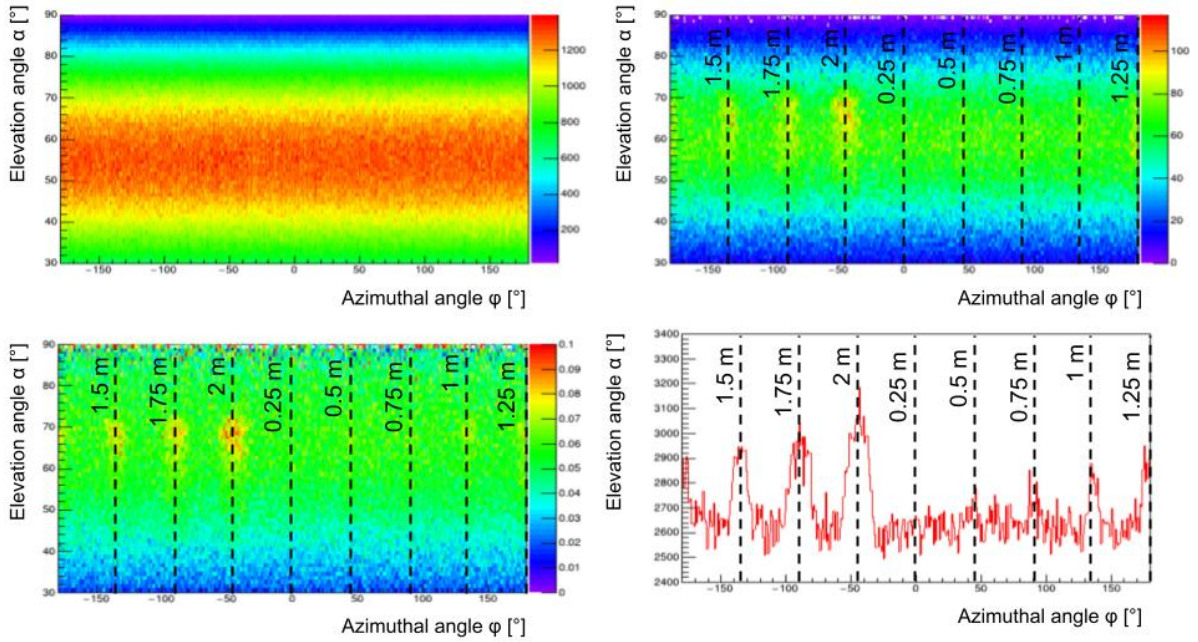

Figure 3.4: Top left: Generated muon distribution; **Top right:** Detected muon distribution. The positions of the surrounding cavities are highlighted by black lines with their respective radius indicated; **Bottom left:** Normalized distribution of the detected muons. **Bottom right:** Number of detected muons as a function of the azimuthal angle.

as:

$$R = \frac{N_{\text{detected}} - N_{\text{ref}}}{\sqrt{N_{\text{detected}} + N_{\text{ref}}}} \tag{3.3}$$

where N_{detected} is the number of detected muons for a given configuration and N_{ref} is the number of detected muons in the reference simulation ie. without any cavity.

3.1.3 Results

The results of the simulation varying the radius parameter are presented in Fig 3.4. From the raw distribution already, the cavities with a radius larger than 1.5 m can easily be spotted. On the 1D distribution integrated along the elevation angle, excess in the number of detected muons can be seen for cavities with radius larger than 0.75 m. If this is already very encouraging, detection performances can be enhanced by choosing an optimal binning of ϕ and α that maximize the residuals. This optimal binning depends on the position and size of the cavity which will be unknown in real cases. A sliding window algorithm is developed aiming to localize and measure a possible cavity:

- **If an anomaly is detected:** a threshold is fixed on the residual to define an anomaly ie. a possible cavity. As an example, the threshold is fixed to 2σ
    1. **Localize the anomaly:** the residuals are computed for a sliding window of $6° \times 6°$ and the position that maximizes the residuals, noted (ϕ_0, θ_0), is defined as the location of the detected anomaly. This is illustrated by Fig 3.5 (Left).
    2. **Characterize the anomaly:** Around the previously found position, the process is repeated this time changing the size of the

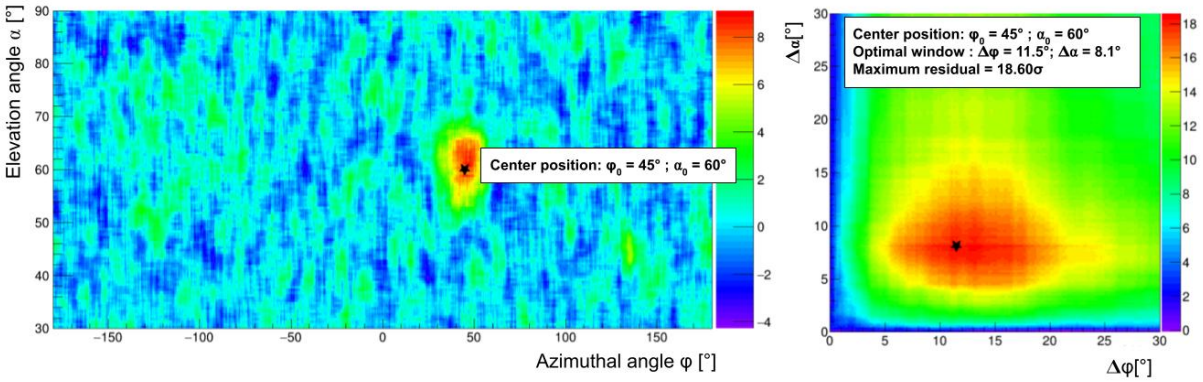

Figure 3.5: Left: Residuals computed for a window of 6°× 6° as a function of azimuthal and elevation angles. The star highlights the position of the detected anomaly; **Right:** Residuals computed by modifying the size of the window around the position obtained previously.

window centered on (ϕ_0, θ_0) and of dimensions $(2\Delta\phi, 2\Delta\theta)$. The optimal binning is defined by the $(\Delta\phi, \Delta\theta)$ that maximizes the residuals. This is illustrated by Fig 3.5 (Right).

This algorithm is tested on a simulated data set containing a single cavity and the results are presented in Fig 3.5: the cavity localisation is reconstructed at $\phi_0 = 45°$ and $\alpha_0 = \pi/2 - \theta_0 = 60°$ with dimensions given by $2\Delta\phi = 23°$ and $2\Delta\alpha = 2\Delta\theta = 16.2°$. This is to be compared with the simulated cavity parameters which are the following:

- Placing the origin at the center of the detector, the center of the cavity coordinates are given by $O_{cav} = (6.125\,\text{m}, 6.125\,\text{m}, 15\,\text{m})$ which gives $\phi_0 = 45°$ and $\theta_0 = 30°$ indeed.
- The cavity is simulated as a cylinder of radius $r = 2.5\,\text{m}$ and height $h = 7\,\text{m}$ which translates into angular dimensions of $\Delta\phi_{cav} = 24°$ and $\Delta\theta_{cav} = 11.9°$

As the parameter of interest is the opacity difference, the performances of the cavity dimensions estimation are affected by the cavity shape as well and position with regard to the detector and density of filling material. But with this example, it is shown that the cavity is correctly located and its angular dimensions are estimated with a precision of 4% on ϕ and 27% on θ with a data set corresponding to approximately 17 days of data taking. In the end, the idea is to install several detectors in a network so the cavity can be better characterized by combining various points of view as explained in the context of the ScanPyramid mission in Section 2.3.2.

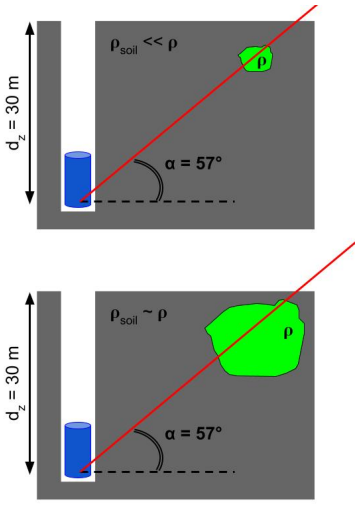

Figure 3.6: Example of extreme situations that could yield an opacity difference of 6%: a small object with a density $\rho \gg \rho_{soil}$ (top) or a very large object with $\rho \sim \rho_{soil}$ (bottom).

Finally, the results of all simulated configurations were compared to produce the curves shown in Fig 3.7 which indicate the opacity difference to which the detector is sensitive for various detection threshold and as a function of the elevation angle and the measurement time. It shows for example that after a month of data taking, it is possible to detect with a 3σ significance an opacity difference of about 6% at an elevation angle of 57°. It can either be a small object with a density very different from the standard soil density or a much larger object with a close density as illustrated by Fig 3.6.

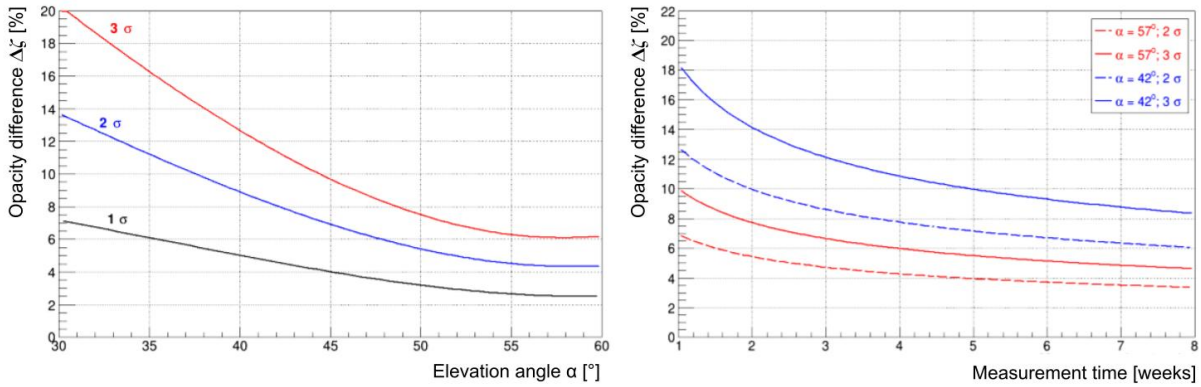

Figure 3.7: Left: Opacity difference detectable at various sensitivities (1σ in black, 2σ in blue and 3σ in red) as a function of the elevation angle α ; **Right:** Opacity difference detectable at various sensitivities (2σ with dashed line and 3σ with solid line) and elevation angles ($\alpha = 42°$ in blue and $\alpha = 57°$ in red) as a function of the measurement time in weeks.

Object size for an opacity difference of 6%

For the example, the detector is placed at a distance $d_z = 30\,\text{m}$ underground and the object is located at an elevation angle $\alpha = 57°$. The total path length of the muon is given by:

$$S_{\text{tot}} = \frac{d_z}{\sin\alpha} = 35.77\ \text{m}$$

Assimilating the object to a sphere of radius r_{obj}, the muon path inside the object is given by $S_{\text{cav}} = 2r_{\text{obj}}$. In this case, the opacity difference is given by:

$$\Delta\zeta = \frac{|\zeta_{\text{tot}} - \zeta_{\text{ref}}|}{\zeta_{\text{ref}}} = \frac{|(S_{\text{tot}} - S_{\text{cav}})\rho_{\text{soil}} + S_{\text{cav}}\rho - S_{\text{tot}}\rho_{\text{soil}}|}{S_{\text{tot}}\rho_{\text{soil}}}$$
$$= \frac{2r_{\text{obj}}|\rho - \rho_{\text{soil}}|}{\frac{d_z}{\sin\alpha}\rho_{\text{soil}}}$$

so that

$$r_{\text{obj}} = \frac{\Delta\zeta d_z \rho_{\text{soil}}}{2\sin\alpha|\rho - \rho_{\text{soil}}|}$$

Case n°1: $\rho_{\text{soil}} \ll \rho$
With $\Delta\zeta = 6\%$ and $\rho = 10 \times \rho_{\text{soil}}$ (*e.g.* Plutonium), it yields

$$r_{\text{obj}} = 0.12\ \text{m}$$

Case n°2: $\rho_{\text{soil}} \sim \rho$
With $\Delta\zeta = 6\%$ and $\rho = 0.9 \times \rho_{\text{soil}}$, it yields

$$r_{\text{obj}} = 10.73\ \text{m}$$

3.2 Detector design

When I joined the CEA muography team for my PhD, D3DT was an R&D project whose design relied heavily on previous experience: the field cage and electronics for example had already been used and characterized for

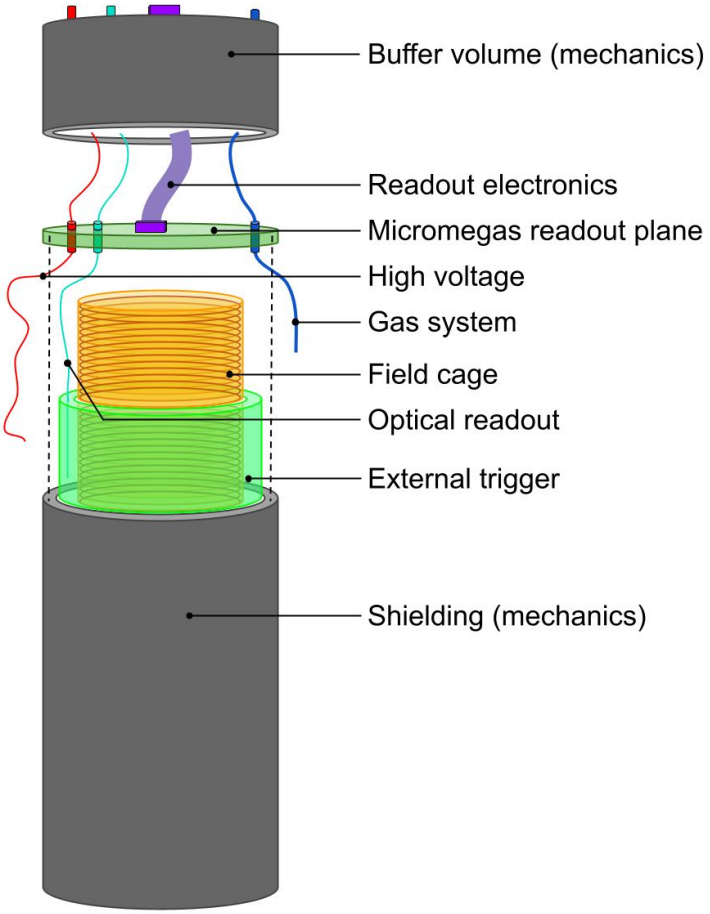

Figure 3.8: Schematic exploded view of D3DT detector design.

other projects. Other parts on the other hand, like the readout plane or the trigger system, were completely innovative concepts.

The global design is presented in Fig 3.8 and consists in a 40 cm drift cylindrical TPC read by a bulk Micromegas detector. A plastic scintillator cylinder is inserted between the stainless steel shielding chamber and field cage to serve as external trigger. The bulk Micromegas readout plane is paved by 1344 hexagonal pixels divided onto three identically mapped sectors, each one read by a DREAM [37] Application Specific Integrated Circuit (ASIC). A FEU card reads the three ASICs and is connected to a Intel NUC mini-PC for data acquisition. At the moment, high voltage is provided by an external Iseg SHR high voltage power supply but at term, a miniaturized version of the readout electronic and power supply should be placed in the buffer volume. The gas is currently circulated through the detector but to facilitate underground operation, the objective would be at term to have a sealed detector. There could be a gas filtration and re-circulation unit inside a larger buffer volume as well.

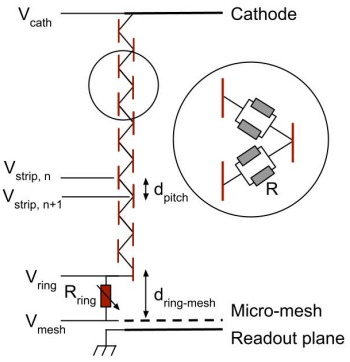

Figure 3.9: Field cage wiring scheme.

3.2.1 Field cage

The field cage has been manufactured at CERN and uses the same wiring as the MINOS [42] TPC field cage. It is made out of a double sided copper-clad 50 µm-thick Kapton foil. The drift space is defined by a

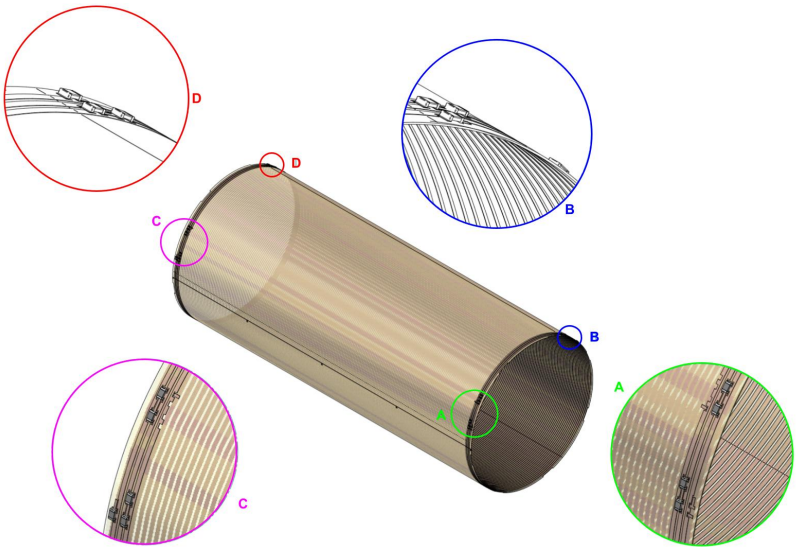

Figure 3.10: Field cage design produced with Solid Edge.

cylinder of 122 mm diameter and 400 mm height which corresponds to a 384.58×400 mm^2 Kapton sheet. Copper strips have a width of 2 mm for a pitch of 3 mm, they are identical on both sides of the Kapton sheet but staggered with a 2 mm displacement between each face. The resistors used to degrade the electric field are SMC (Surface-Mount Component) 0603 (1.6×0.8 mm^2), each one of value $R = 3.9\,\text{M}\Omega \pm 1\%$, and wired as illustrated by Fig 3.9. To ensure the electric drifting field uniformity while the distance between the last copper ring and the micro-mesh is not the same as the pitch, a potentiometer R_{ring} is added and set so that:

$$E_{\text{drift}} = \frac{V_{\text{strip, n+1}} - V_{\text{strip, n}}}{d_{\text{pitch}}} = \frac{V_{\text{ring}} - V_{\text{mesh}}}{d_{\text{ring-mesh}}} \tag{3.4}$$

Fig 3.10 shows the resulting design drawing of the field cage produced by Solid Edge.

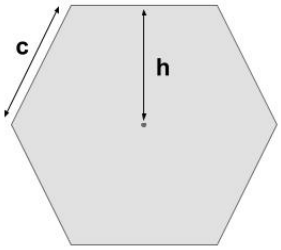

Figure 3.11: Hexagonal pixel dimensions.

3.2.2 2D-multiplexed readout plane

The readout plane consists of a bulk-Micromegas [9] detector with a 128 µm amplification gap paved by 1344 hexagonal pixels depicted by Fig 3.11 and with dimensions $c = 0.17$ cm and $h = c\cos(\pi/6) = 0.15$ cm for a total active area of about 100 cm^2. A grounded guard ring is added to suppress any edge effects in the electric field near the active area limits as shown by Fig 3.13. The pad plane is divided into 3 sectors, each read by an ASIC of 64 electronic channels. Each sector mapping is independent and identical to the others if rotated. In view of minimizing the number of readout electronic channels, each sector is also 2D-multiplexed meaning that each electronic channel is connected to between 6 and 9 pixels. As an example, Fig 3.15 (Left) shows the mapping of electronic channel #36 on each of the three sectors. As a result, routing is particularly difficult and requires in this case a 12 layers PCB as illustrated by Fig 3.15 (Right). This has the effect of increasing the dispersion of the routing length which can affect the input capacitance of each electronic channel, in addition to it being already increased by the multiplexing.

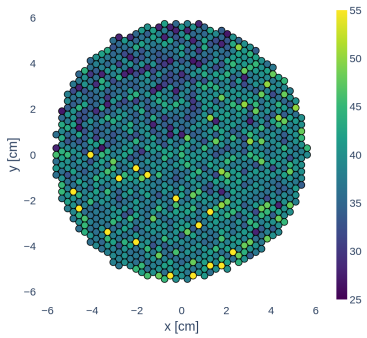

Figure 3.12: Map of the measurement of the input capacitance of each electronic channel in pF. A few pixels (in yellow here) were actually measured at ~ 130 pF but the color scale range was limited to allow for a better visualisation. This is discussed in further details in Section 3.2.2.

Multiplexing is only relevant if it is possible, while analyzing data,

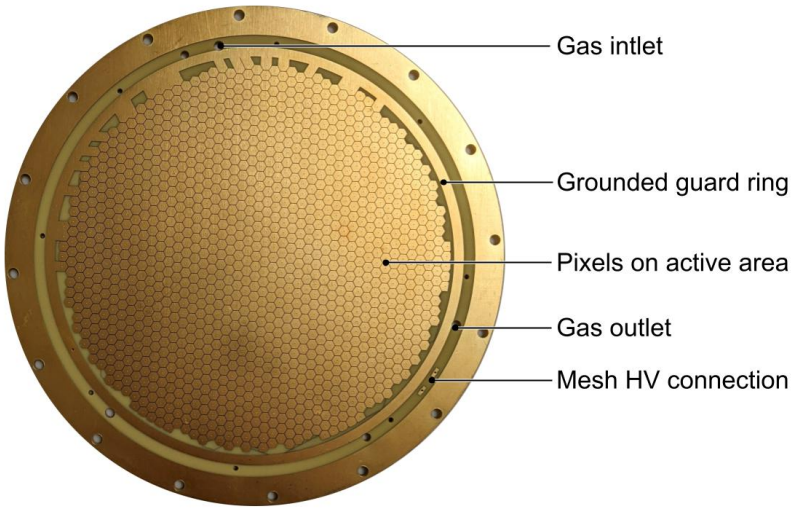

Figure 3.13: Annotated top view photograph of D3DT readout plane PCB before being bulked.

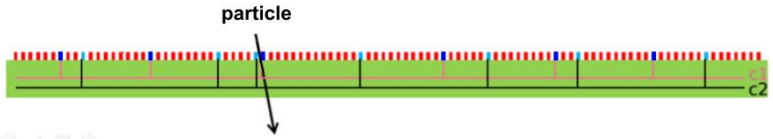

Figure 3.14: Sketch of the principle of genetic multiplexing illustrated by a particle which induces a signal on channel c_1 and c_2. Taken from [43]

to go back to which one of the multiplexed pixels actually collected charge. For example, if the multiplexed pixels were simply juxtaposed to form a macro-pixel, it would only result in a degradation of the spatial resolution compared to the non-multiplexed situation. The objective is thus to find a ingenious way to arrange multiplexed pixels in order not to compromise on reconstruction performances. In this case, the mapping has been generated using reinforcement learning and is based on the 2D generalisation of the genetic multiplexing [43].

Multiplexing algorithm

1D Genetic multiplexing

The principle of genetic multiplexing is illustrated in Fig 3.14. Let consider for example a readout plane covered by N_{strip} multiplexed strips read by N_{channel} electronic channels. Two important hypothesis are made:

1. the system is scaled to ensure that a particle induces signal on at least two strips
2. 2 channels c_1 and c_2 can only once be neighbours on the entire readout plane

Under such conditions, it is possible to infer the particle crossing position as the only point of the readout plane were the two simultaneously fired channels are neighbours. This genetic multiplexing algorithm is used for the MultiGen [16] detectors as further developed in Chapter 2.

Generalisation to 2D

D3DT pixels are too large to ensure that a cluster of primary electrons will induce signal onto multiple pixels. However, instead of a single hit

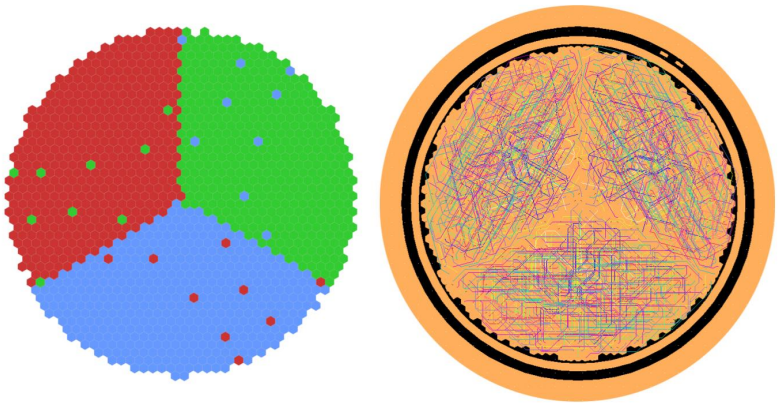

Figure 3.15: Left: Mapping of the electronic channel #36 of each sector; **Right:** Gerber of the 12 layer PCB, each color representing the routing of a layer.

position in a tracker, the expected signal is now a full track projected. Using the track continuity gives an analogous hypothesis as for the 1D situation. The objective is thus to generalize the second hypothesis accordingly and generate the mapping of the detector ensuring that two channels are neighbours only once per sector.

Identified issue with sector 0

From the first laboratory tests, two electronics channels from sector 0[1], channel 13 and 31, showed pedestal RMS values 2 to 3 times larger than the other channels as illustrated by Fig 3.17. It is also the case for a channel of sector 2, however in this case there are no further consequences. As further presented in the next Chapter, channel 13 and 31 of sector 0 also present an input capacitance of about 130 pF while all other channels range between 20 and 50 pF. The resulting waveforms are highly degraded as shown in Fig 3.16. Quick tests ensured that the issue comes from the readout plane and not the readout electronics. It was finally identified that those channels are unwittingly connected to the guard ring. Multiple checks ensured that it did not came from a design error, which is also supported by the fact that it is not replicated on the other two sectors. It is suspected that the error came from the manufacturing process of the PCB although it could not be confirmed by the contractor. Specified attention will be given when producing new readout planes but it should be kept in mind that the data used for this analysis were affected by the issue. To minimize the impact, channels 13 and 31 of ASIC 0 are until further notice suppressed from trigger and usually excluded from the analysis.

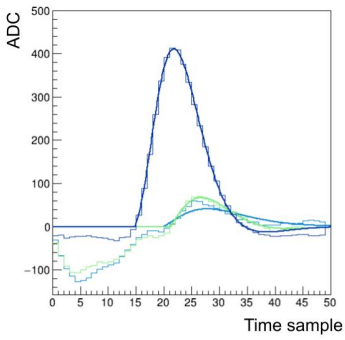

Figure 3.16: Example of waveform obtained involving noisy channels 13 and 31 from sector 0.

1: referred to as sector 0 because usually read by ASIC 0

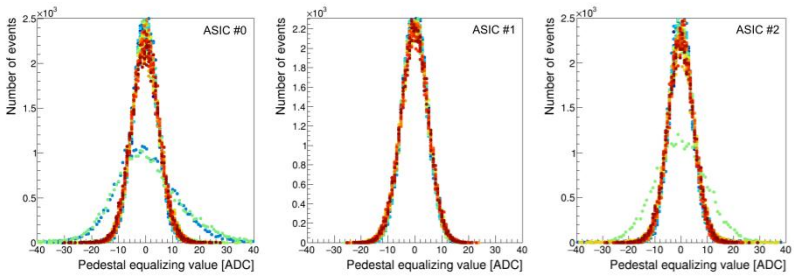

Figure 3.17: Distributions of pedestal equalizing values in ADC for the 64 channels of ASICs 0, 1 and 2 respectively.

3.2.3 Electronics

As mentioned before, each sector of the readout plane is read by a DREAM (Dead-timeless Read-out Electronics ASIC for Micromegas) ASIC [37] initially developed at CEA to read the Micromegas chambers of the CLAS12 experiment tracker. Each of the 64 channels of the chip handles the amplification, the filtering, the discrimination and the analogue storage of the detector signal as illustrated by the block diagram presented in Fig 3.19.

The Charge Sensitive pre-Amplifier (CSA) is optimized to read detectors with large capacitance and accommodate for Micromegas detectors with large areas or, in this case, multiplexed readout. The gain of the CSA is set to 200 fC. The analog filter, or shaper, consists of a Pole Zero Cancellation stage followed by a 2-complex pole Sallen-Key low pass filter. The peaking time of the shaped signal can be selected from multiple values ranging from 50 to 900 ns and is set to 283 ns. The DREAM responses to a 70 fC charge input for multiple peaking times are shown in Fig 3.18. After

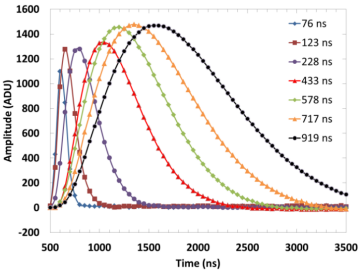

Figure 3.18: DREAM response to a 70 fC charge for various programmed peaking time with a 200 fC range. The variation of amplitude is expected from the design. Taken from [44]

.

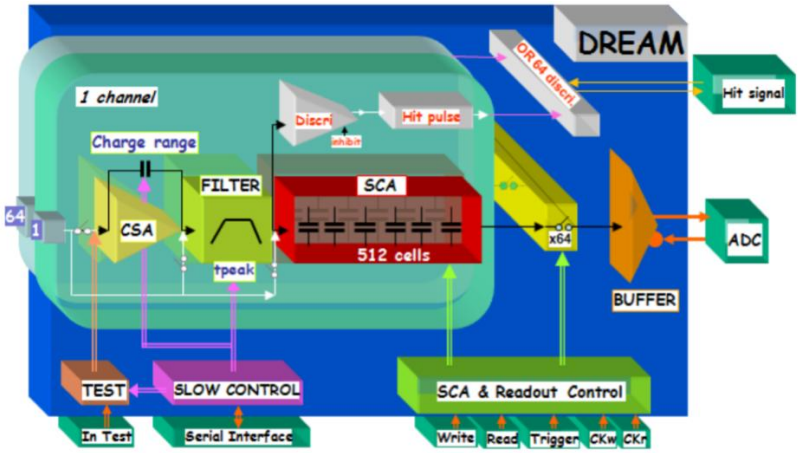

Figure 3.19: Block diagram of the DREAM chip. Taken from the DREAM User Manual.

being shaped, the signal is sent to both the analog memory to be sampled and stored, and the discriminator inputs to check whether or not the signal passed the threshold. The analog memory is made out of a Switch Capacitor Array (SCA) of 512 cells used as a circular buffer where the filtered signal is continuously sampled and stored. If there is no triggering event, the 512 cells keep being overwritten. However if a trigger signal is received, the corresponding cells are frozen before being read out on demand. The readout is asynchronous and performed in FIFO (First In First Out) mode meaning that the first data written in the SCA is the first one to be read out. It is the asynchronous readout, allowing to write the data without stopping the analog storage process, that ensures the "dead-time free" operation of the chip. These three ASICs are read by a Front End Unit (FEU) card, also developed at CEA for the CLAS12 experiment but applicable for the DAQ system of various type of particle detectors due to its flexible design as long as the readout rates are below 20 kHz. This card can host up to 8 DREAM ASICs but only three are used for D3DT. The FEU card reads data through specifically designed Samtec cables illustrated in Fig 3.20 with MEC8 connectors and is powered by 5 V supply. It is also connected to a Intel NUC mini-PC using Gigabit Ethernet links for control and monitoring. Data are written as fdf (file data format) binary files which data packet format is presented in Fig 3.21

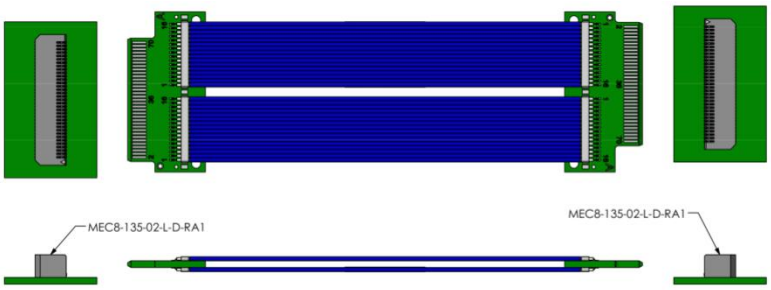

Figure 3.20: Specifically designed Samtec cable for detector to electronics connection. The MEC8 connectors can either be horizontal as illustrated or vertical.

15	14	13	12	11	10	9	8	7	6	5	4	3	2	1	0
HOP	FEU=11		0	SI[8]	Z=0	C	P	FEU Id							
HOP	FEU=11		0	Event Id[11:0]											
HOP	FEU=11		0	Time stamp[11:0]											
HOP	FEU=11		0	Sample index[7:0]								Fine TSTP			
HOP	FEU=11		0	Optional: Event Id[23:12]											
HOP	FEU=11		0	Optional: Time stamp[23:12]											
HOP	FEU=11		0	Optional: Time stamp[35:24]											
HOP	FEU=11		0	0	0	0	Optional: Time stamp[44:36]								
HOP	DrH=01		1	Dream raw header: Trigger Id MSB											
HOP	DrH=01		1	Dream raw header: Trigger Id ISB											
HOP	DrH=01		1	Dream raw header: Trigger Id LSB											
HOP	DrH=01		Err	Dream Id			Dream decoded header								
HOP	Data=00		Msk	Channel 0 data											
HOP	Data=00		Msk	Channel 1 data											
HOP	Data=00		Msk	Channel 63 data											
HOP	DrT=10		1	Dream raw trailer: CMN Chan 0 to 31											
HOP	DrT=10		1	Dream raw trailer : CMN Chan 32 to 63											
HOP	DrT=10		1	Dream raw trailer : Cell Id MSB											
HOP	DrT=10		1	Dream raw trailer : Cell Id ISB											
HOP	DrT=10		1	Dream raw trailer : Cell Id LSB											
HOP	DrT=10		Err	Dream Id			Dream decoded trailer								
HOP	FEU=11		1	EOE	Length										
HOP	VEP														

N x 74 words
N = non-masked Dreams

Figure 3.21: Non-zero suppressed data packet of the fdf binary file.

in the case of non-zero suppression. Dedicated softwares already in use for muon telescopes data acquisition and conversion to ROOT files were updated to also accommodate for D3DT data format. In addition, I developed a monitoring software to allow for online event display as well as some information about the run such as occupation.

In the future, efforts will be made to miniaturize the readout electronics and install it inside the buffer volume in order to facilitate underground installation.

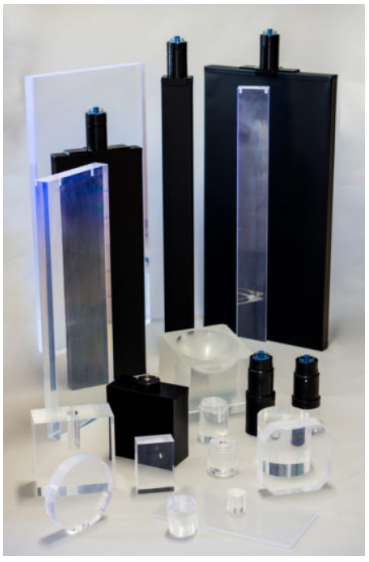

Figure 3.22: Examples of possible plastic scintillator shapes available from the supplier.

3.2.4 Trigger system

As illustrated in Fig 3.8, a plastic scintillator cylinder is placed around the field cage and read by optical fibers. It is produced by NuviaTech Instruments[2] and presents the following characteristics:

- **Light output:** 56% (relative to anthracene)
- **Decay constant:** 4.4 ns
- **Density:** 1.03 g cm^{-3}

- **Softening point:** 70-75°C
- **Refractive index:** 1.57

It should be machined in order for the optical fibers to pass through and to be mechanically fixed to the structure. Hollow cylinders could not be provided by the suppliers that only offers blocks or full cylinders as illustrated by Fig 3.22. Two solutions have thus been considered:

- **Order the full cylinder and drill it hollow:** this has the advantage of providing the final cylinder in a single piece. However, given it should only be a few millimeters thick at most, it will be difficult to drill it hollow without breaking it. In addition, there will be a lot of wasted material and the machining will be made more difficult by the curved surface.
- **Order rectangular blocks to bend and assemble into a cylinder:** in this case, the machining of the pass-through for the optical fibers will be easier and there will be no wasted material. On the other hand, the procedure to bend the scintillator pieces is still experimental and it is unknown whether it will affect its performances. In addition, several pieces will have to be assembled to build the cylinder.

In the end, the adopted solution is the latter: plastic scintillator sheets of 21.2×40 cm^2 are machined before being bent to be half-cylinders. A specific mould and weight have been designed so that the allowed space in between is exactly the shape that the plastic scintillator should take. The mould, plastic sheet and weight are placed into the oven set to 80°C as shown in Fig 3.23 for 24 hours. As the plastic soften from the heat, it will slowly adjust to the mould due to the constraint imposed by the weight. This is done very slowly in order not to create any cracks induced by high mechanical stretches that could affect the light transmission performances of the material. Afterwards, the whole set up is left 24 hours to naturally cool down. Each half cylinder is instrumented with BCF91-A optical fiber using optical glue to optimize light collection. Optical fibers are passed through the anode PCB and connected to an Hamamatsu silicon photomultiplier (MPPC). The digital output is used to produce D3DT trigger signal. In order to validate the trigger system, and especially ensure that the plastic scintillator performances were not affected by the bending procedure, the trigger system is characterized in the lab as further developed in Section 3.3.

At first, when the trigger system was not yet developed, data were acquired using the self-triggering mode of the readout electronics. In this situation, there is no way to extract the absolute z coordinates of drifting electrons but only the difference $z - z_{\text{min}}$ where z_{min} is the absolute z coordinates of the drifting electrons that first arrived to the readout plane and triggered the electronics.

3.2.5 Gas system

At the moment, the gas used is either an Ar-iC_4H_{10} (95:5) gas mixture, mixed in the lab from separate Argon and isobutane gas bottles, or the so called *T2K gas* which is composed of Ar-iC_4H_{10}-CF_4 (95:2:3) and comes premixed. Gas quality (especially water contamination) and flow rate are monitored using either Yoctopuce[3] sensors or Bronkhorst[4] mass flow

2: https://www.nuviatech-instruments.com/

3: http://www.yoctopuce.com

4: https://www.bronkhorst.com/

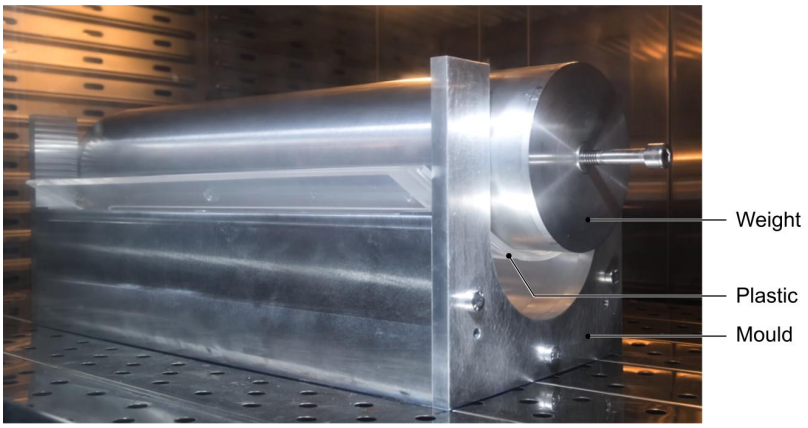

Figure 3.23: Bending of the plastic scintillator.

meter. Concerning the circuit, 6 mm diameter aluminum tube is used within the lab for as long as possible as it was found to limit permeation [40], followed by polyamide tube up to the top cover. In the buffer volume, a 6 mm diameter polyurethane tube is used: its permeation performances are worst but in this case, it is not too much of an issue as sealing is made by the top cover. In addition, it is more flexible allowing to adjust some room for all the elements to place inside the buffer volume. Finally, for a better circulation, a 2 mm diameter tube is passed throughout the plastic scintillator piece so that the gas arrives near the cathode to avoid any perturbation close to the readout plane. Fig 3.24 shows a schematic view of both gas and high voltage systems.

Eventually, the goal would be to fill the detector once and seal it before installing it underground. This requires additional research and development efforts to ensure that:

- the detector is completely hermetic
- the detector is made out of low outgassing materials
- the gas can be purified and re-circulated into the active volume
- the autonomy is sufficient for data taking periods of few months

This could not be done during my PhD but is considered for the future activities of the department.

3.2.6 High voltage

There are three different high voltages (HV) to apply to the system:

- **the cathode power** V_{cath} that creates the drift field and is set to about -10 kV
- **the last ring power** V_{ring} that ensures the uniformity of the drift field close to the micro-mesh as detailed in Section 3.2.1 and is typically set to -580 V
- **the micro-mesh power** V_{mesh} that creates the amplification field and is set to -370 V

All polarities are negatives to allow the electrons to drift towards the readout plane which is grounded. At the moment, an external Iseg SHR HV power supply is used. However, at term the power supply system, just like the readout electronics, should be miniaturized and placed inside the buffer volume in order to minimize the number of cables that need

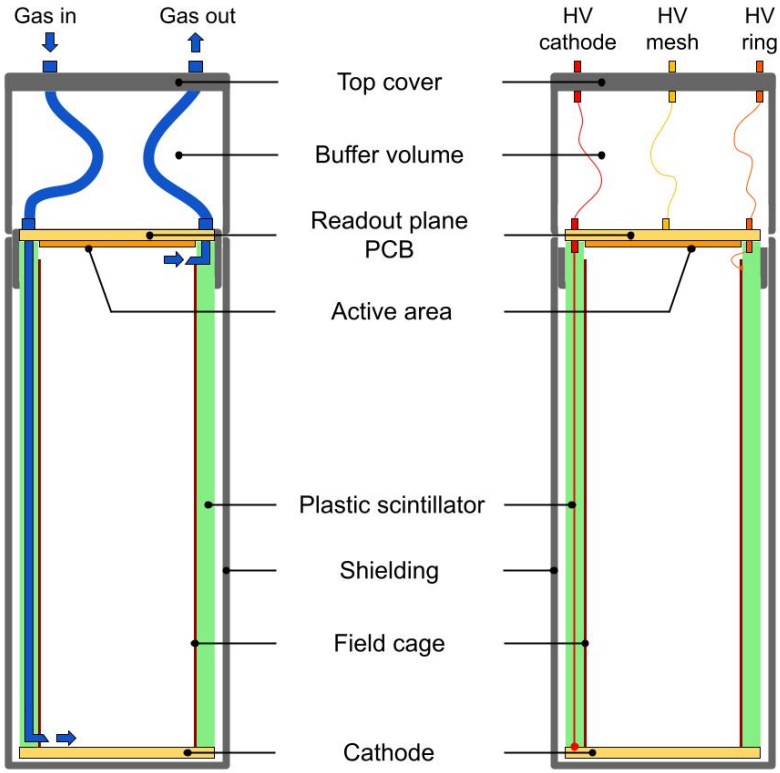

Figure 3.24: Schematic view of the gas and high voltage systems.

to connect the detector underground to the surface. Several options have been considered:

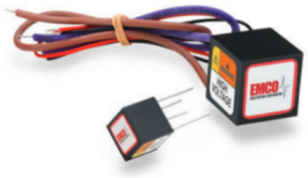

Figure 3.25: XP Power Q15N-12C DC-HVDC converter.

- **a High Voltage Power Supply (HVPS) card**, which is already used on the muon telescopes developed at CEA and can easily be interfaced with the existing readout electronics. The current version hosts 5 miniaturized CAEN DC-DC converter modules, each one providing up to 2 kV outputs from a 12 V inputs. The last ring and micro-mesh could be powered this way but another option or upgraded version of the HVPS card would be required for the cathode.
- **XP Power Q15N-12C DC-HVDC converter**, shown in Fig 3.25, that provides up to 10 kV from a 100 V input and is only 21.6×21.6×21.6 mm^3.
- **Iseg DPS mini model DPn 100 504 24 5**, shown in Fig 3.26, which takes an input between 0 and 24 V to provide up to 10 kV with a stability of $\Delta V_{out}/\Delta V_{in} \sim 0.5$ V. Its dimensions are $103 \times 74 \times 25$ mm^3.

Figure 3.26: Iseg DPS mini High Voltage Power Supply, model DPx 100 504 24 5.

At the moment, both converters have been characterized and the linearity is validated to the level of 0.1%. Concerning the cables, the default option is the HRG58-20-2 coaxial cable from hivolt[5] with SHV connectors. It is suitable for up to 20 kV and can support a minimum bending radius of 37 mm which makes it ideal for D3DT applications. However its external diameter, that is specified of 4.95 mm ± 0.15 mm by the constructor, limits its use to the last ring and micro-mesh power only: the cathode power supply cable must fit into a thin gutter machined on the plastic scintillator piece as further detailed in Section 3.2.4. For such reasons, a different cable is used for the cathode power supply and consists of a

5: https://hivolt.de/produkte/

liquid kapton shielded cable with a diameter of only 0.5 mm that can sustain up to 30 kV. This cable was specifically designed for dark matter searches.

3.2.7 Mechanics

The mechanical design was made by the Systems Engineering Division (DIS) at CEA/Irfu: all the detector pieces were modelled in 3D to test several assembly options and optimize the compacity. The adopted solution is the following:

1. The readout plane PCB is fixed to a 3D-printed guide for the kapton foil field cage using a stainless steel ring piece while the cathode is fixed at the other end. The 3D-printed guide is meant to be replaced by the scintillator trigger system. This first assembly is noted A-1 and shown in Fig 3.28.
2. The buffer volume cylinder piece is screwed on top of A-1 to give the A-2a piece. Two versions were made with a buffer space of eight or 18 cm height, the later allowing more room to arrange the tubing for the gas system as well as the high voltage cables and data readout connections. Jumper cards are used to make the connection between the PCB MEC8 connectors and the top cover and are shown in Fig 3.27. At term, this buffer space could be extended to host a miniaturized version of the readout electronics and high voltage system.
3. A-2b is the stainless steel shielding vessel that is screwed to A2-a thus providing a first level of etancheity for the gas inside the vessel and from the PCB to the cathode.
4. Finally the top cover piece is fixed on top with a gasket to ensure that the closed vessel is airtight. At the moment, gas inlet and outlet, high voltage connectors and MEC8 connectors for the data readout are present on the top cover but ultimately the number of connections will be minimized as everything will be hosted in the buffer volume.

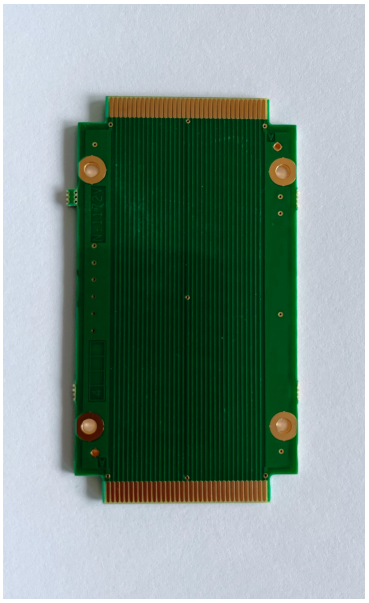

Figure 3.27: Jumper cards used to transfer the data from the readout PCB to the top cover where Samtec specifically designed cables will be used to connect to the Front End Electronics.

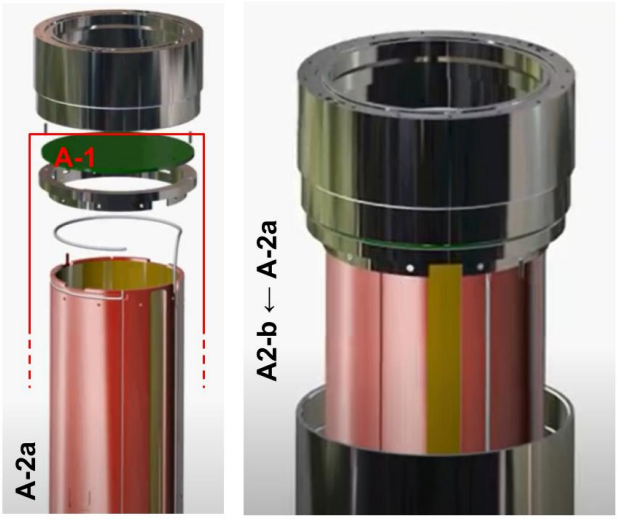

Figure 3.28: Schematic view of D3DT assembly using 3D modelled provided by the DIS department.

The external dimensions of the assembled detector are 165 mm diameter for a 400 mm or 500 mm height depending on the buffer volume.

3.3 Experimental developments

Over the course of my PhD, multiple prototypes were developed in order to test the various sub-systems or the assembly itself depending on what was available at the time. The following sections present the various experimental developments to which I contributed.

3.3.1 Preliminary prototypes

During my first year, 3 Micromegas readout plane had been produced and were ready to be tested but the mechanics and field cage were still in development. 2 prototypes, shown in Fig 3.29, were thus built in order to still be able to test the high voltage system and validate the Micromegas readout planes:

- P1, with a drift space of 3 cm but no field cage, in order to conduct preliminary tests on the Micromegas
- P2, with a drift space of 22 cm and a field cage made by hand: a first attempt was made using aluminum strips but the poor surface condition of the strips degraded the field uniformity and made the resistance welding uneasy. In the end, copper strips were used instead.

Figure 3.29: Photographs of the preliminary prototypes developed during my first year of PhD: 3 cm drift space P1 (top), 22 cm drift space P2 (middle) with copper strips field cage (bottom).

3.3.2 Readout plane characterization prototypes

To better characterize the readout plane and minimize any gas diffusion effects, a 5 mm drift prototype was made with a 20 µm thick Mylar window for cathode to allow calibration using a ^{55}Fe radioactive source. However with this design, the Mylar window is not supported enough and bend under the gas slight overpressure. In addition, in order not to burn the Mylar foil, the high voltage cable was welded onto copper tape, conductor on both faces, and glued on the Mylar but the electric conductivity was unstable which degraded the drift electric field. For such reasons, a stronger cathode design was proposed for the more precise characterization of the readout plane developed in Chapter 4. Both prototypes are shown in Fig 3.30.

3.3.3 Full size prototypes

As mentioned earlier, two full size prototypes were assembled with different buffer volumes of 8 and 18 cm heights. When the first assembly

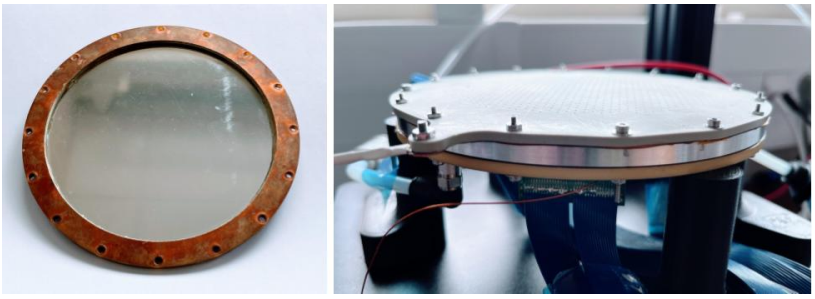

Figure 3.30: Photographs of the Mylar window cathode (left) and thin prototype for readout plane characterization (right).

Figure 3.31: Photographs of the full type prototype with 8 cm long buffer at different stages of assembly.

tests were made with the full size prototypes, the top cover piece was not yet available: this lead to a sealing issue as the PCB fixation to the buffer piece is not designed to be airtight. This was temporarily fixed using silicone seal.

A few difficulties were also met regarding the field cage. First when assembling the 3D-printed guide for the kapton foil to the stainless steel ring piece in order to mount the PCB readout plane, some screws were too long and made contact between the ring piece and the copper strings of the field cage. This lead to shortcuts and sparks inside the chamber but was simply fixed by using shorter screws and adding a protective kapton tape. Nylon screws could also be used in this case. The second one concerned the thin cable used to power the cathode: if bent too much, the shielding seems to wear down. In order so save some material the 3D-printed guide for the field cage presents some wide openings where the HV cable powering the cathode can be in close proximity to the copper rings of the field cage as illustrated by Fig 3.31. This led to multiple shortcuts of the field cage and instability on the power supply but was simply corrected by fixing the HV wire to the 3D-printed structure and using heat-shrinkable sheath to consolidate the shielding of the wire when necessary. Knowing this about the cable, precautions are taken when assembling the detector but it is expected that there will be no issue when using the final trigger system as a specific guide slot is machined onto the scintillator piece for the HV cable specifically.

Finally, there were also some difficulties to power the cathode to 10 kV, in particular with the HV pass-through connectors of the top cover that initially only supported up to 6 kV so that the drift field applied for initial tests was not optimal.

3.3.4 External trigger characterization

In order to validate the trigger system, the scintillators must be characterized with their readout to:

- ensure that enough photo-electrons (p.e.) are collected to detect muons passing through
- set the threshold value of the MPPC in order to trigger on muons

The experimental setup is illustrated by Fig 3.32: the scintillator is wrapped up in Tyvek®diffuser in order to improve light collection and placed inside a black box to minimize the contamination. The system is read by an Hamamatsu MPPC module (C13366-3050G) providing both an analog and digital output. Only the digital output will be used for D3DT trigger but both are tested to characterize the scintillator in order to confront the results.

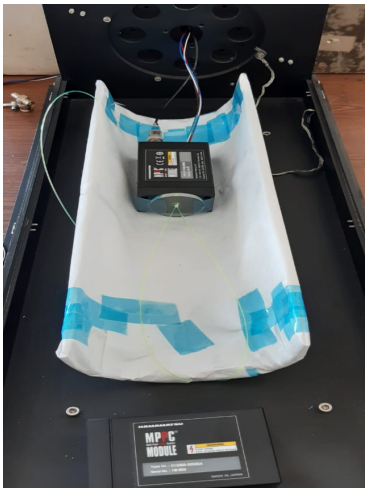

Figure 3.32: Experimental setup for the scintillator characterization: the plastic scintillator piece instrumented with the optic fibers is wrapped with Tyvek®diffuser and placed into a black box to limit contamination. The system is read by Hamamatsu MPPC module using either the analog or digital output.

Fig 3.33 shows examples of signals obtained from the MPPC analog output when calibrated to an amplitude of about 20 mV per photo-electron. For signals corresponding to up to 3 p.e., the high event rate of few kHz indicates that it most likely comes from residual light. The event rate drops down below 10 Hz when setting the threshold to 75 mV which is more consistent with the expected muon rate roughly estimated at 9.5 Hz. A more quantitative study is conducted: the analog output of the MPPC is sampled by an Amptek Multi-Channel Analyzer MCA8000 with the acquisition chain tuned so that 1 p.e.~100 ADC. The obtained spectrum is shown in Fig 3.34 in logarithmic scale and the p.e. peaks are clearly identifiable over the expected muon energy spectrum. The rate is then computed as a function of the threshold in ADC by integrating the spectrum above the threshold and dividing by the acquisition live time of 208 s and is represented by the red line on the same figure. For comparison, the expected muon rate is represented by the green line. For a threshold of 400 ADC, the rate obtained from the integration of the spectrum is of 24.5 Hz where the excess is understood as the tails of 1, 2, and 3 p.e. Poissonian distributions as well as pile up events. The intersection point of the event rate with the expected muon rate is obtained for a threshold of 439 ADC. In addition, the measurements are reproduced using the digital output of the MPPC this time and for various thresholds given in p.e., the data points are reported in Fig 3.34 (red markers). Excluding the 1 p.e. data point which does not seem to follow the same trend curve probably because the large noise contribution, an exponential fit to the data yields:

$$R_{\text{digital}}(x) = 30762.88e^{-1.94x}$$

where x is the threshold level given in p.e. It gives $R_{\text{digital}}(4\,\text{p.e.}) = 13.12\,\text{Hz}$ and the intersection point with the expected muon rate is obtained for a threshold of $x = 4.14$ p.e.

Although the effect the bending procedure on the scintillator performances could not be quantified, this study allows to confirm that the scintillator still produces enough photo-electrons for trigger purposes. The results obtained with the analog and digital outputs are compatible. The trigger threshold for muon-induced events is set to 4 p.e. which leaves some room to go lower in case of a degradation of performances with time. In the final prototype, 2 scintillator pieces will be assembled

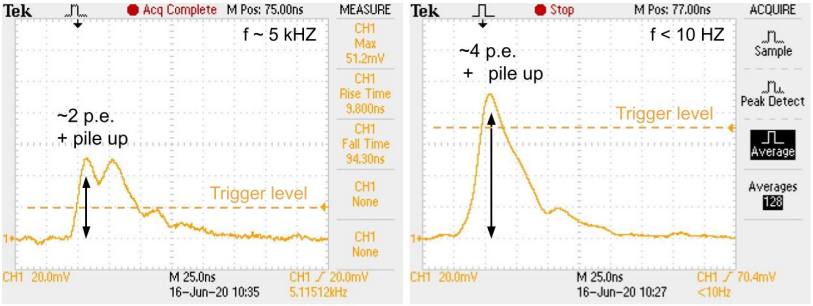

Figure 3.33: Oscilloscope screenshots of signal obtained from the MPPC analog output. The MPPC is calibrated to provide about 20 mV per photo-electron.

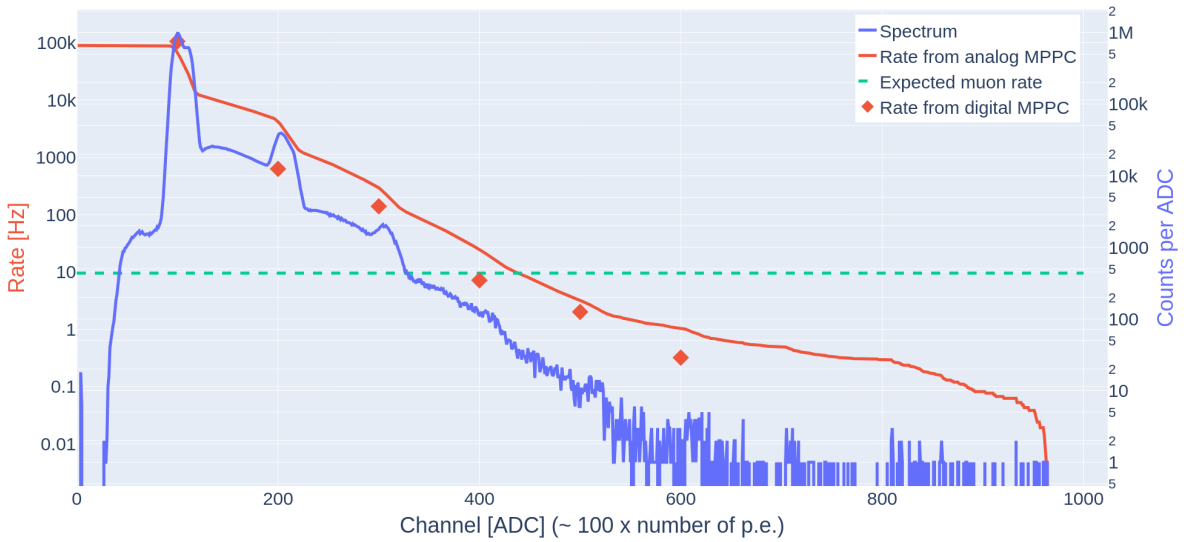

Figure 3.34: Left axis: Rate obtained from spectrum integration (red line) compared to the rate measured using the digital MPPC (red markers) as a function of the threshold level. The expected muon rate is highlighted by the green line; **Right axis:** Spectrum obtained from the output of the analog MPPC by a Multi-Channel Analyzer (blue line);

to form the trigger system: depending on its zenithal angle, muons will pass through the scintillator cylinder one or two times, thus increasing the average expected number of photo-electrons per muon event. In addition, the coupling between the optical fiber and the MPPC should be improved and the light contamination should be reduced by the stainless steel shielding vessel. A calibration will be required with the final trigger system mounted on the prototype but considering the results of this study, good triggering performances are expected.

D3DT READOUT PLANE CHARACTERIZATION 4

As described in further details in Chapter 3, D3DT is the first TPC using a 2D-multiplexed Micromegas readout plane. Usually, if there is a need for multiplexing, the x and y coordinates are multiplexed separately: a first layer of multiplexed strips reads the x coordinate and the signal is induced onto a deeper layer of multiplexed strips placed orthogonally to the first one to read the y coordinate. This is the technology used for example for the muon telescopes presented in Chapter 2 and illustrated in Fig 4.1. In that sense, the behaviour of this new type of readout plane is unknown and needs further characterization. In particular, variations of path length and multiplexing factor from a channel to another are expected to induce variations on the input capacitance of each electronic channels. A measurement of these capacitances is presented in Fig 4.2. Channel 13 and 31 from ASIC 0 have been identified as defective being connected to the guard ring which seems to be a manufacturing error yet to understand. Other channels show a standard deviation of about 4 pF.

In this chapter, a complete characterization of this new type of Micromegas readout plane is presented. First, global performances of the detector are studied by reading the mesh signal in order to validate the functioning. A second part focuses on the uniformity of those performances over the pad plane and the possible correlation with the measured capacitance variations. In each case, the performances of the detector are measured conducting X-ray tests with a ^{55}Fe radioactive source.

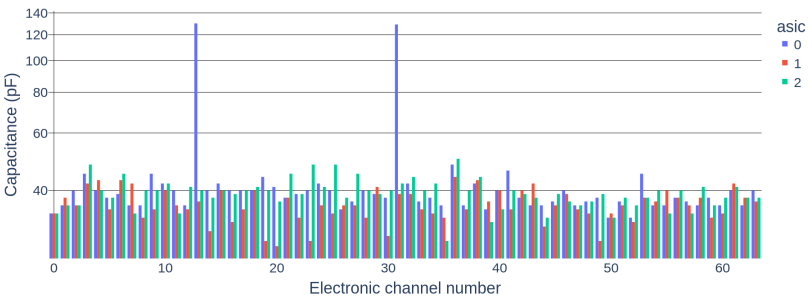

Figure 4.2: Input capacitance of each electronic channel, the color representing the ASIC number. Channels 13 and 31 of the ASIC 0 clearly stand out with an input capacitance more than 3 times larger than the average.

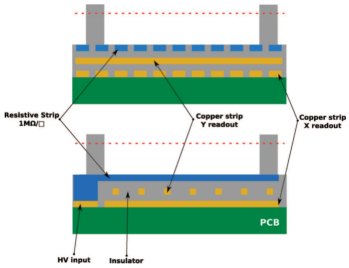

Figure 4.1: Scheme of a Micromegas detector with 2D resistive strips readout taken from [33]

4.1 Reading the micro-mesh signal

To characterize the functioning of the 2D-multiplexed Micromegas readout plane, several studies are conducted:

- **the mesh transparency to electrons** is measured as a function of the ratio E_{amp}/E_{drift}, where E_{amp} and E_{drift} are the amplification and drift fields respectively
- **the amplification gap gain of the detector** is measured as a function of the micro-mesh high voltage V_{mesh}

- **the energy resolution of the detector** is measured as a function of the ratio E_{amp}/E_{drift}

Performances are estimated from a Gaussian fit to the ^{55}Fe K_α photo-peak.

4.1.1 Experimental setup

In order to characterize the readout plane only and minimize any effects due to the field cage or gas diffusion, a specific prototype is assembled with a drift length of only 5 mm and filled with an Ar-iC$_4$H$_{10}$ (95:5) gas mixture. The inner part of the field cage is covered with kapton in order to prevent the bending of field lines, but the radioactive source is preferably placed over the center of the active area to minimize any edge effect. To allow for X-ray injection as well as high voltage setting, the cathode is made out of a 20 µm thick Mylar window. The micro-mesh signal is amplified by successively an Ortec 142B pre-amplifier followed by its corresponding amplifier before being sampled by a Multi-Channel Analyzer to reconstruct the iron energy spectrum. Gas temperature and pressure variations are monitored using Yoctopuce[1] sensors to allow for correction. The complete experimental setup is shown in Fig 4.3.

1: http://www.yoctopuce.com

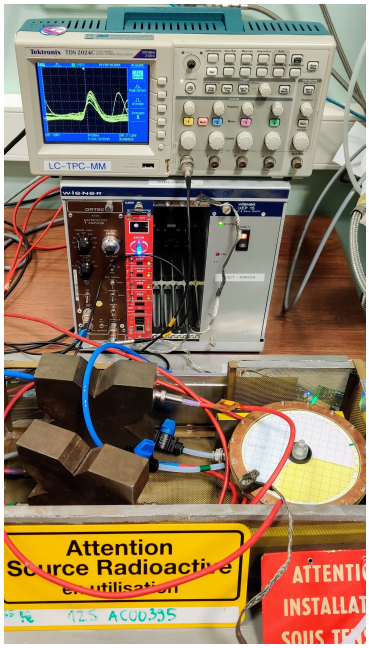

Figure 4.3: Experimental setup for the Micromegas readout plane characterization reading the micro-mesh signal.

4.1.2 Calibration of the mesh electronic readout chain

The amplification gap gain, or gas gain, is defined as:

$$G = \frac{N_{col}}{N_p}$$

where N_{col} denotes the number of collected electrons while N_p is the number of primaries produced in the Ar-iC$_4$H$_{10}$ (95:5) gas mixture. In order to compute G, the electronic readout chain must be calibrated in order to estimate the output signal for a known injected charge. An Ortec 419 Precision Pulse Generator is used to inject signal to a calibration capacitance of C_{calib} = 1.8 pF. The output signal is then passed through the exact same readout chain as for the mesh signal. Fig 4.5 shows the calibration curve obtained without any bias voltage applied on the pre-amplifier (in blue) and with the same bias voltage than during data taking (in red). No difference is observed between the two measurements. A line fit to the calibration gives a slope of 4.110 ± 0.002 which translates into a mesh readout calibration constant of 0.228 ± 0.001 ADC/fC.

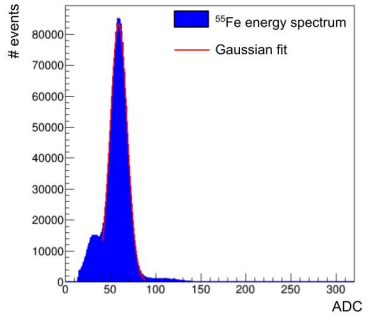

Figure 4.4: ^{55}Fe energy spectrum obtained with the MCA.

4.1.3 Results

A typical iron energy spectrum sampled by the MCA is presented in Fig 4.4 and its associated Gaussian fit is superimposed.

To study the electron transparency, the position of the ^{55}Fe K_α peak in ADC is reported as a function of the amplification and drifting fields ratio with the amplification voltage kept constant. This allows to study how the ratio of the two fields bends the field lines to guide the drifting electrons through the micro-mesh holes independently from the mesh amplification. The obtained curve is displayed in Fig 4.6 (Top) where

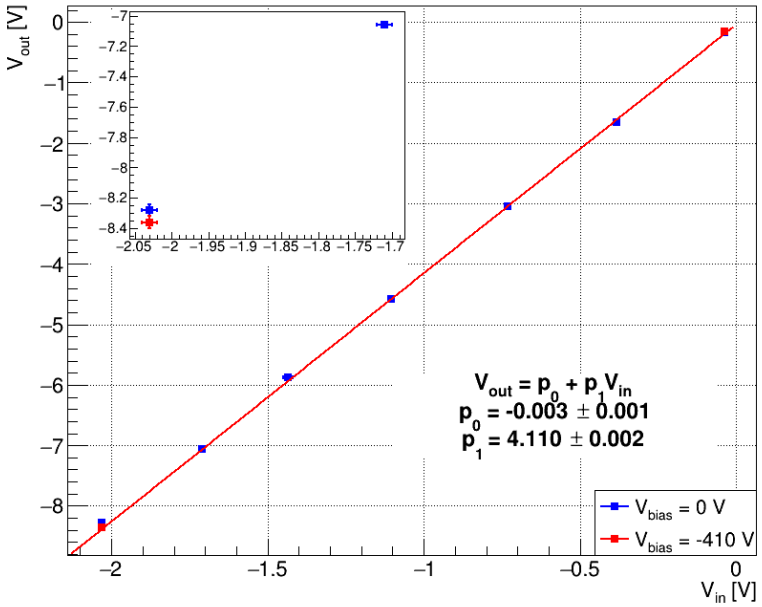

Figure 4.5: Calibration of the electronic readout chain of the mesh signal. The blue data points are taken with no bias voltage while the red ones are taken with a bias voltage of $V_{\text{bias}} = -410$ V as for data taking. No difference is observed.

a plateau is clearly identified allowing to chose a working point of $E_{\text{amp}}/E_{\text{drift}} \approx 110$ given that the average pressure was about 1000 Pa. Having a constant amplification field, the $E_{\text{amp}} \gg E_{\text{drift}}$ region is actually characterized by a lower drift field which results in low energy primary electrons. The decline in electron transparency for high fields ratio can thus be explained by attachment which is more likely to appear at energies below 1 eV [45]. On the contrary, when $E_{\text{amp}} \ll E_{\text{drift}}$, the electrons are strongly guided onto the mesh and cannot pass through also reducing the transparency.

Concerning the gain curves, the position of the ^{55}Fe K_α peak in ADC is studied as a function of the mesh voltage while the drift field is kept constant. Assuming that about 227 primary electrons are produced in the Ar-iC_4H_{10} (95:5) gas mixture[2] and using the result from the mesh readout calibration, the absolute gas gain G is determined and presented in Fig 4.6 (Middle): colors shows the drift field value while the line style indicates whether the amplification voltage is ramped up (solid) or down (dashed) to identify any hysteresis effect. The exponential increase of the gain as a function of the micro-mesh voltage validates the proper functioning of the detector.

As for the energy resolution, it is defined as:

$$\frac{\Delta E}{E} = \frac{\text{FWHM}}{\mu} \approx \frac{2.355 \times \sigma}{\mu} \tag{4.1}$$

where σ is the Gaussian standard deviation and μ the fitted K_α peak position. It is studied as a function of the $E_{\text{amp}}/E_{\text{drift}}$ set by the mesh voltage as the cathode voltage is kept constant. The optimal energy resolution is 28% obtained for $V_{\text{cath}} = -610$ V and $E_{\text{amp}}/E_{\text{drift}} \approx 85$ while the energy resolution at the chosen working point is about 29% for $V_{\text{cath}} = -580$ V.

2: Obtained using [3]: $N_{\text{p}} = \frac{5.9\text{ keV}}{W_I}$ where W_I is the average energy per ion pair and is equal to 26 eV for Ar-iC_4H_{10} (95:5) gas mixture.

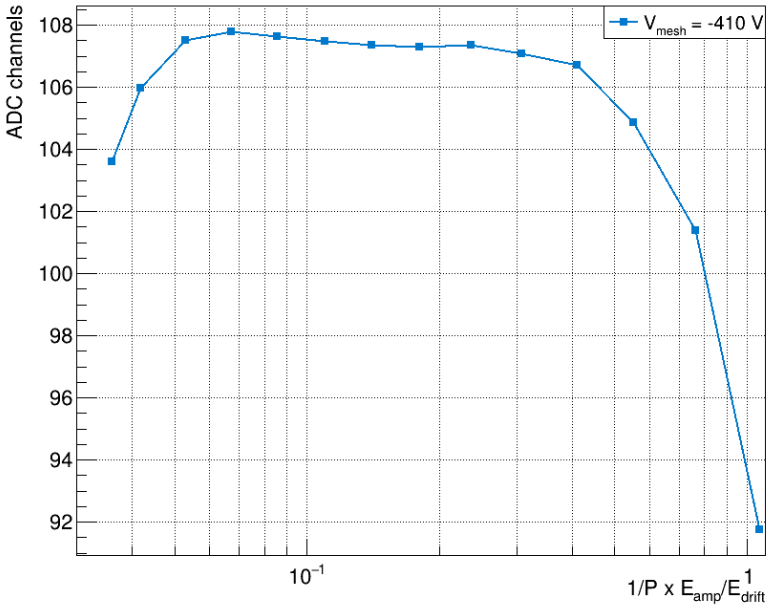

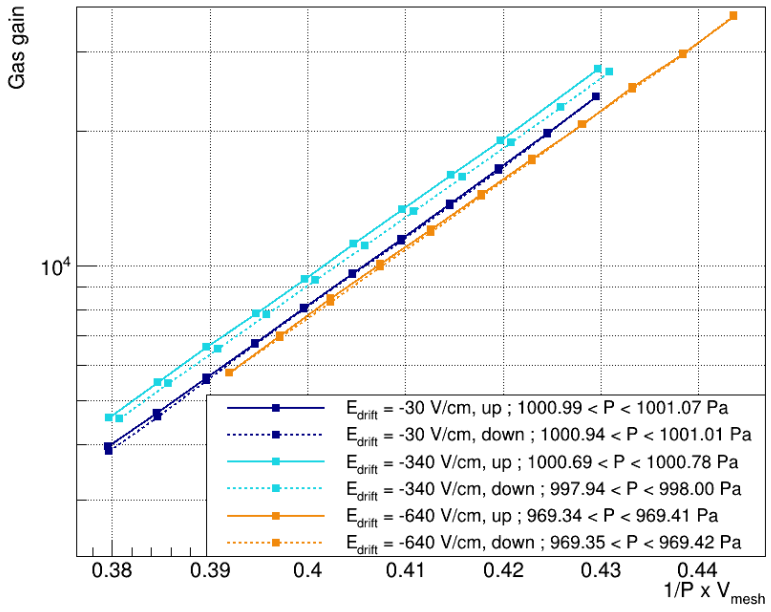

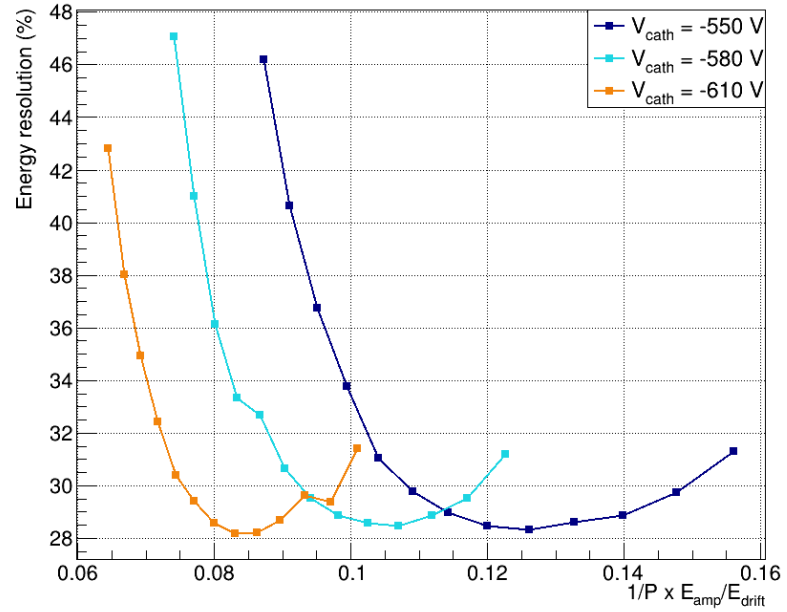

Figure 4.6: Top: Electron transparency of the micro-mesh corrected for pressure variations and with the amplification voltage kept constant; **Middle:** Gas gain as a function of the amplification field corrected for pressure variations. Colors show the value of the constant drift field applied during measurements while the line style indicates whether the voltage was ramped up (solid) or down (dashed) to check for hysteresis effects.; **Bottom:** Energy resolution as a function of the ratio of amplification and drift field corrected for pressure variations and with the drift field kept constant.

4.2 Reading the pixels

The global characterization of the readout plane obtained by reading the micro-mesh signal allows to validate the bulk Micromegas behaviour as a function of the drift and amplification voltages. However in this specific case, a refined characterization is necessary to ensure the uniformity of the detector performances over the readout plane. Indeed, as the multiplexing factor varies between 6 and 9, the input capacitance of each electronic channel as seen by the detector changes as well which can locally affect the response of the detector. To measure these variations, the energy spectrum of a radioactive iron source is reconstructed reading this time the signal of the pixels and for various positions of the source. I proposed to develop an automatized test bench in order to systematically characterize the 1344 pixels.

4.2.1 Experimental setup

The automatized test bench relies on a modified 3D-printer used as a Cartesian robot to precisely move the radioactive source above the readout plane. The Creality CP-01 model shown in Fig4.7 is chosen for several reasons:

- **its printable volume** of $200 \times 200 \times 200$ mm^3 allows to scan the entire readout plane at once with enough space in the transverse direction for gas and electronics connections.
- **its performances** in terms of printing accuracy of ± 0.1 mm sufficient compared to the pixel dimension of ~ 3 mm
- **it is a 3-in-1 printer** meaning that the 3D-printing module can be changed for laser engraving or Computer Numerical Control (CNC) cutting. It is thus easier to replace the 3D-printing module by a radioactive source holder as it is meant to be dismounted. In addition, the laser command signal meant for engraving can be used as a trigger for the acquisition.
- **the absence of existing licensed software** making it easier to interface with our readout electronics
- **its cost** of ~ 500 euros to be compared with the price of industrial Cartesian robots that are usually no less than a thousand euros.

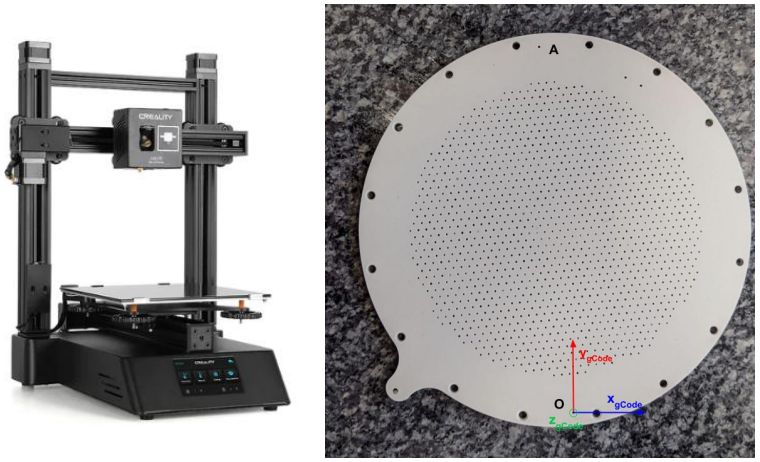

Figure 4.7: Left: Creality CP-01 3D-printer **Right:** Top-view photograph of the final design cathode.

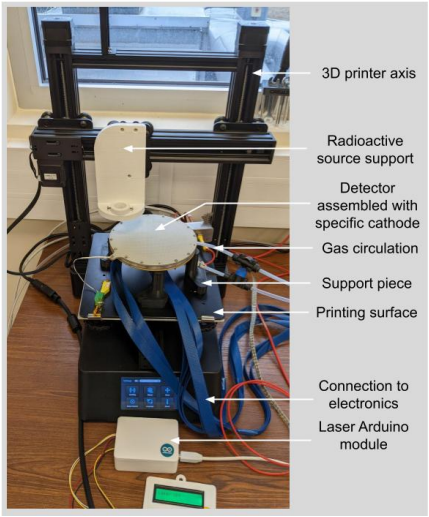

Figure 4.8: Automatized test-bench for Micromegas readout plane characterization.

The same 5 mm-drift prototype is used to minimize the diffusion effects. However, instead of a thin Mylar window, a dedicated cathode is designed to serve as collimator as well. It consists of a 4 mm thick plastic disk with a collimation hole drilled directly on top of each single pixel as presented in Fig 4.7. A preliminary study presented in Section 4.2.4 is conducted to optimize the collimation holes parameters in order to have a reasonable acquisition rate with the minimum multiplicity. A 12 µm thick Mylar foil is glued on the inner face to create the drifting electric field while the high voltage is applied thanks to a small outgrowth. Support pieces are printed to fix the detector onto the printable surface in an elevated position leaving enough room for high voltage, readout and gas flow connections. A source holder is designed to replace the 3D-printing module using the same fixation screws. This printer model does not allow to communicate with a computer, however in order to synchronize it to the acquisition, the signal from the CNC laser command is decoded through an Arduino module and used as a trigger. More details about the acquisition process are given in Section 4.2.2. Finally, as the acquisition will extend over a few days, variations of pressure and temperature are to expect and can affect the gas properties. To correct for those variations, the pressure, temperature and humidity are monitored at the end of the gas line using Yoctopuce[3] sensors. The complete experimental setup is presented in Fig 4.8.

3: http://www.yoctopuce.com

4.2.2 Acquisition process

In order to print a piece, the 3D printer executes a sequence of instructions expressed in G-code, a widely used CNC programming language, and stored on a SD card. To use the 3D printer as a Cartesian robot, the idea is thus to remove from these commands all the actions concerning the printing nozzle or heating bed only to keep the movement to specific coordinates. Pauses are added to acquire data as well as laser pulses to use as trigger. A piece of the minimal G-code used is shown Fig 4.11. Conveniently enough, the cathode was machined using a numerical controlled machine tool that also uses G-code so the same coordinates are passed to the printer to minimize the room for errors. This coordinate

system will be referred to as *gCode coordinates* and must be matched with the *printer coordinates* defined by the printer's axis as well as a manually set origin. This is done through the alignment procedure before each acquisition.

Alignment procedure

When designing the cathode, two additional holes were drilled outside the detector's active area, aligned with the printer's y-axis and diametrically opposed. One of them, O, defines the $(0,0,0)_{\text{gCode}}$ as shown in Fig 4.7 while the other one is $A \equiv (0,140,0)_{\text{gCode}}$ where the coordinates are expressed in mm. A thin pin is fixed where the center of the radioactive source active area should be and moved to adjust the $(0,0,0)_{\text{gCode}}$ point using the motors finest increment of 0.1 mm. This step is the homing of the printer. The pin is then moved to $(0,140,0)_{\text{gCode}}$ and should in principle face A given that the detector is fixed onto the printable surface. However, small rotations are allowed due to looseness and is corrected here. Afterwards, the alignment is tested over a few random points over the active area and the last steps are repeated until satisfactory. The complete procedure is illustrated in Fig 4.9. More complex procedures involving a photo-diode and the laser have been considered, but given that the source aperture is larger than twice the collimating holes diameter it was concluded that such refinement was not necessary.

Communication with the acquisition computer

Once the alignment is done, the acquisition can start. This printer model cannot be piloted by the acquisition computer as it simply executes the program stored in the SD card. The difficulty is thus to synchronize the acquisitions and the printer movements to avoid taking data when the printer is moving and ensure that a single position is scanned in each data file. In addition, given that a scanning of the full detector takes about 3.5 days, it is preferable that a problem happening during data taking does not compromise the entire run.

Given that the printer modules (printing nozzle, laser engraving and CNC) are not used for this application, the cable initially meant to connect the printer motherboard to the modules is actually used to extract the laser signal. The laser for engraving is piloted using the M106 and M107 functions in G-code which are encoded through a 0-24 V square function as illustrated in Fig 4.10. This signal is converted to 0-5 V through a DC-DC transformer and passed to an Arduino digital input. The acquisition pipeline is presented in Fig 4.11: every time the printer reaches a new position it sends a laser pulse to the acquisition computer that reads the Arduino serial port to indicate that it is no longer moving and triggers the data taking. A pause of 4 minutes is performed while the acquisition is stopped after 10000 events or 3 minutes and 20 seconds, whatever comes first, leaving a 40 seconds buffer time to close the data file and write in a log file the current position coordinates as well as the corresponding data file name. Once every five minutes, if a new file has been written it will automatically be processed.

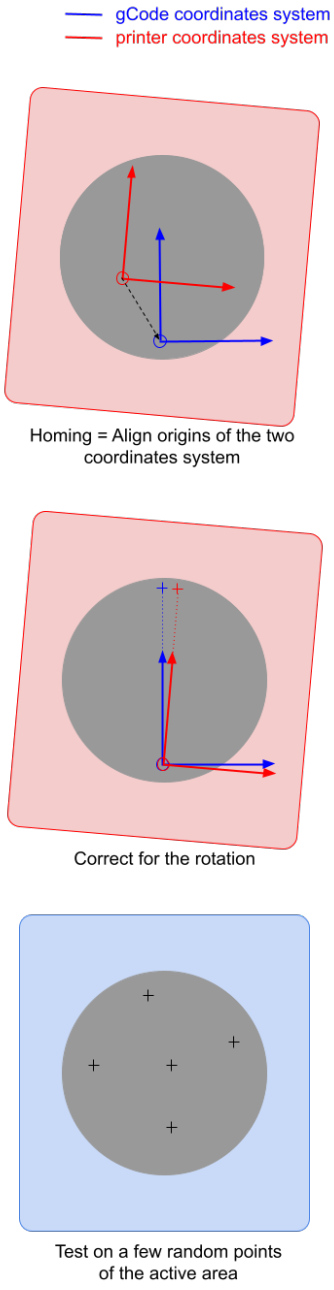

Figure 4.9: Steps of the alignment procedure.

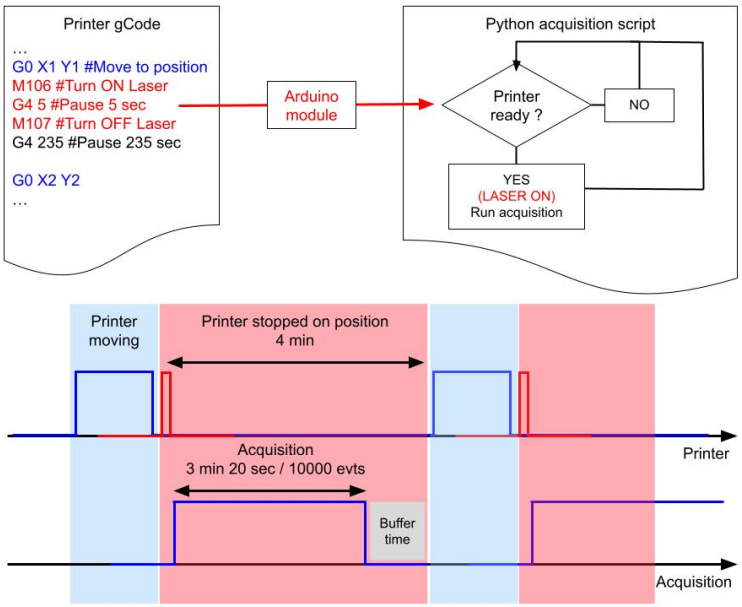

Figure 4.11: Acquisition pipeline.

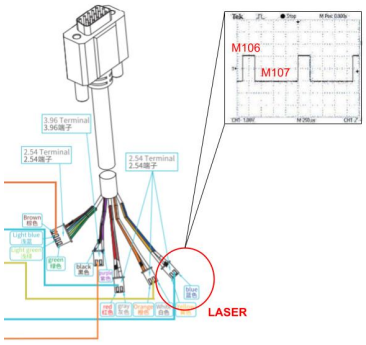

Figure 4.10: Laser piloting functions used to trigger the acquisition.

4.2.3 Data processing

Once the data has been acquired, it must undergo a set of processing steps before the detector performances can be analyzed. First of all, the pedestals are subtracted and the data file is converted to a ROOT format to be analyzed. In a second step, the energy spectrum is reconstructed to allow for the performances of the detector to be estimated in a last step.

Energy spectrum reconstruction

For each event, the maximum of each waveform $A_{\max}$ is found and is said to pass the amplitude threshold if $A_{\max} > 50$ adc. This maximum is obtained at a time bin noted $t_{\max}$ which is required to follow $6 < t_{\max} < 20$ because of the geometry of the detector, the electron drift velocity and the auto-trigger configuration. The number of waveforms passing these selections is defined as the event multiplicity and is required to be smaller than 6 for the event to be considered in the analysis, events with a higher multiplicity being more likely to be cosmic muons or electrical discharge. For the selected events, the charge is estimated as the integral of the waveform between $t_{\max} - \Delta t$ and $t_{\max} + \Delta t$ where $\Delta t = t_{\max} - t_{20\%}$ and $t_{20\%}$ is the time for which $A(t_{20\%}) = 0.2 \times A_{\max}$. Finally, the charge is integrated over the entire pad plane to obtain the event charge which is used to reconstruct the iron energy spectrum. A typical event is illustrated in Fig 4.12.

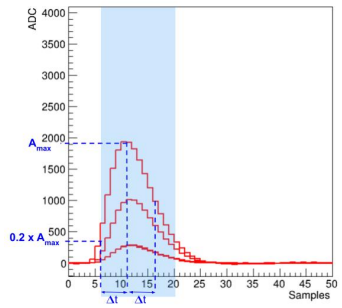

Figure 4.12: Typical event waveforms: the region of interest for ^{55}Fe events is highlighted in blue.

Performances estimation

To estimate the performances of the detector, the 5.9 keV peak is fitted by a Gaussian which mean μ is taken as an estimation of the gain while the energy resolution is computed as in Equation 4.1. Fig 4.13 shows a typical X-ray energy spectrum obtained from the radioactive iron source and fitted by a Gaussian.

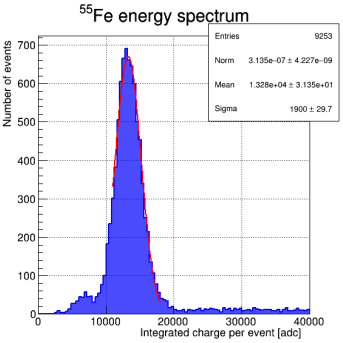

Figure 4.13: Typical energy spectrum reconstructed with its Gaussian fit in red.

The specific case of the ASIC 0 noisy channels

The electronic channels 13 and 31 of the ASIC 0 have been identified as defective: for yet unknown reasons they are connected to the guard ring and present a capacitance increased by a factor 3 compared to the other channels. As a result, those channels are removed from trigger. However, the strong oscillations of the baseline can be mistaken for a signal and be taken into account in the event multiplicity and integrated charge. This would highly degrade the reconstructed spectrum which is why the signal obtained on these channels is forced to zero. As a result, when a position adjacent to a pixel connected to one of these electronic channels is scanned, only 2/3 of the charge will usually be collected. This appears in Fig 4.14 as a second peak on the left hand side of the usually reconstructed 5.9 keV peak. In this case only the right peak is adjusted but the fit quality is degraded.

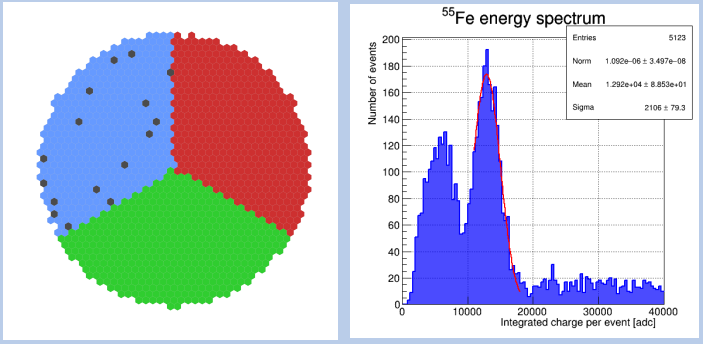

Figure 4.14: Left: Mapping of the 2 noisy channels on ASIC 0; **Right:** Reconstructed spectrum of a position involving one of the noisy channels.

4.2.4 Preliminary study

In order for the measured performances to be characteristic of a given electronic channel, the ideal situation is for all the charge to be collected by a single pixel. This level of resolution is however not achievable: in fact the photo-electron emitted by the ionized Argon tends to travel in a direction transverse to the one of the incident photon with a mean-free-path of the order of the millimeter. Adding to this the transverse diffusion effects that, although being minimized due to a drift length of only 5 mm are not completely suppressed, the expected charge distribution will extend onto multiple pixels. It means that the measured variations will be smoothed by the neighbouring pixels and partially redundant. With this in mind, the question of the position of the collimating holes arises: is it more interesting to target the center of each pixel (CoP) or the intersection of three pixels (IoP) as illustrated in Fig 4.15 ?

As an example, let us consider an hexagonal pixel with a distance between the flats $d = 3$ mm and a circular spot corresponding to the area where the photon can be detected of radius $r = 2.5$ mm. Then for Option A where the spot is centered at the center of the pixel, 40% of the spot area is contained in the central pixel while the remaining 60% are equally distributed among the six neighbours. For Option B, 84% of the spot area is distributed among the three adjacent pixels while the remaining 16% are shared by three neighbours of second order. That is to say that

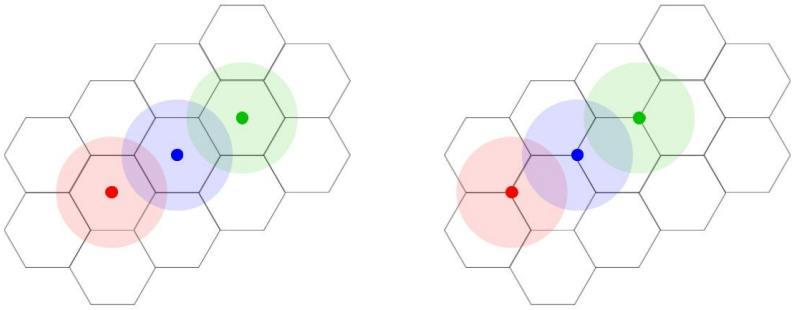

Figure 4.15: Two options for positioning the collimating holes with regard to the pixels.

more than 80% of the spot area is covered by three pixels with the Option B while more than 5 pixels are required to reach the same percentage with Option A. This naive approach suggests that Option B provides information reflecting a smaller detector surface than Option A. However one should also take into account that the photons are not uniformly distributed over the spot area but follow a 2D Gaussian shape centered on the center of the spot.

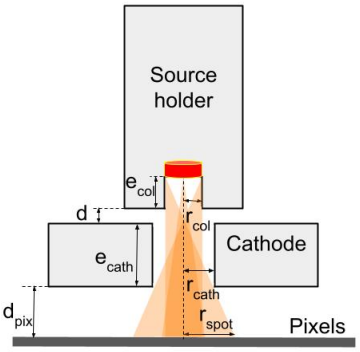

Figure 4.16: Schematic side view of the radioactive source collimation system.

As there is no precise way to predict the effects of the smoothing by the neighbours since the scale of the multiplexing induced variations themselves are unknown, it is decided that a preliminary study is required in order to fix the position of the collimating holes relative to the pixels as well as their diameter. The collimation system of the radioactive source is illustrated in Fig 4.16. The radius of the collimation hole r_{cath} is also experimentally chosen among five available drill bit sizes (0.25 mm, 0.5 mm, 1 mm, 1.2 mm and 1.5 mm) based on the event multiplicity and acquisition rate. The r_{col} parameter is fixed at $r_{\text{col}} = 2$ mm so that $r_{\text{col}} > r_{\text{cath}}$ ensures that no fine alignment is required.

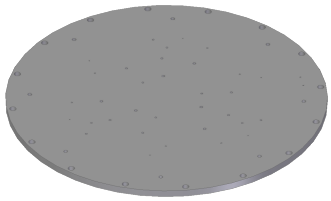

Figure 4.17: Prototype cathode design.

A prototype cathode is machined with, on each sector, a hole of each possible combination of diameter and position as shown in Fig 4.17 allowing to test multiple configurations. The results of this analysis are presented in Fig 4.18 although more details can be found in Appendix A. In each case the energy resolution seems worse on ASIC 0 which is consistent with the fact that this sector is known to be noisier and its performances degraded. In addition, the energy resolution is consistently better when the collimation hole is placed at the intersection of 3 pixels which is understood as a better charge sharing. Finally, the performances obtained for the 0.5 mm and 0.75 mm diameters are very similar, as well as the acquisition rates respectively measured at 110 Hz and 120 Hz. Since both options were acceptable, the solution that makes the manufacturing process easier is chosen so that the final design of the cathode is with collimating holes of 0.75 mm diameter placed at each intersection of 3 pixels.

4.2.5 Results

Monitoring of pressure and temperature

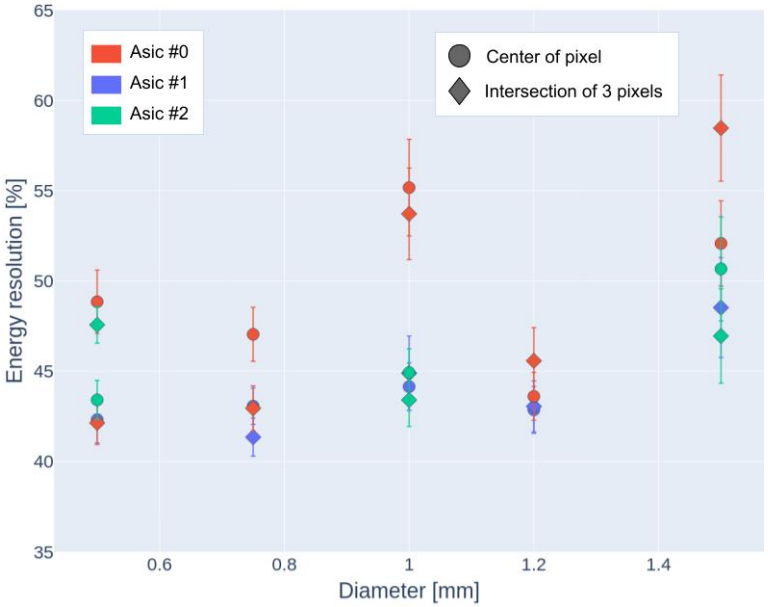

Figure 4.18: Energy resolution as a function of the diameter.

During the acquisition, gas pressure, temperature and humidity are recorded once every 10 seconds and written into a ROOT file with the corresponding timestamp. For every position, the timestamp corresponding to the beginning of data taking is identified allowing to select the corresponding monitored values. The 24 data points selected this way are averaged to extract a single value of pressure, temperature and humidity per position. Those values are reported in Fig 4.21 both as a function of time and associated to the corresponding source position over the readout plane in order to identify any suspicious correlation that would point towards malfunction. For comparison, the path followed by the printer is shown in Fig 4.19. Temperature and humidity show clear day-night cycles while it is less obvious for the pressure. This is explained by the fact that to compensate any potential leak the gas system function in slight over-pressure with a bubbler at the end of the line. Finally, the measured gain of the detector is presented as a function of the averaged gas temperature, pressure, and humidity in Fig 4.20. As no obvious correlations is observed, no correction is applied.

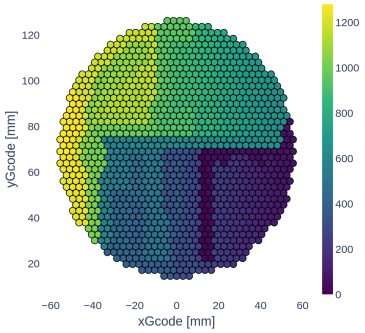

Figure 4.19: Path followed by the radioactive source: color indicates the order in which the positions have been scanned.

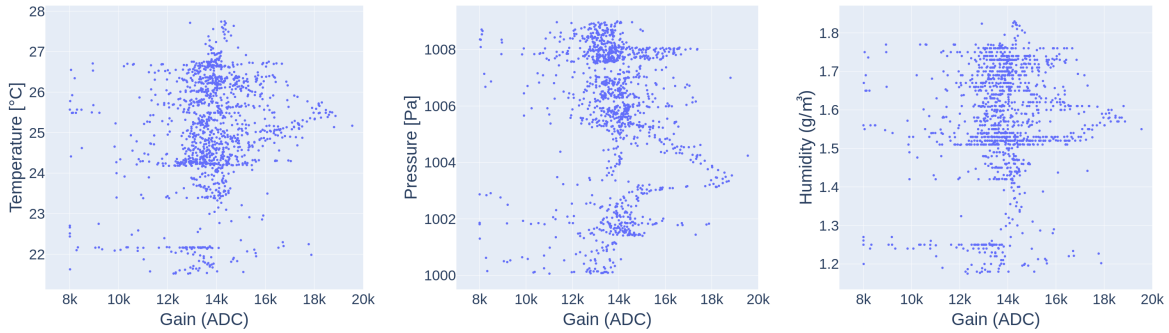

Figure 4.20: From left to right: Correlation between the relative gain and the gas temperature, pressure and humidity respectively.

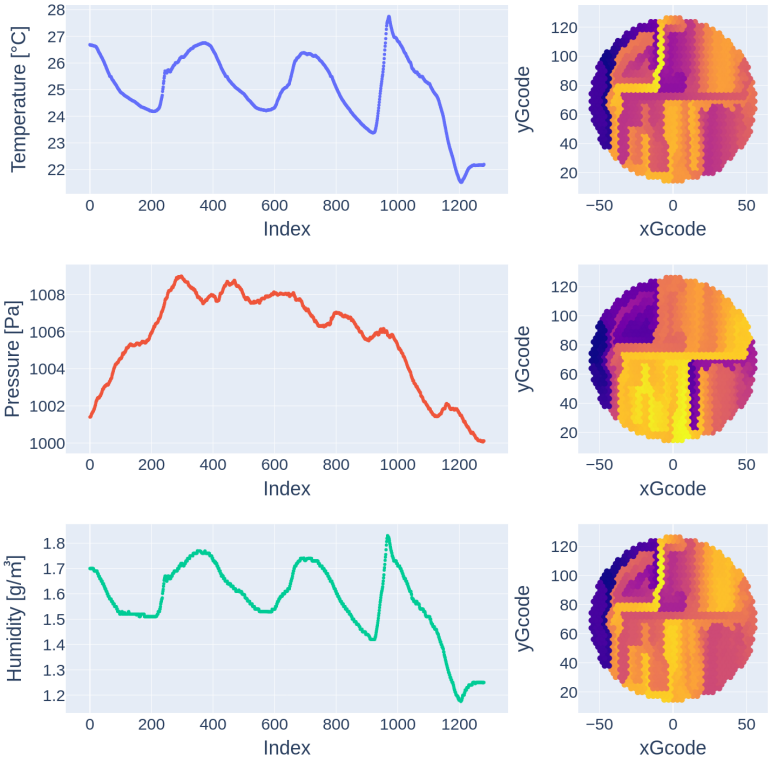

Figure 4.21: Evolution of the conditions of temperature (blue), pressure (red) and humidity (green) as a function of time and reported spatially at its corresponding position.

Relative gain and energy resolution

The map of relative gain and energy resolutions obtained are presented in Fig 4.23 with there associated 1D distributions in Fig 4.25. First of all, the sector read by ASIC 0 particularly stands out as the energy resolution performances seem particularly degraded. Comparing this result with the mapping of the noisy channels shown in Fig 4.22 indicates that the energy resolution is at its worst around the noisy pixels. The corresponding spectra are not really exploitable as no iron peak can be identified as shown in Fig 4.24 (Left). Under such conditions, extreme colors indicate a degradation of performances but the energy resolution associated should not be considered as the fitted distribution was not the iron K_α peak.

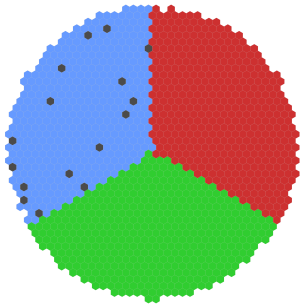

Figure 4.22: Mapping of the ASIC 0 noisy electronic channels.

A few pixels also present an extreme resolution although being read by ASIC 1 or 2: these cases are illustrated by Fig 4.24 (Right). Here the reconstructed spectrum looks completely fine but the fitting procedure failed. The disparity in the reconstructed spectra, mainly due to the noise, makes it difficult to have an automatic fitting procedure efficient in each case. About 10% of the scanned positions are in this situation which explains the long tails observed in Fig 4.25 distributions. Efforts should be made to optimize the fitting procedure once revised PCB with no noisy channels will have been produced.

A diagonal descending line seems present on both maps: although it could not be understood at first, it appeared once opening the detector that the Mylar foil from the cathode was corrugated in this region. The effect is thus attributed to the cathode and not to the readout plane.

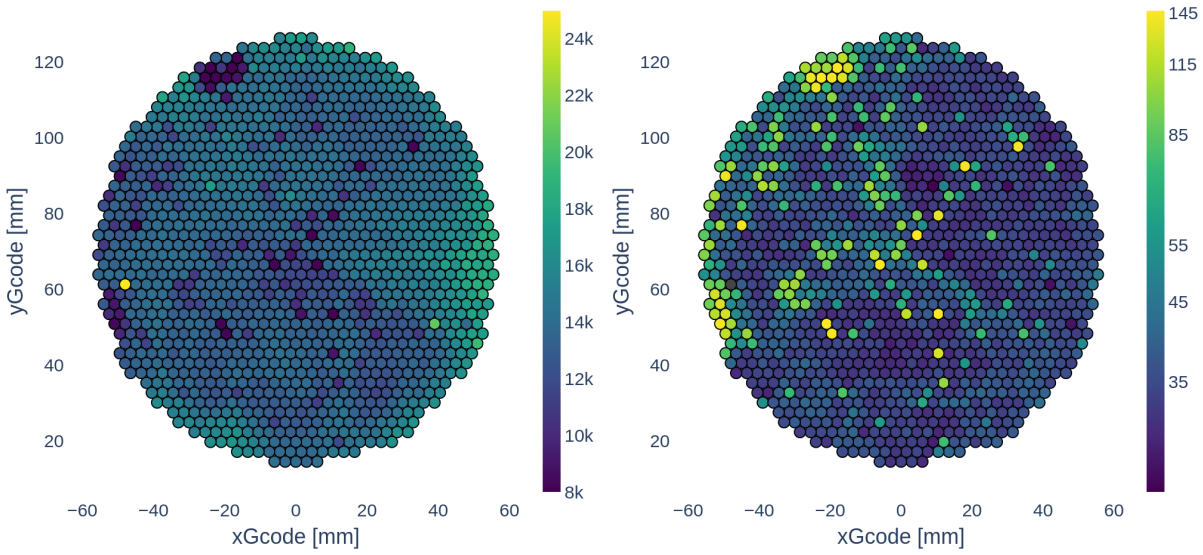

Figure 4.23: Left: Relative gain in ADC as a function of the scanned position; **Right:** Energy resolution [%] as a function of the scanned position.

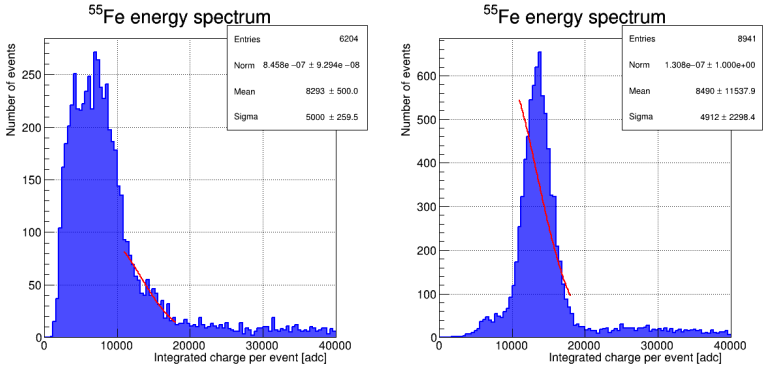

Figure 4.24: Examples of non-exploitable reconstructed iron spectra: from noisy pixels (Left) or fitting error (Right).

Disregarding the previously discussed effects, performances all considered seem uniform over the pad plane. In order to give a more quantitative estimation, $\zeta_{\text{gain rel.}}$ and $\zeta_{\Delta E/E}$ are defined as follows:

$$\begin{aligned} \zeta_{\text{gain rel.}} &= \frac{\text{FWHM}_{\text{gain rel.}}}{\mu_{\text{gain rel.}}} \\ \zeta_{\Delta E/E} &= \frac{\text{FWHM}_{\Delta E/E}}{\text{MPV}_{\Delta E/E}} \end{aligned} \tag{4.2}$$

where $\sigma_{\text{gain rel.}}$ and $\mu_{\text{gain rel.}}$ are respectively the standard deviation and mean parameters of the Gaussian fit to the relative gain distribution while $\sigma_{\Delta E/E}$ and $\text{MPV}_{\Delta E/E}$ are the standard deviation and Most Probable Value (MPV) of the Landau fit to the energy resolution distribution. Fits results yields:

$$\begin{aligned} \zeta_{\text{gain rel.}} &= 0.120 \pm 0.009 \\ \zeta_{\Delta E/E} &= 0.082 \pm 0.002 \end{aligned}$$

Correlations with the multiplexing factor

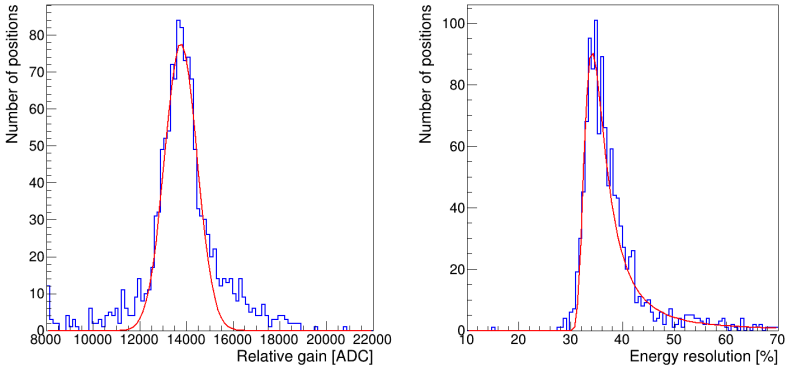

Figure 4.25: Left: Relative gain distribution fitted by a Gaussian; **Right:** Energy resolution distribution fitted by a Landau.

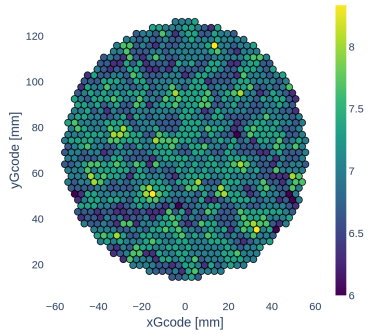

Figure 4.26: Map of the average multiplexing factor.

The multiplexing factor of a given channel is defined as the number of pixels connected to this channel and varies between 6 and 9. For each scanned position, the averaged multiplexing factor of the 3 electronic channels at play is computed and the results are reported on the map shown by Fig 4.26. This allows to study the possible correlations between the local measured performances of the detector and the multiplexing factor. However, Fig 4.27 shows the 2D-histograms of both the relative gain and the energy resolution as a function of the averaged multiplexing factor and in each case, no correlation is observed.

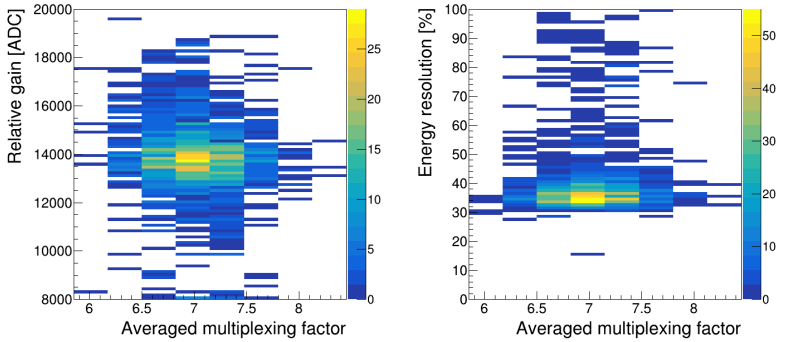

Figure 4.27: 2D-histograms of the correlations .

TRACK RECONSTRUCTION 5

In order to maximize the compacity and limit the power consumption of D3DT, its plane is 2D-multiplexed as explained in further details in Chapter 3. This raises a challenge for track reconstruction as each time a pixel collects charge it is actually between 6 and 9 pixels that detect the hit. Usually, as it is the case for muon telescopes, the x and y coordinates are both multiplexed but read separately. Algorithms exist to unambiguously reconstruct the hit position although multiple channels received signal. However, D3DT is the first 2D-multiplexed TPC and such algorithms need to be developed. This chapter presents a reconstruction algorithm for D3DT events as well as a performances study. At this stage, there is not enough statistics on good quality events recorded with the full size prototype so the reconstruction algorithm is built on GEANT4 simulations which are described in the first section. Nevertheless, the reconstruction algorithm will be tested on real data in the last section.

5.1 Simulated data

Muons are sampled following the Guan parametrization [25] and propagated through the active volume using the G4Tomomu framework [34] which is based on GEANT4 [28]. Energy deposits are then projected onto D3DT pad plane while the z coordinate is binned to mimick time digitisation by the readout electronic.

5.1.1 Muon generation

Muons energy, zenithal angle θ and azimuthal angle ϕ are randomly sampled following Guan parametrization at sea level. The corresponding distributions are shown in Fig 5.2. In order to maximize the number of generated muons that actually pass through the active volume, the generation process is reversed and actually originates from a generation surface close to the active volume. It can be described as follows:

1. Random sampling of the muon direction (θ, ϕ) and energy
2. **Definition of the generation surface S_{gen}:** as illustrated by Fig 5.1, S_{gen} is a disk centered on the center of the active volume and of radius $R_{\text{gen}} = \sqrt{h_{\text{TPC}}^2/4 + r^2}$ where h_{TPC} and r are respectively the height and radius of the cylinder representing the active volume. S_{gen} is rotated to be orthogonal to the muon direction (θ, ϕ).
3. Random sampling of a point P_{gen} on S_{gen}
4. Projection of P_{gen} on a generation sphere of 5 m radius centered on the center of the active volume along the (θ, ϕ) direction.

The muon is then propagated back from the generation sphere to the active volume. This method ensures that, neglecting any deviation, the muon would travel back to P_{gen} thus passing through the active volume. However, physical processes affect its trajectory and in the end only

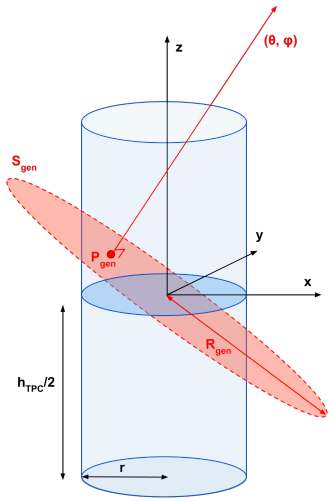

Figure 5.1: Illustration of the reversed muon generation process.

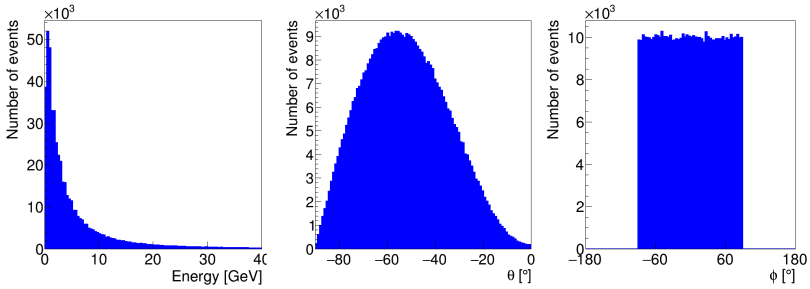

Figure 5.2: From left to right: Distributions of the generated muons energy, zenithal angle and azimuthal angle.

about 25% of the generated muons actually depose energy in the active volume.

5.1.2 Propagation through the active volume

Muons are propagated from the generation sphere and along the sampled direction (θ, ϕ) using GEANT4 [28] and the Livermore[1] models. The active volume is defined as a cylinder of the Ar-iC_4H_{10}-CF_4 (95:2:3) gas mixture and of height $h_{\text{TPC}} = 40\,\text{cm}$ and radius $r = 6\,\text{cm}$ to match the dimensions of D3DT active volume. All the electromagnetic processes relevant for muons are taken into account: multiple scattering, ionization, pair production and Bremsstrahlung. The simulation step is set to 1 mm to minimize the computation time while ensuring continuous tracks once projected onto D3DT pad plane.

1: https://geant4.web.cern.ch/node/1619

5.1.3 Projection onto D3DT pad plane

At this stage, a ROOT [46] file containing, for each generated muon, the following information is obtained:

- the generated muon direction projections along the x, y and z axis
- the generated muon energy
- the number of hits
- for each hit:
  - its position $(x_{\text{hit}}, y_{\text{hit}}, z_{\text{hit}})$
  - the deposited energy

This data has to be projected onto D3DT readout plane in order to test the reconstruction algorithm on similar data that what would be obtained experimentally. The objective is thus to obtain a single effective signal per pixel that collected charge and reproduce this signal onto the multiplexed pixels. A hit, defined by its coordinates $(x_{\text{hit}}, y_{\text{hit}}, z_{\text{hit}})$, contributes to the effective signal of pixel P_i located by the coordinates of its center (x_i, y_i) if:

$$d_{\text{hit}\to\text{pix}} = \sqrt{(x_{\text{hit}} - x_i)^2 + (y_{\text{hit}} - y_i)^2} < h \tag{5.1}$$

where h is the radius of the circle inscribed in the hexagonal pixel. The energy associated to pixel P_i is defined as the sum of the deposited energy of each contributing hit while the z_i variable is set to the average of the z_{hit} of each contributing hit as illustrated by Fig 5.3.

Finally, in order to simulate the timing digitisation introduced by D3DT readout electronic, a new variable z_i^{binned} is created: a Gaussian smearing

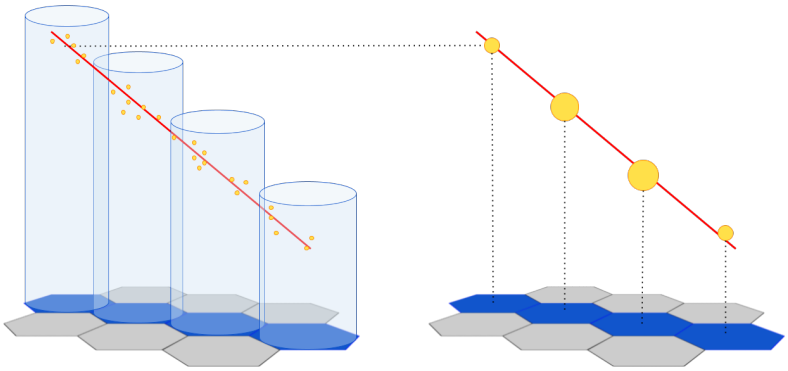

Figure 5.3: Projection of the simulated data onto D3DT readout plane. The muon track is shown in red and the hits are highlighted in yellow.

is applied to z_i that is then binned. The binning is chosen so that the bin width corresponds to the length travelled by drifting electrons during a time sample.

Simulating timing digitisation

The target electric drifting field of D3DT is $E_{\text{drift}} = 270\,\text{V/cm}$. MAGBOLTZ [5] simulations showed that such drifting field yields, for the Ar-iC_4H_{10}-CF_4 (95:2:3) gas mixture, an electron drift velocity v_e of about 7.8 cm/µs. The sampling frequency of the readout electronic leads to time samples of $\Delta t = 40\,\text{ns}$. Thus, the Δz travelled by drifting electrons during one time sample is given by:

$$\Delta z = v_e \times \Delta t = 0.31\ \text{cm}$$

The Gaussian smearing applied is thus of a Gaussian of mean zero and Full Width at Half Maximum (FWHM) of Δz and the bin width chosen is Δz.

5.2 3D Reconstruction algorithm

The global idea behind this algorithm is to cleanup the data by removing as much as possible the fake hits introduced by the multiplexing to be able to do a RANSAC [47] (*see RANSAC box*) fit on the remaining hits. To achieve this, several steps are followed and illustrated in Fig 5.4:

1. **Selection of a point of reference:** this point should be part of the physical track and will be a point of reference for the next step. It is circled in green for illustration in Fig 5.4.
2. **2D selection of a favored direction:** assuming that the point of reference is a physical hit, a gross selection is applied on the 2D data set around the direction that contains the more hits. This is illustrated by the colored sectors in Fig 5.4. Only the data points contained in the green sector are kept for the next step.
3. **First 3D-RANSAC fit to pre-selected data:** the pre-selected data set is fitted using a 3D-RANSAC algorithm. At this stage, some fake hits that were close to the track in the (x, y) plane remain and can bias the fit along the z axis as shown in Fig 5.4, justifying the last 2 steps.

4. **3D selection based on first RANSAC residuals:** the distance of each point to the model extracted from the first RANSAC fit is used as new selection variable which, this time, takes into account the three dimensions.
5. **Second 3D-RANSAC to reconstruct the track:** the final data set is fitted by a 3D-RANSAC algorithm to finally reconstruct the track direction.

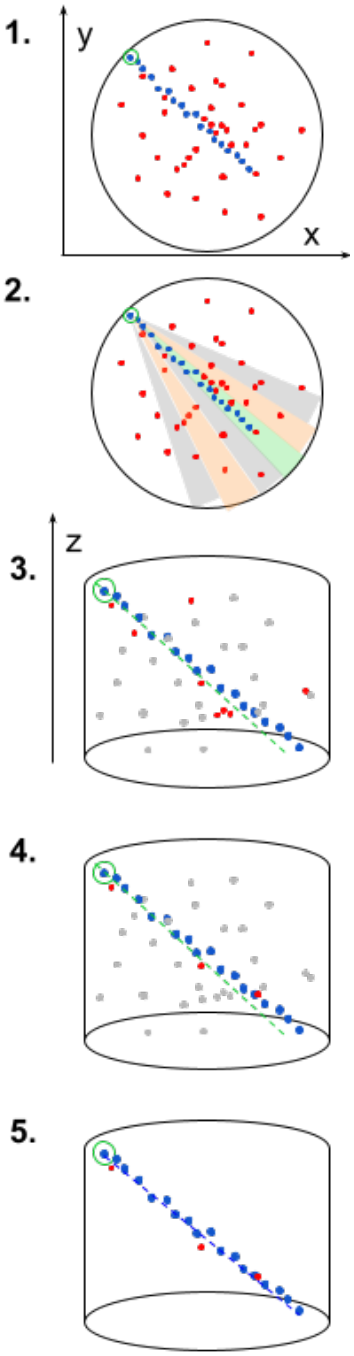

Figure 5.4: Steps of the 3D track reconstruction algorithm. Blue dots show the track data points while the red ones are introduced by the multiplexing.

Random Sample Consensus (RANSAC) algorithm

The RANSAC algorithm is an iterative method that allows to extract a model describing a data set D without being affected by the outliers it contains. It assumes that a set of parameters defining a model to describe the inliers does exist and that this model does not describe the outliers. In addition, it supposes that considering a small sample of inliers, there is an existing procedure to estimate the parameters of the model.

This is particularly adapted to D3DT as all the multiplexing hits can be considered outliers, as well as eventual noise in the case of real data. In this specific case, the parameters of the model are the origin and direction of the 3D line that best fit the inliers, and the existing method to estimate these parameters is the 3D least squares method.

Let's consider a data set D that contains inliers I and outliers O. The RANSAC algorithm proceeds as follows:

1. **Iteration 0:** Randomly select a subset d_0 of D
2. Estimate the model parameters $\{p_i\}_0$ by adjusting d_0
3. For every point of the data set that is not in d_0:
   a) Compute distance with model $\{p_i\}_0$
   b) Either add to inliers subset i_0 or outliers o_0
4. If there are more points in i_0 than d_0:
   a) Estimate new model parameters $\{p_i\}_{0,\text{better}}$ by adjusting i_0
   b) Validate better model or increment iteration and start again from step 1.
5. Otherwise, increment iteration and start again from step 1.

One of the possible drawbacks of this algorithm is that it extracts a unique model and will thus not be efficient if two models coexist in the data set. However this is not a problem in our case, the expected event rate being very low it is very unlikely that two tracks must be reconstructed in the same event.

Another limitation is that it requires a minimal sample size to be able to select and adjust the subsets. This implies that the reconstruction efficiency will be degraded for very short tracks (with typically less than 5-10 physical hits).

A more detailed description of each step is presented in the following sections.

Let's consider a set of simulated data points $P = \{(x, y, z)_n\}$ which contains a physical track $T = \{(x^{\text{track}}, y^{\text{track}}, z^{\text{track}})_i\}$ and the associated fake hits introduced by the multiplexing $M = \{(x^{\text{mult}}, y^{\text{mult}}, z^{\text{mult}})_j\}$. It

is assumed here that the simulations have been propagated onto D3DT pad plane so that the x and y are the coordinates of the center of the corresponding hexagonal pixels. The distance between the centers of two neighboring pixels is noted $2h$ while the side of each hexagon is noted c as illustrated in Fig 5.5.

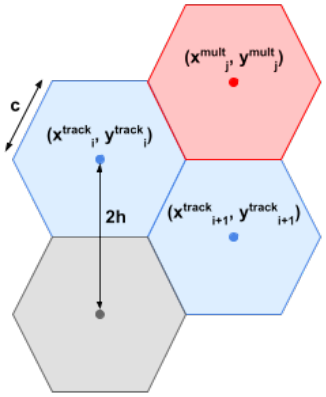

Figure 5.5: Introduction of notations.

5.2.1 Selection of a point of reference

As further developed in Chapter 3, the multiplexing patterns are not random but rather a 2D generalization of the 1D genetic multiplexing [43] obtained by reinforcement learning. It ensures that, considering two sets of multiplexed pixels $S_1 = \{(x_1, y_1, z_1)_i\}$ and $S_2 = \{(x_2, y_2, z_2)_j\}$, there is a single couple of indexes (i, j) such that:

$$d^{ij}_{min} = \min(\sqrt{(x_{2j} - x_{1i})^2 + (y_{2j} - y_{1i})^2}) = 2h \tag{5.2}$$

Using the fact that the physical track is continuous, the two pixels that follow Eq 5.2 should be in T.

In order to select the point of reference, the data set D is sorted by descending order on z_n and S_1 is defined as:

$$S_1 = \{(x_n, y_n, z_n)_i\},\ z_i = \max(z_n) \tag{5.3}$$

while S_2 is defined in a similar way once S_1 has been subtracted from D. This ensures that the physical hits respectively selected in S_1 and S_2 are consecutive. The point of reference noted P_0 is arbitrarily defined as the point from S_1 that fulfills the requirement stated by Eq 5.2.

It is important to note that it could be more complicated if the data set D also contained some noise $N = \{(x^{noise}, y^{noise}, z^{noise})_k\}$, which is more likely the case for real data. This will be discussed in Section 5.4.

5.2.2 2D selection of a favored direction

In order to estimate a favored direction, the polar coordinates of each data point of D are computed taking the point of reference as $(0, 0)$ as shown in Fig 5.6. The favored direction θ_{fav} can thus be defined as the θ value that maximize the histogrammed $\{\theta\}_i$ distribution.

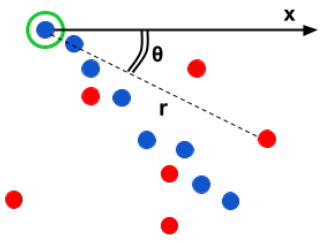

Figure 5.6: Polar coordinate system from the point of reference.

However, in some pathological cases, the favored direction returned this way will not be the direction of the track. Take for example a physical track that draws a chord of the pad plane as illustrated by Fig 5.7: given that the track is short, it is likely that a direction along a diameter actually contains more hits and gets returned as the favored direction instead of the track direction.

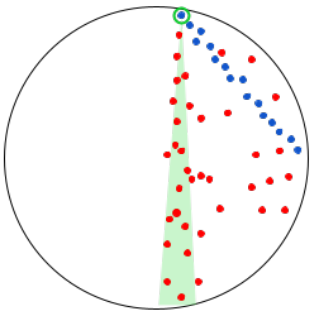

Figure 5.7: Illustration of a case were the naive estimation of the favored direction does not return the track direction.

To overcome this limitation, a new variable θ_{loc} is defined for each hit as follows:

- **If the hit has fewer than 2 immediate neighbours:** θ_{loc} is not defined, the hit is no longer considered at this stage
- **Otherwise:** $\theta_{\text{loc}} = \langle \theta_{\text{immediate neighbours}} \rangle$

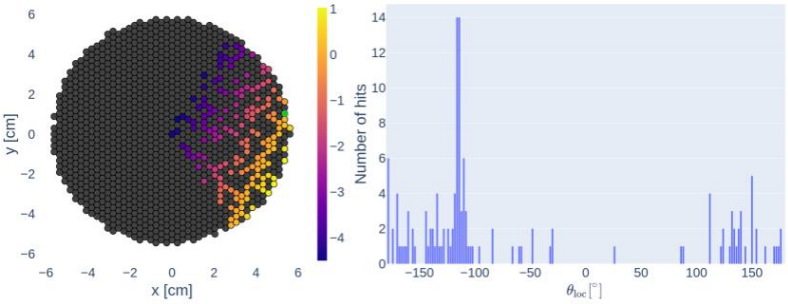

Figure 5.9: Left: Event display of a simulated event: the point of reference is highlighted in green while the color scale shows the value of the selection variable s expressed in cm; **Right:** Corresponding θ_{loc} distribution.

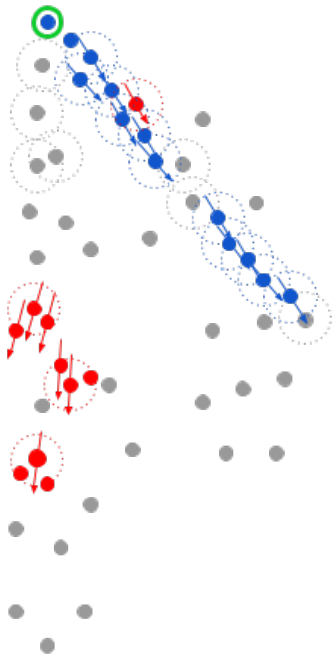

Figure 5.8: Illustration of the computation of the θ_{loc} variable.

This process is illustrated by Fig 5.8 and allows to give more weight to hits that have immediate neighbours and are thus more likely to be within the track. The favored direction can now be obtained looking at the histogrammed $\{\theta_{\text{loc}}\}_i$ distribution. The chosen binning offers a resolution of 2° on θ_{fav}. A selection variable s is built as:

$$s_i = r_i \sin(\theta_i - \theta_{\text{fav}}) \tag{5.4}$$

which is the orthogonal distance, expressed in centimeters, of each hit to the line defined by the reference point and the favored direction. The pre-selected data set is defined as:

$$\{(x, y, z)_n, |s_n| < 2h\} \tag{5.5}$$

This cut value is chosen so that the selected hits do not spread further than a pixel away from the favored direction. Fig 5.9 shows an example of event display where the color corresponds to the selection variable s, as well as the corresponding $\{\theta_{\text{loc}}\}_i$ distribution that allowed to determine θ_{fav}.

5.2.3 First 3D-RANSAC fit to pre-selected data

If the number of pre-selected hits is smaller than 10, it means that at most 2 physical hits remain and it does not make sense to further try reconstructing the event. It shows that either something went wrong in one of the previous steps, for example that the point of reference has been misidentified, or that the simulated event multiplicity was too low for the event to be interesting in the analysis. This is accounted for when estimating the efficiency of the reconstruction algorithm. Otherwise, the pre-selected data set is adjusted by a 3D line using a RANSAC algorithm. The scikit-image Python library[2] is used for the implementation. A minimum sample size of 2 is requested for the randomly selected subsets and the residual threshold is set to $2h$. The event used as an example during the previous step is shown here as well in Fig 5.10. Given that RANSAC is specifically designed to extract the model, the fit is usually in good agreement with the data already at this stage as it will be further studied in Section 5.3. As a result, the next two steps can be avoided when processing simulated events but might be relevant for real data that also contain some background. Indeed, given that the pre-selection is based on two dimensional information only, the purity of the selected data set can be further improved by the RANSAC based selection, as shown in Section 5.3.

2: https://scikit-image.org/

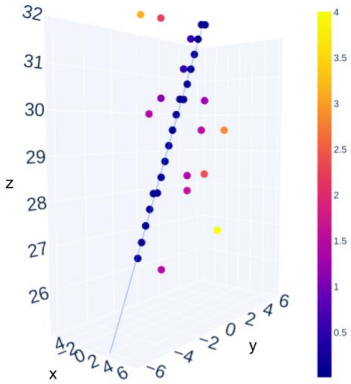

Figure 5.10: 3D RANSAC fit to pre-selected data. The color scale indicates the value of the residuals between data and fit.

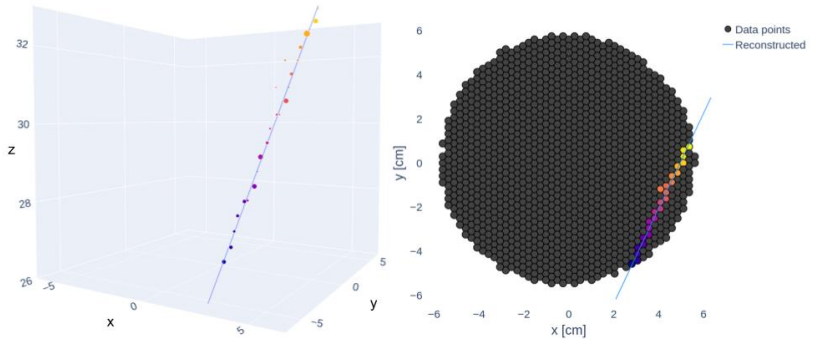

Figure 5.11: Example of track reconstruction. Color shows the z variable while, on the left plot, marker size is proportional to the hit deposited energy.

5.2.4 3D selection and second 3D-RANSAC

Starting back from the entire data set, a new selection variable s_{3D} is defined, for each point, as the residual between the data point and the previously estimated line model, or in other words the minimal distance in 3D between the data point and the previously reconstructed line. The final data set is defined as:

$$\{(x, y, z)_n, |s_{3D,\,n}| < 0.5\} \tag{5.6}$$

This cut value is slightly looser than for the 2D selection because of the timing digitisation: this cut value ensures a spread smaller than a pixel in x and y and a time bin in z. A similarly parameterized RANSAC is applied to the finally selected data set to obtain the final track reconstruction. An example of final reconstruction is shown in Fig 5.11.

5.3 Study of performances on simulated events

A data set of 9339 simulated events that hit the active volume is projected onto D3DT readout plane, among which 8740 have a multiplicity high enough to try running the algorithm. The efficiencies of the 3D reconstruction algorithm are estimated using this data set.

The reconstruction performances are also investigated by studying the difference between the generated and reconstructed muon directions. This residual is the result of the convolution between detector and reconstruction performances. It is interesting to study the residuals R_θ and R_ϕ separately as they bring information about different aspects of our detector:

$$\begin{aligned} R_\theta &= \theta_{\text{gen}} - \theta_{\text{reco}} \\ R_\phi &= \phi_{\text{gen}} - \phi_{\text{reco}} \end{aligned} \tag{5.7}$$

The developed reconstruction algorithm performances affects both residuals in a similar way as it is a 3D reconstruction. However, the detector effects at play are not the same: R_θ is mostly affected by vertical effects such as drift field disruption, time digitisation by the electronics or longitudinal diffusion, while R_ϕ will be degraded by the multiplexing, the finite pad segmentation and the transverse diffusion. Various residuals distributions are studied in order to decorrelate detector effects from

reconstruction performances and draw conclusions about the algorithm performances as well as the expected detector performances.

5.3.1 Efficiencies

Identification of the point of reference

This step is really important in the reconstruction algorithm because if the point of reference identified is not actually in the track, it is very unlikely that the favored direction used for the pre-selection will be the one of the track. The efficiency of the identification of the point of reference is defined as:

$$\epsilon_{\text{P.o.R}} = \frac{N_{\text{correctly identified}}}{N_{\text{processed}}} \tag{5.8}$$

where $N_{\text{correctly identified}}$ is the number of events for which the identified point of reference was indeed in the track and $N_{\text{processed}}$ the number of events passed to the algorithm. It is evaluated at $\epsilon_{\text{P.o.R}} = 0.90 \pm 0.01$ where the uncertainty is statistical.

RANSAC algorithms

Assuming that the point of reference has been correctly determined, it is possible that not enough data points remain after the pre-selection to run the RANSAC algorithm in which case the track will not be reconstructed. This is taken into account in the first RANSAC efficiency defined as:

$$\epsilon_{\text{RANSAC1}} = \frac{N_{\text{RANSAC1 applied}}}{N_{\text{correctly identified}}} \tag{5.9}$$

where $N_{\text{RANSAC1 applied}}$ is the number of events for which the first RANSAC algorithm converged. Similarly, the second RANSAC efficiency is defined as:

$$\epsilon_{\text{RANSAC2}} = \frac{N_{\text{RANSAC2 applied}}}{N_{\text{RANSAC1 applied}}} \tag{5.10}$$

The first RANSAC efficiency is estimated to $\epsilon_{\text{RANSAC1}} = 0.88 \pm 0.01$ while $\epsilon_{\text{RANSAC2}} = 1.00 \pm 0.01$ where the errors are statistical only. This is consistent with the fact that there is not much difference between the pre-selected data and the data selected post first RANSAC when it comes to simulated data with no background other than the multiplexed hits.

Total efficiency

The total reconstruction efficiency is defined as:

$$\epsilon_{\text{reco}} = \epsilon_{\text{P.o.R}} \times \epsilon_{\text{RANSAC1}} \times \epsilon_{\text{RANSAC2}} \tag{5.11}$$

and yields $\epsilon_{\text{reco}} = 0.79 \pm 0.02$ where the error is statistical only.

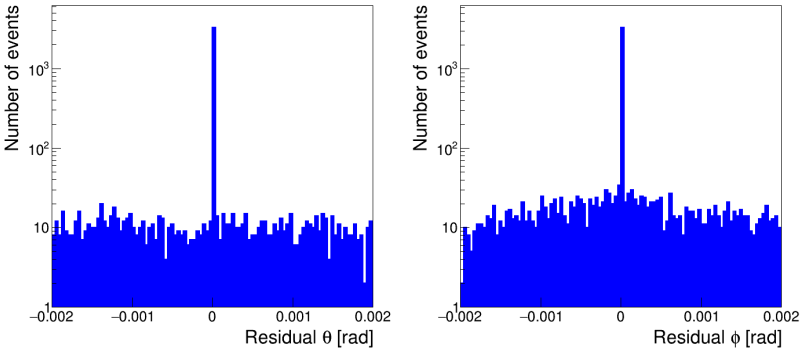

Figure 5.13: Residual between the muon direction, defined by the angles θ and ϕ, as reconstructed by the algorithm and linear regression.

5.3.2 Performances of the 3D reconstruction algorithm

Effect of multiplexing

The reconstructed direction is compared to the direction obtained by making a linear regression to the track hits only thus defining the following residuals:

$$\begin{aligned} R_{\theta}^{\text{algo}} &= \theta_{\text{lin}} - \theta_{\text{RANSAC2}} \\ R_{\phi}^{\text{algo}} &= \phi_{\text{lin}} - \phi_{\text{RANSAC2}} \end{aligned} \tag{5.12}$$

This procedure allows to cancel out performances degradation due to the detector by comparing the reconstructed direction to the best case scenario. Fig 5.13 presents the distributions of R_{θ}^{algo} and R_{ϕ}^{algo} and illustrates that this algorithm can reconstruct the muon tracks as if the readout plane was not multiplexed with a precision approaching 0.01 mrad.

This is made possible by the very good purity of the selected data set, as illustrated by Fig 5.12, as well as the capacity of the RANSAC algorithm to handle outliers.

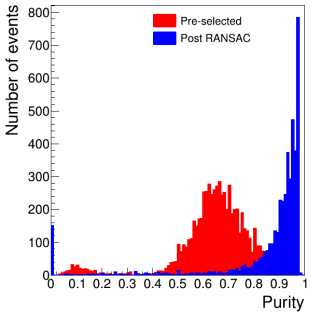

Figure 5.12: Purity of the pre-selected (in red) and finally selected (in blue) data sets.

Hough transformation

In TPCs it is quite common to use Hough transformation (*see Hough transformation box*) in order to achieve track reconstruction as it is an algorithm initially developed to detect lines in photographs [48] and updated since for broadest applications. However, due to the multiplexing, it was estimated in our case that the data would present too much noise to be efficiently reconstructed using such algorithm. It was nonetheless implemented and tested on the 2D data set to validate the previous hypothesis and confront our reconstruction algorithm performances to an existing one. Fig 5.14 illustrates on an event the various steps of the track reconstruction using Hough transformation:

1. the data set $\{(x, y)\}_i$ is transformed into an image to be processed: to do this the data set is used to fill a 2D-histogram which binning has been set so that the bins are centered on the pads center positions and there can only be one data point in each bin. In the end the bin width is $w = 0.125\,\text{mm}$ which is about half of the

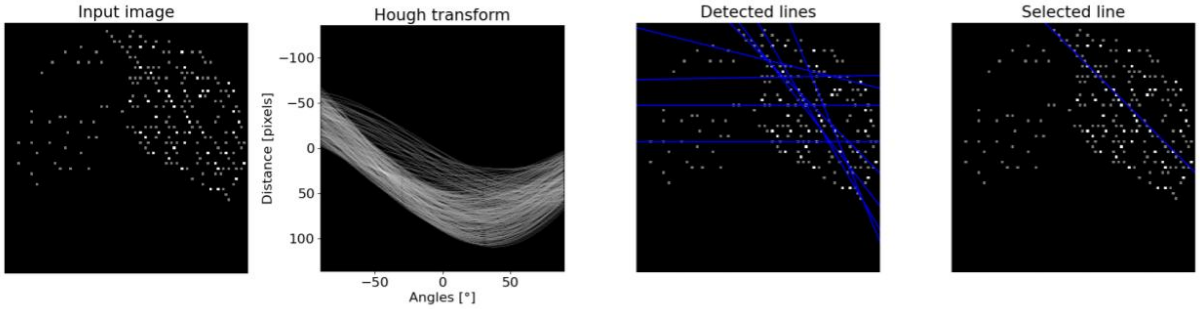

Figure 5.14: Illustration of the Hough transform based algorithm for track reconstruction. From left to right: transformation to image; Hough transform; detected lines and finally reconstructed track.

distance between two centers. However it should be noted that, since the pixels are hexagonals, there is a shift from a column to the other so that this transformation slightly biases the data. A refined binning was also tested still centered on the centers positions but lines were no longer detected.

2. Hough transformation is applied using an angular step $\Delta\phi_{\text{Hough}} = 0.5\,\text{mrad}$ much smaller than the obtained residuals distribution standard deviation to ensure that this is not the limiting factor on the algorithm performances. The `scikit-image`[3] Python library is used for the implementation.
3. Multiple lines are detected
4. A single one is selected based on the intensity of the peak detected in the Hough space.

3: https://scikit-image.org/

Hough Transformation

A line can be uniquely parametrized in the (x, y) plane by 2 parameters a and b such that:

$$y = ax + b$$

or, using polar coordinates:

$$y = -\frac{\cos\theta}{\sin\theta}x + \frac{r}{\sin\theta}$$

where θ is the angle between the line and the x-axis while r is the orthogonal distance from the line to the origin of the (x, y) plane. The Hough space is defined as the $(\theta, r$ phase-space in which a line is represented by a point. On the contrary, a single point is mapped in the Hough space to all the lines that can pass through that point yielding to a sine-line. As an example, two points of the (x, y) plane are represented in the Hough space by two curves which single intersection gives the parameters of the unique line passing by those points. If all the points from an input image are transformed into Hough space, lines can thus be identified as intersection points.

First of all, it seems that the Hough transformation is actually quite robust to the multiplexing induced noise and the obtained results are better than what could be initially expected. However, the bias introduced by the image transformation is definitely a limitation. No other binning could be tested to estimate the effect on the performances: a refined binning

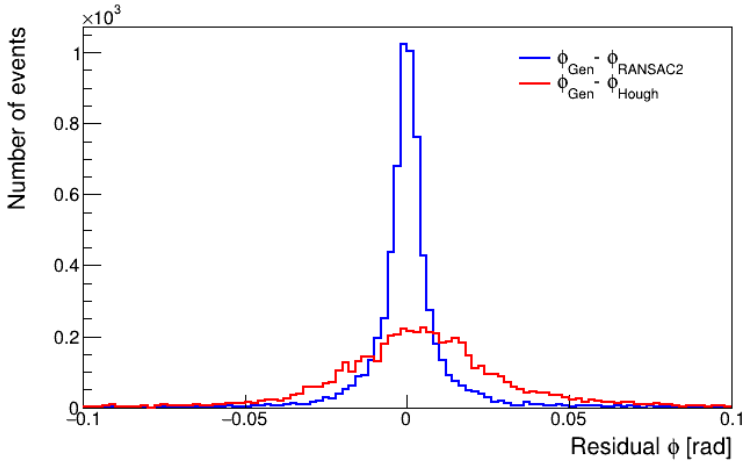

Figure 5.15: Distributions of the residuals R_ϕ^{RANSAC2} in blue and R_ϕ^{Hough} in red.

still centered on the pad positions prevents any line to be detected while a larger binning would be limiting compared to the initial readout segmentation. If estimated relevant by the team, future efforts could be made to implement a Hough transform algorithm that does not require the input data to be transformed into an image as it is the case here.

Finally, the residuals R_ϕ^{RANSAC2} and R_ϕ^{Hough} are defined by Eq 5.7 and their distributions are shown in Fig 5.15. It should be kept in mind that here the reconstructed azimuthal angles ϕ are compared but in the case of the RANSAC2 algorithm it comes from a 3D reconstruction while the Hough implementation is only 2D at the moment. In addition, as mentionned before, the bias introduced by the pixelisation of the input image for the Hough method could not be estimated and might thus explain the difference of performances obtained here.

5.3.3 Performances of the detector

The residuals as defined by Eq 5.7 including both detector and reconstruction effects, the standard deviation of their distribution can be interpreted as the angular resolution that can be achieved with the complete set up. It is an optimistic view as the simulated data do not contain any noise at this stage. Fig 5.16 shows the Gaussian fit to both $R_\theta^{\text{RANSAC2}}$ and R_ϕ^{RANSAC2} which result are presented in Table 5.1. Combining those results yields a global angular resolution of 6.5 mrad at worst, which is to be compared with the telescopes angular resolution that ranges from a 4 to 10 mrad depending on the muon angle with the telescope aiming line.

The same distributions are presented in Fig 5.17 in blue and compared to the distributions obtained when the z coordinate is not binned in red. As could be expected, no effect is observed on the azimuthal angle residuals, while the angular resolution on the zenithal angle is improved by 45% when using non-binned data. This indicates that reconstruction performances could be enhanced by tuning the sampling parameters of the electronics to optimize the timing resolution.

Finally, the same residuals are presented in a 2D-histogram as a function of the number of pixels in the track as shown by Fig 5.18. A net improvement

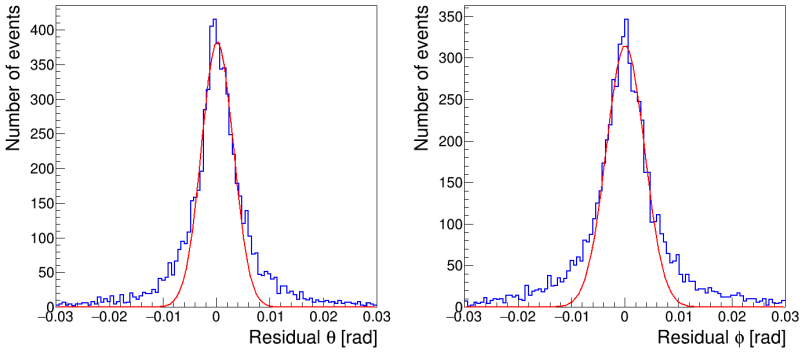

Figure 5.16: Residual between the muon direction, defined by the angles θ and ϕ, as reconstructed by the algorithm and generated with their associated Gaussian fit in red.

Table 5.1: Gaussian fit results to the residuals distributions presented in Fig 5.16.

Parameter [mrad]	Fit value
$\mu_{R_\theta^{\text{RANSAC2}}}$	0.14 ± 0.08
$\sigma_{R_\theta^{\text{RANSAC2}}}$	2.99 ± 0.11
$\mu_{R_\phi^{\text{RANSAC2}}}$	1.15 ± 1.04
$\sigma_{R_\phi^{\text{RANSAC2}}}$	3.55 ± 0.15

is observed for longer tracks encouraging, when possible, to tilt the detector in order to maximize the number of long tracks.

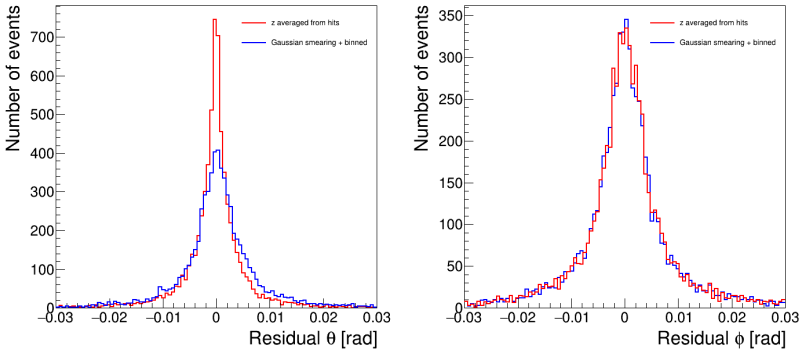

Figure 5.17: Residual between the muon direction, defined by the angles θ and ϕ, as reconstructed by the algorithm and generated with (in blue) or without (in red) a binning and Gaussian spread of the z coordinate to simulate the electronics digitization.

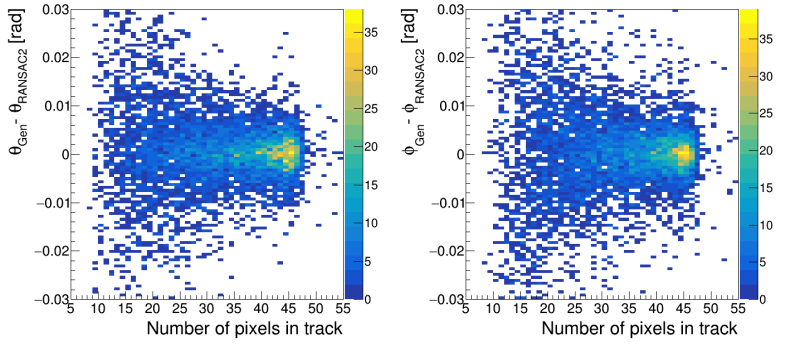

Figure 5.18: Residual between the muon direction, defined by the angles θ and ϕ, as reconstructed by the algorithm and generated as a function of the number of pixels in the track.

5.4 Test on real data

Over the time of my PhD, the first prototype of D3DT with final dimensions, was successfully operated and recorded a few thousands of events. However, the data taking conditions were not yet optimized:

- Our current power supply option only allow to set up the high voltage up to 6 kV instead of the 10 kV required for an optimum drift velocity. In these conditions the drift field is of only 140 V/cm.
- The readout Micromegas still suffers from the defective channels that introduce a lot of electronic noise on ASIC 0.
- Some data were taken before the field cage problems discussed in Section3.3.3 could be identified and fixed and are thus not usable.
- Some data were taken before the sealing could be properly done so the gas quality may also have been affected, resulting in electron attachment.

Nonetheless, some nice events were detected and a few examples are illustrated in Fig 5.19. The reconstruction algorithm is applied on the 2D projection of the data as some discontinuities are observed on z due to the poor quality of the drift field at the time. An example of reconstructed event is shown in Fig 5.20: on the left plot, the color indicates the time corresponding to the maximum of the waveform while on the right, it shows the distance to the RANSAC fit used to select the data. The point of reference is highlighted in red while the selected points are circled in blue.

At the moment, the difficulty is that the data taken in self-triggering mode contains a lot of noise and too few events with a track identifiable to the naked eye to test the algorithm on. Given the performances of the algorithm on simulated data, we are confident that it will work on real data as well, eventually with the addition of a pre-processing phase to clean the noise and ensure a correct identification of the point of reference which is critical for a good track reconstruction. However, more efforts are needed towards the development of the detector to obtain better data to work with.

In the mean time, the track reconstruction algorithm can be further tested by adding random noise to the data set in order to ensure its robustness facing lower and lower signal to noise ratio. The addition of the external trigger system will also be very beneficial to the track reconstruction as it will allow to identify the electronic channel that triggered the event, thus simplifying the identification of the point of reference.

All things considered, these first data shed light on the main difficulty of developing a detector such as D3DT which is the high voltage operation in a confined environment. The risk for sparking or current leaks is increased by the proximity and intensity of the electric potentials at play which translates into noise of disruption of the drift field. But the current results are very encouraging and now that the detector can be operated and tested, we expect to be able to acquire better data in a near future.

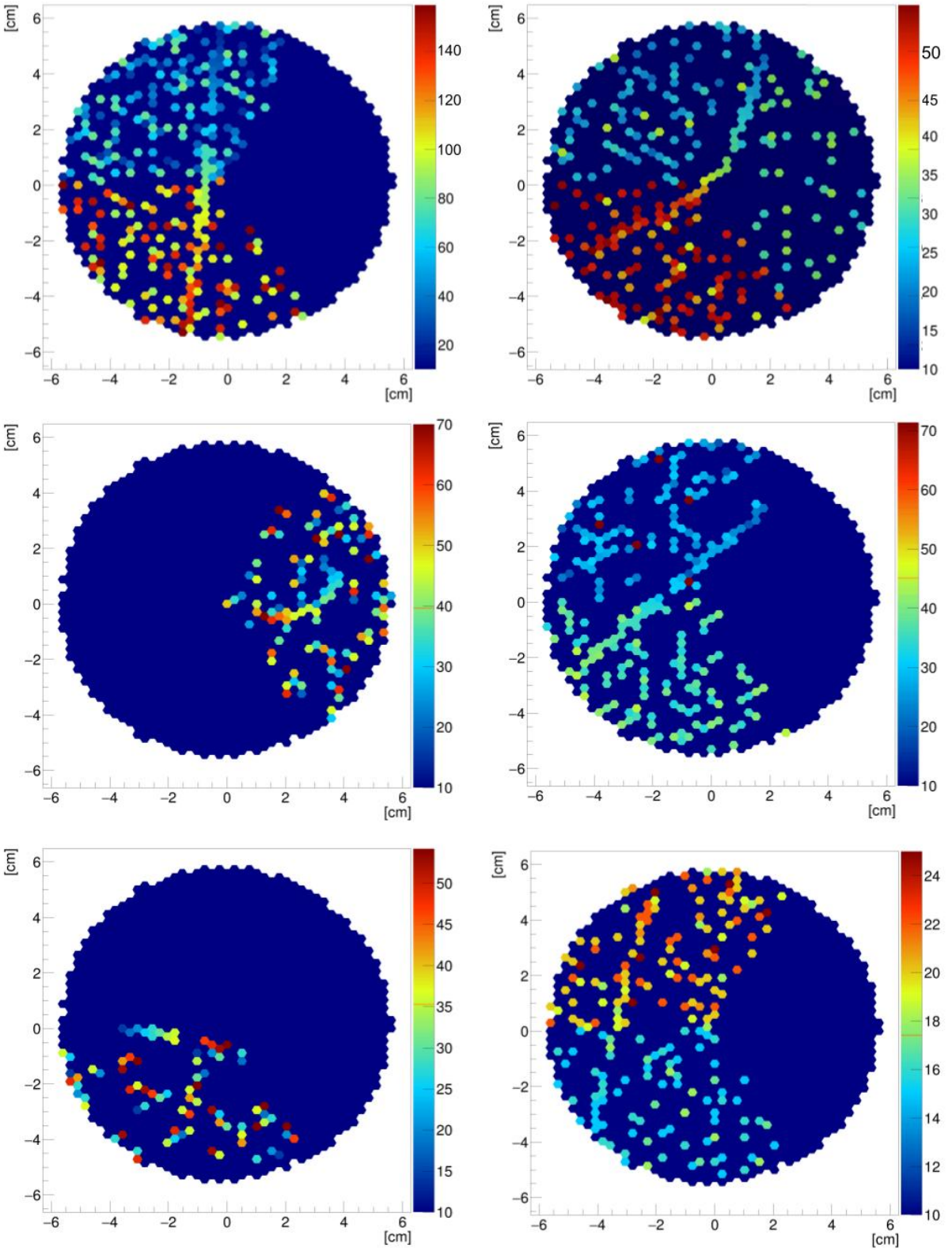

Figure 5.19: Event display of cosmic events with V_{cath} =6000 V and V_{mesh} = 380 V. Color shows the time sample corresponding to the maximum of the waveform for each pad, thus a physical track is expected to present a continuous color gradient depending on its inclination angle.

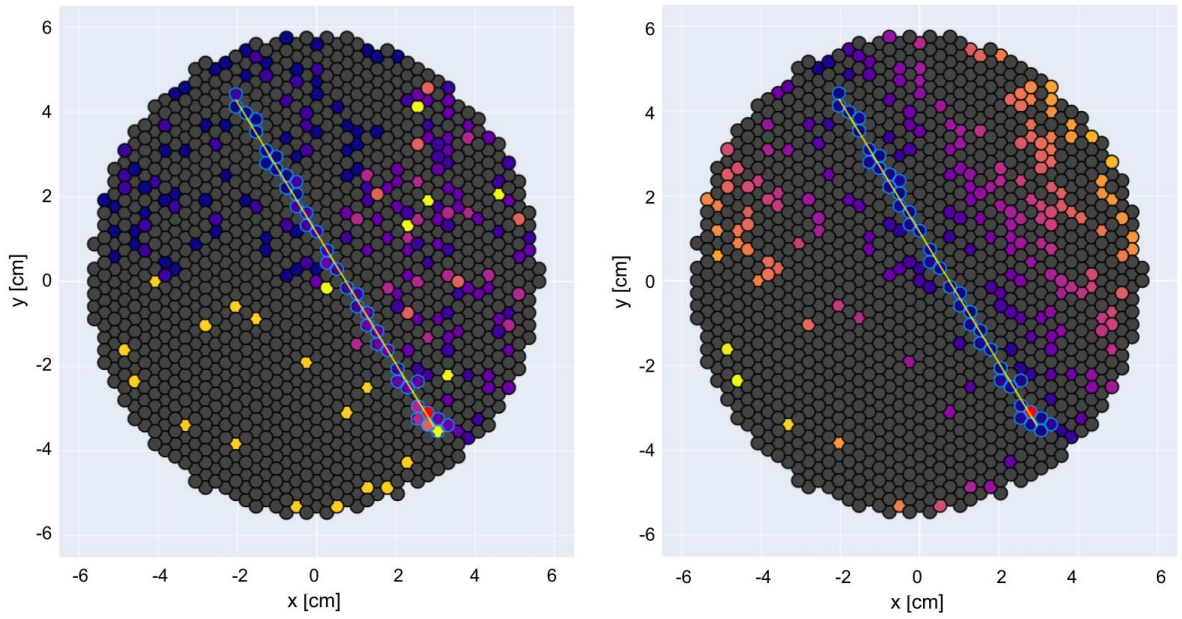

Figure 5.20: Example of 2D track reconstruction on actual data. Color indicates the time corresponding to the maximum of the waveform (left) and the distance to the RANSAC fit used to select the data (right). The point of reference is highlighted in red while the selected points are circled in blue.

Part III

Upgrade of T2K near detector

THE T2K EXPERIMENT: TOWARDS AN UPGRADE

6

The first observation of neutrino oscillation in 1998 by the Super-Kamiokande (SK) experiment [49] ignited a new line of research since this process is not consistent with the neutrino mass being null as postulated by the Standard Model. The T2K experiment, being a long-baseline experiment as shown in Fig 6.1, has been designed to study the neutrino oscillation by looking at ν_e appearance in a ν_μ beam. To do so, a near detector ND280 located in Tokai precisely characterize the incident neutrino beam that is later on sampled by the SK far detector 295 km away. By comparing the neutrino spectrum reconstructed at both locations it is possible to extract information about the neutrino oscillation process and thus shed light on the neutrino mass scale. This detector is in operation since 2010 and is currently being upgraded with a commissioning phase expected in early 2023.

This chapter will present in more details the physics goal of the T2K experiment, how the detectors have been designed to study neutrino oscillation and the important results that have already been obtained during the first 10 years of activity. Finally, the motivations for an upgrade will be presented as well as its implications for the near detector specifically.

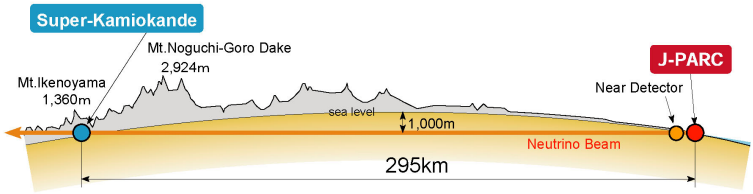

Figure 6.1: Schematic view of the T2K experiment.

6.1 From physics case to detector design

6.1.1 T2K physics goal

In the Standard Model, fermions are categorized in three generations which, in the exception of the neutrinos, can be correlated to the mass range of the particles. To illustrate, muons and taus would be respectively second and third generation of electrons. Similarly, 3 flavors of neutrinos are predicted by the Standard Model and called ν_e, ν_μ and ν_τ in reference to the charged lepton they partner with in the charged-current weak interaction. Those three states are flavor eigenstates of the weak interaction but differ from the Hamiltonian mass eigenstates denoted by ν_1, ν_2 and ν_3. The unitary matrix U allowing to rotate from the mass eigenbase to the other is called the Pontecorvo–Maki–Nakagawa–Sakata or PMNS matrix and is parametrized as follows :

$$U = \begin{pmatrix} 1 & 0 & 0 \\ 0 & c_{23} & s_{23} \\ 0 & -s_{23} & c_{23} \end{pmatrix} \begin{pmatrix} c_{13} & 0 & s_{13}e^{-i\delta_{CP}} \\ 0 & 1 & 0 \\ -s_{13}e^{i\delta_{CP}} & 0 & c_{13} \end{pmatrix} \begin{pmatrix} c_{12} & s_{12} & 0 \\ -s_{12} & c_{12} & 0 \\ 0 & 0 & 1 \end{pmatrix} \begin{pmatrix} e^{i\alpha_1/2} & 0 & 0 \\ 0 & e^{i\alpha_2/2} & 0 \\ 0 & 0 & 1 \end{pmatrix} \tag{6.1}$$

where $c_{ij} \equiv \cos\theta_{ij}$ and $s_{ij} \equiv \sin\theta_{ij}$. θ_{ij} are called the mixing angles and δ_{CP} is the CP violation phase. The last matrix is only physically relevant if neutrinos are Majorana particles and does not affect the neutrino oscillation probabilities since the matrix elements cancel out when the matrix is squared. Each flavor eigenstate can thus be described as a superposition of mass eigenstates and oscillate from one to the other.

The T2K experiment was designed to study the oscillation of neutrinos and more specifically to measure the θ_{13} parameter, the last unknown mixing angle. The probability for $\nu_\mu \rightarrow \nu_X$ processes, where X can be either e, μ or τ, is shown in Fig 6.2 as a function of the ratio between the baseline of the experiment L (distance between production and detection points) and the beam energy E. It shows that the θ_{13} can be accessed through the maximal amplitude of $P(\nu_\mu \rightarrow \nu_e)$ but also that this process is highly suppressed compared to the other two. In order to maximize the probability of $\nu_\mu \rightarrow \nu_e$ and not to be dominated by the $\nu_\mu \rightarrow \nu_\mu$ channel, the neutrino beam energy must be tuned so that $L/E \approx 500$. In that case, $P(\nu_\mu \rightarrow \nu_e) \approx \sin^2\theta_{13}\sin^2\theta_{23}$ in fact allows to measure the θ_{13} parameter while $P(\nu_\mu \rightarrow \nu_\mu) \approx \sin^2 2\theta_{23}$ makes it possible to precisely measure the θ_{23} parameter. If the beam energy can be slightly tuned, the period of the $\nu_\mu \rightarrow \nu_\mu$ process probability can be estimated, giving a direct access to the Δm^2_{32} parameter, defined as $\Delta m^2_{32} = m^2_{\nu_3} - m^2_{\nu_2}$. Finally, although the $\nu_\mu \rightarrow \nu_\tau$ process is dominant at the optimal L/E value, it does not compromise T2K measurements as the detector is mostly blind to ν_τ. Indeed, in the case of T2K, L =295 km translates to a beam energy tuned around $E \approx 0.6$ GeV. This energy being far below the τ lepton mass, which is around 1.78 GeV, the ν_τ charged current (CC) interactions are highly suppressed. Neutral current (NC) interactions are still possible but would mostly result in π^0 production with no associated charged lepton to identify the flavor of the neutrino.

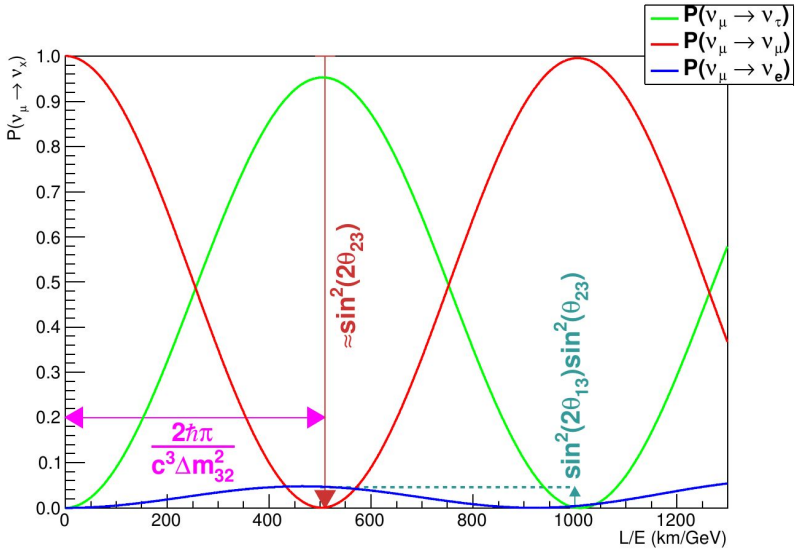

Figure 6.2: Oscillation probability for the $\nu_\mu \rightarrow \nu_X$ modes with $X = e, \mu$ or τ.

6.1.2 Strategy and design

The success of such measurements lies in the ability to correctly reconstruct the oscillated neutrino spectrum at the far detector. Neutrinos are not directly detected but rather through their interactions with the detector meaning that the observed rate of neutrinos is actually a convolution of several components. Taking the example of the rate of ν_e of energy E measured on the far detector $\Phi^{\text{far}}_{\nu_e}(E)$:

$$\Phi^{\text{far}}_{\nu_e}(E) = [\ \underbrace{\Phi^{\text{near}}_{\nu_\mu}(E) \times P_{\nu_\mu \to \nu_e}(E)}_{\text{Expected number of } \nu_e \text{ from } \nu_\mu}\ ] * \sigma_{\nu_e}(E) * \varepsilon(E) + \Phi_{\text{bckg}}(E)$$

where $\Phi^{\text{near}}_{\nu_\mu}$ is the ν_μ rate measured close to the production point, σ_{ν_e} is the ν_e interaction cross-section and ε the detector efficiency. The background component Φ_{bckg} includes all ν_e contributions which do not come from oscillations and are thus not interesting for the experiment (solar neutrinos, beam contamination that did not oscillate, etc.). This equation highlights some important constraints on the T2K experiment to make it possible to reconstruct the oscillated neutrino spectrum:

- **A precise characterization of the neutrino beam near the production point** in order to minimize the systematic uncertainties propagated on the final result
- **A precise measure of the neutrino energy** in order to correctly predict the interaction cross-section which is energy dependant
- **A precise model of the neutrino-matter interactions at play** to both reconstruct the neutrino energy as well as steer the technological choices to be made in terms of detector conception

Being subject to the weak force, neutrinos interactions with the nuclei of the detector targets are mediated through either a neutral Z boson and thus referred to as Neutral Current (NC) interactions, or a charged $W^{\pm}$ boson in which case they are referred to as Charged Current (CC) interactions. However, the identification of the neutrino flavor is only possible in the case of CC interactions as it is based on the identification of the associated charged lepton emitted. This is why in the case of an oscillation experiment, the signal comes from CC interactions while NC interactions constitute a source of background.

As the existing water Cherenkov Super-Kamiokande detector is repurposed to serve as far detector for the T2K experiment, neutrinos are meant to be detected via CC interactions with the neutrons of the water target. However, the Cherenkov threshold is too high for protons of the final state to be detected meaning that the neutrino energy will have to be inferred from the charged lepton reconstruction only. At T2K energy, the dominant type of interaction is the charged current quasi-elastic (CCQE), which Feynman diagram is presented Fig 6.3, and where the neutron from the initial state is bound inside a nucleus. For the neutrino energy to be reconstructed using only the lepton kinematics, the knowingly wrong assumption that the target nucleon is at rest has to be made. This simplification along with the fact that this is a two-body interaction

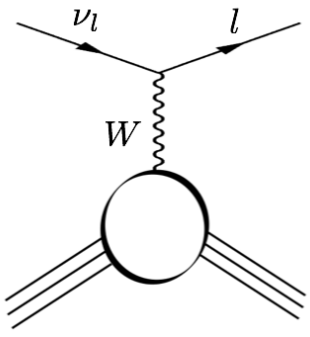

Figure 6.3: Feynman diagram of a charged current interaction between a neutrino and a nucleus.

allows to write the reconstructed neutrino energy E_ν^{rec} as follows:

$$E_\nu^{rec} = \frac{m_p^2 - (m_n - E_b)^2 + m_l^2 + 2(m_n - E_b)E_l}{2(m_n - E_b - E_l + p_l \cos\theta_l)} \tag{6.2}$$

with m_p, m_n and m_l the masses of the proton, neutron and lepton respectively, E_l and p_l the energy and momentum of the lepton, and E_b the binding energy of the target nucleus. Equation 6.2 dictates that the far detector performances must ensure the identification of the lepton flavor as well as a precise measurement of its energy and momentum.

This method of reconstruction, known as "inclusive", presents two major limitations: it introduces a bias from assuming that the nucleus is at rest and is highly dependant of the nuclear inclusive models predictions. With this in mind, a different approach has been chosen for the near detector which, unlike the far detector, has been designed and constructed specifically for the T2K experiment. The objective is to precisely reconstruct the neutrino non-oscillated spectrum using this time a full exclusive reconstruction of all final state particles as well as characterize the various background contributions that may be detected at the SK detector. This translates, in terms of detector requirements, to:

- **A large angular acceptance and low threshold** to detect all final state particles
- **A good momentum and dE/dx resolution** to allow for particle identification

More specifically, the particles that need to be identified at the near detector and coming either from neutrino interactions or background contributions are muons, electrons, pions, and kaons. π^0 produced by neutrino interactions via NC decay into a pair of photons which, at T2K energies, convert into electron-positron pair. Given that SK cannot separate electrons from positrons, a partially reconstructed converted photon can be mistaken for an electron produced by a neutrino interaction and thus constitutes a concerning background component. This justifies a dedicated π^0 detector to estimate the rate of neutral pions production. To study possible CP violation effects in case $\theta_{13} \neq 0$, neutrinos should be distinguished from their anti-particles. Tracking charged particles under a magnetic field allows to measure the particle momentum as well as flag neutrinos and anti-neutrinos based on the charge of their associated lepton. This motivates the use of Time Projection Chambers in a magnetized environment.

The following section describes in more details the neutrino beam production and detection line that resulted from these considerations.

6.2 Neutrino production beam line and T2K detectors

6.2.1 Beam line

The neutrino production beam line is illustrated in Fig 6.4. A 30 GeV proton beam accelerated at J-PARC is directed onto the target, producing

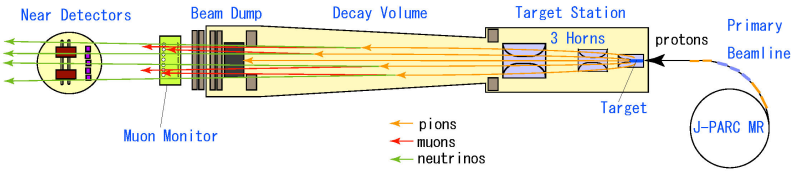

Figure 6.4: Schematic drawing of the neutrino production beam line.

mainly pions and a minor component of kaons. Depending on the desired channel (ν or $\bar{\nu}$), the polarity of the horns is set to focus the mesons with the proper charge towards the decay volume. There, the charged mesons will decay following either $X^+ \rightarrow \mu^+\nu_\mu$, where X refers to a meson, or $X^- \rightarrow \mu^-\bar{\nu}_\mu$. Other decay modes exist but their contribution can be neglected: for example the branching fraction of $\pi^+ \rightarrow \mu^+\nu_\mu$ is larger than 99.9%.

If muons are left to decay themselves, electron neutrinos will be produced thus contaminating the muon neutrino beam. Instead, the beam dump is placed just downstream the decay volume to stop all charged particles except for the muons with an energy $E_\mu > 5\,\text{GeV}$. This way, the electron neutrinos are no longer issued from in flight decay but rather emitted isotropically, which highly suppresses the ν_e background at the far detector. In addition, the high energy muons remaining can be used to precisely monitor the neutrino beam direction and precisely control the associated ν_e contribution.

Finally, if used as such, the neutrino beam energy spectrum is quite broad as the charged mesons are produced with a large energy range. However, as it was previously mentioned in Section 6.1.1, the energy of the neutrino beam must be precisely tuned for the $\nu_\mu \rightarrow \nu_e$ process to be favored. The so-called "off-axis" concept is applied to select a sample of neutrino which spectrum peaks at the right energy. Neutrinos are mostly produced via the pions 2-body decay, in which case the energy of the neutrino on the laboratory frame can be written as a function of the angle θ between the neutrino and pion momenta. There is an angle for which the neutrino energy hardly depends on the parent momentum and peaks at $E_\nu \approx 0.6\,\text{GeV}$ which is called the off-axis angle and is estimated at 2.5°. Thus, the near and far detectors are actually placed at a 2.5° angle with respect to the beam axis. The effect of moving off axis on the neutrino energy spectrum is illustrated in Fig 6.5.

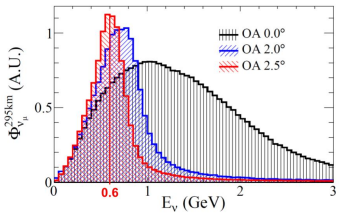

Figure 6.5: Effect of moving off-axis on the neutrino energy spectrum. The energy enhancing the $\nu_\mu \rightarrow \nu_e$ channel is highlighted by the red vertical line. Taken from [50].

6.2.2 Near detector ND280

The ND280 complex, shown in Fig 6.6, serves multiple purposes: the first one is to precisely monitor the neutrino beam properties which is achieved by the only on-axis detector INGRID, the second one is to provide a measurement of the non-oscillated neutrino spectrum as well as a characterization of the various background components to better reconstruct the oscillated spectrum at the level of the far detector. The latter is performed by a set of detectors which are placed off-axis, in the direction of the SK far detector. An overview of the ND280 complex is presented in Fig 6.7 and highlights the different sub-structures presented in the following section. The same coordinate convention is used for all detectors where z is along the nominal neutrino beam while x and y are the horizontal and vertical respectively.

Figure 6.6: Top-view photograph of the ND280 complex in the pit.

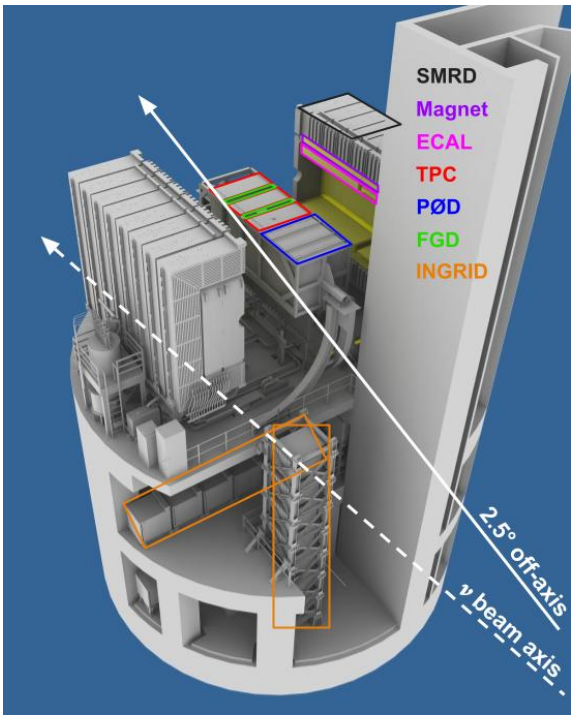

Figure 6.7: Overview of the ND280 complex with the various substructures highlighted.

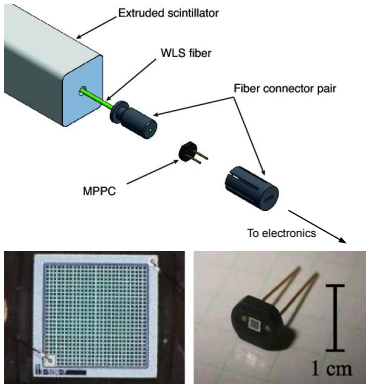

Figure 6.8: Top: Schematic of a scintillator bar read by a wavelength-shifting fiber combined with a multi-pixel photon counter; **Bottom:** Photograph of a multi-pixel photon counter.

Wavelength-shifting fiber readout using Multi-Pixel Photon Counter

Most of the ND280 sub-detectors use scintillator detectors read by wavelength-shifting (WLS) fiber coupled to Multi-Pixel Photon Counters (MPPCs) because of the constraining experimental environment, especially the magnetic field of 0.2 T, that makes it impossible to use multi-anode photo multiplier tubes. MPPCs consists of an array of pixel working each as a Geiger micro-counter, with a gain comparable to the one of a vacuum photomultiplier and the advantage that they are insensitive to magnetic field. The signal read by a single pixel does not provide information about the number of electrons detected, but rather the number of fired pixels. The dynamic range of this type of detector is thus limited by the finite number of pixels. For T2K, custom MPPCs have been designed with a 26×26 pixel array for an active area of 1.3×1.3 mm^2.

Interactive Neutrino GRID (INGRID)

The INGRID detector is an on-axis detector which purpose is to monitor the beam direction and intensity with enough statistics to provide daily measurements. It consists in 16 modules, 14 arranged in a cross shape aligned with the beam center and 2 off-axis as shown Fig 6.9. Each module is essentially a 125 side cube made of a repeated stack of iron plate and scintillator plane for a total iron mass serving as neutrino target of 7.5 tons. The scintillator tracking planes are made of two layers of scintillating bars, one horizontal and one vertical, to read both x and y coordinates with a 5 segmentation. Each bar is extruded in its center to insert the WLS fiber for light collection and connected to MPPC for amplification before readout. Four additional planes of scintillator bars this time segmented in the beam direction are placed around the stack to

be used as veto planes.

Finally, a different module, the Proton Module, made only of tracking planes with a finer segmentation, has been added in between the two central modules to detect recoil protons and muons produced during neutrino interactions. The goal is to identify the dominant quasi-elastic channel mode in order to compare and eventually tune the Monte Carlo simulations.

Figure 6.9: Left: Overview of the INGRID on-axis detector with its 14 modules arranged in a cross shape (2 additional off-axis modules are not represented here). **Right:** Exploded view of a single INGRID module: tracking planes are represented in blue and interleaved with iron plates, veto planes are the external planes shown in black.

Pi-zero detector (PØD)

The pi-zero detector [51] is meant to identify and measure NC processes $\nu_\mu + N \rightarrow \nu_\mu + N + \pi^0 + X$, which contribute to the background of the experiment, by detecting the produced π^0. Scintillator modules, similar to those used for INGRID except for their finer segmentation, are interleaved with fillable water targets. Charged particles as well as electromagnetic showers from electrons or photons can be reconstructed allowing to detect the $\pi^0 \rightarrow \gamma\gamma$ events.

Time Projection Chambers (TPCs)

TPCs are gaseous detectors that performs 3D reconstruction of the charged particle tracks as developed in more details in Chapter 1. If combined with a magnetic filed, it allows to measure the final state particles momenta and energy loss per unit of length for particle identification (PID), as well as identify the neutrino interaction at play based on the number of tracks.

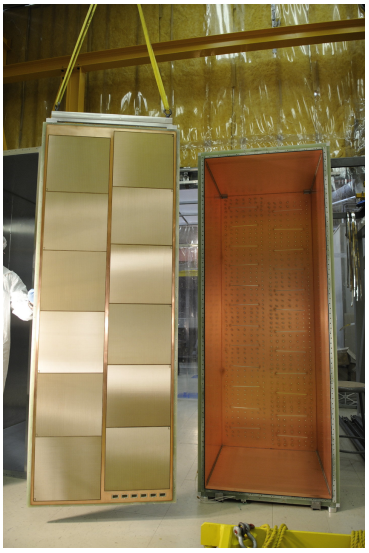

Figure 6.10: Photograph of an open T2K TPC with the 2 columns of Micromegas modules.

Each TPC consists of a 2.3 m × 2.4 m × 1.0 m drift cage where E and B are both aligned with the x-axis. The electrons produced when an ionizing particle passes through are drifted towards the readout planes to be amplified and sampled. Two columns, each of six 342 mm × 358 mm Micromegas modules, cover the anode plane as presented in Fig 6.10 and are offset by a few millimeters so that the small dead areas in between modules do not align. Each module uses 128 µm amplification gap bulk-Micromegas [9] read by 1728 (36 × 48) pads of 7.0 × 9.8 mm^2. The gas used to operate the TPCs is a Ar-iC_4H_{10}-CF_4 (95:2:3) mixture because of its good performances: it allows for a high electron drift velocity but also a limited transverse diffusion coefficient. For an electric field of $E_{\text{drift}} = 270\,\text{V/cm}$ it yields $v = 7.8\,\text{cm}\,\mu\text{s}^{-1}$ and $\sigma_T(B = 0.2\,\text{T}) = 267\ \mu\text{m}/\sqrt{\text{cm}}$.

Isobutane serves as quencher with the bonus effect of increasing the gain via Penning effect.

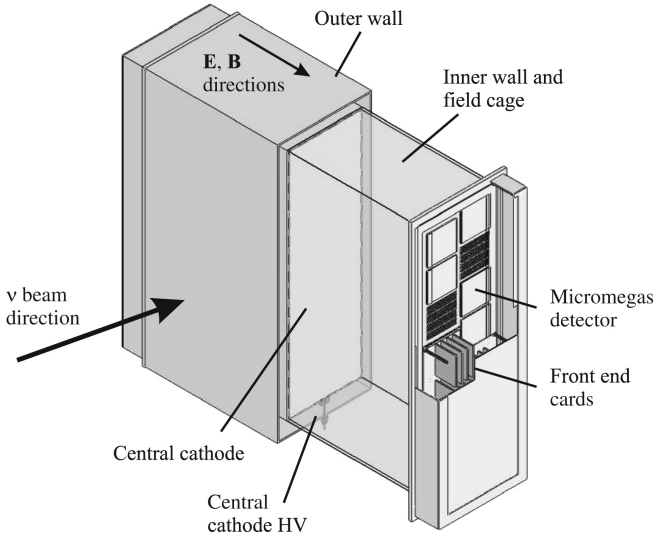

Figure 6.11: Schematic view of the TPCs design.

Fine Grain Detectors (FGDs)

Two FGDs modules, serving both as target for neutrino interaction and tracker for the charged particles, are inserted between the TPCs as illustrated by the event display shown in Fig 6.13. Each one of the modules is a $2 \times 2 \times 0.3$ m^3 made out of stacked layers of plastic scintillator bars aligned along x and y alternatively and contains about a ton of target material. Each scintillator bar is 1.9 m long for a section of 9.61×9.61 mm^2 and is read by a WLS optical fiber connected to a MPPC.

Figure 6.12: Photograph of one of the T2K FGDs.

In the second module, as for the PØD, the scintillator layers are alternated with fillable water modules so that the cross section of the neutrino interaction with water can be measured. This measurement is important to reduce the systematic uncertainties associated to the model dependant energy reconstruction of the neutrinos at the far detector.

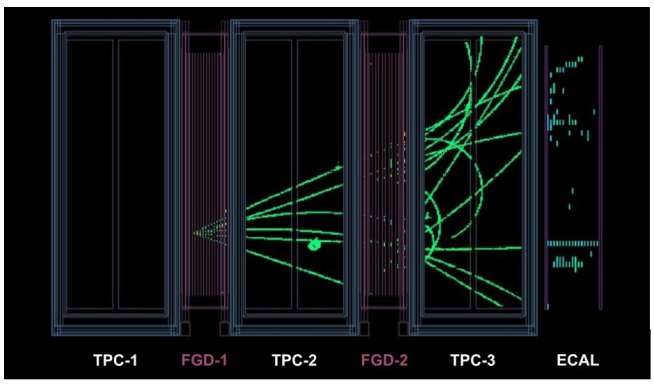

Figure 6.13: ND280 event display of a neutrino interaction.

Electromagnetic CALorimeter (ECAL)

The ECAL completey encapsulates the ND280 inner detectors (PØD, TPCs and FGDs) and provides a complementary information to the PØD by measuring the escaping energy carried by photons to reconstruct the π^0 produced inside the tracker detectors. It also detects charged particles exiting the inner volume and brings additional information to the tracking system relevant for PID. It is particularly useful to separate muons for example, as they leave a clean track in the ECAL while electrons and hadrons produce a shower. The ECAL is made out of active scintillator bars planes, read by WLS optical fibers coupled with MPPC, alternated with lead absorber sheets. Each scintillator bar has a section of 4×1 cm^2.

Side Muon Range Detectors (SMRD)

The outermost piece of ND280 is the SMRD which consists of 1.7 cm thick active scintillator modules inserted in the innermost gaps of the magnet yokes. The scintillators are instrumented with a serpentine-routed WLS optical fiber read by a MPPC. Being the external detector, it allows to veto events triggered by cosmic rays or neutrino interactions coming from outside the detector. SMRD is also used to detect high angle muons escaping the detectors and measure their momenta as there are no TPCs in this direction.

6.2.3 Super-Kamiokande (SK) far detector

The far detector of the T2K experiment is located in the Kamioka mine, 1000 m underground in order to minimize the background contribution from cosmic ray muons, and 295 km away from the neutrino beam production site. In consists of a 39.3 m diameter and 41.4 m tall cylindrical tank filled with 50 kt of water used as target for neutrino interactions as illustrated by Fig 6.14. The Cherenkov light emitted by the charged leptons produced from the neutrino interaction is detected by the 11200 Photo-Multiplier Tubes (PMTs) covering 40% of the tank internal area. The electrons, being more subject to Bremsstrahlung due to their lighter mass, will produce distorted rings compared to the muons as shown on the SK event display in Fig 6.15. It allows to identify the associated neutrino flavor with less than 1% error.

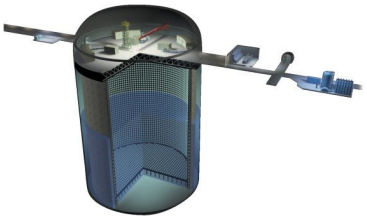

Figure 6.14: Schematic view of the Super-Kamiokande detector.

As the cross-section of neutrino interactions is very small, it is all the more important to suppress the background. In particular, high energy cosmic muons or muons produced by neutrino interactions in the rock around the detector should be vetoed. To achieve this, the SK detector is separated into an inner and outer detectors, optically isolated, so that any event producing signal in the outer detector can be removed from the analysis. Another important background contribution comes from the atmospheric neutrino and in this case it is the timing information from the beam monitoring that is used to discriminate the background events.

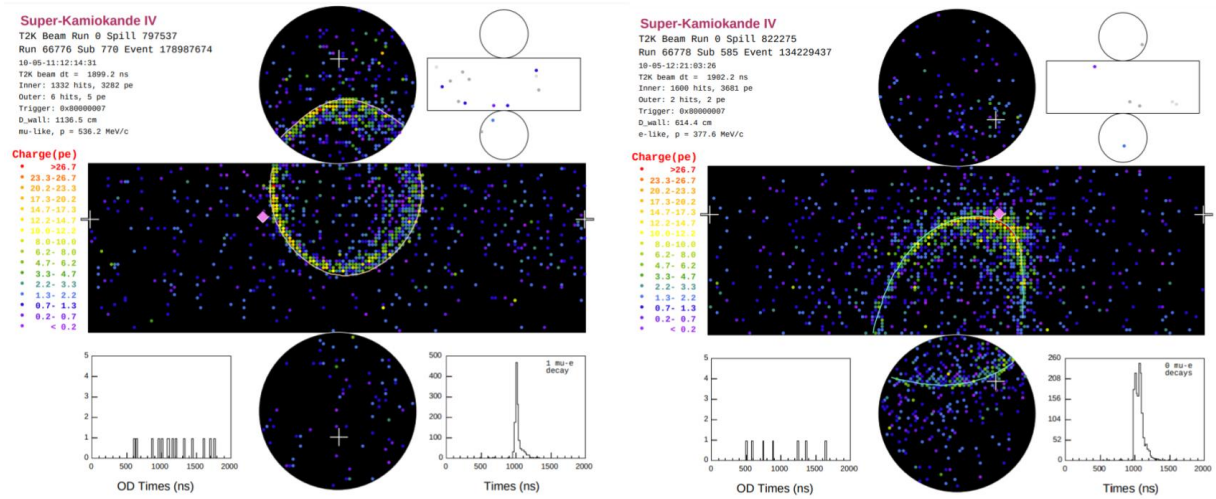

Figure 6.15: Example of reconstructed T2K events in the Super-Kamiokande detector for a muon-like ring (left) and electron-like ring (right). Taken from [52].

6.3 Important results

Only four years after its commissioning phase, the T2K experiment observed for the first time the appearance of ν_e in the ν_μ beam, thus confirming the non-zero value of the θ_{13} mixing angle [53]. A total of 28 ν_e events were detected with expected 4.92 ± 0.55 background events, which corresponds to a significance larger than 7σ. The reconstructed energy spectrum is presented in Fig 6.16 and gives a best fit value of $\sin^2 2\theta_{13} = 0.140^{+0.038}_{-0.032}$ in the hypothesis of normal hierarchy and $\sin^2 2\theta_{13} = 0.170^{+0.045}_{-0.037}$ for the inverted one.

Following this successful result, the T2K collaboration published the most precise measurement of θ_{23} mixing angle using this time the disappearance channel [54]. A campaign of precise measurements of various neutrino interaction cross-sections also lead to several publications [55][56].

Finally, the first significant constraints were put on the CP violation phase δ_{CP} with a 3σ confidence interval [57]. This motivates the new physics program of the T2K experiment focusing on the study of CP violation in

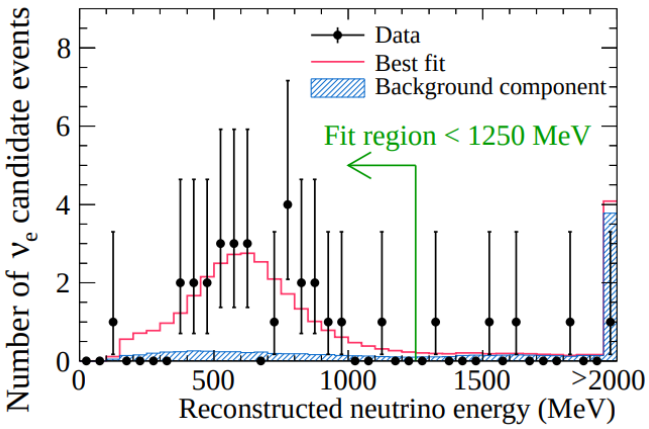

Figure 6.16: E_ν^{rec} distribution of the ν_e candidate events. The best fit is shown here for normal hierarchy. Taken from [53].

neutrino oscillation as well as providing more precise measurements of the θ_{23} and Δm^2_{23} parameters.

6.4 Upgrade general motivations

If the T2K experiment was supposed to acquire about 7×10^{21} Protons on Target (POT) between 2010 and 2020, the successful results discussed in the previous section motivated the T2K collaboration to extend the run up to 20×10^{21} POT with T2K-II. But in order to achieve even more precise measurements of mixing parameters and probe CP violation effects in neutrino oscillation, statistics must be largely improved. This motivated the upgrade of the neutrino production beam line to increase the rate of events, thus reducing the statistical errors. The systematic errors should also be reduced accordingly in order not to become limiting. The systematic errors lie, for the main part, in the neutrino flux estimation and the knowledge of neutrino interactions cross-sections. In both cases, the ND280 near detector complex can help reduce those systematics which is why it is also being upgraded for T2K-II. Fig 6.17 (Left) presents the expected sensitivity to CP violation in neutrino oscillation as a function of the true δ_{CP} value, assuming that the mass hierarchy is unknown, and for both the 7×10^{21} and 20×10^{21} POT data sets. An improvement via a reduction by a factor $2/3$ of the systematics errors is also assumed. It shows that in these conditions, the sensitivity reaches 3σ or higher for the oscillation parameter region favored by T2K latest results ($\delta_{CP} \approx -\pi/2$, and $0.43 < \sin^2 2\theta_{23} < 0.6$). The effect of the systematics reduction on the expected sensitivity is highlighted on Fig 6.17 (Right).

The following section will present in more details the upgrade of the ND280 detectors.

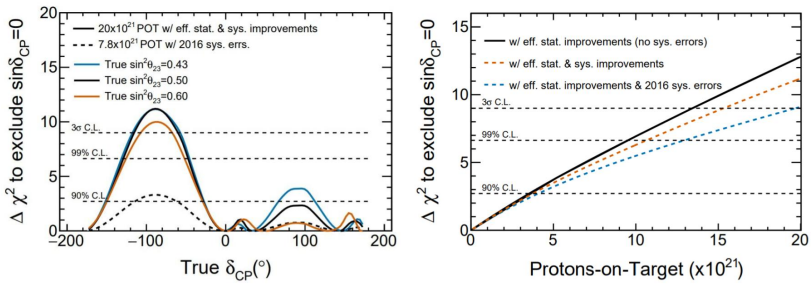

Figure 6.17: Left: Sensitivity to CP violation as a function of true δ_{CP} for the full T2K-II exposure of 20×10^{21} POT with a 50% improvement in the effective statistics, a reduction of the systematic uncertainties to $2/3$ of their current size, and with assumption of unknown mass hierarchy and the right is with known mass hierarchy; **Right:** Sensitivity to CP violation in neutrino oscillation with respect to POT and for different assumptions on the T2K-II systematic errors. Here a value of $\sin^2 2\theta_{23} = 0.5$ is supposed. Taken from [58].

6.5 Impact on ND280

When designing the T2K experiment, it was thought that the most limiting background would be the π^0 production which drove the efforts toward a precise reconstruction of the π^0 events with the PØD and ECAL. However, the progress that was made thanks to the new reconstruction algorithm implemented at SK [59] allowed for a more powerful and efficient background rejection from neutrino NC interactions with π^0 in the final state, thus making the PØD detector obsolete. Instead, the detector acceptance could be increased in order to be more similar to what happens in SK and reduce the corresponding systematics, and efforts could be made to further improve the PID performances.

The actual design of ND280 presents two main limitations when it comes to PID: limited phase space coverage and threshold of particle detection.

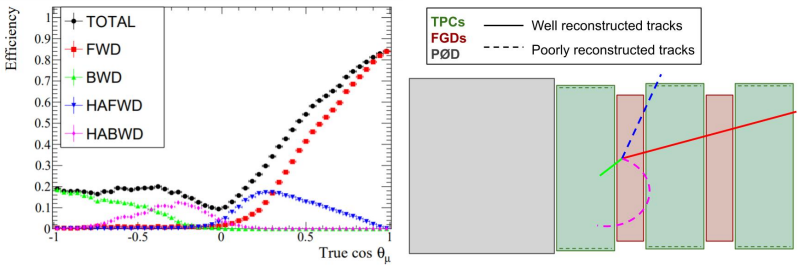

Figure 6.18: Left: Reconstruction efficiency of the muon tracks as function of angle against beam axis. Depending on the combination of sub-detectors, forward-going (FWD), backward-going (BWD) high-angle forward (HAFWD) and high-angle backward (HABWD) tracks are reconstructed. Taken from [58]; **Right:** Scheme of the ND280 trackers with examples of poorly reconstructed tracks.

The muon selection efficiency as a function of its angle with the beam axis is shown in Fig 6.18 (Left) for different types of tracks and it clearly highlights a degradation of performances for backward-going and high-angle tracks. This can be explained by the fact that such tracks, due to the geometry of the detector, do not leave enough signal in the TPCs to allow for a precise estimation of the particle momentum, or even pass selection criteria in terms of hit multiplicity. In an extreme case, a track could even fall entirely within a single FGD vertical scintillator bar so that tracking is simply impossible. Some examples of tracks that are poorly reconstructed at the moment are illustrated in Fig 6.18 (Right).

In addition, while muon penetration power ensures that they will leave long tracks in the detector, it is not the case for protons that are mostly low energetic when produced by neutrino interactions. At the moment, in order to be reconstructed, a particle has to depose energy in at least 2 FGD scintillator bars in both x and y direction which corresponds to traversing at least 38 cm of plastic. This imposes a detection threshold on the particle momentum of about 500 MeV while the proton spectrum generated with NEUT [60] starts peaking from 200 MeV as illustrated in Fig 6.19.

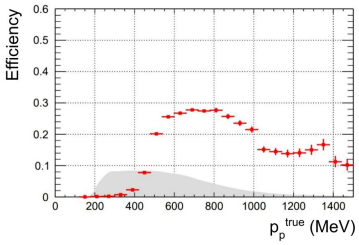

Figure 6.19: Proton reconstruction efficiency in ND280. The grey histogram corresponds to the spectrum of generated protons according to NEUT MC. Taken from [61].

In order to cope with these limitations, a new design of ND280 is proposed [61], leaving untouched the tracker (TPCs and FGDs) and downstream calorimeter systems but replacing the PØD by new horizontal target (Super-FGD or SFGD) and high-angle TPCs (HA-TPCs) as illustrated by Fig 6.21. Time Of Flight (TOF) detectors will encapsulate the SFGD and HA-TPCs although they do not appear on the scheme.

The SFGD will consist of a $182 \times 184 \times 56$ cm^3 volume made out of 1 cm^3 scintillator cubes individually read by WLS optical fiber. This fine granularity allows to reduce the detection threshold in addition to reconstruct the tracks in 3D. Moreover, these additional 2 tonnes of target material double the fiducial mass of ND280.

The TOF detectors, covering the entire upstream part of ND280, are made out of scintillator bars of 2 m long for a 1×12 cm^2 section and read by an array of MPPCs. TOF detectors will measure the crossing time of charged particles and help discriminating background events coming from the detector surroundings.

Finally, the horizontal HA-TPCs will be placed above and below the SFGD and increase the reconstruction efficiency of high angle or backward-going tracks. The reconstruction performances of the HA-TPCs should be similar to the ones of the existing TPCs. However, due to a lack of ASICs for the readout electronics, a larger pad segmentation is imposed.

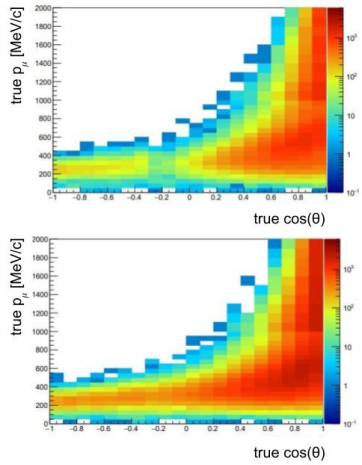

Figure 6.20: Phase-space of selected muons with the current (top) and upgraded (bottom) ND280. Taken from [61].

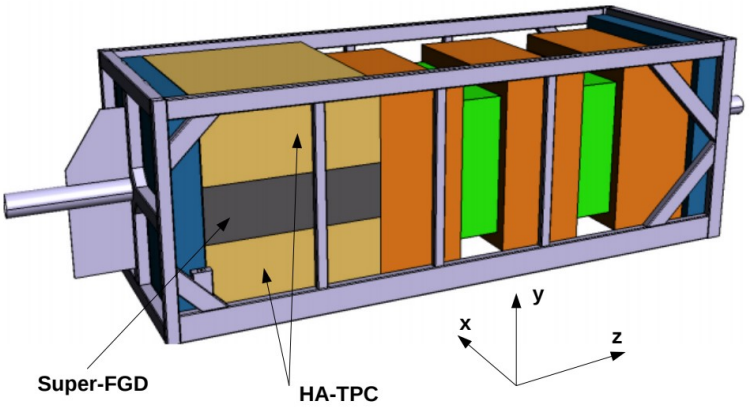

Figure 6.21: 3D model of the upgraded ND280. The tracker part is left untouched and PØD is replaced by the Super-FGD and HA-TPCs. TOF detectors are not shown. Taken from [61].

This motivated the use of resistive bulk-Micromegas to read the HA-TPCs: the spatial resolution degradation introduced by the larger pads is compensated by the charge spreading induced by the resistive layer. More details about the HA-TPCs design are given in the next section.

GEANT4 [28] simulations were conducted in order to estimate the performances improvements allowed by the upgraded ND280. Fig 6.20 highlights the increase in statistics of detected muons in the currently allowed phase-space as well as a larger acceptance for high angle tracks, backwards-going tracks and low momentum tracks.

6.6 HA-TPCs & ERAM modules

Each HA-TPC consist of two 90 cm drift length TPCs joined by a central cathode and read at both ends by 8 resistive bulk-Micromegas modules referred to as ERAM for Encapsulated Resistive Anode Micromegas as illustrated by Fig 6.22. The overall dimensions are of $2 \times 0.8 \times 1.8$ m^3 and the whole structure is placed under a 0.2 T magnetic field. The same gas mixture as the other TPCs is used which is a Ar-iC_4H_{10}-CF_4 (95:2:3) gas mixture, yielding a maximum electron drift velocity of 7.8 cm μs^{-1} for $E_{\text{drift}} = 275$ V/cm and a transverse diffusion coefficient $\sigma_T = 265\,\mu m/\sqrt{cm}$.

An ERAM module is a resistive 128 µm amplification gap bulk-Micromegas which anode is segmented into 36×32 pads of 10.09×11.18 cm^2. The resistive layer, which is a Diamond-Like Carbon (DLC) foil glued on top of the pads, basically acts as a 2D-RC network where the charge deposited by an electronic avalanche is governed by the 2D telegrapher's equations. For a point charge deposited at $t = 0$ in $r = 0$, the charge density ρ can be approximated by:

$$\rho(r,t) \propto \frac{RC}{4\pi t} e^{-r^2 RC/(4t)} \tag{6.3}$$

where R and C are the resistivity per unit area and capacitance respectively. In the context, the resitivity R is the one of the resistive layer while the capacitance is tuned by the glue thickness.

The addition of the resistive layer also allows to implement a new High Voltage powering scheme where the mesh is grounded while the resistive

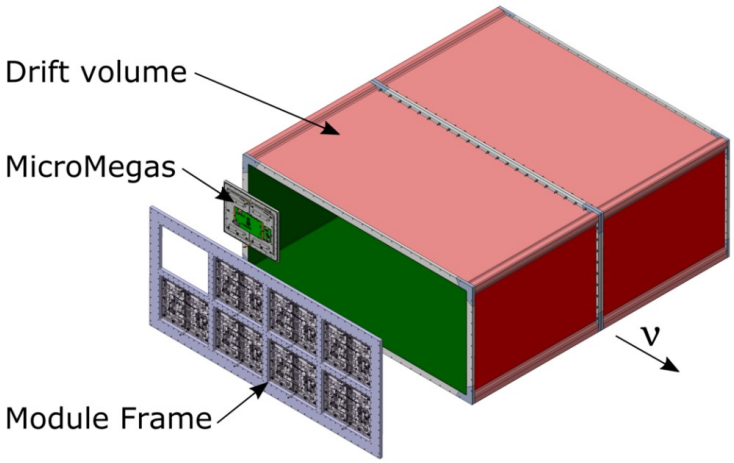

Figure 6.22: Schematic view of the HA-TPC.

anode is set to a positive amplification voltage. It provides more flexibility in the operation as the gain of each module can be adjusted without degrading the drift field uniformity.

The 32 modules will be produced by CEA in collaboration with the CERN. When I joined the T2K team for my PhD, the first prototype had just been developed and was about to be tested. I contributed to the development of the ERAM modules, particularly in the optimization of the DLC foil resitivity and glue thickness parameters before production. The evolution of the ERAM modules, from the first prototype to the final production design, is presented in the next chapter.

ERAM MODULES DEVELOPMENTS 7

Following the acceptance of the upgrade proposal and the publication of the T2K ND280 Upgrade Technical Design Report [61], the T2K collaboration entered an R&D phase aiming to develop and perfection the conceptualized detectors to production scale. Looking more specifically at HA-TPCs, it consists in testing and validating the use of the resistive bulk-Micromegas technology and making sure that the required performances can be achieved.

In this Chapter, I will retrace the evolution of the ERAM module illustrated in Fig 7.1, from its non-resistive predecessor to the final production version, highlighting my personal contributions. These developments are the result of a strong collaboration between the CEA Saclay, the CERN and the LPNHE.

Detector requirements

In order to ensure track reconstruction and PID performances at least as good as the TPCs already in use, the requirements on the detector are the following:

- A resolution on the particles momentum of about 10% at 1 GeV/c which, in terms of spatial resolution, translates to $\sigma_{r,\phi} < 800\,\mu m$
- A resolution on the particles dE/dx of 8%

7.1 Status when I started working on T2K

I joined the T2K team as a master student in April 2019. At this point, the data collected during a test beam at CERN in 2018 was being analyzed and the first prototype with the new pad plane geometry was being developed to be tested at DESY in June.

7.1.1 MM0 prototype and CERN 2018 test beam results

The so-called MM0 detector is the first step towards the ERAM modules: it is a resistive bulk Micromegas detector with the readout plane geometry and PCB of the already existing TPCs. It allows to test the production technique of the new resistive layer based on DLC and its performances by comparison with the TPCs already in use on T2K.

The MM0 module presents the following characteristics: it consists of a resistive bulk Micromegas with a readout plane of 34×36 cm^2 and an amplification gap of 128 µm. The active area is paved by rectangular pads of 7×9.8 mm^2 and is covered by a 2.5 MΩ/□ DLC foil. The glue thickness, controlling the capacitance of the resistive layer, is set to 200 µm.

For the test beam conducted at CERN in 2018 [62], the MM0 detector is installed inside the HARP field cage [63] and exposed to a beam

composed mainly of electrons, positrons, pions, protons and kaons. The analysis was conducted on the events trigged by either protons, pions or electrons and with a momenta of 0.8 GeV/c. The readout electronics used to collect the data is the same as the one already in use on the T2K TPCs, based on the AFTER chip [64] and the ARC card.

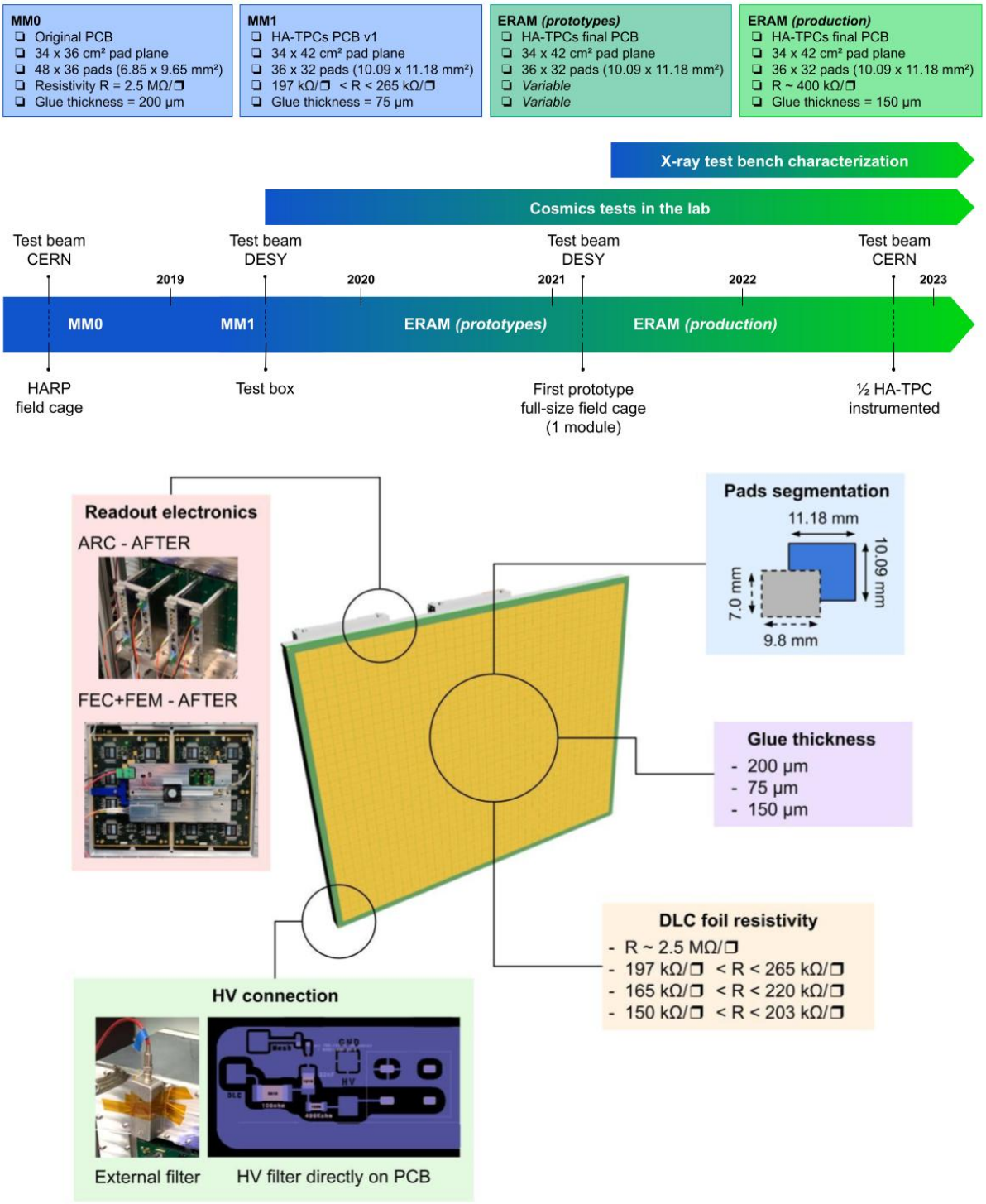

Figure 7.1: Schematic view of the evolution of the ERAM modules and its readout electronics. The main parameters of each versions are reported as well as the important phases of development. The main modifications that were implemented on the ERAM modules throughout its developments are highlighted on the bottom plot.

The charge spreading caused by the resistive layer is studied and the results are presented in Fig 7.2. It shows that the cluster multiplicity is predominantly larger than 1, but that more than 70% of the charge is collected by the pad with the largest signal, or main pad. In such conditions, the signals collected on the adjacent pads might present an amplitude too low to be correctly taken into account in the analysis. This points toward the fact that a lower resistivity will be needed to further increase the charge spreading for the next prototypes, especially considering that the pads will be larger.

Nevertheless, a spatial resolution of 300 µm was achieved reconstructing horizontal electron tracks crossing the TPC at a 30 cm drift distance, with a deposited energy resolution of 9% for a single module extrapolated to 7% with two modules. These results fully satisfies the detector requirements.

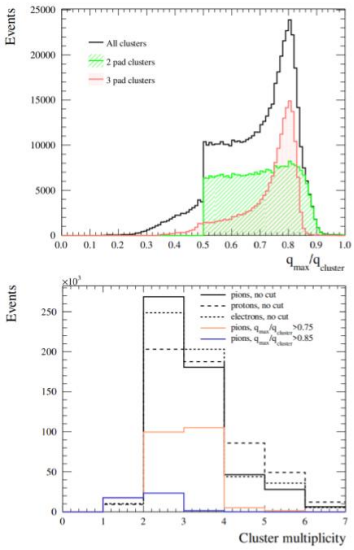

Figure 7.2: Top: Fraction of the cluster charge collected in the pad with the largest signal; **Bottom:** Pad multiplicity in the clusters. This histograms for pions, electrons and protons are normalized to the same area. Taken from [62].

7.1.2 Development of the MM1 prototype

Design

In light of these encouraging results, the first prototype with the final readout plane geometry was being assembled to be tested at the DESY test beam facility in June 2019. It is referred to as the MM1 module and presents the following characteristics: the active area is now 34×42 cm^2 and the pad size is increased to 10.09×11.18 mm^2. As presented in the previous chapter, the charge spreading can be approximated by a time dependant 2D Gaussian spread which standard deviation is given by:

$$\sigma(t) = \sqrt{\frac{2t}{RC}} \tag{7.1}$$

As such, the charge spread can be increased by reducing both the resistivity of the DLC foil and the capacitance which is inversely linked to the glue thickness. For the MM1 prototype, the resistivity specification is lowered down to 500 kΩ/□ and the glue thickness is set to 75 µm.

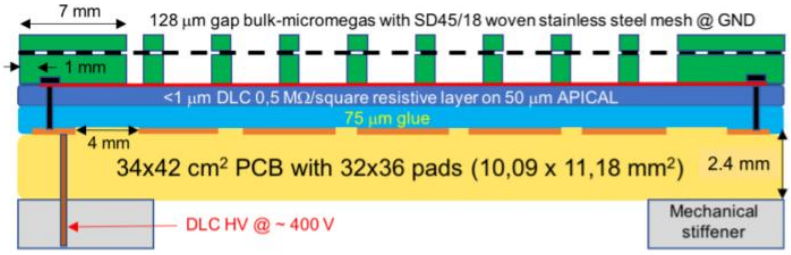

Figure 7.3: Schematic cross section of the MM1 detector and specifications.

Difficulties with DLC foils production

The resistivity of the DLC foil measured on the MM1 detector ranges between 197 and 265 kΩ/□ instead of the 500 kΩ/□ requirements. This observation lead to further investigations of the DLC foils production process and measurements to study the uniformity of the resistivity over the DLC foil.

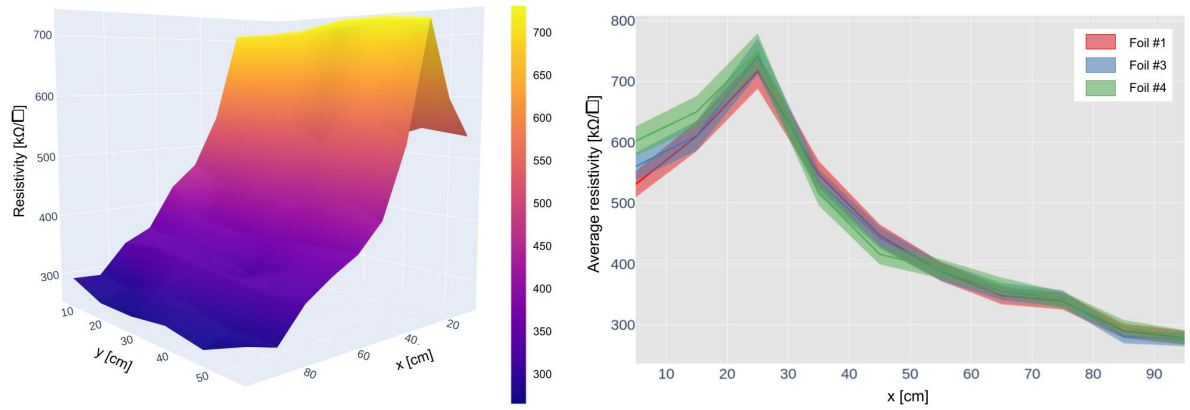

Figure 7.4: Left: Results of the resistivity measurements for foil #1; **Right:** Resistivity per square averaged along y as a function of the x position along the foil and for 3 different foils of the first production batch. The error band corresponds to the 4% error of the probe.

The resistivity measurements were made at CERN using a custom-made probe calibrated beforehand on DLC coated films of known area and resistivity. A calibration coefficient of 1.06 is estimated, yielding an uncertainty on the measured resistivity per square of 4%. The results of the measurements on one of the foil is shown in Fig 7.4 (Left): if the resistivity seems relatively uniform along the y direction, it varies from 220 to more than 700 kΩ/□ which is out of specification given at 500 kΩ/□ ± 150 kΩ/□. The measurements were reproduced on 3 different foils and the average along the y axis of the resistivity is reported as a function of the x position along each foil in Fig 7.4 (Right). The three foils presenting the exact same pattern indicates that the problem is more likely related to the manufacturing process of the DLC foils.

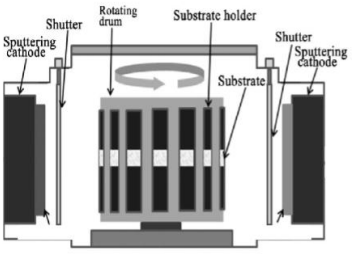

Figure 7.5: Schematic view of the DLC production process using sputtering technique.

The DLC foils used have been produced in Japan by the Be-Sputter company[1] using sputtering technique: the substrate is fixed onto a 4.5 m diameter rotating drum and placed inside a vacuum chamber filled with Argon gas. Two separate cathodes sputter Diamond like particles of molecular size onto the rotating substrate thus deposing successively very thin layers of carbon as illustrated by Fig 7.5. The resistivity of the produced foil decreases with the thickness of deposited material. This can explain the continuous variation along the x axis which is the direction coiled around the drum. As no other option was available to produce the DLC foils, the 34×42 cm^2 pieces needed to make the modules are carefully selected to minimize the resistivity variations.

Finally, it was observed that the resistivity measured on the detector after production was not consistent with the measurements made on the foil before assembly: the values were smaller by a factor 2. Further investigations showed that the 220°C annealing changed the resistivity of the DLC. The variations of the resistivity with the annealing time and temperature were carefully studied in order to use this property to try to compensate the initially out of specifications resitivities of the foils.

It is difficult to control the resistivity of the DLC foil as well as its uniformity as it strongly depends on the conditions during production. However precise measurements at different stages of production allowed to better understand the resistivity variations and limit the consequences on the detector production.

1: http://www.be-sputter.co.jp/

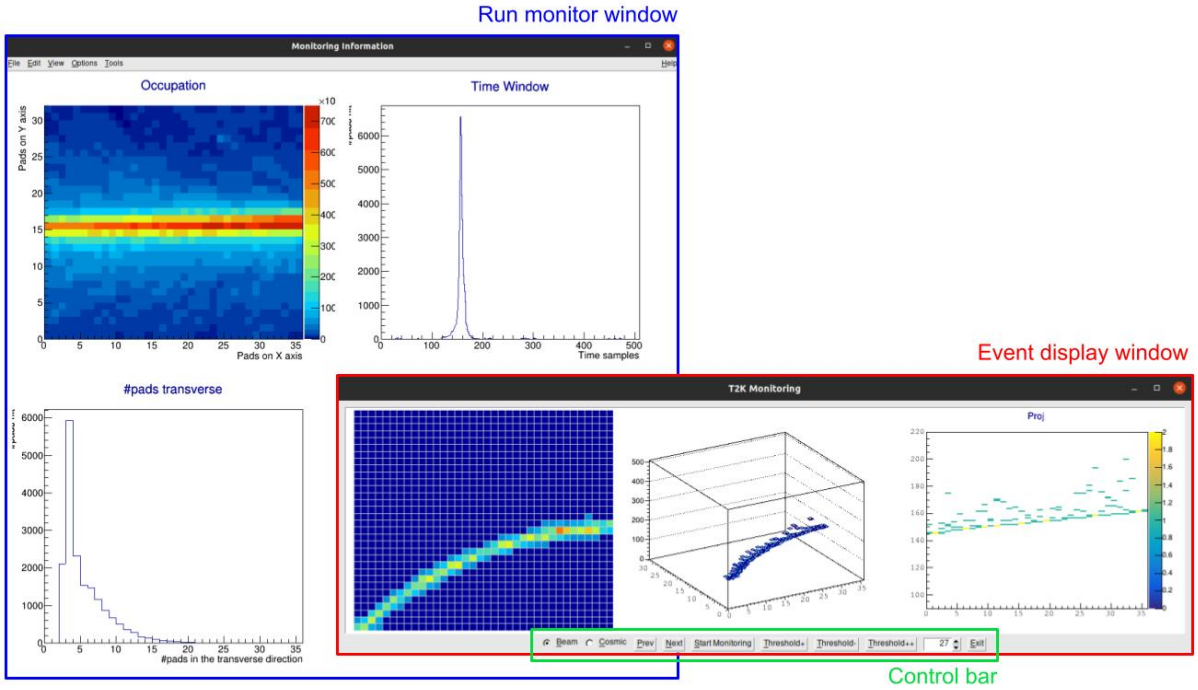

Figure 7.6: Screenshot of the monitoring software interface with the run monitor window highlighted in blue and the event display window circled in red. The monitoring software is controlled using the buttons and selectors on the control bar highlighted in green.

7.2 Development of a monitoring software

When I joined the T2K team in 2019, they were actively preparing for a test beam at DESY the next month to test the MM1 detector. However, although the readout electronics had not changed, the format of the produced binary data file was different due to the new PCB and mapping and they did not have any way to decode and analyze it. In addition, being able to visualize the events inside the TPC is very valuable during test beam: it allows to save a lot of time when aligning the beam or adjusting the acquisition parameters so that there are more time left for data taking. This is why I developed a ROOT/C++ based Graphical User Interface (GUI) to decode the binary files and display basic monitoring information even while the acquisition is running. If run on a pedestal file, this software can also draw the 2D map of the pedestals mean and Root Mean Square (RMS) to measure and control the noise.

Fig 7.6 shows an overview of the monitoring software interface which consists of the run monitor window and the event display window. The run monitor window shows raw information about the run that are accumulated when navigating through the events of the file. On the contrary, the event display window only shows information about the current event.

7.2.1 Run monitor window

Occupation plot (top left): 2D-histogram of the waveforms maxima. This plot is particularly useful to visualize the beam direction.
Time window plot (top right): Distribution of the time sample corresponding to the maximum of the waveforms. When looking at cosmics,

the time distribution has a step function shape which width corresponds to the total drift length while it is very peaked in case of a beam parallel to the readout plane. This plot is used to visualize the beam distance to the readout plane and eventually tune the acquisition sampling frequency and trigger delay settings to fit the entire time distribution into the acquisition window.
Cluster multiplicity (bottom): Depending on the mode selected on the control bar (Beam or Cosmic), the plot shows the distribution of the number of hit pads along each column or row. This plot might be the most affected by the absence of selection or pre-processing: for example if there are multiple tracks in the same event, the number of hit pads will be different from the cluster multiplicity which is the actual quantity of interest. In addition, in presence of a magnetic field for example, the definition of transverse direction might not correspond to either a row or column. This plot is thus to interpret with much care but can, if the conditions are met and enough statistics is accumulated, give a rough estimation of the cluster multiplicity and thus the charge spread.

7.2.2 Event display window

2D event display (left): 2D event display showing the projection of the track on the readout plane. Color shows the signal amplitude defined as the maximum of the waveform.
3D event display (middle): 3D scatter plot of the hits which coordinates (i, j, t) correspond to the column number [0, 35], the row number [0, 31] and the time sample corresponding to the maximum of the waveform [0, 511]. As for the 2D display, color shows the amplitude of the signal.
(x, t)-Projection (right): Projection of the 3D event display in the (x, t) plane where the x axis would usually be the beam direction in case of beam test.
Control bar: The possible actions are the following:

- Mode selector: in *Beam* mode the tracks are expected to be horizontal so that the multiplicity shown on the bottom plot of the Run monitor window is computed on the columns, while in *Cosmic* mode the tracks are expected to be mostly vertical and the multiplicity is computed on the rows.
- *Prev/Next* buttons: allows to navigate through the events
- *Start Monitoring* button: automatically accumulate events at the rate of 1 Hz. When clicked, the button changes to *Stop monitoring* and another click stops on the current event.
- *Threshold+/Threshold−* buttons: By default there is no selection applied but an amplitude threshold can be set by clicking those. The threshold value changes by increment of 10 ADC.
- Event number: the text box displays the event number of the current event. It can also be used to manually enter an event number to jump to. In this case the events in between will not be accumulated in the Run monitor window plots.
- *Exit* button: close both windows.

This monitoring software proved to be very helpful during the test beam campaign in 2019 as well as for the tests in the lab ever since. It was updated to also work with the new readout electronics in 2020 and additional features were added like the possibility to display the

waveform when clicking on a pad of the 2D event display. In addition, using the layer of code that decodes the binary files, I also developed the first version of the ROOT file converter that made it possible to provide the collaboration with data in an exploitable format.

7.3 Test beam campaign at DESY

7.3.1 Experimental setup

The test beam took place in DESY Test beam area T24.1 and lasted 2 weeks. As the prototype of the 1 m drift length field cage was not finalised, the MM1 detector was tested using a 15 cm gas chamber which 3D model is shown in Fig 7.31. It is the same test box as the one used for the cosmic bench in the lab (see Sec 7.5). The TPC was installed into a superconducting magnet, usually operated at either 0 T or 0.2 T, and exposed to an electron beam with an adjustable momentum ranging from 1 to 6 GeV/c. Fig 7.8 shows the experimental setup after installation. The objective of this test was to study the detector performances as a function of the drifting length, amplification voltage and angle of the tracks.

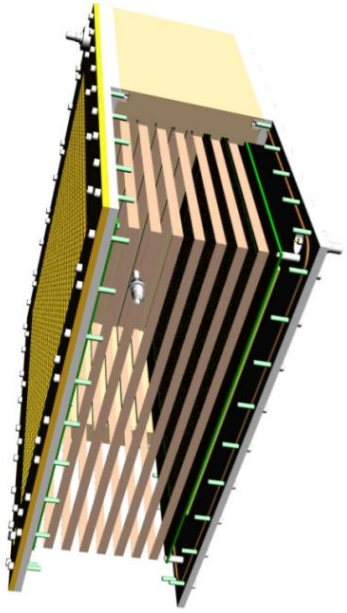

Figure 7.7: CAD model of the field cage used on the test bench.

I was present for the detector installation and actively contributed to the data taking during the first week. I was also strongly involved in the data analysis that followed. All things considered the test beam was very successful as we were able to quickly install the detector and acquire data. The only complication happened on the night of June 12th, the detector was no longer stable and could not hold the amplification high voltage. It also presented a 1.4 mA current indicating that a dust was probably creating a shortcut with the grounded micromesh. Thanks to the monitoring software we were able to locate the dust which presented itself as a heat spot on the occupation plot. The detector was flushed while gentle shocks were applied at the identified position and the detector was running again at 12:00 a.m the next day.

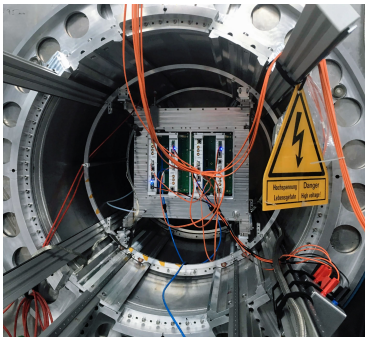

Figure 7.8: Photograph of the TPC installed inside the magnet in the T24 test beam area at DESY.

7.3.2 Definitions for data analysis

The pad plane is oriented with its longer side along the beam direction noted x. A cluster is defined as a group of hit pads along the direction transverse to the track, ie. along the column in this particular case. In the case of cosmics for example, the tracks are mostly vertical so that the clusters are defined for each row. Note that this definition no longer holds for high angle tracks as the transverse direction is neither along rows or columns. Several options of more complex patterns have been tested and can be optimized depending on the angle of the track [17] but for this analysis, unless stated otherwise, tracks with a small angle are selected so that the clusters are defined for each column.

An example of cluster is highlighted in Fig 7.9 with the corresponding waveforms. The pad with the highest signal, referred to as *leading pad*, would be the pad directly underneath the avalanche while the *neighbouring pads* receive signal a few time bins later via the charge spread into the resistive layer, thus explaining the different shapes of the waveforms.

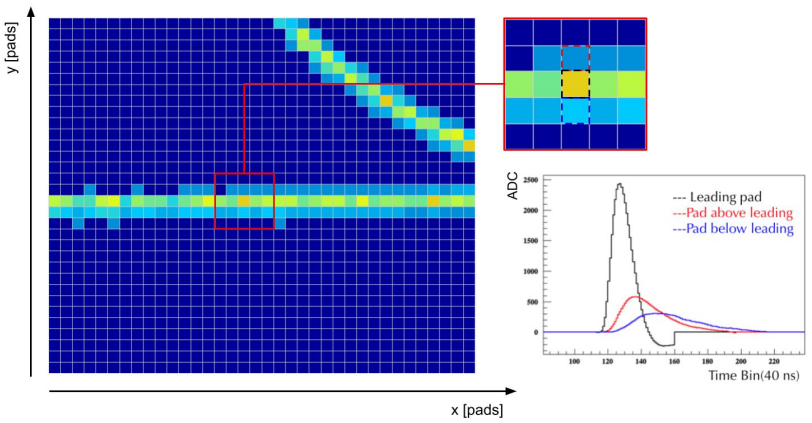

Figure 7.9: Example of a track and waveforms to illustrate the definition of quantities necessary for data analysis.

This vision is a bit simplifying and the definition of leading pad can be ambiguous when two pads present a similar amplitude and time, indicating that the avalanche was probably in between the two pads.

The use of linear preamplifiers in the readout electronics ensures that the maximum amplitude of a waveform is proportional to the charge detected on the corresponding pad. The charge collected on the pad identified by its coordinates (i, j) is noted $Q_{i,j}$ while the charge of the cluster is computed at

$$Q_{\text{cluster } i} = \sum_j Q_{i,j} \tag{7.2}$$

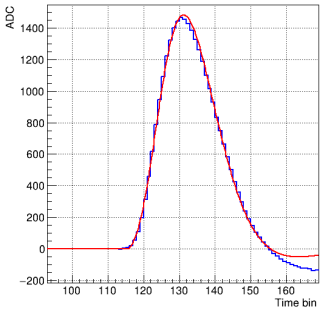

Figure 7.10: Example of fitted leading pad waveform.

The time $t_{i,j}$ associated to the pad signal is defined as the time that yields the maximum amplitude of the waveform. The charge $Q_{i,j}$ and time $t_{i,j}$ can be estimated

- either as the maximum of the waveform histogram and the bin associated bin number respectively,
- or by fitting the waveform to then extract the maximum of the fitted shape for the charge and x value corresponding for the time.

The fit model is different depending if the pad is a *leading pad*, in which case the signal shape is dominated by the electronics response $R(t)$, or if the pad is a *neighbour* and the signal is described by the convolution of the electronic response with the derivative of the charge spread $Q(t)$. At that time, the model for the electronic response was phenomenological and based on Gumbel functions:

$$R(t) = A \exp\left(-\exp\left(\frac{t - t_{\max} - a}{\tau_1}\right)\right) \exp\left(\frac{t - t_{\max}}{\tau_1}\right) \sin\left(\frac{t - t_{\max}}{\tau_2}\right) \tag{7.3}$$

where A is an amplitude factor, $t_{\max}$ the time of the maximum, and a, τ_1 and τ_2 parameters. Investigations were conducted later on to improve the electronic response parametrisation and are detailed in Sec 7.4.2. The charge spread is derived from the Telegraphic equations integrated over

the pad area:

$$Q(t) = \frac{Q_0}{4}\left[\mathrm{erf}\left(\frac{x_{\mathrm{high}} - x_0}{2\sigma(t)}\right) - \mathrm{erf}\left(\frac{x_{\mathrm{low}} - x_0}{2\sigma(t)}\right)\right] \left[\mathrm{erf}\left(\frac{y_{\mathrm{high}} - y_0}{2\sigma(t)}\right) - \mathrm{erf}\left(\frac{y_{\mathrm{low}} - y_0}{2\sigma(t)}\right)\right] \quad (7.4)$$

where Q_0 is the charge deposited by the avalanche in (x_0, y_0), x_{high} x_{low}, y_{high} and y_{low} are the coordinates of the pad borders, and $\sigma(t)$ characterizes the resistive layer and is given by:

$$\sigma(t) = \sqrt{\frac{2t}{RC}} \quad (7.5)$$

The avalanche position (x_0, y_0) is extracted from the track reconstruction and can thus be unknown at an early stage of the analysis when trying to extract $Q_{i,j}$ and $t_{i,j}$. In this case, as a first estimation, one can either replace (x_0, y_0) by the coordinates of the center of the leading pad, or simply fit all signals as if they were leading pads. The latter is used in the following discussion.

For the analysis presented here, we select the single event horizontal tracks crossing the full detector. A cut on the cluster multiplicity, optimised for each amplification voltage, allows to reject multiple track events where the tracks are parallel and cannot be separated. Examples of such events are illustrated in Fig 7.11.

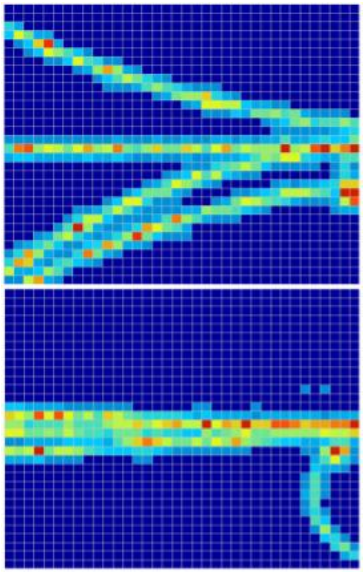

Figure 7.11: Example of rejected events.

7.3.3 Charge spread

As a reminder, we want to spread the charge onto several pads transversely to the track direction in order to reconstruct the hit position using the Pad Response Function approach (developed in the following section) resulting in a spatial resolution better than what should be possible with the given segmentation. The charge spreading must be optimized to have both large cluster multiplicities and signal amplitudes.

Fig 7.12 shows both the fraction of the cluster charge collected by the leading pad (Left) and the cluster multiplicity as a function of the amplification voltage. It shows that almost all clusters have a multiplicity of 3 or more, which is an improvement compared to the MM0 even if the pads are now larger. Furthermore, Fig 7.12 (Right) proves that, in addition

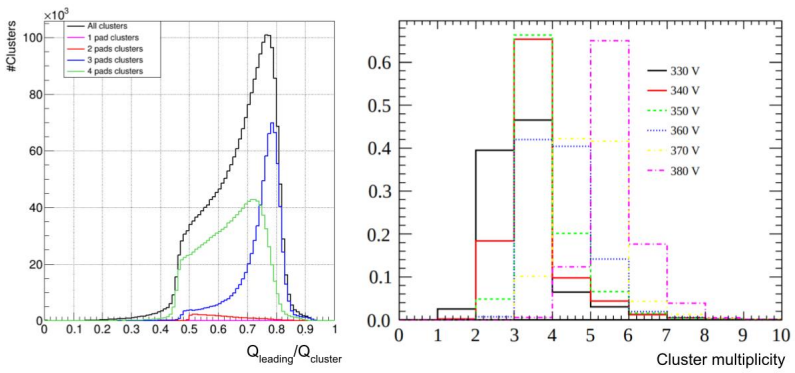

Figure 7.12: Left: Fraction of the cluster charge collected by the leading pad for an amplification voltage of 360 V and a peaking time of 412 ns; **Right:** Cluster multiplicity for different voltages applied on the DLC.

to the resistivity of the DLC, the amplification voltage can be used to tune the cluster multiplicity and improve the spatial resolution. However, it is not recommended to operate the detectors at high gain in order not to compromise the high voltage stability: for reference, the nominal gain of the actual T2K TPCs is $G \sim 1500$ obtained with an amplification voltage of $V_{\text{mesh}} = 350\,\text{V}$.

Finally, Fig 7.13 shows the distributions of $Q_{i,j}$ for various rows, in particular $j = 15$ in blue is the row directly under the beam direction. It shows that the amplitude of the signal of leading pads peaks around 1000 ADC, while the amplitude of spread signal, represented in red and green, peaks below 500 ADC.

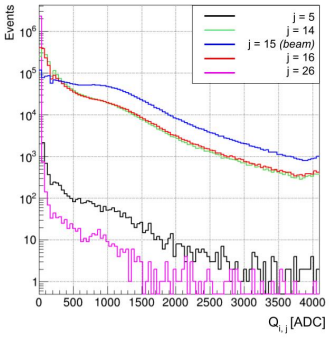

Figure 7.13: Distribution of pad amplitudes separated for different rows. The row $j = 15$, being directly underneath the beam direction, corresponds to leading pads.

7.3.4 Track reconstruction and spatial resolution

The first approach to reconstruct the avalanche position based on multiple signals $Q_{i,j}$ would be a weighted mean and is generally referred to as the *Center of Charge* (CoC) method. It consists in computing the barycenter of the coordinates of the pads in the cluster, using the collected charge as weight. However, this method is all the more precise that many pads are considered and that the pads are small. In our specific case, with a cluster multiplicity of about 3 and pad dimensions of the order of the centimeter, it was demonstrated that it is not the best option [65].

Instead, we use the *Pad Response Function* (PRF) method which uses data to iteratively calibrate the charge spread in the cluster as a function of the avalanche. It is defined as follows:

$$PRF(y_{i,j} - y_{\text{track},i}) = Q_{i,j}/Q_{\text{cluster } i} \tag{7.6}$$

where $y_{i,j}$ is the y coordinate of the center of the pad (i, j) and $y_{\text{track},i}$ is the reconstructed position of the track in column i. The PRF is parametrised empirically by a function proposed in [66]:

$$PRF(y, \Gamma, \Delta, a, b) = A \times \frac{1 + a_2 y^2 + a_4 y^4}{1 + b_2 y^2 + b_4 y^4} \tag{7.7}$$

where A is an amplitude factor and the four parameters a_2, a_4, b_2 and b_4 can be expressed as a function of more physical parameters such as the FWHM noted Γ, the base width Δ and two scale parameters a and b:

$$\begin{aligned} a_2 &= -4(1+a)/\Delta^2 \\ a_4 &= 4a/\Delta^2 \\ b_2 &= \frac{4[1-b-2(1+a)]}{\Delta^2} + \frac{8a\Gamma^2}{\Delta^4} \\ b_4 &= 16/\Gamma^4 \end{aligned} \tag{7.8}$$

These parameters are determined using an iterative process based on data to better describe the charge spread in the conditions of data taking. Once the PRF has been calibrated, the track position in each cluster is obtained by minimizing the following χ^2_i:

$$\chi^2_i = \sum_{j \text{ in cluster } i} \left[\frac{Q_{\text{cluster } i} \times [Q_{i,j}/Q_{\text{cluster } i} - PRF(y_{i,j} - y_{\text{track},i})]}{Q_{\text{cluster } i}\sqrt{Q_{i,j}} + Q_{i,j}\sqrt{Q_{\text{cluster } i}}} \right]^2 \tag{7.9}$$

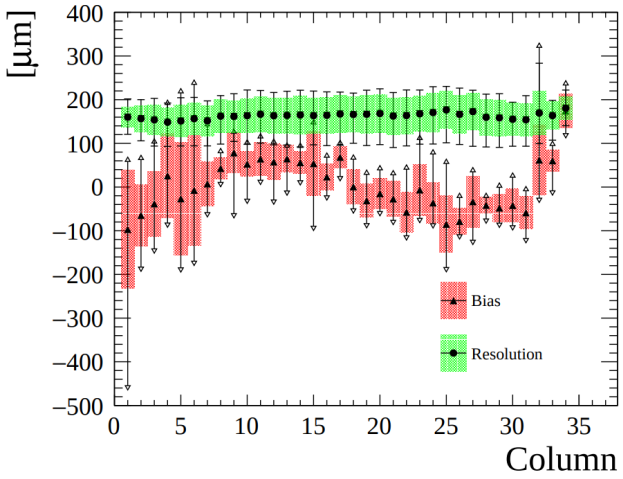

Figure 7.15: Spatial resolution and bias fluctuations as a function of the column number i. Markers represent the mean value, filled areas the RMS and error bars the minimum and maximum values.

PRF calibration

Iteration 0: The track position reconstructed in cluster i $y_{\text{track},i}$ at iteration 0 is taken as the result of the CoC method. The following steps are then iterated until the track fit quality no longer improves (usually 5 to 10 iterations):

1. For each pad, fill the 2D-histogram $(y_{i,j} - y_{\text{track},i}, Q_{i,j}/Q_{\text{cluster }i})$ illustrated in Fig 7.14.
2. Fit the 2D-histogram with the model given in Eq 7.7 to parametrise the PRF
3. Obtain new values of $y_{\text{track},i}$ by minimizing the χ^2_i given in Eq 7.9

Several variations have been investigated, such as using the result of a global fit to the track for the first estimation of $y_{\text{track},i}$, or profiling the 2D-histogram before fitting with the PRF model, but no major effect was observed.

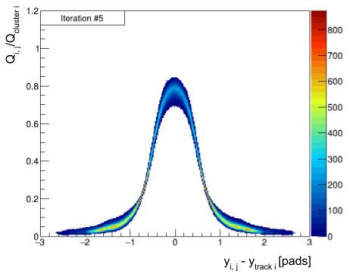

Figure 7.14: 2D histogram $(y_{i,j} - y_{\text{track},i}, Q_{i,j}/Q_{\text{cluster }i})$ of the 5$^{\text{th}}$ iteration of the PRF calibration.

The distribution of the residuals between the reconstructed position in cluster i_0 and the position obtained from a global fit to the reconstructed positions of all the clusters of the track with $i \neq i_0$ is fitted by a Gaussian which mean corresponds to the bias of the measurement while the standard deviation is the spatial resolution.

The results obtained for the horizontal tracks are presented in Fig 7.15. Individual PRFs are calibrated for each column in order to account eventual charge spread variations due to the non-uniformity of the DLC foil. A spatial resolution better than 200 µm is obtained, which is an improvement compared to the 300 µm obtained with the MM0 prototype and fully satisfies the detector requirements that impose a spatial resolution better than 800 µm.

Because of gas diffusion effects, the spatial resolution is expected to be degraded for longer drift distances or without magnetic field (detailed in Chapter 1). A drift distance scan is performed and validates the detector performances for all measured drift length. However the field cage being only 15 cm long, a similar study will have to be conducted with a 1 m drift length field cage to match the HA-TPCs design.

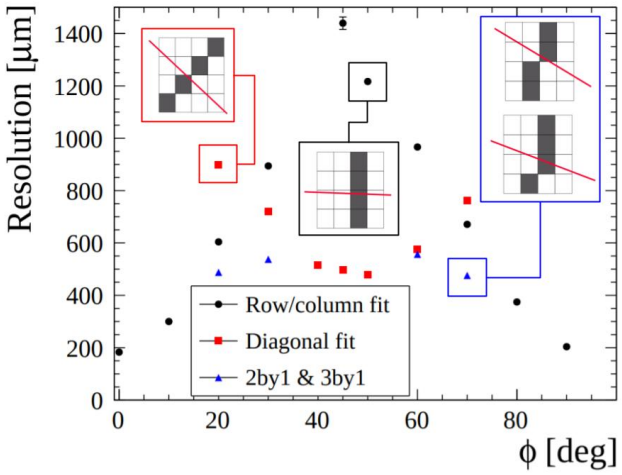

Figure 7.16: Spatial resolution as a function of the track angle using various cluster definitions for the track reconstruction.

Finally, the spatial resolution of high angle tracks is also expected to be worse than horizontal tracks, which is simply due to the fact that the PRF reconstruction method heavily rely on the definition of the clusters. Fig 7.16 shows the result of the spatial resolution as a function of the track angle: without any adjustment the spatial resolution falls out of requirements for track angles ranging between 30° and 70° but implementing new cluster definitions allows to obtain a spatial resolution below 600 µm for all angles.

The PRF method used here allows to reconstruct the avalanche y coordinate assuming that the x coordinate is at the center of the pad. In all cases, the track obtained spatial resolution is within requirements. Nonetheless, there is room for improvements to reconstruct both avalanche coordinates ($x_{\text{track } i,j}$, $y_{\text{track } i,j}$) by developing a reconstruction algorithm based on the current PRF method and generalized to 2D. This is all the more important for high angle tracks where the hypothesis that the x coordinate is at the center of the pad becomes debatable. Simulations were conducted in order to obtain a better 2D description of the charge spread in the resistive layer and help building this 2D-reconstruction algorithm. This is presented in Chapter 8.

Concerning the biases, it is not yet understood why they are so large or distributed this way. More recent analysis from another test beam points towards the direction of $\vec{E} \times \vec{B}$ effects that distorts the tracks following an S-shape. However such effect depends on the drift length and is not expected to be so pronounced with only 15 cm. No conclusion could be drawn for the MM1 prototype but the biases of other modules tested more recently are well under control.

7.3.5 Other results

To validate PID performances of the detector, the resolution on the dE/dx measurements is also studied. The truncated mean method is used to estimate the energy loss along a given track: the cluster charge $Q_{\text{cluster } i}$ are sorted in ascending order and a fraction of the lowest charges are kept for the analysis in order to reject eventual δ-rays or high-energy events due to ionization fluctuations as discussed in Chapter 1. In this

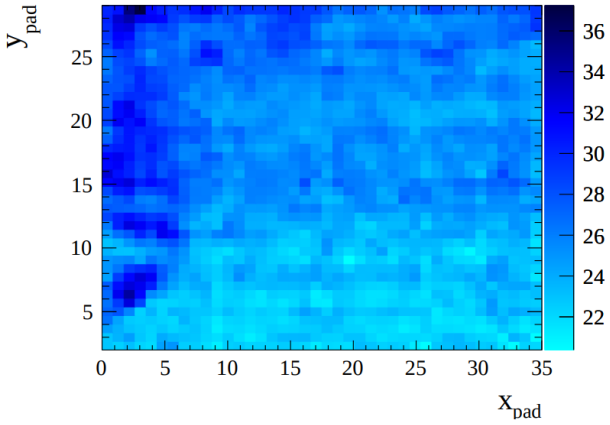

Figure 7.17: RC map [ns/mm^2] obtained from a fit to the waveforms.

analysis, a truncation fraction of 0.7 is used yielding an energy resolution better than 9%.

Once the tracks are reconstructed and the avalanche position $y_{\text{track } i}$ are known, a fit to the waveform as developed in Section 7.3.2 allows to extract the local RC value of the DLC foil. The obtained RC map is shown in Fig 7.17 and the variations observed are consistent with the resistivity measurements made at CERN and presented in Fig 7.4.

Despite some complications with the production of the DLC foils, this test beam campaign allowed to validate the performances of the detector against the requirements imposed by the T2K experiment. Yet, we expect that even better results could be achieved if the cluster multiplicity was increased to 4-5 so the RC parameter of the next prototypes is decreased in order to further spread the charge.

The monitoring software, that ensured the good quality of the recorded data, as well as my contributions to the production of the ROOT data file and their analysis were essential to obtain the results mentioned above. The results of this detector characterization have been published and can be found here [17].

7.4 A new readout electronics

Up to now, the prototypes were read using a versatile electronic front-end card called ARC (Another Readout Card) [67] developed in the framework of the Harpo project [68]. The ARC supports the AFTER chip [64], the AGET chip [69] and the ASTRE chip [70]. As illustrated in Fig 7.18 (top), 4 ARC cards are plugged vertically to read a module. However, due to the limited space allowed for the HA-TPCs electronics, a new design is proposed where the readout cards are directly plugged flat against the detector back as shown in Fig 7.18 (bottom).

Figure 7.18: Photographs of the readout electronics used for T2K TPCs: the ARC cards, versatile card with AFTER chips (top), and the new design for the HA-TPCs using FEC cards synchronized by a FEM (bottom).

7.4.1 Description

The new readout electronics is based on the same chip AFTER operated at a sampling frequency of 25 MHz, a peaking time of 412 ns and gain of 120 fC. Each ASIC reads 72 electronic channels connected to an array of

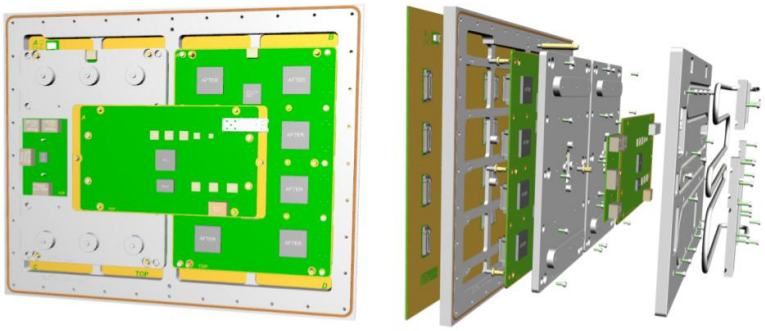

Figure 7.19: CAD of the electronics mounted on the detector (left) and in exploded view (right) to also visualise the shielding and cooling system.

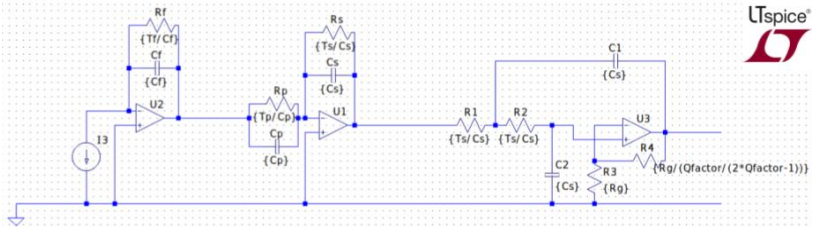

Figure 7.20: Implementation of an ideal AFTER chip in LTspice®. The values of the various components are fixed to those of the chip: $C_f = 200\,\text{pF}$, $C_p = 1.8\,\text{pF}$, $C_s = 1\,\text{pF}$, $R_g = 100\,\text{k}\Omega$, $T_f = 50\,\mu\text{sec}$, $T_p = 50\,\mu\text{sec}$, $T_s = 220\,\text{n sec}$, $Q \sim 2/3$.

9×8 pads. A Front End Card (FEC) hosts 8 AFTER ASICs and performs the digitization of the signal. Two FECs are needed to read a single module and are directly plugged against the detector PCB as illustrated in Fig 7.19. Finally, a Front End Mezzanine (FEM) comes on top of the two FECs and synchronizes signal digitization with a master clock. Shielding covers are designed to allow the electronics to be placed and operated, along with the TPCs, inside the magnetic field. The temperature of the electronics is kept under control thanks to a cooling system circulating water throughout copper pipes in a close proximity to the ASICs. Finally, the data coming from all 16 ERAM modules of a HA-TPC are send to the Trigger and Data Concentrator Module (TDCM) through an optic fiber.

As the first prototypes of the FEC and FEM cards were being produced, I adapted the monitoring software to this new readout so that, after being validated on a dedicated test bench, the new electronics could be tested on the detector with cosmics. The possibility to test the full data acquisition (DAQ) system (ERAM + FEC + FEM + TDCM) in the lab helped to fix some stability issues in the readout card firmware at early stages of development.

7.4.2 Calibration and new model

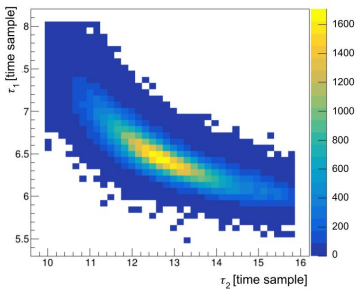

Figure 7.21: Correlations between the τ_1 and τ_2 parameters of the former electric shape $R(t)$.

As previously developed in Section 7.3.2, the waveforms are fitted by the convolution between the electronic response and a model for the charge deposition and spreading in the resistive layer. The objective here is to decorrelate electronic effect from the charge spread that needs to be studied in details to improve the track reconstruction. However, until now the electronic model was an empirical Gumbel based function with 5 parameters that were neither fixed nor constrained by electronic settings considerations and that present correlations as illustrated by Fig 7.21. As a result, the physical parameters such as RC, x_0 or y_0 extracted from the fit could easily be affected by fluctuations in the electronic shape that should be fixed. With the new readout electronics came the opportunity to find a new modelisation of the electronics response, parametrised by

quantities that can be physically constrained and allowing to decorrelate the charge spread.

A new model $R_{\mathrm{AFTER}}(t)$ is proposed to describe the electronic shape based on the computation of the analytical response to a Dirac function of a simulated AFTER chip (ideal components) using LTspice® as shown in Fig 7.20:

$$R_{\mathrm{AFTER}}(t) = \frac{C_p}{C_f C_s}\frac{w_s^2}{2Q-1}\left[e^{-w_s t}+ e^{-w_s t/2Q}\left(\sqrt{\frac{2Q-1}{2Q+1}}\sin\left(\frac{w_s t}{2}\sqrt{4-\frac{1}{Q^2}}\right)-\cos\left(\frac{w_s t}{2}\sqrt{4-\frac{1}{Q^2}}\right)\right)\right] \tag{7.10}$$

where A is an amplitude factor and depends on the input signal, C_p, C_f and C_s are fixed to the values of the chip components so that the only remaining parameters are w_s and Q which are expected to depend only on the acquisition settings (sampling frequency, gain and peaking time).

To test this model, calibration data sets are produced using the FEM internal pulser with peaking times of 200 and 412 ns, various amplitudes, and with or without the detector connected. The pulses are fitted using $R_{\mathrm{AFTER}}(t)$ first to ensure that this new model correctly describes the electronic shape, but also to extract the Q and w_s parameters values and study the uniformity of the electronic responses between ASICs. Ideally, what we hope is that w_s and Q can be fixed independently from the amplitude of the input signal so that, when fitting the waveforms in the analysis, the amplitude factor can be taken into account in the charge deposition function and the electronic shape is completely determined.

An example of fitted pulses is shown in Fig 7.22 for each of the 16 ASICs and the obtained results are presented in Fig 7.23. The top plots show, for Q and w_s respectively, the 2D-histogram of the fit χ^2/ndof, where ndof stands for number of degrees of freedom, as a function of the parameter value. In both cases, it shows that the parameters fit values are distributed around a center value with a cluster around $\chi^2/\mathrm{ndof} \sim 1$, indicating that the $R_{\mathrm{AFTER}}(t)$ analytical shape describes well the electronic response with a fixable parametrisation. It yields $\sigma(Q)/Q \sim 4\%$ and $\sigma(w_s)/w_s \sim 2\%$ which is consistent with the tolerance specified on the chip components. The middle plots show Q and w_s distributions separately for each ASIC. These distributions are each fitted by a Gaussian which mean and standard deviation are presented in the bottom plots to show the dispersion between ASICs which is estimated to be lower than 1%.

This study allowed to validate both the consistency of the response of the new readout electronics as well as the analytical model to describe it. This new electronic shape is now used in the analysis and strongly improves the convergence of the fit to the waveforms.

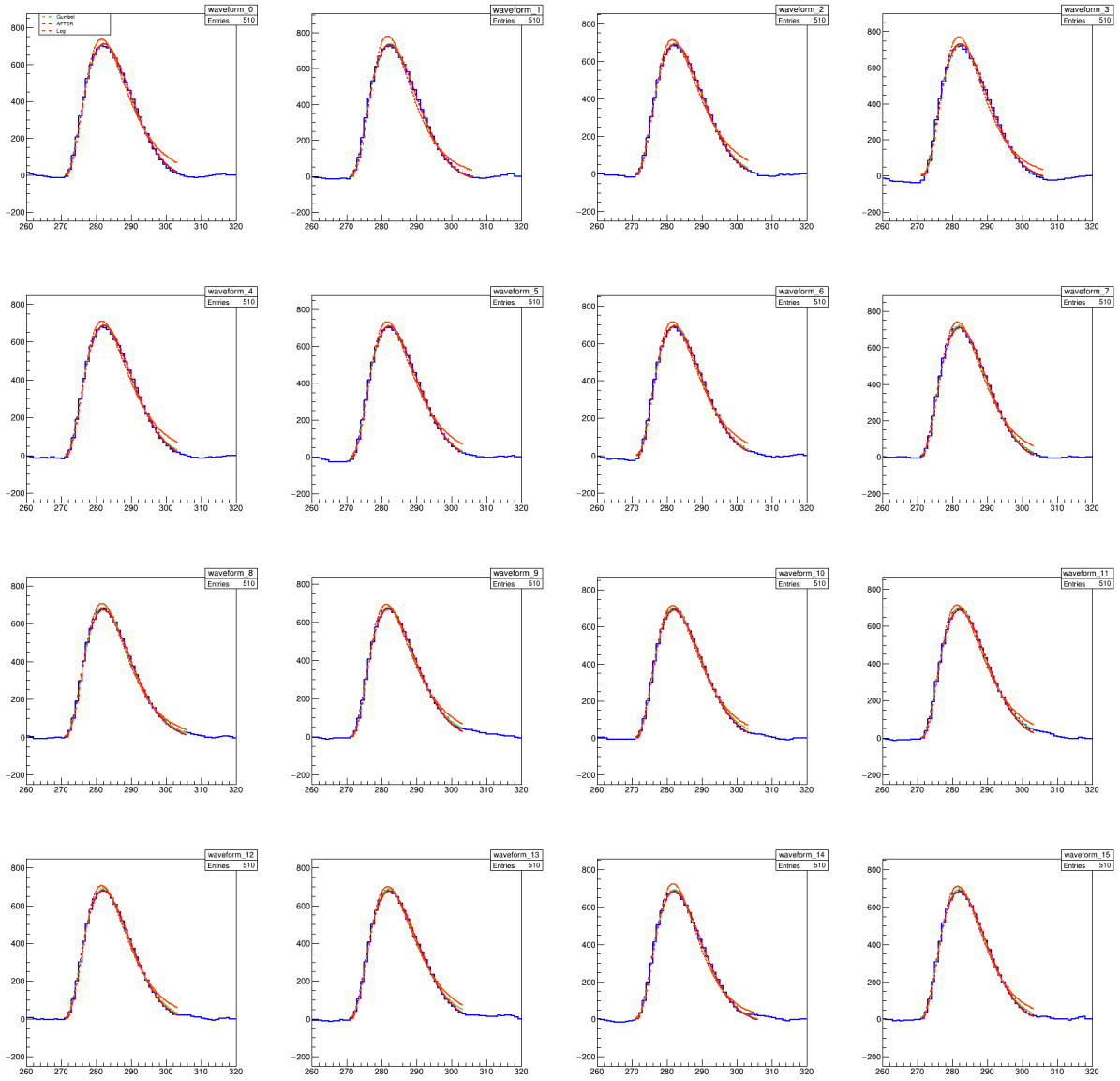

Figure 7.22: Calibration pulses fitted by different electronic shapes: the empirical Gumbel-based model (in green), the new analytical model based on the simulation of the chip AFTER (in red) a log-normal distribution model (in orange) which was abandoned because the fit quality was worse.

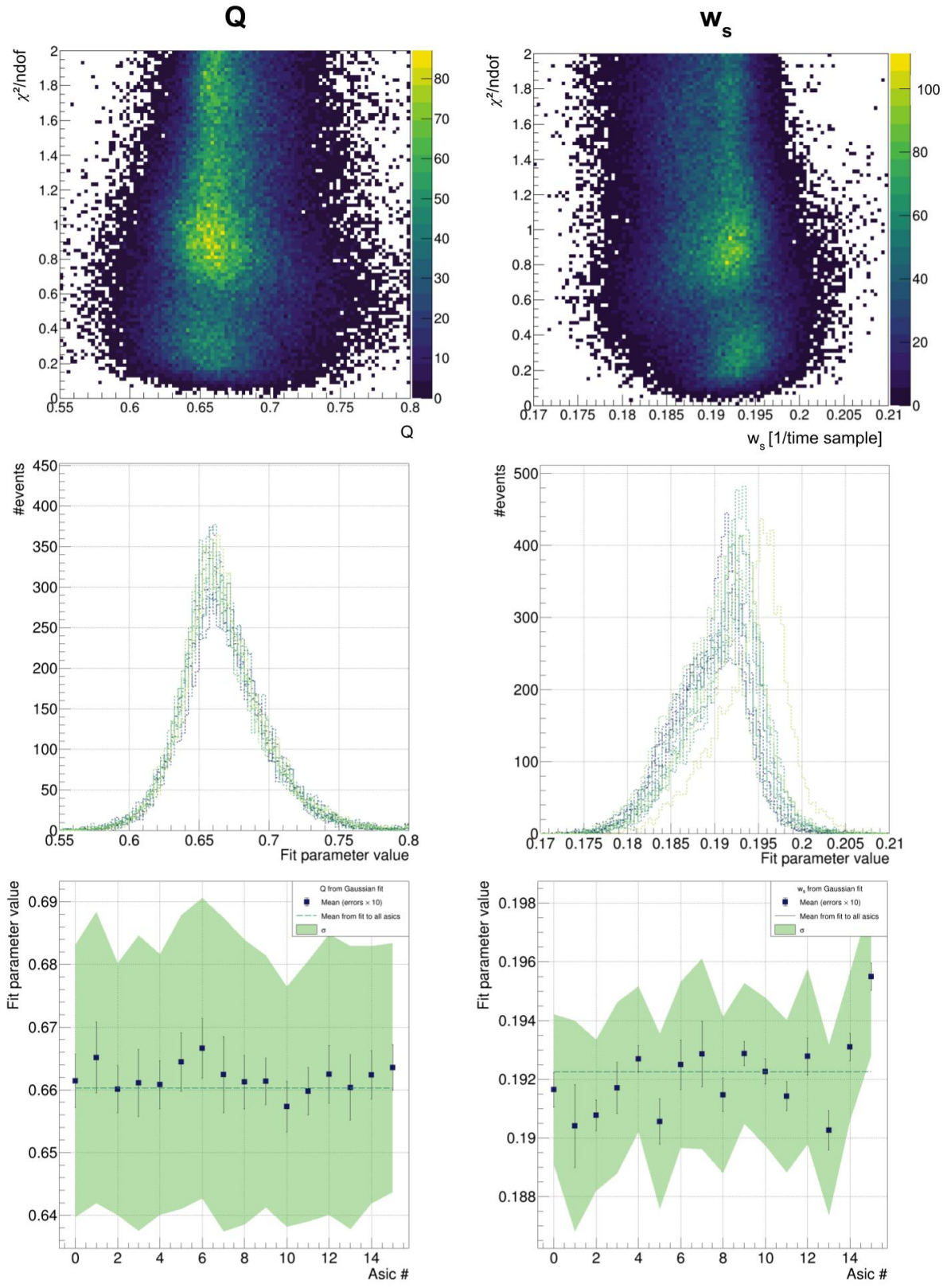

Figure 7.23: Top: 2D-histogram of the fit χ^2/ndof, where ndof stands for number of degrees of freedom, as a function of the parameter value; **Middle:** Fit parameter distributions for each ASIC separately; **Bottom:** Results of a Gaussian fit to the distributions of the fit parameters values as a function of the ASIC number.

7.5 Characterization and fine tuning of ERAM modules

Following the test beam at DESY in 2019 and the operation of the final readout electronics, a long cosmics test campaign started at Saclay to characterize and compare the various ERAM prototypes being produced in order to decide the final parameters of the resistive layer. Table 7.1 presents the specifications of the various detectors that were available at the time. The MM1-P2 is supposed to be identical to the MM1 detector tested at DESY in 2019 while the ERAM prototypes have a lower resistivity and thicker glue layer. The name was changed from MM1 to ERAM to account for the PCB version but in each case, the pad dimensions are the ones that will be used in the HA-TPCs ie. 11.18×10.09 mm^2.

Table 7.1: Prototypes available during the cosmics test campaign conducted at CEA Saclay.

Name	Surface resistivity	Glue thickness
MM1-P2	197-265 kΩ/□	75 µm
ERAM-P2	165-220 kΩ/□	200 µm
ERAM-P3	150-203 kΩ/□	200 µm

The gain, cluster multiplicity and spatial resolution of the different modules are compared in this study. The gain is estimated as the mean of a Gaussian fit to the truncated dE/dx distribution. The spatial resolution is obtained using the same Pad Response Function (PRF) method as for the track reconstruction as developed in Section 7.3.4. The obtained results are presented in Fig 7.24.

The gain shows an exponential behavior as a function of the amplification voltage as can be expected of a Micromegas detector. The gain is larger for the ERAM prototypes than for the MM1 which was at first counter-intuitive given that the glue thickness is increased. Given that the gain is estimated here based on the cluster multiplicity, the interpretation is that the potential amplitude loss is compensated by an increased cluster multiplicity. Finally, the spatial resolution is largely improved from MM1-P2 with 700 µm to the ERAM prototypes with 300 µm. These values are far from the 200 µm obtained with the MM1-P1 at DESY but this is explained by the fact that we are now looking at cosmics instead of beam data: the tracks angles and drift length are now continuously distributed and the PRF cannot be calibrated and optimized for each situation. This is thus a pessimistic view of the performances that could actually be achieved with such detectors that, in any cases, fully satisfy the requirements of the T2K experiment.

The risk of going lower and lower in surface resistivity, as it was the case for the ERAM prototypes, is to loose in detector stability. In particular, the detector can become more sensitive to sparks which is not desirable. For such reasons, and considering that the requirements were fully satisfied with all the tested configurations, the parameters fixed for the production are the following: the surface resistivity targeted is 400 kΩ/□ (so that eventual fluctuations during the manufacturing process remain in the acceptable range) and the glue thickness is fixed to 150 µm.

I presented these results to a panel of external reviewers during a Production Readiness Review (PRR) in November 2020 that resulted in the publication of an internal report [71].

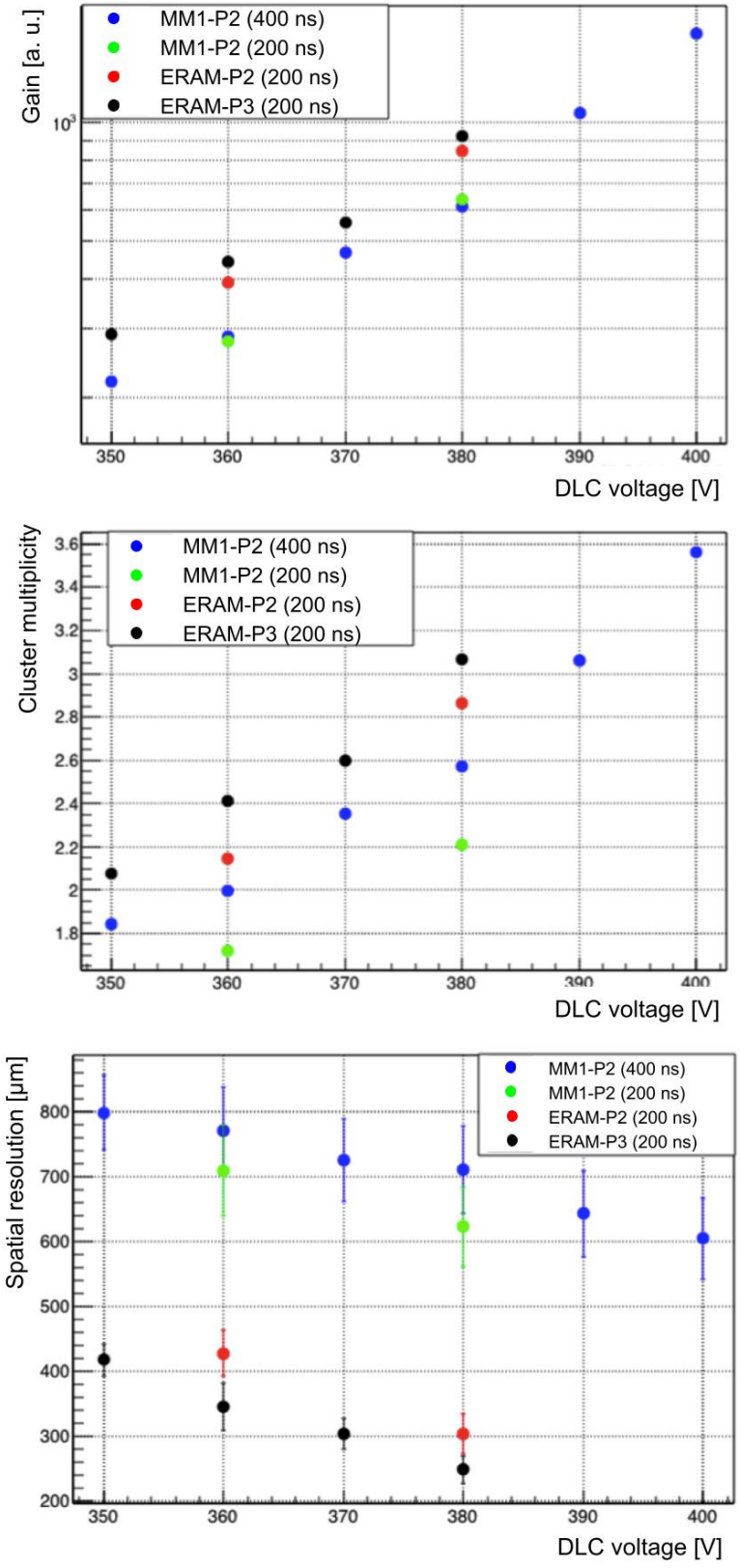

Figure 7.24: Top: Gain in arbitrary units as a function of the DLC voltage for multiple prototypes and peaking times; **Middle:** Cluster multiplicity as a function of the DLC voltage for multiple prototypes and peaking times; **Bottom:** Spatial resolution as a function of the DLC voltage for multiple prototypes and peaking times.

7.6 Improving the PCB design

In parallel to the test campaign aiming to tune the parameters of the resistive layer, some smaller adjustment were made to improve the PCB design.

7.6.1 DLC HV filter

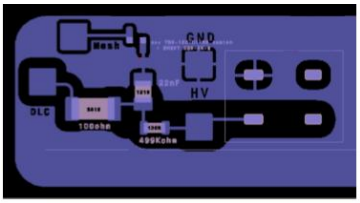

Figure 7.25: Screenshot of the Gerber file showing the on-board HV filter. It is composed of two SMC resistors of 100 Ω and 499 kΩ respectively and a capacitance of 22 nF.

At first, the filter for the DLC High Voltage (HV) power supply was an external box of about $5 \times 10 \times 3$ cm^3. However this could not be a permanent solution for the final detector because there would not be enough room for the eight filter boxes required to operate each endplate of a TPC. The chosen solution was to add the HV filter on the left corner and top layer of the ERAM PCB itself. However, the first tests showed an increase in the pedestal RMS to 17-20 ADC compared to the usual value of 7-8 ADC. After further investigations, a grounding issue was found with the on-board HV filter and corrected.

The on-board HV filter are now fully operational and also come with an optional and independent mesh connection allowing to inject a signal on the mesh (procedure referred to as *mesh pulsing*) thus inducing a signal on all pads simultaneously. This feature is used to validate the performances of the ERAM modules and is further developed in the corresponding section.

7.6.2 Centering pin issue

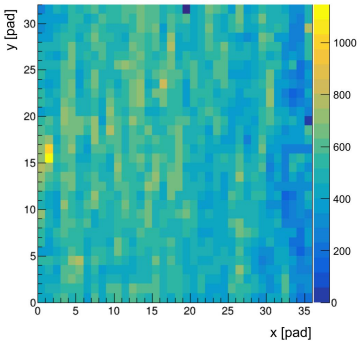

Figure 7.26: 2D map of the averaged signal amplitude for ERAM-P1.

During summer 2021, ERAM prototype P1, that was being tested with cosmics at Saclay, presented a localized high current. Fig 7.26 shows the 2D map of the pedestals RMS highlighting the area in question. As the detector was no longer holding amplification voltage, it was opened in clean room to be cleaned: TFD4 foaming degreasing detergent is applied with a flat brush and the detector is washed out with warm water. Deionized water is then used for pressure washing after what the detector is left to dry at 50°C for about 5 hours. An HV test is conducted in clean room before installing the detector back on the test bench. This cleaning procedure seemed to fix the issue, so it was thought that the issue came from a dust that had been washed out. When the same problem came back after only a few days, a more permanent fix was implemented: a drop of Araldite glue was deposited on the critical pad, resulting in a 4 pads inactive area but allowing to operate the detector again. However, this repair was not sufficient and after few days of operation the high current appeared again.

On August 24th, the ERAM prototype P2 was delivered from CERN and glued on its stiffener. ERAM-P2 was tested in cosmics instead of the ERAM-P1 that was still undergoing repairs, and after 10 days of operation a 380 µA current appeared at the exact same location.

After further investigations, it was found that the critical pad corresponded to the exact location of the centering pin of the stiffener, meant to be inserted inside a corresponding hole on the PCB for alignment. It turned out that the hole depth in the stiffener was not long enough for

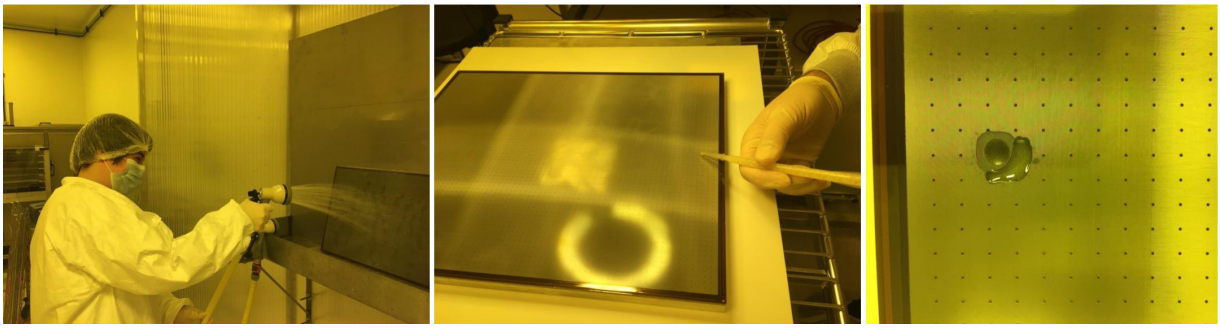

Figure 7.27: Photographs of clean room operations to fix the ERAM-P1 prototype. **From left to right:** Rinsing the ERAM-P1 module with warm water; Deposition of Araldite glue; Critical area after 2 repairs.

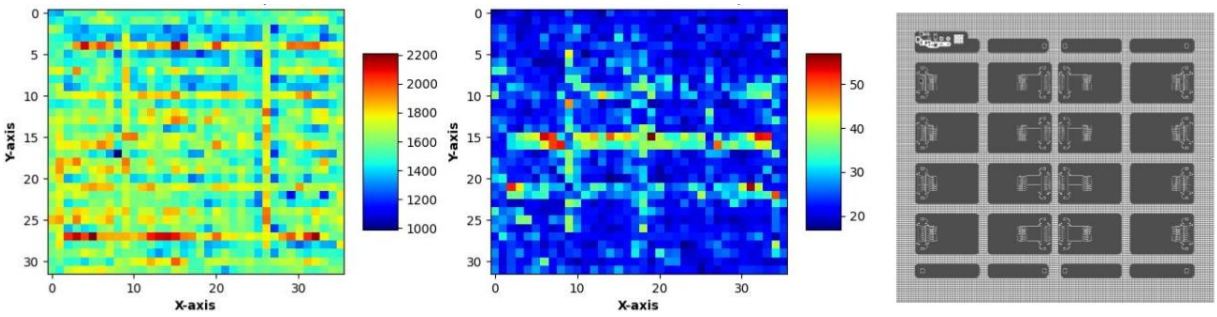

Figure 7.28: Left: 2D map of the relative gain in ADC of the ERAM-15 module; **Middle:** 2D map of the energy resolution in % of the ERAM-15 module; **Right:** PCB top layer: the grey area are 20-35 µm thick copper + 50 µm soldermask while the crosshatched area is made of copper mesh only.

the centering pin to fit so that, when the detector was pressed against the stiffener to be glued, the amplification gap was locally reduced. This resulted in a locally increased electric field which occasionally creates plasma damaging the DLC. The stiffener design was adjusted and, by precaution, the alignment pins were moved outside the active area.

7.6.3 Removing the PCB soldermask

As will be further detailed in the next section, an X-ray test bench was installed in order to scan each pad of the detector individually and draw 2D maps of the ERAM modules performances to ensure its uniformity. However, the first maps were showing grid pattern strangely similar to the green soldermask of the PCB top layer as illustrated by Fig 7.28.

The understanding that we have of the problem is illustrated by Fig 7.29: when pressing the PCB as well as gluing the detector onto the stiffener, the non-uniformity of the PCB bottom layer results in an unequal distribution of mechanical constraints leading to a reduction of the amplification gap aligned with the stiffener grid. Considering the electric fields in the amplification gap, a variation of only few microns is enough to explain the measured gain fluctuations. To solve this problem, the soldermask and copper plates are replaced by a uniform copper mesh. Fig 7.30 shows the performances of the detector after correction of the PCB bottom layer.

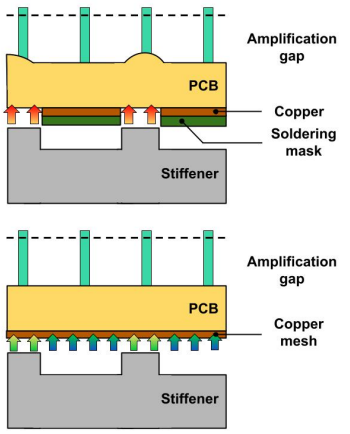

Figure 7.29: Schematic view of the assembly of the detector onto its mechanics resulting in the non-uniformities observed on the 2D gain and energy resolution maps. The arrows represents the mechanical constraints applied which are evenly distributed when the soldermask is removed and replaced by the copper mesh.

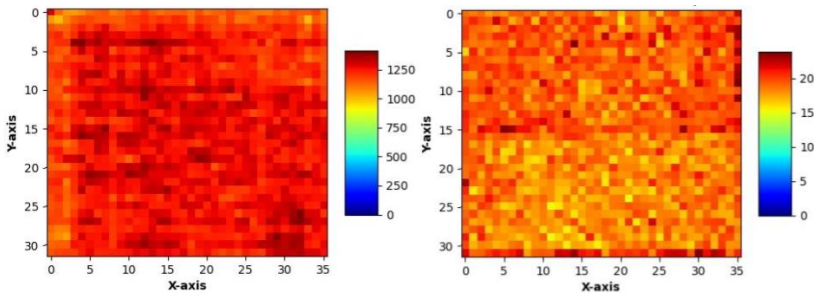

Figure 7.30: 2D map of the relative gain in ADC (left) and the energy resolution in % (right) after modification of the PCB bottom layer. To be compared with Fig 7.28.

7.7 Validation of performances and status of production

The production of the detectors started in December 2020 with the final design fixed in the PRR and latest improvements of the PCB. The detectors are now referred to as ERAM-XX where XX is replaced by the production number of the detector. The resistive bulk-Micromegas are integrated at CERN and then shipped to Saclay to be glued onto the mechanics and tested. In total, 32 ERAM modules have to be produced to be installed on the two HA-TPCs, with an additionnal 4 spares.

A procedure to validate the performances of the detectors at different stages of production have been perfected to ensure a good operation of the HA-TPCs once installed in Japan.

- **At CERN:** the resistive bulk Micromegas are qualified at different stages of production before a final test during which high voltage is applied over a long period of time to ensure the stability of the detector during future operation.
- **Mesh pulsing:** taking advantage of the optional mesh connection on the latest version of the PCB, a signal is injected on the mesh to be read simultaneously on all pads. As the injected signal is unique, the expected response is uniform over the pad plane so this procedure allows to quickly detect any localized defect. Eventual dead pads can also be identified during this test: a tolerance of 4 dead pads on a module is set as long as they are not adjacent. The mesh pulsing is repeated before and after gluing the detector onto the mechanics.
- **X-ray scanning:** a dedicated X-ray test bench made by the Warsaw University of Technology has been installed in Saclay first (and moved later on at CERN) to characterize the detectors by scanning each pad individually and precisely measure the uniformity of the gain and energy resolution over the pad plane. A non-uniformity of 10-15 % is tolerated.

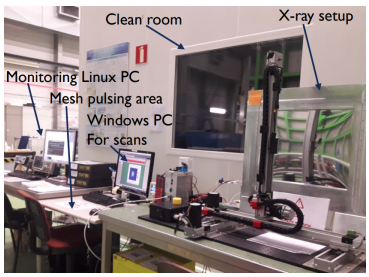

Figure 7.31: Photograph of the validation of performances test bench area at CERN. Courtesy of L. Munteanu.

The validation of performances test bench area is shown in Fig 7.31. The efficiency of the developed procedure has been established when the mesh pulsing allowed to identify a defect reproduced on three detectors and presented in Fig 7.32 (left). The detectors were sent back to CERN to be further investigated and it was found that the mesh was locally peeled off from the pillars. The detectors in question were repaired and validated by the same procedure.

At the moment, 24 detectors have been produced and validated. A half HA-TPC has been fully instrumented to be successfully tested during a

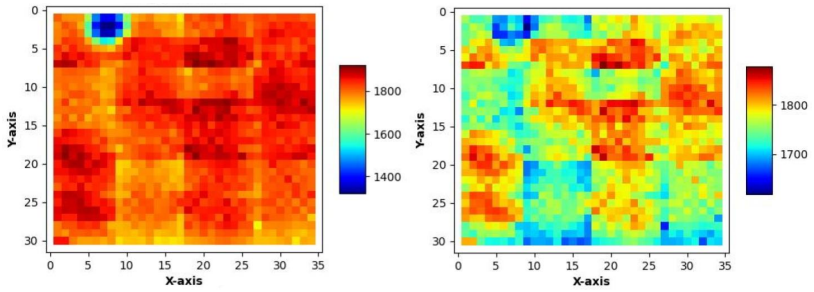

Figure 7.32: Mean amplitude of the waveforms during the mesh pulsing of ERAM-20 before (left) and after (right) repairing the detector. The defect is still visible but the non-uniformities are now within acceptable range.

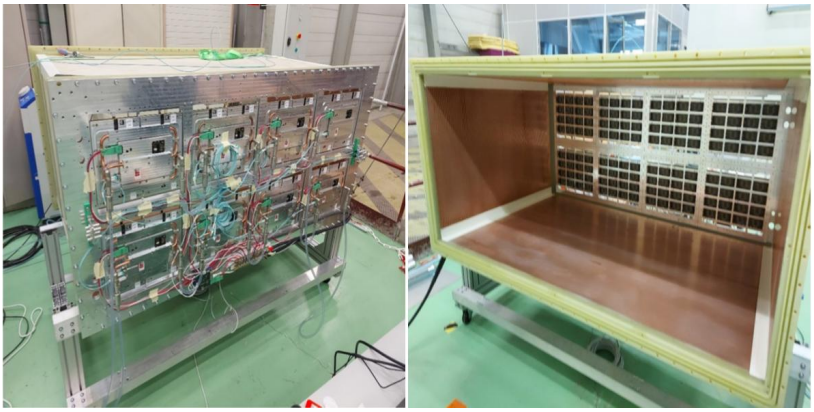

Figure 7.33: Photographs of the half HA-TPC tested in test beam at CERN in September 2022 from the readout end plate (left) and cathode side (right).

test beam at CERN in September 2022. A photograph of the TPC viewed from each endplate (readout and cathode) is shown in Fig 7.33.

SIMULATIONS OF RESISTIVE LAYER 8

If the ERAM modules developed for the upgrade of the T2K ND280 detector fully satisfy the requirements of the experiment, it is thought that the performances could be further improved if the track reconstruction algorithm could be intrinsically 2D. The development of such algorithm could benefit from a deeper knowledge of the charge spreading in a resistive layer which is what motivated these various simulation efforts.

In the first section, experimental data from a detector able to resolve primary electrons are analyzed to give an idea of how the charge deposits are actually deposited for data taking conditions very similar to those of the T2K-HA-TPCs.

The second section discusses the modelisation of the charge induced on a pad underneath a resistive layer by comparing the current description used on T2K based on the derivation of the Telegraph equations with a different model proposed by Werner Riegler.

Finally, in the data collected by T2K, one track position is reconstructed for each pad collecting enough signal. But in reality, the signal obtained on a given pad is the result of multiple deposits as illustrated in the first section. The third section will thus present a toy study aiming to understand how the signals are affected when multiple physical hits are reconstructed as one to try to correct for this bias in future reconstructions.

8.1 Retrieving gas ionisation properties using experimental data from Octopuce module

An Octopuce module, composed of 8 InGrid Micromegas detectors integrated on TimePix chips [72], was used to record data during a test beam campaign in December 2010. Each of the InGrid Micromegas is composed of a post-processed structure of aluminium defining the mesh and SU8 photoresist defining the pillars on top a silicon chip. It is read by a 256×256 array of $55 \times 55\ \mu m^2$ pixels allowing to resolve the primary electrons. In addition, the data taking conditions were very similar to the ones used in my thesis: the gas mixture used was the T2K gas, with a drift field of $E_{drift} = 270\,V/cm$, an amplification gap of $50\,\mu m$ and a mesh voltage of $V_{mesh} = 380\,V$. These data offer a unique opportunity to study the gas ionization properties and charge deposition in data taking conditions as close as possible to the ones used with the detectors currently in development.

About 20000 events are analyzed and 13000 tracks reconstructed. The track multiplicity per event can be quite high and the data contains some noise as illustrated by Fig 8.1 showing a raw event display. This makes the reconstruction more difficult and requires tight selections on the hit multiplicity. Events passing this selection undergo several steps:

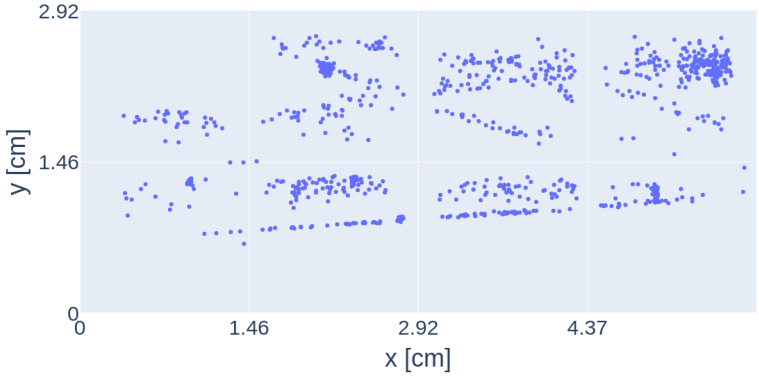

Figure 8.1: Raw event display of an Octopuce event.

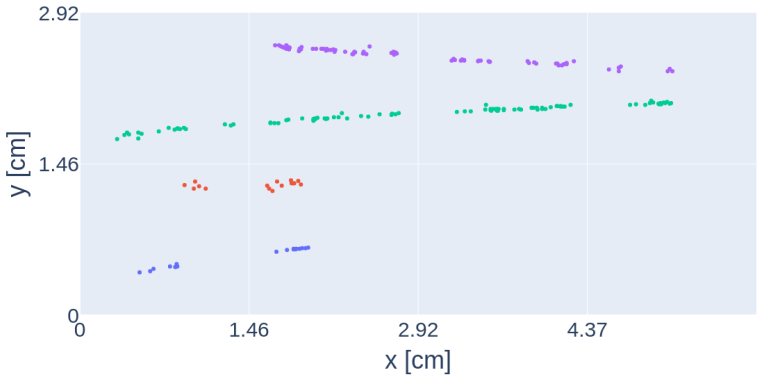

Figure 8.2: Cleaned and reconstructed event: colors indicate the various identified tracks.

1. a DBScan algorithm is applied to identify the clusters and remove as much noise as possible
2. the clusters are grouped by "macro-clusters" depending on their time, giving a subset of hits that should correspond to a track
3. the macro-clusters are fed to a RANSAC algorithm (more details about RANSAC can be found in Chapter 5) to reconstruct the tracks

An example of cleaned and reconstructed event is shown in Fig 8.2, where the colors indicate the different reconstructed tracks. The track length can then be computed in order to obtain the distribution of the number of primary electrons per track centimeter displayed in Fig 8.3. Fitting a Landau distribution yields a Most Probable Value of MPV $= 28.09 \pm 0.13$ cm^{-1}. This is to be compared with the tabulated values for the Ar-iC_4H_{10}-CF_4 (95:2:3) gas mixture:

$$N_P = 0.95 \times N_P^{\text{Ar}} + 0.02 \times N_P^{\text{i-C}_4\text{H}_{10}} + 0.03 \times N_P^{\text{CF}_4} = 27.44$$

which only differ by about 2%. This demonstrates the value of the data collected and the possible studies to conduct with such detector: experimentally obtained distributions characterizing the charge deposition on the readout plane could be used for fast simulations.

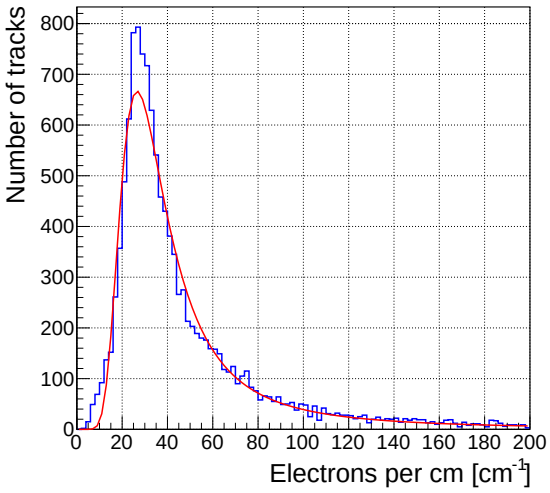

Figure 8.3: Distribution of the number of primary electrons per centimeter fitted by a Landau.

8.2 Computing the charge induced on a pad underneath a resistive layer

Let us consider a resistive Micromegas readout plane of dimensions $a \times b$. It is modeled as two layers of thickness d_1 (resistive foil and insulator) and d_3 (amplification gap) with a permittivity of ε_1 and ε_3 respectively. Both layers are separated by an infinitely thin resistive layer with a surface resistivity R and capacitance C. The whole system is bound by two grounded layers. A point charge Q_0 deposited at $t = 0$ and position (x_0, y_0) on the resitive layer. A schematic representation of the situation is presented in Fig 8.4.

The charge induced on the pad centered on (x_i, y_j), where the indices i and j refer to the coordinates of the pad in the readout plane array, and of dimensions $w_x \times w_y$ can be approximated by a derivation of the Telegraph equation integrated on the pad surface and yields[1]:

1: noted $Q^{\mathrm{T}}_{\mathrm{ind}}(x_0, y_0, x_i, y_j, t)$ for Telegraph

$$Q^{\mathrm{T}}_{\mathrm{ind}}(x_0, y_0, x_i, y_j, t) = \frac{Q_0}{4} \left[\mathrm{erf}\left(\frac{x_i + w_x/2 - x_0}{2\sigma(t)}\right) - \mathrm{erf}\left(\frac{x_i - w_x/2 - x_0}{2\sigma(t)}\right)\right] \left[\mathrm{erf}\left(\frac{y_j + w_y/2 - y_0}{2\sigma(t)}\right) - \mathrm{erf}\left(\frac{y_j - w_y/2 - y_0}{2\sigma(t)}\right)\right] \quad (8.1)$$

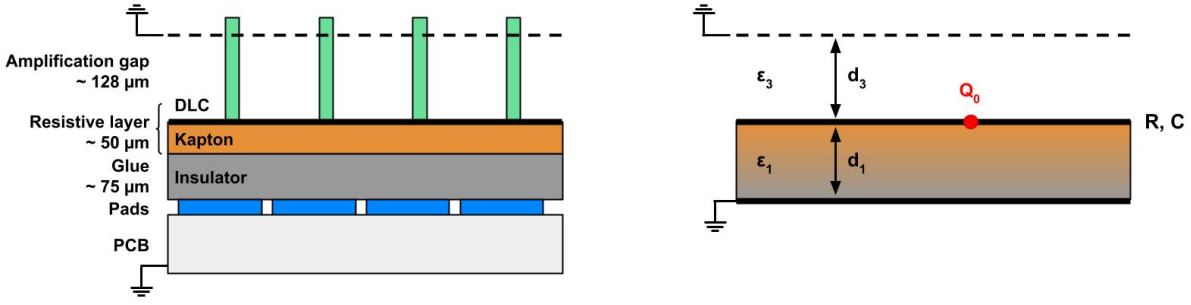

Figure 8.4: Schematic view of the Micromegas readout plane (left) as simulated (right).

with $\sigma(t) = \sqrt{\frac{2t}{RC}}$.

In February 2020, at the occasion of a RD51 collaboration meeting at CERN, Werner Riegler presented a new formalism he had been working on [73] allowing to include the electrode resistivity and signal propagation into detector simulations[2]. In particular, he proposed a way to compute the time dependant weighting fields that can be used to formulate the response of any detector sensitive to the movement of charged particules and was looking for students to implement this computation for specific geometries. As I was myself looking to develop a simulation tool for the ERAM detectors in order to improve the track reconstruction algorithm, I offered to work with him and implement this formalism using the analytic expression computed for the specific geometry of the ERAM modules.

2: Link to W. Riegler's presentation

I was provided with the following expression[3] of a double infinite sum over two independent variables α and β:

3: noted $Q_{\text{ind}}^{\text{WF}}(x_0, y_0, x_i, y_j, t)$ for Weighting Field

$$Q_{\text{ind}}^{\text{WF}}(x_0, y_0, x_i, y_j, t) = \Theta(t)\frac{16Q_0}{\pi^2} \sum_{\alpha=1}^{\infty}\sum_{\beta=1}^{\infty} \frac{\sin\left(\alpha\pi\frac{w_x}{2a}\right)\sin\left(\alpha\pi\frac{x_0}{a}\right)\sin\left(\alpha\pi\frac{x_i}{a}\right)}{\alpha} \frac{\sin\left(\beta\pi\frac{w_y}{2b}\right)\sin\left(\beta\pi\frac{y_0}{b}\right)\sin\left(\beta\pi\frac{y_j}{b}\right)}{\beta} h(k_{\alpha,\beta}, t) \quad (8.2)$$

with

$$\begin{aligned} k_{\alpha,\beta} &= \pi\sqrt{\frac{\alpha^2}{a^2} + \frac{\beta^2}{b^2}} \\ h(k_{\alpha,\beta}, t) &= \frac{\varepsilon_1 e^{-t/\tau(k_{\alpha,\beta})}}{\varepsilon_1\cosh(k_{\alpha,\beta}d_1) + \varepsilon_3\coth(k_{\alpha,\beta}d_3)\sinh(k_{\alpha,\beta}d_1)} \\ \tau(k_{\alpha,\beta}) &= \frac{R}{k_{\alpha,\beta}}[\varepsilon_1\coth(k_{\alpha,\beta}d_1) + \varepsilon_3\coth(k_{\alpha,\beta}d_3)] \end{aligned} \quad (8.3)$$

With this formalism, the signal consists of an infinite sum of terms that decay with a time constant $\tau(k_{\alpha,\beta})$, which is the longest for $\alpha = \beta = 0$ and, assuming $a = b$ and $a \gg d_{1,3}$, can be approximated to:

$$\tau(k_{0,0}) \approx \frac{R}{2\pi^2}\left(\frac{\varepsilon_1 a^2}{d_1} + \frac{\varepsilon_3 a^2}{d_3}\right) = \frac{R(C_1 + C_3)}{2\pi^2} \quad (8.4)$$

where $C_1 + C_3$ is the total capacitance between the resistive layer and the ground.

Now in order to implement this formalism for a simulation tool one needs to define limits to the infinite sums. The parameter p is introduced and defines the accuracy that should be reached during summation: for the smallest term of the sum to be of the order of e^{-p}, $k_{\alpha,\beta}$ maximum value should be:

$$k_{\max}(t) = \frac{p}{d_1 + \frac{t}{R(\varepsilon_1 + \varepsilon_3)}} \quad (8.5)$$

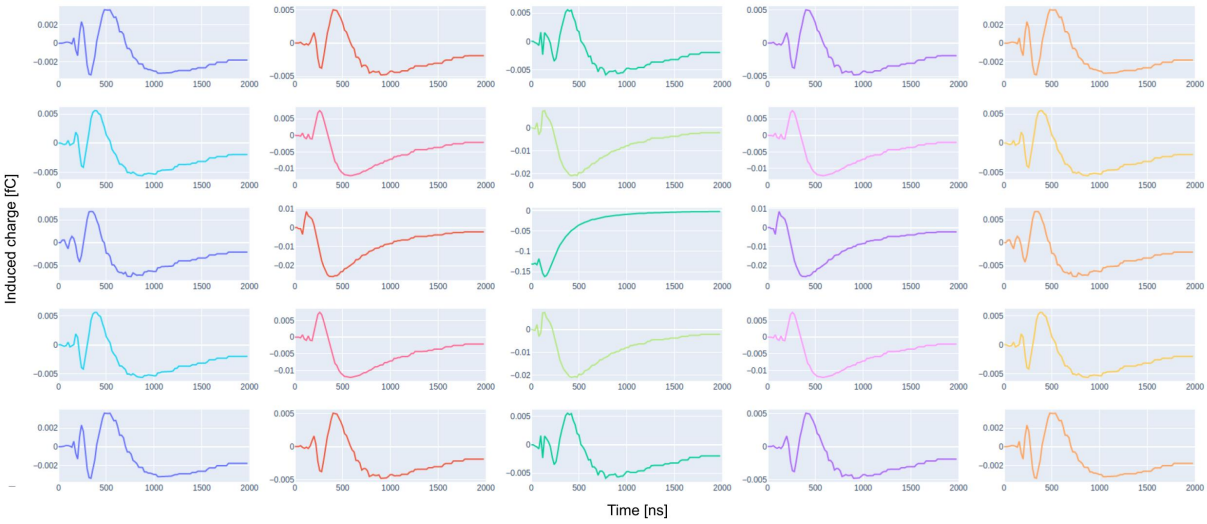

Figure 8.5: Induced charge as a function of time for each pad of the 5×5 readout plane simulated. The charge is deposited at $t = 0$ and at the center of the central pad.

This translates, in term of summation limits, to:

$$\begin{aligned} \alpha_{\max} &= k_{\max} a/\pi \\ \beta_{\max}(\alpha) &= b\sqrt{\frac{k_{\max}^2}{\pi^2} - \frac{\alpha^2}{a^2}} \end{aligned} \tag{8.6}$$

It was first thought that the double sum would give accurate results for p between 5 and 10.

At first, a simple situation is simulated which is a 36×32 readout plane with $10.09 \times 11.18\ \text{mm}^2$ pads and a surface resistivity of $R = 400\,\text{k}\Omega/\square$ to reproduce ERAM specifications. A charge $Q_0 = 1e$ is deposited at $t = 0$ at the center of a pad near the center of the readout plane to be as far away from possible to any edge effects. The accuracy parameter is set to $p = 10$. The obtained results are presented in Fig 8.5 that shows the induced charge as a function of time for 5×5 pads centered on the pad on which was deposited Q_0.

As expected due to the geometry of the problem, the signal of the pad directly above and below the central pad are identical, as goes for the pads on the left and right of the central pad. Because of the slight asymmetry of the pads, the induced charge on a neighbouring pad along a column is not identical to the one along the row. In addition, the absolute value of the induced charged at $t = 0$ on the central pad has been confirmed by an independent Matlab computation.

However, the oscillations observed at short time ($t < 500\,\text{ns}$) are not physical. Looking in particular at the pad where the charge is deposited (of coordinates (3, 3) in the 5×5 array of pads represented), the amplitude of the induced charge should only decrease with time as the charge spreads so that:

$$Q_{\text{ind}}^{\text{WF}}(x_0, y_0, x_3, y_3, t) \leq Q_{\text{ind}}^{\text{WF}}(x_0, y_0, x_3, y_3, t = 0) \tag{8.7}$$

As a comparison, Fig 8.7 presents the induced charge on the pad where $Q_0 = 1000e$ is initially deposited computed using $Q_{\text{ind}}^{\text{T}}$ (in red) and

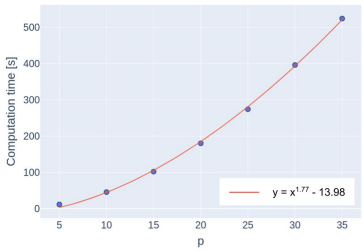

Figure 8.6: Computation time as a function of p for a single pad simulated.

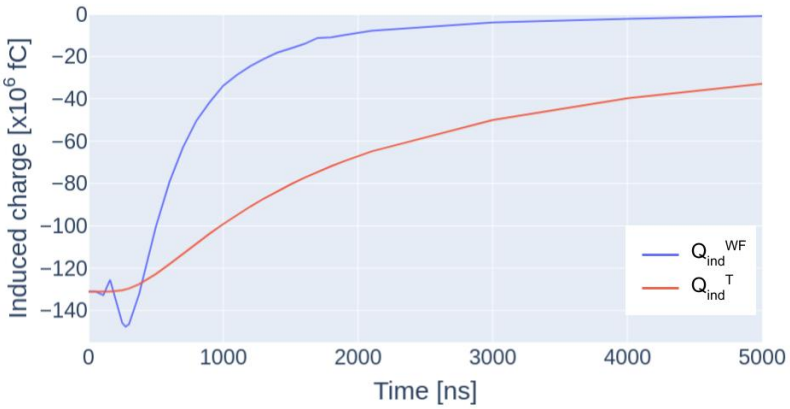

Figure 8.7: Induced charge as a function of time on the pad where $Q_0 = 1000e^-$ is deposited at $t = 0$ using Q_{ind}^T model (in red) and Q_{ind}^{WF} model (in blue).

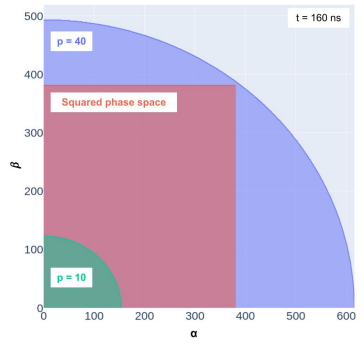

Figure 8.8: Example of different summation phase spaces at $t = 160$ ns.

Q_{ind}^{WF} (in blue). The first hypothesis to explain this oscillation is that the summation does not include enough terms.

Playing with the p parameter seems to attenuate the oscillation, but the computation time increases as a power law of p as illustrated by Fig 8.6 for a single pad simulated and the memory is not sufficient for $p > 35$. Given that the objective is to simulate potentially large readout planes, adjusting the p parameter is not a possible solution.

To further investigate this effect, I focused on the induced charge computed on the pad where the charge is deposited varying the summation limit. To simplify the problem, I decided to sum over a square phase space ie. $\alpha_{max} = \beta_{max} = N$. An example of the different summation phase spaces is illustrated in Fig 8.8.

Fig 8.9 shows the induced charge computed for $t = 275$ ns as a function of the summation limit N and compared with the value of the induced charge at $t = 0$ (in blue) and the value obtained with the previous summation limits (in dashed green) with $p = 10$. Eq 8.6 yields $\alpha_{max} = 90$ and $\beta_{max}(\alpha = 1) = 72$ ($\beta_{max}(\alpha)$ decreases with α so the maximum value is obtained for $\alpha = 1$) while Fig 8.9 shows that the charge induced computed by summing over a square phase space does not converge before $N \sim 170$. In addition, the computed values of induced charge do not respect the physical constraint given in Eq 8.7 for $N \lesssim 115$. Fixing the ε to define convergence at $\varepsilon = 0.001$ fC, the minimum value of N that both allows convergence of the induced charge and fulfills the constraint set by Eq 8.7 is extracted for multiple times and presented in Fig 8.10. These points are used to extrapolate a summation limit N_{lim} at each time as :

$$N_{lim}(t) = 5350t^{-0521} \tag{8.8}$$

which allows to perform a new computation of the induced charge on the pad that received the direct charge.

The final results are presented in Fig 8.11 that compares the induced charge as a function of time for various models: solid lines shows the computation based on the weighting fields description with the α_{max} and $\beta_{max}(\alpha)$ summation limits (in blue) and the newly extrapolated $N_{lim}(t)$ (in red). The computations derived from the Telegraph equation are represented using dashed lines for different values of capacitance for the resistive layer.

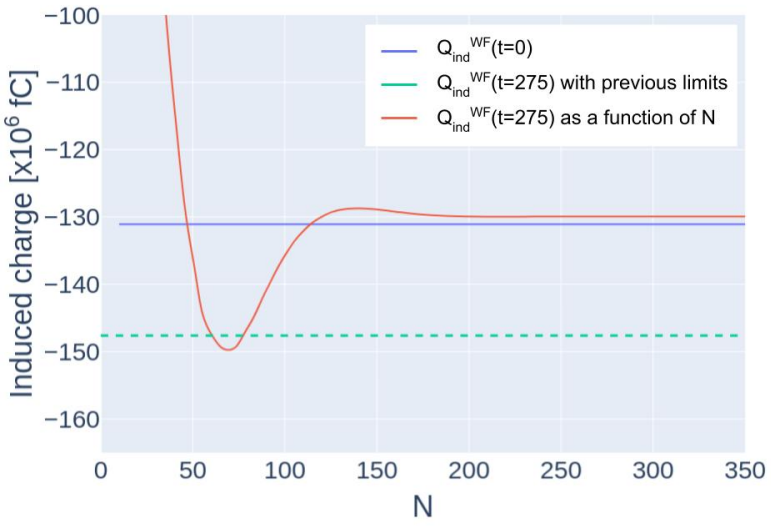

Figure 8.9: Induced charge for $t = 275\,\text{ns}$ computed by summing over a squared phase space of size N as a function of N. For comparison, the value of the induced charge at $t = 0$ is shown in blue and the value obtained with the previous summation limits is shown in dashed green.

The first observation is that summing over a squared phase space of dimension $N_{\text{lim}}(t)$ completely fixes the oscillation problem. Once corrected with these new summation limits, the weighting field description seems to be in perfect agreement with the Telegraph model with the same surface resistivity R and a capacitance tuned to $C = 75\,\text{pF}$.

Efforts could be made in order to refine the summation limits to minimize the computation time which is currently of 15 min to compute the induced charge on each pad of the 5×5 array over 500 time steps. For example, the ε defining convergence could easily be increased by a factor 10. Moreover, further investigations would be required to express the new summation limits as a function of parameters of the problems instead of an empirical formula, otherwise the whole process will have to be reproduced for each variation of the geometry.

However, due to the very good agreement between the two descriptions and the need of the T2K collaboration, it is decided that the Telegraph model will be used to simulate the charge spread as it is easier to implement and yields smaller computation time. The project in collaboration with Werner Riegler is abandoned due to the combination of the COVID pandemic and a new position of higher responsibilities in the ALICE collaboration on his part.

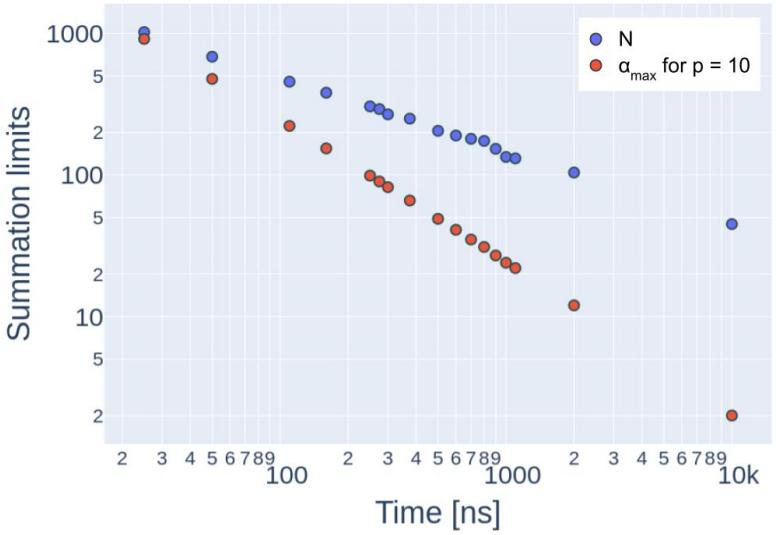

Figure 8.10: Summation limits as a function of time.

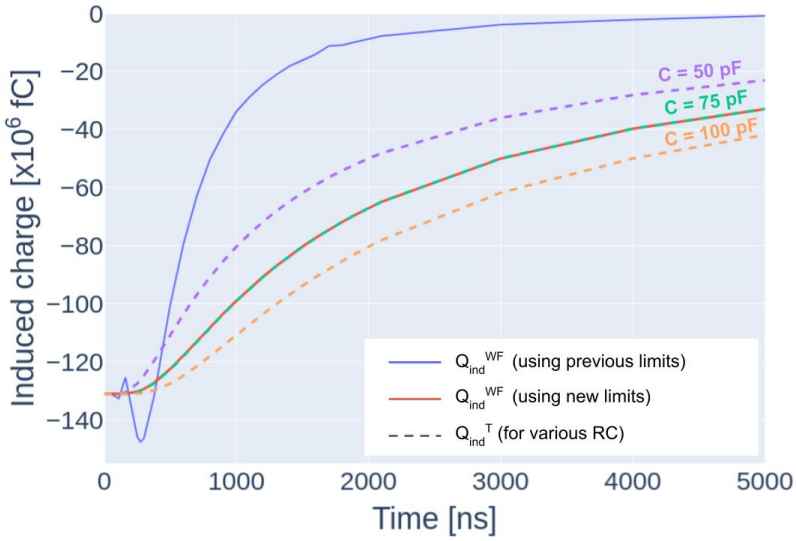

Figure 8.11: Induced charge as a function of time for the pad where $Q_0 = 1000e$ is deposited at $t = 0$ computed for various models: solid lines show the weighting fields computation using the previous summation limits (in blue) and the new extrapolated $N_{\text{lim}}(t)$ (in red) while dashed lines show the computation derived from the Telegraph equations for various capacitance C of the resistive layer.

8.3 Effect of charge deposition on the induced charge

In the previous section, it was demonstrated that the Telegraph description of the charge spreading onto the resistive layer, which is a simplified view, was in good agreement with a more physical and complicated description derived from the computation of weighting fields. However, the charge deposit was punctual and unique over the pad surface while in reality, as shown in the experimental data presented in Section 8.1, there are about 28 primary electrons per track centimeters which would result in at least as many electron avalanches over an ERAM pad surface. The idea of this toy study is thus to estimate the bias introduced when making the assumption that there is a single punctual charge deposit per pad.

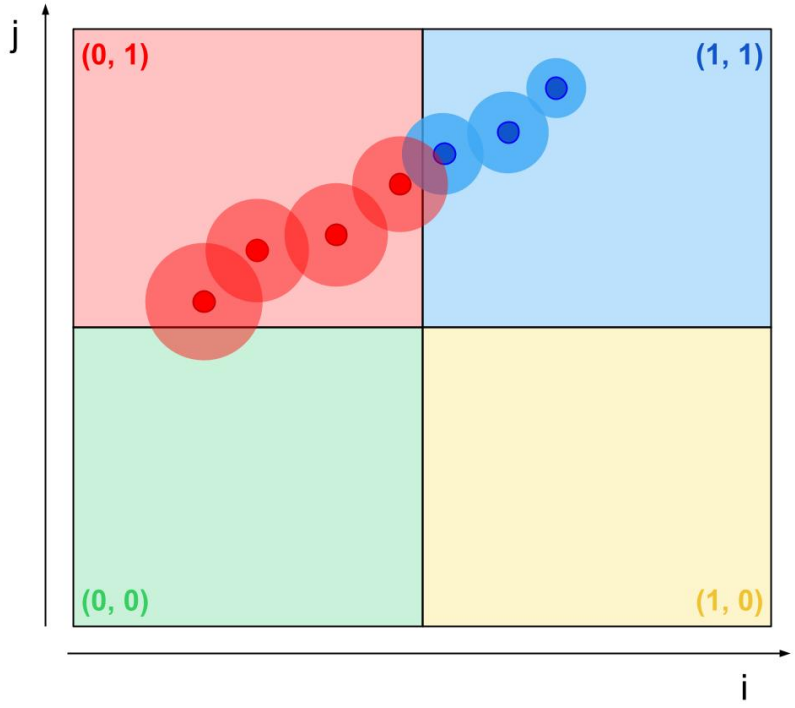

Figure 8.12: Illustration of the toy study configuration on an example track. The larger circles represent the charge spread. On this example, charges were deposited from left to right.

A simple 2×2 readout plane is simulated with 10×10 mm^2 pads. Each pad is identified through its coordinates (i, j) as illustrated on the example situation in Fig 8.12. Track parameters a and b are randomly sampled so that the track is defined by its equation:

$$y = ax + b \tag{8.9}$$

We introduce a step $dx = 0.5\,\text{mm}$ so that the coordinates (x_n, y_n) of the charge deposits are defined as follows:

$$\begin{aligned} x_n &= n \times dx + \text{Gaus}(0, dx) \\ y_n &= a(n \times dx) + b + \text{Gaus}(0, dx) \end{aligned} \tag{8.10}$$

where $\text{Gaus}(0, dx)$ is a random spread sampled from a Gaussian distribution centered on zero and with a standard deviation of dx. The time associated to each deposit t_n is computed as $t_n = n \times dt$ where the time

step dt is fixed to:

$$dt = \frac{100\,\text{ns}}{N} \tag{8.11}$$

where N is the total number of charge deposits along the track. Finally, at the moment each charge deposit carries the same charge Q.

Based on the results discussed in the previous section, the charge spread on the resistive is described using the derivation of the Telegraph equation so that the charge density ρ can be approximated by:

$$\rho(r,t) = \rho_0 \frac{RC}{4\pi t} e^{-r^2 RC/4t} \tag{8.12}$$

where ρ_0 corresponds to the charge density at $(r = 0, t = 0)$ and is thus a singularity but is defined, for the computation, as the charge Q deposited at $t = 0$. In order to estimate the impact of charge deposition on the computation of the induced charge as well as decorrelate the contributions from each pad, three different computations of the induced charge Q_{ind} on a given pad are implemented:

- **Inclusive:** noted $Q_{\text{ind}}^{\text{incl}}((i,j),t)$, each charge deposit (x_n, y_n) is spread using Eq 8.12 and the resulting charge density is integrated over the pad (i,j) area. Taking the example of Fig 8.12, it means that the signal spreading from a charge deposit on the pad (1, 1) will eventually be taken into account in $Q_{\text{ind}}^{\text{incl}}(0,1,t)$.
- **Exclusive:** noted $Q_{\text{ind}}^{\text{excl}}((i,j),(k,l),t)$, only the charge deposit $(x_n, y_n)_{i,j}$ that are on pad (i,j) are taken into account and the resulting charge density is integrated over the surface of pad (k,l). Coming back to Fig 8.12, this means for example that $Q_{\text{ind}}^{\text{excl}}((0,0),(0,0),t) = 0$ even if some signal spreads from pad (0, 1).
- **Effective:** noted $Q_{\text{ind}}^{\text{eff}}((i,j),(k,l),t)$, an effective charge deposit is computed as the barycenter of all charge deposits on pad (i,j) carrying $Q_{\text{eff}} = \sum_{i,j} Q$ and with a time $t_{\text{eff}} = \langle t_n \rangle_{i,j}$. This effective deposit is then spread using Eq 8.12 and the resulting charge density is integrated over the surface of pad (k,l).

The exclusive method is used to separate the contributions from the different pads but it is expected that summing all exclusive contributions will yield the same results as the inclusive computation.

An example of simulated event is shown in Fig 8.13. The resulting signals obtained on pad $(0,0)$ and pad $(1,1)$ for the various computation methods are presented in Fig 8.14. From these computations, it seems that the effective method yields minor differences compared to the inclusive method, especially considering that those would be smoothed by the convolution with the response of the readout electronics. What is really interesting however is to observe each contribution separately: in particular it is worth noticing that the contribution of the pad $(0,0)$ on the signal received by the pad $(1,1)$ (ie. diagonal neighbour) cannot be neglected after a few hundreds of nanoseconds.

At the moment, in T2K track reconstruction of horizontal tracks, the longitudinal correlations between clusters is not taken into account while part of the charge on cluster n actually comes from the spread of cluster $n-1$. Such simulations could be really helpful to study those correlations as well as characterize the diagonal spreading to build a reconstruction algorithm for high angle tracks. With more time, this is something I would

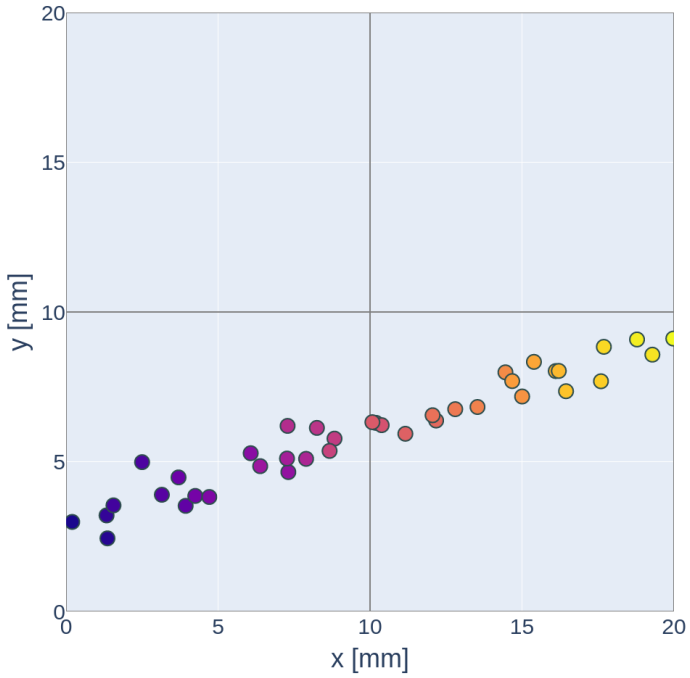

Figure 8.13: Example of simulated event. Color indicates the time associated to each charge deposit.

have been really interested in studying. This code could be improved to take into account the ionization fluctuations or non-punctual charge deposits by spreading the charge density from an ellipse.

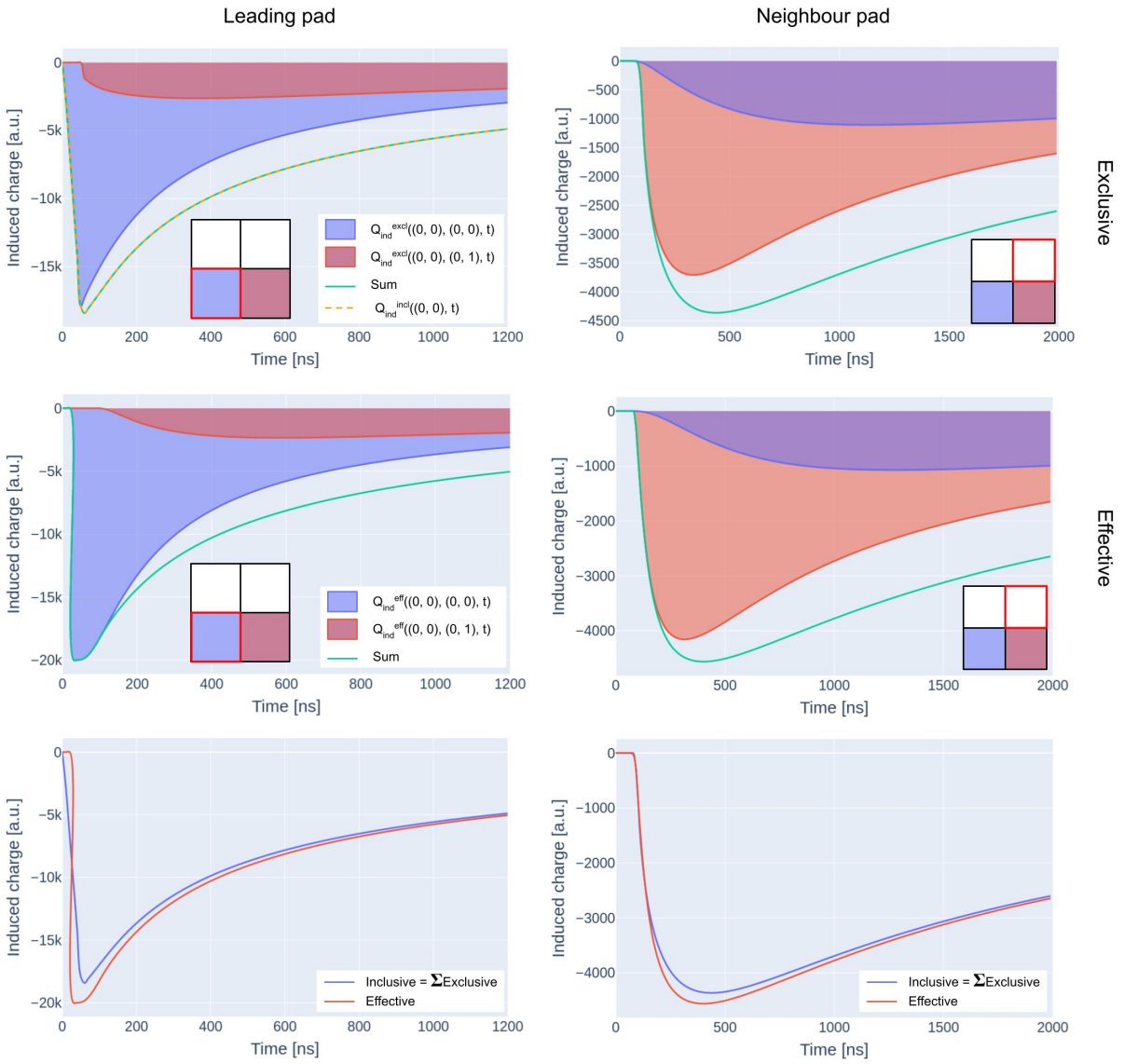

Figure 8.14: Induced charges as a function of time for an example of leading pad (left) and neighbour pad (right) and the different computation methods: the top row shows the results obtained using the exclusive computation method and separating the contributions from each pad, the middle row is the same but for the effective computation method, and the last row compares both methods.

Part IV

Conclusion

Conclusion

Over the course of my PhD, I had the chance to approach scientific research through two very different angles. First, as a member of a small team of 5-6 persons to develop D3DT, which started as a R&D project made possible thanks to a 60 k€ funding from DRF Impulsion. But also as a member of the international collaboration that is the T2K experiment, gathering more than 500 persons to study the oscillation of neutrinos.

At each occasion, I was able to contribute to the hardware development as well as the analysis. Being at the interface allowed me to work in close collaboration with electronics experts who provided me with invaluable help to decode the binary files for the monitoring software and insight to build the new electronic shape.

Looking back at D3DT, we manage to assemble the first full size prototype and validate the external trigger that should be integrated in the next few months. The first muon tracks have been observed! But there are still some work to do especially on the high voltage power supply to improve the quality of the data. The readout plane, which is the first 2D-multiplexed Micromegas detector used to read a TPC, has been precisely characterized which allowed to highlight a manufacturing error on the PCB. In addition, this automatized test bench can be adapted to any small area Micromegas detector and will thus benefit the entire lab. Finally, on the software side, the track reconstruction algorithm is ready and already showed great performances on simulated data. With more time, I would have liked to develop a more accurate simulation tool using the REST[4] (Rare Event Searches ToolKit for Physics) framework. This work will be continued by master students in the following weeks.

4: https://sultan.unizar.es/rest/

Focusing now on the development of the ERAM detectors for the upgrade of the T2K near detector, I feel extremely grateful to have been able to contribute to the entire process, from the refinement of the design to the beginning of production. This experience taught me a lot about the management of an international project with strict deadlines, especially in this particularly complicated geopolitical context due to both the COVID crisis and the war in Ukraine. If I used to underestimate the impact that the international environment has on scientific research, I realise now that both are deeply entangled and that it is important to take it into consideration if we want to keep doing the job we love.

A lot has been achieved in three years: from the development to the monitoring software allowing a successful and important test beam in 2019, to the installation of a fully instrumented half HA-TPC at CERN in September 2022. In retrospect, I wish I could have dedicated more time to the simulations presented in the last chapter as our understanding of the charge spreading on a resistive layer is still not sufficient in my opinion.

As hard as it is to take a step back from these detectors I spent years of my life working on, I am also looking forward to bring my expertise to contribute to another experiment and keep learning new skills along the way. I am beyond happy to come back to the LHCb collaboration where I started as a master student and work on the development of the TORCH detector as a member of the Warwick group.

Appendix

D3DT readout plane characterization: preliminary study

A

A prototype cathode is machined with, on each sector, a hole of each possible combination of diameter and position and is shown on Fig A.1. The naming scheme to reference the various positions is presented in Table A.1.

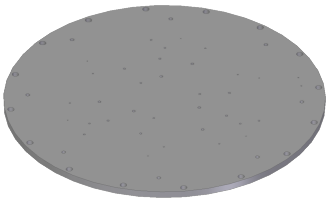

Figure A.1: Prototype cathode design.

For each of those positions, runs of 10000 events are recorded using the 18SAC00033 radioactive source. The reconstructed energy spectra of each position are presented on Fig A.2 while Fig A.3 shows the associated event multiplicity. First of all the presence of a double peak is attributed to the high activity of the source: the left peak is identified as the expected 5.9 keV peak while the right one is understood as double events. For this study, only the left peak is considered and a source with smaller activity will be used for the final analysis. The two largest diameters present a degradation of the event multiplicity peaking at 5 or more instead of 4 for the lower diameters and are for such reason no longer considered. The energy resolution is computed as presented in Section 4.2.3 and the results are shown on Fig A.4. In each case the energy resolution seems worse on Asic 0 which is consistent with the fact that this sector is known to be noisier and its performances degraded. In addition, the energy resolution is consistently better when the collimation hole is placed at the intersection of 3 pixels which is construed as a better charge sharing. Finally, the performances obtained for the 0.5 mm and 0.75 mm diameters are very similar, as well as the acquisition rates respectively measured at 110 Hz and 120 Hz. Since both options were be acceptable, the solution that makes the manufacturing process easier is chosen so that the final design of the cathode is with collimating holes of 0.75 mm diameter placed at each intersection of 3 pixels.

Asic	**Diameter** [mm]	**Position**	**Name**
0	0.5	CoP	PA0
0	0.75	CoP	PB0
0	1	CoP	PC0
0	1.2	CoP	PD0
0	1.5	CoP	PE0
0	0.5	IoP	IA0
0	0.75	IoP	IB0
0	1	IoP	IC0
0	1.2	IoP	ID0
0	1.5	IoP	IE0
1	0.5	CoP	PA1
...			

Table A.1: Naming scheme of the various positions considered for the preliminary study.

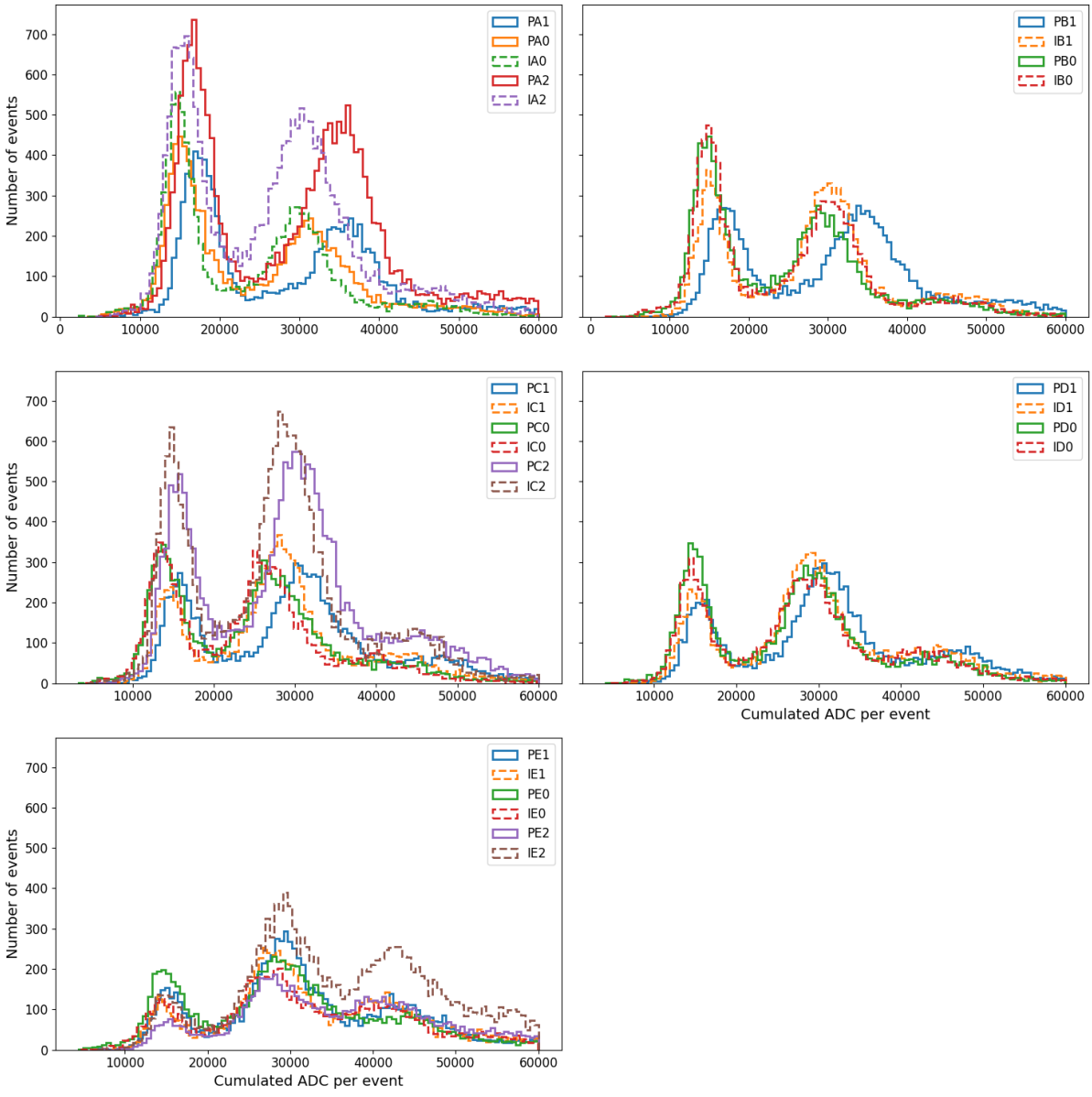

Figure A.2: Reconstructed ^{55}Fe energy spectrum for each position; Each subplot corresponds to a different diameter in ascending order: from top to bottom and left to right 0.5 mm, 0.75 mm, 1 mm, 1.2 mm and 1.5 mm. The solid lines correspond to CoP positions while dashed lines are for IoP positions.

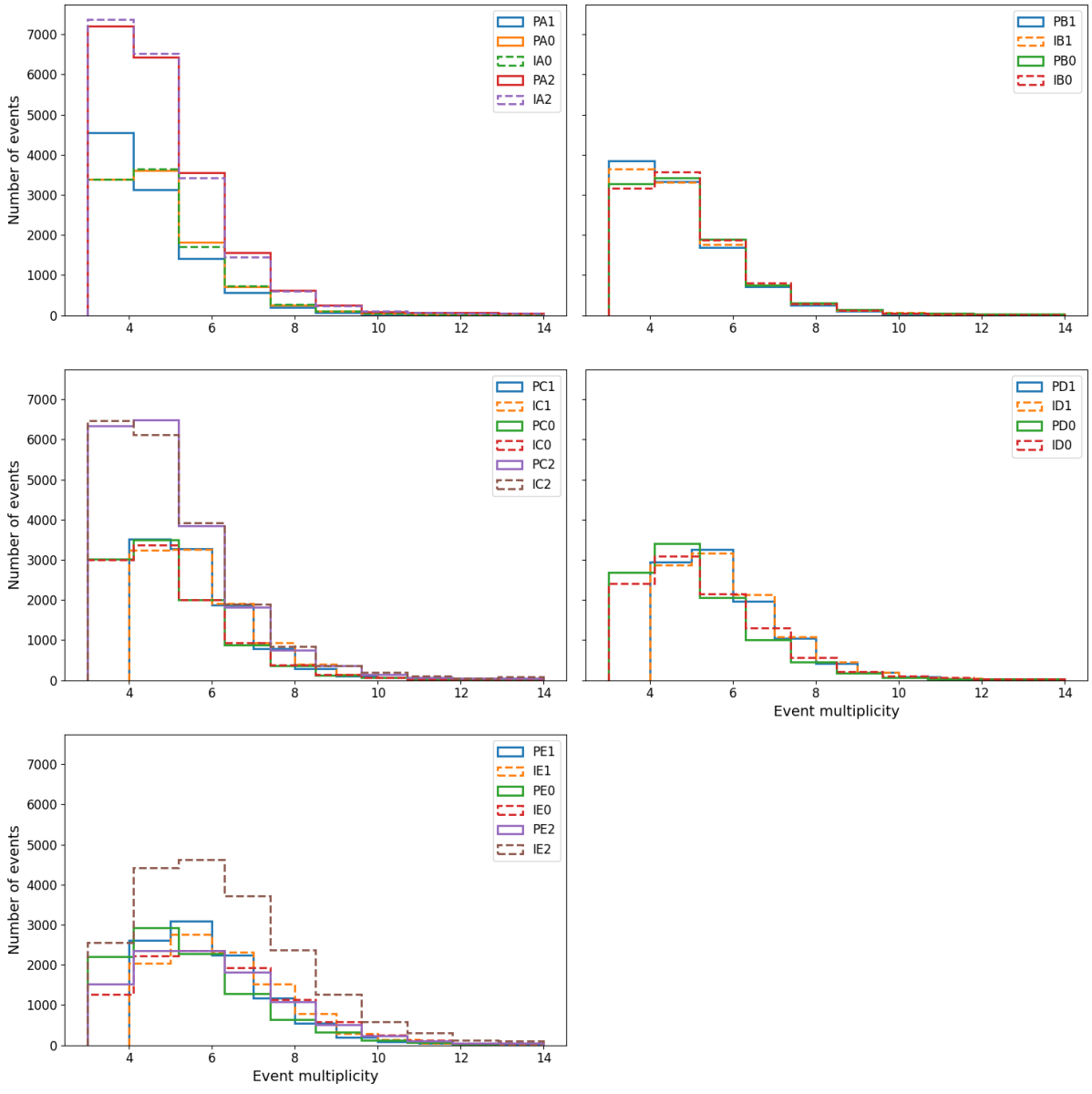

Figure A.3: Event multiplicity for each position; Each subplot corresponds to a different diameter in ascending order: from top to bottom and left to right 0.5 mm, 0.75 mm, 1 mm, 1.2 mm and 1.5 mm. The solid lines correspond to CoP positions while dashed lines are for IoP positions.

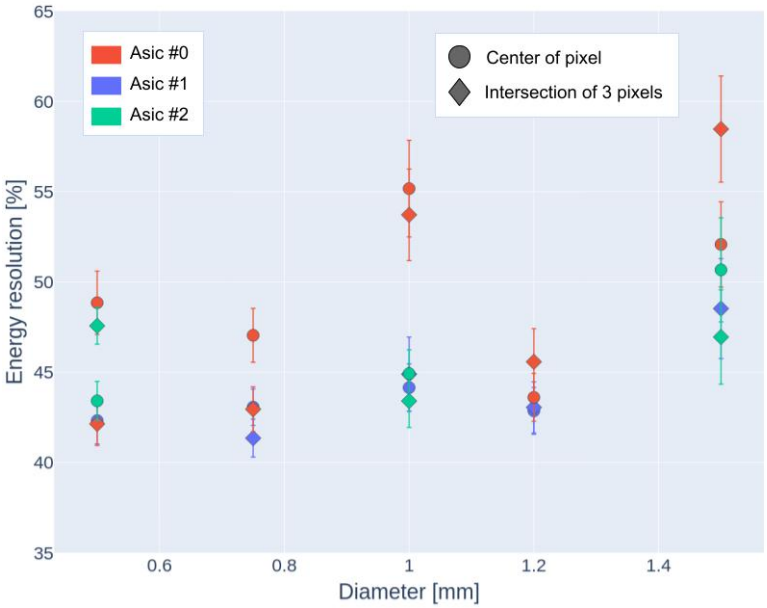

Figure A.4: Energy resolution as a function of the diameter.

Bibliography

Here are the references in citation order.

[1] Wilson Charles Thomson Rees. 'On the method of making visible the paths of ionising particles through a gas'. In: 85.578 (1911), pp. 285–288. DOI: 10.1098/rspa.1911.0041 (cited on page 5).

[2] Georges Charpak et al. 'The Use of Multiwire Proportional Counters to Select and Localize Charged Particles'. In: *Nucl. Instrum. Meth.* 62 (1968), pp. 262–268. DOI: 10.1016/0029-554X(68)90371-6 (cited on page 5).

[3] R.L. Workman et al. 'Review of Particle Physics'. In: (). to be published (2022) (cited on pages 6, 8, 10, 22, 26, 33, 57).

[4] Weilin Yu. 'Particle identification of the ALICE TPC via dE/dx'. In: *Nuclear Instruments and Methods in Physics Research Section A: Accelerators, Spectrometers, Detectors and Associated Equipment* 706 (2013), pp. 55–58. DOI: 10.1016/J.NIMA.2012.05.022 (cited on page 9).

[5] *MAGBOLTZ*. http://cyclo.mit.edu/drift/www/aboutMagboltz.html (cited on pages 10, 11, 71).

[6] Chengxun Yuan, Anatoly A Kudryavtsev, and Vladimir I Demidov. 'Ionization in the electric field and the first Townsend coefficient'. In: *Introduction to the Kinetics of Glow Discharges*. 2053-2571. Morgan Claypool Publishers, 2018, pp. 2–10. DOI: 10.1088/978-1-64327-060-9ch2 (cited on page 11).

[7] 'MICROMEGAS: a high-granularity position-sensitive gaseous detector for high particle-flux environments'. In: *Nuclear Instruments and Methods in Physics Research Section A: Accelerators, Spectrometers, Detectors and Associated Equipment* 376 (1 June 1996), pp. 29–35. DOI: 10.1016/0168-9002(96)00175-1 (cited on pages 12, 29).

[8] David Attié et al. 'Current Status and Future Developments of Micromegas Detectors for Physics and Applications'. In: *Applied Sciences* 11.12 (2021), p. 5362. DOI: 10.3390/app11125362 (cited on pages 12, 29).

[9] I. Giomataris et al. 'Micromegas in a bulk'. In: *Nuclear Instruments and Methods in Physics Research Section A: Accelerators, Spectrometers, Detectors and Associated Equipment* 560 (2 May 2006), pp. 405–408. DOI: 10.1016/J.NIMA.2005.12.222 (cited on pages 12, 41, 93).

[10] A. Acker et al. 'The CLAS12 Forward Tagger'. In: *Nuclear Instruments and Methods in Physics Research Section A: Accelerators, Spectrometers, Detectors and Associated Equipment* 959 (Apr. 2020), p. 163475. DOI: 10.1016/j.nima.2020.163475 (cited on pages 12, 14).

[11] S Andriamonje et al. 'Development and performance of Microbulk Micromegas detectors'. In: *Journal of Instrumentation* 5.02 (2010), P02001–P02001. DOI: 10.1088/1748-0221/5/02/p02001 (cited on page 12).

[12] M. Chefdeville et al. 'An electron-multiplying 'Micromegas' grid made in silicon wafer post-processing technology'. In: *Nuclear Instruments and Methods in Physics Research Section A: Accelerators, Spectrometers, Detectors and Associated Equipment* 556.2 (2006), pp. 490–494. DOI: 10.1016/j.nima.2005.11.065 (cited on page 13).

[13] J. Derré and I. Giomataris. 'Spatial resolution and rate capability of MICROMEGAS detector'. In: *Nuclear Instruments and Methods in Physics Research Section A: Accelerators, Spectrometers, Detectors and Associated Equipment* 461.1-3 (2001), pp. 74–76. DOI: 10.1016/S0168-9002(00)01171-2 (cited on page 14).

[14] J. Bortfeldt et al. 'PICOSEC: Charged particle timing at sub-25 picosecond precision with a Micromegas based detector'. In: *Nuclear Instruments and Methods in Physics Research Section A: Accelerators, Spectrometers, Detectors and Associated Equipment* 903 (2018), pp. 317–325. DOI: 10.1016/J.NIMA.2018.04.033 (cited on page 14).

[15] D. Thers et al. 'Micromegas as a large microstrip detector for the COMPASS experiment'. In: *Nuclear Instruments and Methods in Physics Research Section A: Accelerators, Spectrometers, Detectors and Associated Equipment* 469.2 (2001), pp. 133–146. DOI: 10.1016/S0168-9002(01)00769-0 (cited on page 14).

[16] S. Bouteille et al. 'A Micromegas-based telescope for muon tomography: The WatTo experiment'. In: *Nuclear Instruments and Methods in Physics Research, Section A: Accelerators, Spectrometers, Detectors and Associated Equipment* 834 (2016), pp. 223–228. DOI: 10.1016/J.NIMA.2016.08.002 (cited on pages 14, 27, 29, 30, 42).

[17] D. Attié et al. 'Characterization of resistive Micromegas detectors for the upgrade of the T2K Near Detector Time Projection Chambers'. In: *Nuclear Instruments and Methods in Physics Research Section A: Accelerators, Spectrometers, Detectors and Associated Equipment* 1025 (Feb. 2021), p. 166109. DOI: 10.1016/J.NIMA.2021.166109 (cited on pages 14, 109, 115).

[18] Wenxin Wang. 'A Large Area Micromegas TPC for Tracking at the ILC'. Theses. Université Paris Sud - Paris XI, June 2013 (cited on page 14).

[19] D. Attié. 'TPC review'. In: *Nuclear Instruments and Methods in Physics Research Section A: Accelerators, Spectrometers, Detectors and Associated Equipment* 598.1 (2009). Instrumentation for Collding Beam Physics, pp. 89–93. DOI: 10.1016/j.nima.2008.08.114 (cited on page 15).

[20] M Huk, P Igo-Kemenes, and A Wagner. 'Electron attachment to oxygen, water, and methanol, in various drift chamber gas mixtures'. In: *Nuclear Instruments and Methods in Physics Research Section A: Accelerators, Spectrometers, Detectors and Associated Equipment* 267.1 (1988), pp. 107–119. DOI: 10.1016/0168-9002(88)90635-3 (cited on page 16).

[21] T. Alexopoulos et al. 'A spark-resistant bulk-micromegas chamber for high-rate applications'. In: *Nuclear Instruments and Methods in Physics Research Section A: Accelerators, Spectrometers, Detectors and Associated Equipment* 640.1 (2011), pp. 110–118. DOI: 10.1016/J.NIMA.2011.03.025 (cited on page 16).

[22] Christian Lippmann. 'Performance of the ALICE Time Projection Chamber'. In: *Physics Procedia* 37 (2012), pp. 434–441. DOI: 10.1016/J.PHPRO.2012.02.390 (cited on page 18).

[23] Andreas Mathis and on collaboration on. 'Study of the $\mathrm{d}E/\mathrm{d}x$ resolution of a GEM Readout Chamber prototype for the upgrade of the ALICE TPC'. In: *EPJ Web of Conferences* 174 (July 2017). DOI: 10.1051/epjconf/201817401002 (cited on page 18).

[24] Carl D. Anderson and Seth H. Neddermeyer. 'Cloud Chamber Observations of Cosmic Rays at 4300 Meters Elevation and Near Sea-Level'. In: *Phys. Rev.* 50 (4 Aug. 1936), pp. 263–271. DOI: 10.1103/PhysRev.50.263 (cited on page 21).

[25] Mengyun Guan et al. *A parametrization of the cosmic-ray muon flux at sea-level*. 2015. DOI: 10.48550/ARXIV.1509.06176 (cited on pages 22, 24, 69).

[26] Alessandro Lechmann et al. 'Muon tomography in geoscientific research – A guide to best practice'. In: *Earth-Science Reviews* 222 (Oct. 2021), p. 103842. DOI: 10.1016/j.earscirev.2021.103842 (cited on page 23).

[27] Prashant Shukla and Sundaresh Sankrith. *Energy and angular distributions of atmospheric muons at the Earth*. 2018 (cited on page 24).

[28] S. Agostinelli et al. 'GEANT4 - A simulation toolkit'. In: *Nuclear Instruments and Methods in Physics Research, Section A: Accelerators, Spectrometers, Detectors and Associated Equipment* 506 (3 July 2003), pp. 250–303. DOI: 10.1016/S0168-9002(03)01368-8 (cited on pages 25, 31, 32, 69, 70, 100).

[29] H. A. Bethe. 'Molière's Theory of Multiple Scattering'. In: *Phys. Rev.* 89 (6 Mar. 1953), pp. 1256–1266. DOI: 10.1103/PhysRev.89.1256 (cited on page 26).

[30] Yung-Su Tsai. 'Pair production and bremsstrahlung of charged leptons'. In: *Rev. Mod. Phys.* 46 (4 Oct. 1974), pp. 815–851. DOI: 10.1103/RevModPhys.46.815 (cited on page 27).

[31] S. Pesente et al. 'First results on material identification and imaging with a large-volume muon tomography prototype'. In: *Nucl. Instrum. Meth. A* 604 (2009), pp. 738–746. DOI: 10.1016/j.nima.2009.03.017 (cited on page 28).

[32] Sridhar Tripathy et al. 'Material Identification with Cosmic Ray Muons using RPCs'. In: *Journal of Instrumentation* 14 (July 2019), pp. C07007–C07007. DOI: 10.1088/1748-0221/14/07/C07007 (cited on page 28).

[33] Kunihiro Morishima et al. 'Discovery of a big void in Khufu's Pyramid by observation of cosmic-ray muons'. In: *Nature* 552.7685 (2017). DOI: 10.1038/nature24647 (cited on pages 29–31, 55).

[34] S Procureur et al. 'First 3D imaging of a nuclear reactor using muography measurements (submitted)'. In: *Science Advances* () (cited on pages 29, 35, 69).

[35] S Procureur et al. 'Muon metrology and positioning: the POMME experiment'. In: (). DOI: 10.1088/1748-0221/16/07/P07013 (cited on page 29).

[36] 'Muons tomography applied to geosciences and volcanology'. In: *Nuclear Instruments and Methods in Physics Research Section A: Accelerators, Spectrometers, Detectors and Associated Equipment* 695 (Dec. 2012), pp. 23–28. DOI: 10.1016/J.NIMA.2011.11.061 (cited on page 29).

[37] C. Flouzat et al. 'Dream: a 64-channel front-end chip with analogue trigger latency buffer for the Micromegas tracker of the CLAS12 experiment'. In: *Proc. of TWEPP conference* (2 2014). DOI: 10.1016/J.NIMA.2005.12.222 (cited on pages 29, 40, 44).

[38] Kunihiro Morishima et al. 'Precise characterization of a corridor-shaped structure in Khufu's pyramid by observation of cosmic-ray muons'. In: *Accepted in Nature Communication* (2022) (cited on pages 30–32).

[39] 'A spark-resistant bulk-micromegas chamber for high-rate applications'. In: *Nuclear Instruments and Methods in Physics Research Section A: Accelerators, Spectrometers, Detectors and Associated Equipment* 640 (1 June 2011), pp. 110–118. DOI: 10.1016/J.NIMA.2011.03.025 (cited on page 31).

[40] S. Procureur et al. 'Why do we flush gas in gaseous detectors?' In: *Nucl. Instrum. Meth. A* 955 (2020), p. 163290. DOI: 10.1016/j.nima.2019.163290 (cited on pages 31, 47).

[41] Sophie Wuyckens et al. 'A portable muon telescope based on small and gas-tight resistive plate chambers'. In: (). DOI: 10.1098/rsta.2018.0139 (cited on page 33).

[42] A. Obertelli et al. 'MINOS: A vertex tracker coupled to a thick liquid-hydrogen target for in-beam spectroscopy of exotic nuclei'. In: (). DOI: 10.1140/epja/i2014-14008-y (cited on page 40).

[43] S. Procureur, R. Dupré, and S. Aune. 'Genetic multiplexing and first results with a 50×50 cm2 Micromegas'. In: *Nuclear Instruments and Methods in Physics Research Section A: Accelerators, Spectrometers, Detectors and Associated Equipment* 729 (Nov. 2013), pp. 888–894. DOI: 10.1016/J.NIMA.2013.08.071 (cited on pages 42, 73).

[44] C. Flouzat et al. 'DREAM: a 64-channel Front-end Chip with Analog Trigger Latency Buffer for the Micromegas Tracker of the CLAS12 Experiment'. In: *TWEPP 2014 – Topical Workshop on Electronics for Particle Physics* () (cited on page 44).

[45] H. J. Hilke and W. Riegler. 'Gaseous Detectors'. In: *Particle Physics Reference Library: Volume 2: Detectors for Particles and Radiation*. Ed. by Christian Wolfgang Fabjan and Herwig Schopper. Cham: Springer, 2020, pp. 91–136. DOI: 10.1007/978-3-030-35318-6_4 (cited on page 57).

[46] Rene Brun and Fons Rademakers. 'ROOT - An Object Oriented Data Analysis Framework'. In: *Nuclear Instruments and Methods in Physics Research Section A: Accelerators, Spectrometers, Detectors and Associated Equipment* 389 (1997), pp. 81–86 (cited on page 70).

[47] Martin A. Fischler and Robert C. Bolles. 'Random Sample Consensus: A Paradigm for Model Fitting with Applications to Image Analysis and Automated Cartography'. In: *Commun. ACM* 24.6 (1981), pp. 381–395. DOI: 10.1145/358669.358692 (cited on page 71).

[48] Richard O. Duda and Peter E. Hart. 'Use of the Hough Transformation to Detect Lines and Curves in Pictures'. In: *Commun. ACM* 15.1 (1972), pp. 11–15. DOI: 10.1145/361237.361242 (cited on page 77).

[49] Fukuda Y. et al. 'Evidence for oscillation of atmospheric neutrinos'. In: *Physical Review Letters* 81.8 (1998), pp. 1562–1567. DOI: 10.1103/PhysRevLett.81.1562 (cited on page 87).

[50] K. Abe et al. 'T2K neutrino flux prediction'. In: *Phys. Rev. D* 87 (1 Jan. 2013), p. 012001. DOI: 10.1103/PhysRevD.87.012001 (cited on page 91).

[51] S Assylbekov et al. 'The T2K ND280 off-axis pi–zero detector'. In: *Nuclear Instruments and Methods in Physics Research Section A: Accelerators, Spectrometers, Detectors and Associated Equipment* 686 (2012), pp. 48–63. DOI: https://doi.org/10.1016/j.nima.2012.05.028 (cited on page 93).

[52] K. Abe et al. 'The T2K experiment'. In: *Nuclear Instruments and Methods in Physics Research Section A: Accelerators, Spectrometers, Detectors and Associated Equipment* 659.1 (2011), pp. 106–135. DOI: 10.1016/j.nima.2011.06.067 (cited on page 96).

[53] K. Abe et al. 'Observation of Electron Neutrino Appearance in a Muon Neutrino Beam'. In: *Phys. Rev. Lett.* 112 (6 Feb. 2014), p. 061802. DOI: 10.1103/PhysRevLett.112.061802 (cited on page 96).

[54] T2K Collaboration et al. 'Precise Measurement of the Neutrino Mixing Parameter θ_{23} from Muon Neutrino Disappearance in an Off-axis Beam'. In: (2014). DOI: 10.48550/arxiv.1403.1532 (cited on page 96).

[55] and K. Abe et al. 'Measurement of the charged-current electron (anti-)neutrino inclusive cross-sections at the T2K off-axis near detector ND280'. In: *Journal of High Energy Physics* 2020.10 (2020). DOI: 10.1007/jhep10(2020)114 (cited on page 96).

[56] K. Abe et al. 'Measurement of the inclusive ν_μ charged current cross section on carbon in the near detector of the T2K experiment'. In: *Phys. Rev. D* 87 (9 May 2013), p. 092003. DOI: 10.1103/PhysRevD.87.092003 (cited on page 96).

[57] K Abe et al. 'Constraint on the matter-antimatter symmetry-violating phase in neutrino oscillations Check for updates'. In: *Nature* (). DOI: 10.1038/s41586-020-2177-0 (cited on page 96).

[58] Ko Abe et al. 'Proposal for an Extended Run of T2K to 20×10^{21} POT'. In: (Sept. 2016) (cited on pages 98, 99).

[59] Andrew D. Missert. 'Improving the T2K Oscillation Analysis With fiTQun: A New Maximum-Likelihood Event Reconstruction for Super-Kamiokande'. In: *Journal of Physics: Conference Series* 888 (Sept. 2017), p. 012066. DOI: 10.1088/1742-6596/888/1/012066 (cited on page 98).

[60] Yoshinari Hayato and Luke Pickering. 'The NEUT neutrino interaction simulation program library'. In: *The European Physical Journal Special Topics* 230.24 (2021), pp. 4469–4481. DOI: 10.1140/epjs/s11734-021-00287-7 (cited on page 99).

[61] K. Abe et al. 'T2K ND280 Upgrade - Technical Design Report'. In: (Jan. 2019) (cited on pages 99, 100, 103).

[62] David Attié et al. 'Performances of a resistive Micromegas module for the Time Projection Chambers of the T2K Near Detector upgrade'. In: *Nuclear Instruments and Methods in Physics Research Section A: Accelerators, Spectrometers, Detectors and Associated Equipment* 957 (Mar. 2020), p. 163286. DOI: 10.1016/j.nima.2019.163286 (cited on pages 103, 105).

[63] G. Prior. 'The HARP time projection chamber'. In: *Nuclear Physics B - Proceedings Supplements* 125 (2003), pp. 37–42. DOI: 10.1016/S0920-5632(03)90963-7 (cited on page 103).

[64] Pascal Baron et al. 'AFTER, an ASIC for the Readout of the Large T2K Time Projection Chambers'. In: *IEEE Transactions on Nuclear Science* 55.3 (2008), pp. 1744–1752. DOI: 10.1109/TNS.2008.924067 (cited on pages 104, 115).

[65] D Attié. 'Beam tests of Micromegas LC-TPC large prototype'. In: *Journal of Instrumentation* 6.01 (2011), pp. C01007–C01007. DOI: 10.1088/1748-0221/6/01/c01007 (cited on page 112).

[66] K. Boudjemline et al. 'Spatial resolution of a GEM readout TPC using the charge dispersion signal'. In: *Nuclear Instruments and Methods in Physics Research Section A: Accelerators, Spectrometers, Detectors and Associated Equipment* 574.1 (2007), pp. 22–27. DOI: 10.1016/j.nima.2007.01.017 (cited on page 112).

[67] Denis Calvet. 'Back-end Electronics for Low Background and Medium Scale Physics Experiments Based on an Asymmetric Network'. In: (2018). DOI: 10.48550/ARXIV.1806.07618 (cited on page 115).

[68] Denis Bernard et al. 'HARPO: a TPC as a gamma-ray telescope and polarimeter'. In: 9144 (2014). Ed. by Tadayuki Takahashi, Jan-Willem A. den Herder, and Mark Bautz, p. 91441M. DOI: 10.1117/12.2055307 (cited on page 115).

[69] S. Anvar et al. 'AGET, the GET front-end ASIC, for the readout of the Time Projection Chambers used in nuclear physic experiments'. In: (2011), pp. 745–749. DOI: 10.1109/NSSMIC.2011.6154095 (cited on page 115).

[70] D. Baudin et al. 'ASTRE: ASIC with switched capacitor array (SCA) and trigger for detector readout electronics hardened against Single Event Latchup (SEL)'. In: *Nuclear Instruments and Methods in Physics Research Section A: Accelerators, Spectrometers, Detectors and Associated Equipment* 912 (2018). New Developments In Photodetection 2017, pp. 66–69. DOI: 10.1016/j.nima.2017.10.043 (cited on page 115).

[71] HA-TPC ERAM detector group. 'Encapsulated Resistive Anode Micromegas Production Readiness Review'. In: *Internal document* (2020) (cited on page 120).

[72] X. Llopart et al. 'Timepix, a 65k programmable pixel readout chip for arrival time, energy and/or photon counting measurements'. In: *Nuclear Instruments and Methods in Physics Research Section A: Accelerators, Spectrometers, Detectors and Associated Equipment* 581.1 (2007). VCI 2007, pp. 485–494. DOI: 10.1016/j.nima.2007.08.079 (cited on page 127).

[73] W. Riegler. 'Electric fields, weighting fields, signals and charge diffusion in detectors including resistive materials'. In: *Journal of Instrumentation* 11.11 (2016), P11002–P11002. DOI: 10.1088/1748-0221/11/11/p11002 (cited on page 130).

université PARIS-SACLAY

ÉCOLE DOCTORALE
Particules, hadrons, énergie et noyau : instrumentation, imagerie, cosmos et simulation (PHENIICS)

Titre : Développement de nouvelles chambres à projection temporelle pour applications sociétales et académiques : tomographie muonique en environnement restreint et upgrade du détecteur proche de T2K

Mots clés : Tomographie muonique, Micromégas, Instrumentation, T2K

Résumé : La tomographie muonique est un exemple de comment la recherche fondamentale en physique des particules peut profiter à la société. Des télescopes à muons basés sur la technologie Micromegas ont été développés et ont permis la détection de cavités inconnues jusqu'alors dans la pyramide de Gizeh. De ce premier succès sont nées de nouvelles applications possibles pour la tomographie muonique souterraine qui requièrent le développement d'un nouvel instrument capable de reconstruire les traces en 3 dimensions et dans un environnement restreint. Le design de D3DT (Détecteur 3D pour Tomographie muonique) est décrit et les premiers prototypes sont développés et caractérisés. Les performances d'un nouvel algorithme de reconstruction sont testées sur des données simulées. Les premiers prototypes ont pu être utilisés pour acquérir des données sur lesquelles la nouvelle reconstruction a été utilisée.

En parallèle, l'expérience T2K qui étudie les différences de masse et le mélange des saveurs des neutrinos en mesurant leurs oscillations est en phase d'upgrade. En particulier, de nouvelles Chambres à Projection Temporelle (TPCs) vont être installées sur le détecteur proche afin d'améliorer l'efficacité de reconstruction des traces à grand angle. Un test faisceau est réalisé afin d'optimiser le design du prototype avant la phase de production puis les performances des différents modules sont validées. De potentielles améliorations de l'analyse sont également investiguées.

Title : Development of new Time Projection Chambers for societal and academic applications : muon tomography in confined environment and T2K upgrade of the near detector.

Keywords : Muon Tomography, Micromegas detector, instrumentation, T2K

Abstract : Muon tomography is an example of how fundamental research in particle physics can benefit society. Micromegas-based telescopes were developed and successfully detected unknown cavities in Khufu's pyramid. With this first success came the possibilities for novel underground applications requiring the development of a new instrument capable of performing 3D track reconstruction in a confined environment. The design of D3DT (Detector 3D for muon Tomography) is discussed and the first prototypes are developed and characterized. The performances of a new reconstruction algorithm are also tested on simulated data. D3DT first prototypes are successfully operated and the reconstruction algorithm is applied on the acquired data.

At the same time the T2K experiment, which probes the mass differences and mixing of neutrinos by measuring neutrino oscillations, is being upgraded. In particular, new Time Projection Chambers (TPCs) have to be installed on the near detector to ensure a better efficiency of the high angle tracks reconstruction. A test beam is conducted in order to fix the prototype design before production and a validation of performances is achieved. Potential improvements of the analysis are also investigated.